Author:
Moss, Joanna J

Title:
Investigating the role of autophagy in musculoskeletal development and homeostasis using zebrafish

Investigating the Role of Autophagy in Musculoskeletal Development and Homeostasis using Zebrafish

by

Joanna J. Moss

Department of Life Sciences

UNIVERSITY OF BRISTOL

March 2022

A dissertation submitted to the University of Bristol in accordance with the requirements for award of the degree of Doctor of Philosophy in the Faculty of Life Sciences.

Word count: 58,746

Abstract

Autophagy is a key catabolic process responsible for the removal of waste and damaged cell components by lysosomal degradation. It plays an important role in fundamental cell processes, including ER stress mitigation, control of cell metabolism, and cell differentiation and proliferation, all of which are essential for the development and survival of bone and cartilage cells, and for skeletogenesis. Correspondingly, autophagy dysregulation has been implicated in several skeletal disorders, including the joint disease, osteoarthritis (OA). OA is the most common cause of arthritis globally and one the biggest causes of disability, affecting 15% of the UK population. It is characterised by the progressive degeneration of articular cartilage at the joint interface, leading to exposure of the underlying bone and joint misalignment, pain, and loss of function.

In this thesis, the role of autophagy-related genes: *atg13* and *lmx1b,* in skeletal development and joint function was explored using zebrafish lines mutant for these genes. Loss of autophagy activity in the *atg13* mutants caused an acceleration to chondrocyte (cartilage cell) maturation, leading to changes in extra-cellular matrix (ECM) formation and restricted jaw joint mobility. These results are consistent with autophagy contributing to the regulation of chondrocyte maturation which supports joint formation and function. Meanwhile, characterisation of the *lmx1b* mutant lines demonstrated that the *lmx1b* paralogues, *lmx1ba* and *lmx1bb* have divergent roles in zebrafish development, affecting skeletal and neuronal development, and renal development, respectively. Whilst loss of both paralogues (*lmx1b dKO*) resulted in muscular abnormalities and reduced body growth. As adults, loss of *lmx1b* caused skeletal changes reminiscent of premature OA and behavioural changes, suggesting a role for *lmx1b* in skeletal and neuronal development and maintenance. Overall, these results expand our understanding of the roles played by autophagy and *lmx1b* in cartilage and joint development, among other systems, broadening our understanding of OA pathogenesis.

Acknowledgements

Firstly, I would like to thank my two supervisors, Jon and Chrissy. Thank you both for accepting me into your labs and for the time you've both dedicated to teaching, guiding, supporting and directing me. Your consistent encouragement and belief in my ability have been pivotal in my growth as a scientist, and I know I come away from this PhD as a more confident, independent and competent researcher because of your input. Thank you for being exactly the supervisors I needed and for helping me to accomplish all that I have in this PhD.

To members of the Lane and Hammond labs, and the Richardson and Martin labs, thank you for the contributions of your help and time to this project and for making my PhD so enjoyable. I feel so privileged to have been a part of such a great group of scientists and people and I don't think I could have found a better team to do my PhD with. In particular, thank you to Natalia for showing me everything I needed to know in the Lane lab and for giving me a benchmark to strive for as a PhD student and Postdoc. To Erika, thank you for all of the time and help you've given me, for answering my many questions, and for always being on my case. And to Lucy, Lizzie and Georgie, and the rest of my PhD cohort, Beth, Hope, Eddie and Ted. It has been a joy to work with each of you, thank you for helping to make this PhD the best experience it could have been.

I would also like to thank members of the Wolfson Bioimaging facility for their help and expertise, especially Stephen Cross for his image analysis wizardry and Chris Neal for being the best EM-kidney-fishy specialist in the business. To the ASU staff in the fish facility, particularly Mathew Green; thank you for your time, help and knowledge – without you the work in this PhD would not have been possible. And to the Wellcome Trust, who generously funded this PhD at the University of Bristol.

To my small group family, it was at my first small group meeting that you told me to go for the 'fish project' because zebrafish sounded cool, and 4 years later, you weren't wrong. Thank you all for your continual encouragement, wisdom, joy and prayers (for me and the

fish); my time in Bristol would not be the same without you. To Emily, you, of course, were the inspiration behind all of my mutants. To Laura, thank you for always being there with encouraging words when I needed them, and to Andrew, for laughing at me when things went wrong. You are two of my favourites and it has been a joy to be your friend and co-leader. And to the lovely Greens; Dan, Karen, Jaz, Layla, Noah and Trixie, thank you for letting me share in your family's life these last 4 years. You have been one of the biggest blessings in my life in Bristol and I can't adequately express how grateful I am for you all except to say that your home is one of my favourite places to be in Bristol.

To my friends, both in Bristol and beyond: Michael, Sarah and Emma, Laura, Ellie, Zoë and Rachel, Leah and Kevin, and Joanna. Your support and love mean the world to me, and I feel blessed that I get to share this life, and all of its highs and lows, with each of you. And to Charlotte, thank you for making me laugh most days and for ensuring that my feet remain firmly on the ground.

To my brothers, who I'm not sure have supported me that much through my PhD but have always had an unwavering confidence in my ability to achieve whatever I set out to do. To all four of you, Rich, Dave, Rob and Matt, thank you for believing in me more than I do and for teaching me to laugh at myself. And thank you to Rich and Em, Rob and Hannah for giving me two of the best gifts, my gorgeous niece and nephew. Boaz and Isabella, you have been like two bright suns of joy in my life this last year and I love you both more than I knew to be possible.

To my parents, Malcolm and Joy, you have been the ones cheering me on every step of the way in my journey through academia. Thank you for your steadfast support and for always being on the other end of the phone when I needed your encouragement or advice, or the space to lament or celebrate. I cannot thank you enough for all that you have done for me, I am so grateful to have you as my parents and I am proud to be your daughter. I love you.

Finally, to the Author and Creator of it all. You have been the One guiding me through every step and I know I wouldn't be where I am today without You. As I look ahead, I pray that I can keep trusting and following the steps You lay out for me.

Author's declaration

I declare that the work in this dissertation was carried out in accordance with the requirements of the University's Regulations and Code of Practice for Research Degree Programmes and that it has not been submitted for any other academic award. Except where indicated by specific reference in the text, the work is the candidate's own work. Work done in collaboration with, or with the assistance of, others is indicated as such. Any views expressed in the dissertation are those of the author.

SIGNED: ..... [redacted] **..... DATE:**17/03/22.....

Table of Contents

Chapter 3. Exploring the role of autophagy in coordinating chondrocyte development and maturation in zebrafish

List of Figures

FIGURE **PAGE**

List of Tables

TABLE **PAGE**

List of Abbreviations

The table below lists abbreviations included in this thesis, abbreviations are ordered alphabetically and are case sensitive.

Table I - List of abbreviations found in this thesis

5-HT	5-hydroxytryptamine (serotonin)
ADHD	Attention Deficit Hyperactivity Disorder
ANOVA	Analysis of Variance
ATG	Autophagy-related
ATG13	Autophagy-related 13
BafA1	Bafilomycin A1
Beclin1	Coiled-coil myosin-like BCL-2-interacting protein
BMP	Bone Morphogenic Proteins
Cas9	CRISPR-associated protein 9
CMA	Chaperone Mediated Autophagy
Col2a1	Collagen Type II α1
Col9a3	Collagen Type IX α3
Col10a1	Collagen Type X α1
Col11a2	Collagen Type XI α2
CRISPR	Clustered Regularly Interspaced Short Palindromic Repeats
crRNA	CRISPR RNA
CTSK	Cathepsin K
DA	Dopamine
DAPI	4′,6-diamidino-2-phenylindole

dCas9	Deactivated Cas-9 protein
ddH_2O	Double Distilled H_2O
dHet	Double Heterozygous mutant (*lmx1ba*$^{-/-}$;*lmx1bb*$^{-/-}$)
dKO	Double Knock-out mutant (*lmx1ba*$^{-/-}$;*lmx1bb*$^{-/-}$)
DMSO	Dimethyl Suphoxide
DNA	Deoxyribonucleic Acid
dpf	days post-fertilisation
ECM	Extracellular Matrix
EDTA	Ethylenediaminetetraacetic Acid
EdU	EdU (5-ethynyl-2'-deoxyuridine)
ER	Endoplasmic Reticulum
FACS	Fluorescent Activated Cell Sorting
FIP200	Focal adhesion kinase family Interacting Protein of 200 kDa
FOXO	Forkhead box O
G	Generation
GABARAP	Gamma-Aminobutyric Acid Receptor-Associated Protein
GAG	Glycosaminoglycan
GAPDH	Glyceraldehyde-3-phosphate Dehydrogenase
GBM	Glomerular Basement Membrane
GDF5	Growth/Differentiation Factor 5
GFP	Green Fluorescence Protein
gRNA	Guide RNA
GWAS	Genome Wide Association Study
HD	Homeodomain
HEK293T	Human Embryonic Kidney 293T
HORMA	Hop1/Rev7/Mad2
hpf	hours post-fertilisation
HSCs	Hematopoietic Stem Cells
ICZ	Intercalation Zone
IDR	Intrinsically Disordered Region

IH	Interhyal
IMA	Intermandibularis Anterior
IMP	Intermandibularis Posterior
IsO	Isthmic Organiser
KO	Knock-out
KO;Het	*lmx1ba* knock-out;*lmx1bb* heterozygous mutants (*lmx1ba*$^{-/-}$;*lmx1bb*$^{-/+}$)
LAMP	Lysosome-Associated Membrane Protein
LC3-I	Unlipidated LC3
LC3-II	Lipidated LC3
LIM	Lin-11, Islet-1, Mec-3
LIR	LC3 Interacting Region
LMX1B	LIM homeobox transcription factor 1 Beta
LRO	Lysosome-Related Organelles
LysoT	LysoTracker
MAP1LC3	Microtubule-Associated Protein 1A/1B-Light Chain
mCherry	Monomeric Cherry
mDA	Midbrain Dopaminergic
MHB	Midbrain-hindbrain boundary
MIA	Modular Image Analysis
ml	Millilitres
mm	Millimetres
mM	Millimolar
mpf	Months post-fertilisation
mRNA	Messenger RNA
MS222	Tricaine methanesulfonate
MSCs	Mesenchymal Stem Cells
mTORC1	Mammalian Target of Rapamycin Complex 1
NHEJ	Non-homologous End Joining
nm	Nanometre
NPS	Nail-patella Syndrome

O	Oligo
OA	Osteoarthritis
°C	Degrees Celsius
PBS	Phosphate Buffered Saline
PCR	Polymerase Chain Reaction
PFA	Paraformaldehyde
PE	Phosphatidylethanolamine
PI3KC3	Phosphatidyl Inositol 3-Kinase Complex I
PI3P	Phosphatidylinositol-3-Phosphate
qRT-PCR	Quantitative Reverse Transcription Polymerase Chain Reaction
RIPA	Radioimmunoprecipitation Assay
RNA	Ribonucleic Acid
RNP	Ribonucleoprotein
ROI	Region of Interest
ROS	Reactive Oxygen Species
RUNX2	Runt-related factor 2
SNP	Single-Nucleotide Polymorphism
SOX9	SRY-related HMG-box 9
Tg	Transgenic
TH	Tyrosine Hydroxylase
tracrRNA	Transactivating crRNA
TUNEL	Terminal deoxynucleotidyl transferase dUTP Nick End Labelling
ULK	Unc51-like kinase
V-ATPase	Vacuolar-type H+ -ATPase
WNT	Wingless-related Integration site
wt	Wild-type
μCT	Micro-computed Tomography
μm	Micrometre
μM	Micromolar

Chapter 1. Introduction

At a glance…

This introductory chapter will initially focus on the autophagy pathway and its roles in the body, concentrating in particular on the skeletal system and its associated cell types. Next, the implications of autophagy dysregulation on joint homeostasis and disease states, such as osteoarthritis will be discussed. This will be followed by an explanation on how zebrafish can be used as a model to investigate the contribution of autophagy activity to skeletal development. Finally, the autophagy transcriptional regulator, LMX1B, will be introduced as a gene of interest along with the pleiotropic phenotype of its associated disorder, Nail-patella syndrome, before concluding with the aims of this thesis.

CHAPTER

1

Introduction

Some of the text and figures within this chapter have been previously published in a review within Histochemistry and Cell Biology (1). Text and some figures and figure legends from the publication have been adapted for this thesis, as noted in the figure legends where appropriate. For this publication, I was first author, and I was responsible for writing and editing the manuscript, generating all figures and figure legends, and responding to the reviewers' comments.

1.1 Autophagy

Autophagy is a catabolic process which enables the breakdown of cytosolic components into basic biomolecules by lysosomal degradation so that they may be recycled for further use. It is a dynamic and adaptive process that is continually active within cells and is vital to the maintenance of cellular homeostasis. One of its main functions is to mobilise nutrients to sustain vital cellular functions during stress, although it has various other cellular functions that extend beyond basic housekeeping roles (2). Under normal cell conditions autophagy occurs at a basal level, however, in response to certain types of environmental stress, including nutrient deprivation, growth factor depletion, infection and hypoxia, a dramatic induction in autophagy is triggered (3).

There are three defined forms of autophagy; chaperone-mediated autophagy, microautophagy and macroautophagy, with each being delineated by the method of cargo delivery to the lysosome for degradation (Figure 1.1). In chaperone-mediated autophagy (CMA), target proteins are selected for degradation by the chaperone protein Hsc70 and associated co-chaperones which recognise a 5 peptide sequence (typically KFERQ) within the protein (4). These chaperones direct proteins to the lysosome where they are received by the transmembrane protein, lysosome-associated membrane protein type 2A (LAMP-2A; an isoform of LAMP-2), unfolded and delivered to the lysosomal lumen for degradation (5). CMA differs from the following two forms of autophagy as it is extremely selective in the proteins it targets for degradation (6).

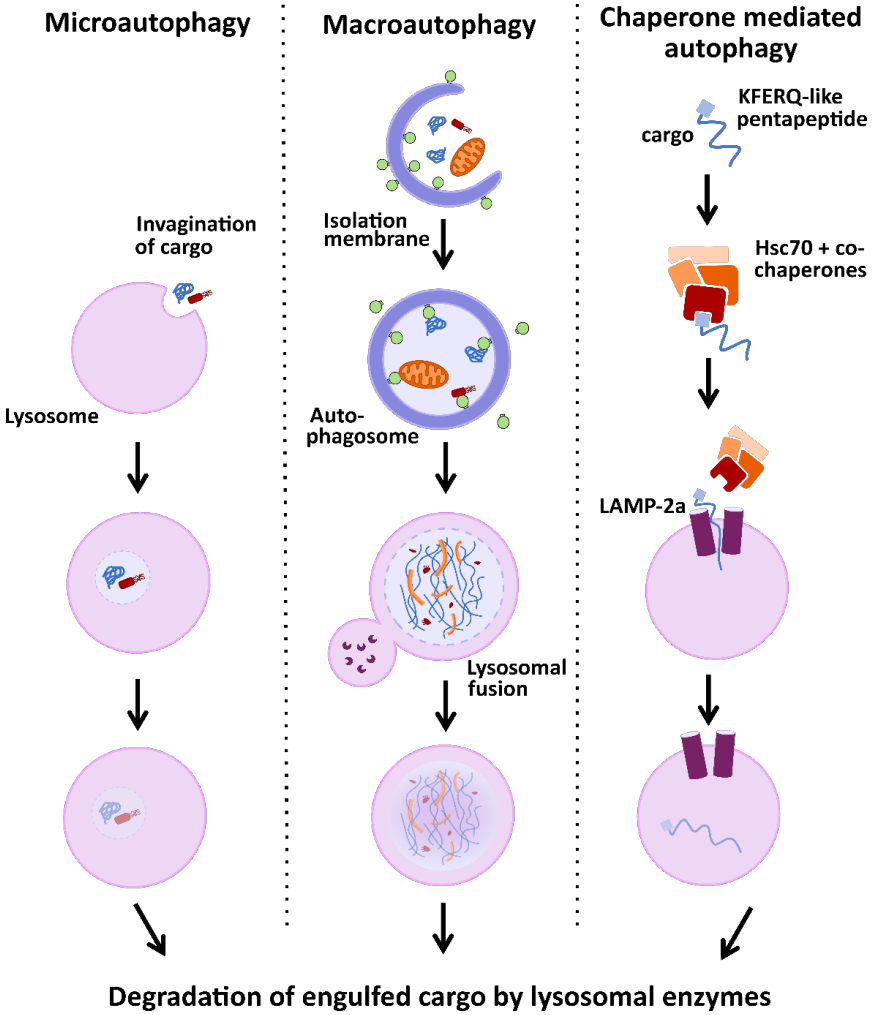

Figure 1.1 – The three distinct mechanisms of autophagy, Simplified schematic showing the main steps involved in the three autophagy pathways.

In microautophagy, cytosolic components are engulfed directly by lysosomes through inward invagination of the lysosomal membrane. By contrast, macroautophagy involves the *de novo* formation of an intermediate organelle, the autophagosome, to deliver cargo to the lysosome for degradation. The autophagosome is a unique double-membrane structure which captures proteins, organelles, and other cellular debris within the cytoplasm before fusing with the lysosome to form a degradative autolysosome. This sequestration of cytosolic components can operate as a non-selective or selective process, with the former considered as a bulk, non-specific degradative process, whilst the latter requires specific receptor proteins to recognise and sequester target proteins, molecules, organelles, or invading pathogens. Macroautophagy is thought to be the major form of autophagy and compared to CMA and microautophagy, is the most widely studied (7). Therefore, for the remainder of this thesis, macroautophagy will be referred to as autophagy.

1.1.1 The mechanism of autophagy

The autophagy pathway is a tightly regulated, multi-step process that is largely mediated by highly conserved ATG (autophagy-related) genes (Figure 1.1.1) (6, 8). The ATG genes were first identified and characterised by Yoshinori Ohsumi and colleagues in the early 1990's, after identifying 15 yeast mutants that had defective autophagy (9, 10). To date, over 40 ATGs have been identified in yeast, most of which are also conserved across higher eukaryotes (11, 12). Following the discovery of these ATG genes, there has been an explosion of research focussed on delineating the fundamental mechanisms guiding the autophagic pathway, leading, in 2016 to a Nobel Prize in Physiology or Medicine being awarded to Ohsumi for his isolation and dissection of molecular processes of autophagy (13, 14). Broadly, the autophagic pathway can be split into three major steps: initiation and formation of the autophagosome, autophagosome elongation and finally, lysosomal fusion. At each of these steps, dedicated ATG proteins and complexes are recruited and activated at distinct sites of autophagosome assembly known as autophagosome initiation sites. As the nascent autophagosome is expanded, sealed, and trafficked to the lysosome, essential contributions are made by proteins co-opted from other cellular membrane trafficking pathways such as ESCRT complex proteins, tethers and SNAREs (15).

As this thesis focuses primarily on components of the zebrafish autophagy pathway, which is very similar to the mammalian system, only proteins pertinent to this pathway will be discussed. The initial step of the autophagy process is orchestrated by two main complexes. The first is the Unc-51-like kinase 1/2 (ULK1/2) complex, consisting of ULK1/2, ATG101, FIP200 and ATG13. As the first complex to form within the autophagy pathway, the correct assembly and function of this complex is critical to initiating autophagy activity. ATG13 plays an important role in this process as it provides a scaffold for ATG101 and ULK1/2 recruitment and binding (16). Therefore, loss of ATG13 would severely impair autophagy function, as shown by several *Atg13* knock-out models (17). As a gene of interest in this thesis, the roles and function of *atg13* will be discussed further in Chapter 3.

Upon autophagy induction, the ULK1/2 complex translocates to the isolation membrane of the nascent autophagosome where it phosphorylates components of the second complex, the class III phosphatidyl inositol 3-kinase complex I (PI3KC3), comprising VPS34, Beclin1, ATG14, AMBRA1 and p115, which are involved in autophagy initiation and autophagosome formation. This helps to trigger production of phosphatidylinositol-3-phosphate (PI3P) at the isolation membrane site, which acts as a signal for the recruitment of PI3P effector proteins, WIPI2 and DCFP1 and the formation of an omegasome; a membrane platform connected to the ER where the remaining core autophagy machinery are recruited. Together, the action of these proteins and complexes forms an initial cup-shaped membrane known as an autophagosome.

Following this, elongation of the autophagosome begins and requires two conjugation systems: ATG5–ATG12-ATG16L and ATG8–ATG3. First, WIPI2 binds to ATG16L1 to recruit the ATG12-ATG5–ATG16L1 complex to the autophagosome. The localisation of this complex to the autophagosome membrane helps enhance the conjugation of the ATG8 family of proteins: MAP1LC3A, B, C, GABARAP, and GABARAPL1 and L2. These proteins are processed at their C-termini by the cysteine protease, ATG4, then activated by the E1-like enzyme ATG7. ATG3, an E2-like enzyme, then conjugates the ATG8 proteins to the lipid phosphatidylethanolamine (PE) present on the autophagosome to form membrane-anchored lipidated ATG8 proteins. Efficient conjugation of the ATG8's to PE is aided by the ATG12-

ATG5 conjugate which stimulates ATG3 by its E3-like activity. In the case of selective autophagy, receptor proteins such as p62/SQSTM-1, optineurin and NDP52 can specifically recognise and target polyubiquitinated cargo to the autophagosome. ATG8s are required for the elongation and closure of the autophagosome and are assisted by the recruitment of ATG9-containing vesicles to the omegasome which help deliver additional lipids and proteins to contribute to the lengthening and expansion of the membrane. Eventually, the membrane seals to form a double-membraned vesicle containing cargo it has engulfed from the cytosol.

In the final step, the autophagosome undergoes maturation in preparation for fusion with the lysosome. This occurs as the lipidated ATG8 proteins are removed from the autophagosome outer membrane, allowing it to fuse with a lysosome to form an autolysosome. Hydrolytic enzymes within the lysosome breakdown and degrade the trapped cargo before releasing salvaged nutrients back into the cytoplasm to be reused again by the cell.

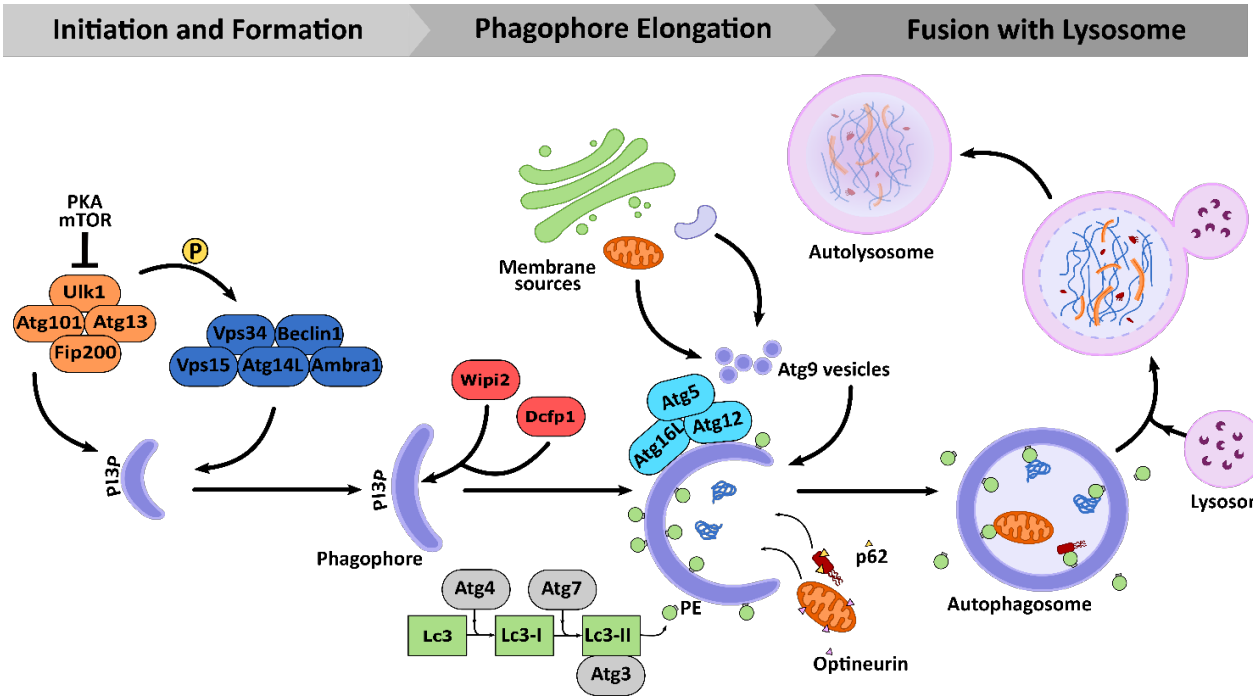

Figure 1.1.1 – Overview of the autophagy pathway within zebrafish cells, Autophagy is induced by cell stress causing activation of the Ulk1 complex and PI3KC3 complex which translocate to autophagy assembly sites at the isolation membrane of the nascent autophagosome. Atg9-positive vesicles are recruited to this site and help with its expansion and elongation as they deliver membrane materials donated by different cellular sources such as recycling endosomes, mitochondria, and Golgi complex. Wipi2 and Dcfp1 recruit the conjugation systems Atg5–Atg12-Atg16l and Atg8–Atg3 to the autophagosome membrane. Here, the Atg8, Lc3-I is conjugated to form Lc3-II, aiding in phagophore maturation and closure, as cargo are targeted to the inner autophagosome membrane by adaptor proteins (e.g., p62, optineurin). The autophagosome undergoes maturation and is transported to the lysosome by microtubules where fusion occurs to form an autolysosome and the autophagosomal contents is degraded. P, Phosphorylation event. This figure has been adapted from Moss *et al.* (1).

1.1.2 Initiation and regulation of autophagy

Autophagy may be induced by either physiological or pathological stimuli. Certain physiological signals ensure that in the majority of cells and tissues, autophagy is constitutively active at basal levels, helping to maintain organismal homeostasis through the continual turnover of cytosolic components and removal of damaged proteins and organelles (18). Studies in yeast and in higher eukaryotes have shown that levels of basal autophagy vary between cell and tissue types (19). In particular, maintaining basal levels of autophagy tends to be more critical for highly or terminally differentiated cells such as neurons, hepatocytes, myocytes, chondrocytes, and osteocytes, to ensure protein and organelle quality control and for cytoplasmic clearance (20). This has been demonstrated through various knock-out studies in mammals involving key ATG genes which have shown that whole-body loss of autophagy leads to the degeneration and dysfunction of differentiated cells and consequentially, embryonic, or postnatal lethality (21-24).

Autophagy activity can also be induced or increased by a range of intracellular and extracellular stressors, such as nutrient deficiency, hypoxia, pathogen invasion or protein aggregation. Increases in autophagy activity help release required metabolites and biomolecules, remove pathogens and clear cytoplasmic debris to ensure cell health and survival (25, 26). However, when dysregulated or uncontrolled, aberrant autophagy activity can become deleterious and disease-causing, with many studies implicating autophagy dysregulation in the development of multiple neurological, cardiovascular, metabolic, and more recently, skeletal diseases (6, 27, 28). Therefore, as an essential organismal process, the

regulation and induction of autophagy is a tightly controlled and sensitive system. Many factors have been identified as inducers and regulators of autophagy, however, one of the most conserved pathways in autophagy initiation is the mechanistic target of rapamycin (mTOR) pathway (29, 30). mTOR is an evolutionarily conserved serine/threonine protein kinase which belongs to the PI3K-related kinase (PI3KK) superfamily. It is central to the formation of two major complexes termed, mTOR complex 1 (mTORC1) and 2 (mTORC2). mTORC1 plays a key role in cell growth control and is sensitive to fluctuations in the levels of intra- and extracellular nutrients, growth factors, cellular energy, organic molecules, and primarily, amino acids (31). mTORC1 activity is regulated by nutrient availability and under nutrient sufficiency, mTORC1 acts as a suppressor of autophagy by phosphorylating key autophagy-induction proteins at multiple residues to block their activation (32, 33). Following its activation, mTOR phosphorylates ULK1 at Ser757 (32), and ATG13 at Ser258 (34). Phosphorylation at these sites suppresses the catalytic activity of ULK1, blocking its ability to interact with ATG13 and FIP200 to form the autophagy-initiating ULK1 complex. However, upon amino acid deprivation, activation of mTORC1 on the lysosomal surface is lost, resulting in rapid dephosphorylation of ULK1 and ATG13, ULK1 kinase activation and autophagy induction.

Chemical compounds can be used to target this pathway to artificially induce autophagy. The most common option is the antifungal agent, rapamycin which potently inhibits mTORC1 activity. Rapamycin achieves this through formation of a complex with the 12-kDa FK506-binding protein which specifically binds to mTORC1 as an allosteric inhibitor, thereby inactivating it (35). Drugs such as rapamycin have been used successfully in animal models to induce autophagy and investigate the subsequent effects on development and disease. Likewise, other chemicals can be used to inhibit the autophagy pathway to explore the effect of loss of autophagy on a cell system, early development, or disease progression. There are many pharmacologic agents which have been found to inhibit autophagy both *in vitro* and *in vivo* (36), however, the one used in this thesis is the lysosomal H+ ATPase inhibitor, BafilomycinA1 (BafA1). BafA1 is from a family of macrolide antibiotics produced from *Streptomycetes griseus*. It specifically targets vacuolar-type H+ -ATPase (V-ATPase) enzymes which are membrane spanning proton pumps that help acidify the lysosome (37).

Without acidification of the lysosome, certain lysosomal proteases such as cathepsins are inactivated meaning that engulfed cargo can no longer be degraded. This leads to an accumulation of autolysosomal structures as well as other autophagy markers, such as MAP1LC3 and p62, and the blocking of autophagic flux (36).

A diverse range of transcription factors have also been implicated in the regulation of autophagy through their activity on autophagy-related genes (38). For example, the cAMP-dependent PKA (protein kinase A) pathway induces the phosphorylation of MAP1LC3 to block its activation. PKA can also phosphorylate and activate mTORC1, through inactivating AMP-activated protein kinase (AMPK), an intracellular energy-sensing kinase which detects changes to AMP/ATP levels and also regulates autophagy. Another factor is TFEB (transcription factor EB) which activates autophagy under starvation conditions. Under basal levels, TFEB is phosphorylated by mTOR and retained within the cytosol but upon starvation, TFEB translocates to the nucleus, inducing lysosomal gene expression to enhance the degradative capacity of the cell. Another, less well studied autophagy regulator is the transcription factor, LMX1B. Later in this thesis, the role of LMX1B on the regulation of autophagy and its impact in skeletal development and disease will be explored.

1.1.3 Role of autophagy in the body

Since the first mechanistic descriptions of the autophagy process in 1967 by Christian de Duve (39), extensive research has been carried out to understand the autophagy pathways and their molecular control. These studies have highlighted autophagy as a vital pathway for many essential cellular processes and as having a key role in maintaining cell health and survival within most cell types. This is most clearly demonstrated in animal models with mutations in key autophagy genes. For example, mouse knock-out models have demonstrated that, generally, loss of upstream autophagy genes causes lethality earlier in development compared to *Atg* genes encoding members of the conjugation systems. *Atg13, Fip200, Beclin1* and *Vps34* knock-out models are all embryonically lethal (22, 40), whereas genes acting later (*Atg3, Atg5, Atg7, Atg9a, Atg12, Atg16L1* and by contrast, Ulk1/2) show neonatal lethality (see Table 1 in (12)). A pattern also mirrored in knock-out zebrafish lines for the equivalent *atg* genes (41). This is likely due to loss of upstream autophagy factors

having a greater impact on the abrogation of autophagy activity compared to later proteins. This has been postulated to be due to autophagosomes still being able to form, although in smaller numbers, even when conjugation systems are absent (42, 43). Alternatively, it could also be due to the loss of other, non-autophagy roles performed by some early *Atg* genes which are required for cell survival, as many have kinase activity or are kinase scaffolds (16, 44, 45). Therefore, these results demonstrate that autophagy is essential for animal survival.

Whilst these studies have established an integral role for the autophagy pathway within cellular homeostasis, they have also highlighted the vast number of other cellular functions mediated by its machinery (46, 47). Aside from directing intracellular clearance and recycling, autophagy has also been shown to participate in cell differentiation and development, innate and adaptive immunity, cell metabolism, tumour suppression, ER stress mitigation, ageing and cell death; processes essential to most cell types, including cells of the skeletal system (46, 48-50). Therefore, it is clear that the autophagy pathway and ATG genes interact and intersect with multiple other physiological cell processes, expanding and complicating its role and functions in the body. By understanding the distinct functions performed by autophagy in specialised cells and the key factors involved in its regulation, we can better grasp the influence of autophagy during the development of diseases, and how the autophagic pathway can be manipulated for therapeutic benefit.

Although autophagy has been shown to be important in many different cell types and its dysregulation implicated in several diseases, this thesis will specifically explore the role of autophagy within the skeletal system. In particular, this thesis will focus on the role that autophagy and two key autophagy-related factors (Atg13 and Lmx1b) play in development of cartilage cells and in skeletal formation, as well as highlighting any potential links between autophagy dysregulation and the development of osteoarthritis.

1.2 Autophagy and the skeletal system

Autophagy has been shown to play a variety of roles in bone physiology, bone and cartilage cell survival, differentiation and functioning, and bone-related disease pathogenesis. Given that the skeletal system undergoes constant remodelling to fulfil its functions, autophagy

plays a key role in this by helping to maintain the fine balance between bone formation and bone resorption (51). Alongside this, autophagy is a crucial player in chondrogenesis – the formation of cartilage from condensed mesenchymal tissue, as well as cartilage cell metabolism and protection from stress-induced cartilage cell death (52, 53). Dysregulation of autophagy has been implicated in the development of several skeletal disorders, including osteoporosis (54, 55) and osteopetrosis (56), Paget's disease of the bone (57), juvenile arthritis (47) and osteoarthritis (49, 58, 59), emphasising the importance of autophagy in cartilage and bone health. These diseases also show a varying skeletal phenotype, for example with osteoporosis being characterised by loss of bone density, whilst osteopetrosis by excessive bone density. This highlights the complex relationship with skeletal cells and their function, and the importance of maintaining their homeostasis and activity.

Multiple studies have implicated autophagy in the development and maintenance of the skeletal system. From the very early stages of development, autophagy plays essential roles in the differentiation, transformation and functional activity of key skeletal cells, such as osteoblasts (bone secreting cells), osteoclasts (bone absorbing cells), osteocytes (embedded cells that maintain bone) and chondrocytes (cartilage secreting cells) (Figure 1.2) (60). Post-development, emerging evidence shows that once terminally differentiated, these cells require a constitutive level of basal autophagy to ensure proper functioning and survival in the hypoxic, nutrition-deficient and hypertonic environments they reside in (20).

During embryonic development, the vertebrate skeleton, and its associated bone, cartilage, and connective tissues, are formed from mesenchymal stem cells (MSCs), whilst osteoclasts derive from haematopoietic stem cells (HSCs). To form the skeleton, cells migrate to the appropriate region within the embryo for skeletal formation, where they aggregate and proliferate to form mesenchymal condensations that subsequently differentiate into either osteoblasts or chondrocytes. From these cells, bone is formed either by intramembranous ossification or endochondral ossification. Studies have highlighted vital roles for autophagy within this differentiation process and within the differentiation capabilities of MSCs. For example, MSCs have been shown to have high levels of basal autophagy (61), whilst

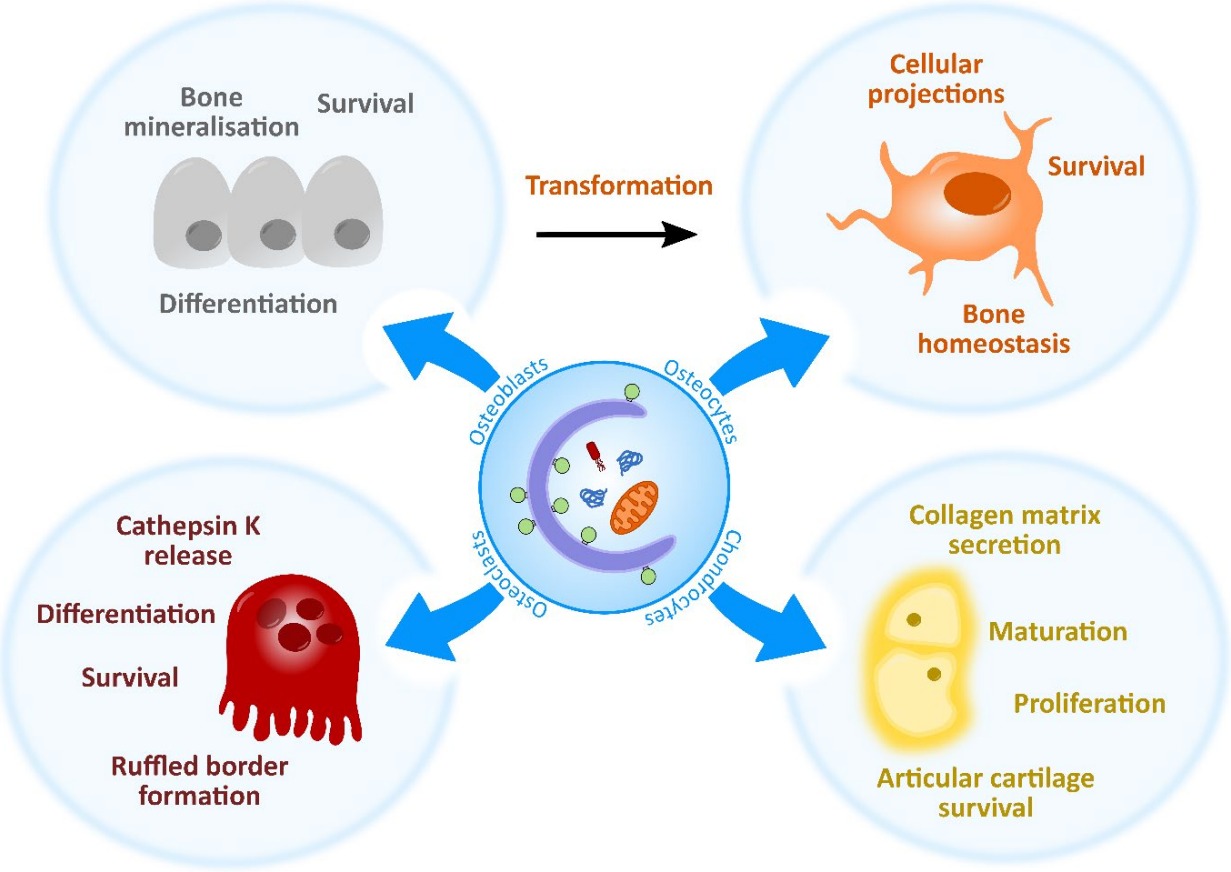

Figure 1.2 – Overview of the roles autophagy plays in bone and cartilage cells, Autophagy helps maintain the homeostasis, survival and function of osteoblasts, osteoclasts, osteocytes, and chondrocytes. This figure and figure legend have been adapted from Moss *et al.* (1).

treatment of MSCs isolated from young mice with the class III PI3Kinase inhibitor 3-Methyladenine (3-MA), which blocks autophagy induction, was shown to cause a reduction in the capacity of MSCs to differentiate into osteoblasts (62). Further to this, a study in primary human MSCs showed that during osteoblast differentiation from MSCs, these cells accumulate large numbers of autophagic vacuoles which are later broken down to provide energy (63). The authors concluded that autophagy is required to help balance energy supply during the differentiation process and that it is therefore vital for MSC differentiation and function (64). An *in vitro* study using primary murine osteoblast cells also showed that blocking autophagy through the knock-out of FIP200, an essential component of the mammalian ULK1 complex, inhibited osteoblast differentiation, further demonstrating the importance of autophagy during the establishment of the osteoblast population (65).

From osteoblast and chondrocyte cells, bone is formed via two different mechanisms. In intramembranous ossification, bone is secreted directly by osteoblasts which is how much of the skull and clavicles are formed in mammals, whilst in zebrafish, this is how parts of the craniofacial skeleton, and vertebral column and fins are formed (66). Conversely, in endochondral ossification, chondrocytes first form a cartilaginous skeletal template which is then gradually replaced by bone. For tetrapods, this is how long bones form, whilst in zebrafish the ceratohyal (lower jaw bone) and hypurals (bone supporting fin rays) are formed this way (67). As the organism develops, bone is lengthened and modelled until the final skeleton is formed, although constant remodelling of the skeleton in response to changes in mechanical loading or bone fractures continues throughout life (68).

This process of bone modelling and remodelling is mediated by osteoblasts, osteoclasts, and osteocytes. Osteoblasts line the surface of the bone and are responsible for synthesising, secreting, and mineralising the bone matrix. Osteoblasts that become trapped within bone further differentiate into osteocytes and form a mechano-sensing network where they connect and interact via dendritic extensions. Through this network, osteocytes help direct the recruitment of osteoblasts and osteoclasts to local bone areas. Meanwhile, osteoclasts differentiate from hematopoietic precursors and migrate to areas of active bone remodelling to help degrade and resorb bone. The coordinated activity of these cells is essential to ensuring bone homeostasis as disturbances to this equilibrium can lead to disease (Table 1.1). Autophagy is one process that has been shown to be essential for maintaining this balance and for regulating bone and cartilage cell differentiation, formation, and function.

1.2.1 Autophagy in cartilage formation and maintenance

Cartilage forming chondrocytes play a critical role within skeletal development and function. Chondrocytes are responsible for forming both the initial cartilaginous skeleton during endochondral ossification and the articular cartilage layer between bones, which enables fluid joint movement, as well as other permanent cartilaginous structures such as the trachea and septum. As with the other skeletal cell populations, autophagy has been shown to be a vital process for chondrocyte differentiation, function, and survival (69, 70).

Table 1.1 - Changes to autophagic proteins seen in specific skeletal disorders.

Disease	Cell Types Involved	Phenotype	Autophagy Proteins Involved	Effect on Autophagy	Ref
Paget's Disease of the Bone	Osteoclasts	Disorganised and weakened bone; excessive bone resorption and accelerated bone turnover	SQSTM-1	Impaired autophagic flux	(71, 72)
Osteopetrosis	Osteoclasts	Increased bone mineral density; impaired bone resorption; reduced lysosomal trafficking and acidification	PLEKHM1	Altered autophagy activity; reduced MAP1LC3-II turnover	(73, 74)
Osteogenesis Imperfecta	Osteoblasts	Fragile and brittle bones; defective type I collagen production	ATG7, ATG5, BECN1, MAP1LC3-II, CTSK	Increased autophagy activity	(75, 76)
Osteoporosis	Osteoclasts, osteoblasts	Progressive loss of bone mass; increased bone fragility and fracture risk	ATG5, ATG7, ATG12, BECN1, PRKAA2, PIK3C3, IFNA13, GABARAPL1	Increased autophagy activity	(77)
Glucocorticoid-induced osteoporosis	Osteoblasts and osteoclasts	Reduced bone density; increased fracture risk; reduced osteoblast proliferation; enhanced osteoclast survival	MAP1LC3	Increased autophagy activity	(78)
Osteoarthritis	Chondrocytes and osteoblasts	Progressive loss of articular cartilage; increased chondrocyte apoptosis; synovial inflammation; stiffening of joints	ULK1, BECN1, MAP1LC3	Decreased autophagy activity; impaired autophagy flux	(49, 59)
Multiple Sulfatase Deficiency	Chondrocytes	Skeletal dysplasia; deficiency in sulphate removal from GAGs	MAP1LC3	Increased autophagosomes due to defective fusion with lysosomes	(79)

During endochondral bone formation, chondrocytes form the cartilage anlage of the future bone through the secretion of a collagen-rich matrix. This process continues until the chondrocytes reach a non-proliferative, hypertrophic state at which point the cells undergo apoptosis, triggering the resorption of cartilage and its mineralisation into bone by invading

osteoblasts (80). Some chondrocytes remain within regions near to the end of the forming bone known as growth plates, where the chondrocytes continue to proliferate and secrete a cartilage matrix to enable longitudinal bone growth via ossification. During this process of chondrocyte proliferation and differentiation, *in vitro* studies have shown there is a positive correlation with levels of autophagy activity (69), and maturing chondrocytes show high MAP1LC3 expression (81). In growth plate chondrocytes, mice with a chondrocyte specific deletion of ATG7 showed impaired matrix secretion due to the retention of synthesised type II procollagen (a major component of cartilage matrix) within the ER (82). Meanwhile another study showed that the conditional loss of ATG5 or ATG7 in mice enhanced chondrocyte cell death and decreased cell proliferation resulting in reduced growth plate activity and growth retardation (69).

1.2.2 Autophagy in bone formation

Osteoblasts are the primary cell type responsible for bone formation and both their survival and function are regulated by autophagy. The differentiation of osteoblasts from MSCs is regulated by the transcription factors Runt-related factor 2 (RUNX2) and SP7 (also known as Osterix). During this process, studies have shown that autophagy is upregulated to help these cells survive the hypoxic bone environment and to combat oxidative stress (63), as manipulation of autophagic activity levels positively correlates with osteoblast survival (83).

Beyond survival, autophagy activity is closely linked to osteoblast mineralisation. Osteoblasts form mineralised bone through the deposition of hydroxyapatite crystals into the collagen based bone matrix. As the matrix matures, these crystals are organised into a lattice structure within the collagen, forming bone. These hydroxyapatite crystals have been identified in autophagic vacuoles within osteoblasts, and the inhibition of autophagic flux has been shown to block the outward extrusion of these minerals (63). Further to this, depletion, or deletion of ATG5, ATG7 or Beclin1, which are essential for autophagosome formation, have all been shown to cause decreased bone mass and mineralisation (63, 84). In the case of targeted ATG7 loss in mice, an increased number of bone fractures were recorded and suggested to be associated with induced ER stress and decreased osteoblast numbers (85, 86). Meanwhile, another *in vitro* study showed that deletion of FIP200 in osteoblasts

impaired their terminal differentiation, inhibiting bone formation, and causing an osteopenia phenotype (65).

There are several bone disorders linked to osteoblast dysfunction whose pathogenesis has also been linked to autophagy dysregulation, such as osteogenesis imperfecta and osteoporosis (Table 1.1). For all bone disorders which are caused by excessive and disorganised or insufficient bone formation, treatment options are limited. This is because there are few drugs available which can effectively and safely target and promote osteoblast numbers and activity (87, 88). Therefore, influencing osteoblast activity through an alternative target, such as autophagy, could be a useful therapeutic mechanism, emphasising the need for more research into understanding the role of autophagy in osteoblast development and function.

1.2.3 Autophagy in bone resorption

At sites of bone remodelling, hematopoietic mononuclear myeloid stem cells, primarily residing in the bone marrow, can differentiate into osteoclasts and migrate to the bony tissue surface in a process mediated by colony-stimulating factor 1 and RANK ligand (RANKL) (89). Once differentiated and activated, osteoclasts attach to the bone surface, forming a seal via actin rings and begin bone resorption through the secretion of lysosomal proteases, metalloproteinases, and cathepsin K (CTSK). In mice, autophagy has been shown to play a role in osteoclast differentiation as HSC-specific loss of ATG7 caused increased genomic and cellular damage to HSCs and a failure to differentiate (90), indicating that autophagy may be important for the maintenance of HSCs. In addition to differentiation, autophagy helps osteoclasts survive in the locally hypoxic environment of the bone surface. *In vitro* studies have shown that in hypoxic environments, autophagy is upregulated in osteoclasts to reduce cell stress and to protect against apoptosis (91, 92). Correspondingly, increased autophagy activity enhances osteoclast differentiation (93).

Autophagy has also been shown to be involved in osteoclast activity and function. Osteoclasts resorb bone through the secretion of matrix-degrading molecules onto bone via secretory lysosomal vesicles. They have a characteristic ruffled border where the exocytosis

of lysosomes occurs, and these lysosomes have been shown to be labelled with MAP1LC3 (94). Through the use of conditional knock-out mouse models, roles for the ATG conjugation machinery in osteoclast formation and resorptive activity have been suggested (94). Loss of ATG5 and ATG7 has been shown to impair ruffled border formation and lysosomal trafficking and secretion, causing a reduction in bone-resorption capacity, and increasing trabecular bone volume. These mice also showed a decrease in MAP1LC3 and RAB7 (a RAB GTPase) localisation to the ruffled border and inhibited CTSK release, which likely explains the effect on resorptive activity. Similarly, when MAP1LC3A – a specific sub-form of MAP1LC3 – was knocked down, both actin ring formation and CTSK release were blocked, thereby inhibiting resorption activity (95). Taken together, these data suggest that ATG proteins have a clear role in regulating osteoclast activity. This is further highlighted in the pathogenesis of bone disorders caused by defective osteoclast function which are also linked to mutations in autophagy related proteins, as mentioned in Table 1.1.

1.2.4 Autophagy in bone maintenance

Osteocytes are terminally differentiated cells formed from osteoblasts which have become trapped within the bone matrix. They are vital for bone health and maintenance and are responsible for regulating the bone remodelling process. Through the extension of dendrite-like processes within the bone matrix, osteocytes connect to form a vast network which detects and responds to hormonal and mechanistic changes within the bone environment by directing the recruitment of osteoblasts and osteoclasts to local bone areas.

Just as autophagy has a key role in osteoblast differentiation and function, autophagy has been shown to be important for osteocyte health and maintenance. Firstly, during the osteoblast to osteocyte transition, the cells must undergo a dramatic change in cell shape and composition which requires an active recycling of organelles (96). Secondly, a study using human and rat bone tissue demonstrated that osteocytes show an accumulation of MAP1LC3 puncta and that this expression is higher in osteocytes than osteoblasts (84). This indicates a high basal level of autophagy which is likely to be necessary to survive the nutrient and oxygen poor environment of the bone matrix.

Looking into the role of autophagy in osteocyte functioning, when autophagy activity was inhibited in mice by the osteocyte specific deletion of ATG7, there was a significant decrease in bone mass which was associated with reduced osteoblast and osteoclast numbers, and a disturbance in bone homeostasis (97). Similarly, in mice with ATG7 deficient osteoblasts, osteocytes showed decreased cellular projections and reduced ER degradation and turnover (85). Together, these results indicate a clear role for autophagy in osteocyte function, whilst also demonstrating the level of interaction between these skeletal cell types and how the dysfunction of one can impact the activity of others. This, therefore, has a significant impact upon bone health and homeostasis and should be an important consideration when studying bone disorders and selecting possible drug targets.

1.3 Joint development and homeostasis

Altogether these studies demonstrate a clear link for autophagy activity within early skeletal development and later cellular maintenance, as exemplified by the many examples of autophagy dysregulation in skeletal disorders. One of the most common skeletal disorders and a focus of this thesis is osteoarthritis.

Osteoarthritis (OA) is a form of joint disease and is the most common cause of arthritis in the world, most frequently affecting the hip, knee and finger joints (98, 99). In the UK alone, 15% of the population are estimated to suffer with OA and it has been found that one third of over 45's has received a consultation for OA. It is also one the biggest causes of disability, costing the economy almost £15bn per year in lost working days and forced early retirement (100).

OA affects all structures of the joint and is characterised by the progressive degeneration of cartilage, causing synovial inflammation, bone-to-bone contact, osteophyte formation, ligament damage, bone misalignment and stiffening of joints to the point that they become painful to use (101, 102) (Figure 1.3). OA causes specific degradation to the highly specialised tissue, known as articular cartilage, found at the surface or interface between joints. Articular cartilage is responsible for distributing mechanical loads across the joint and

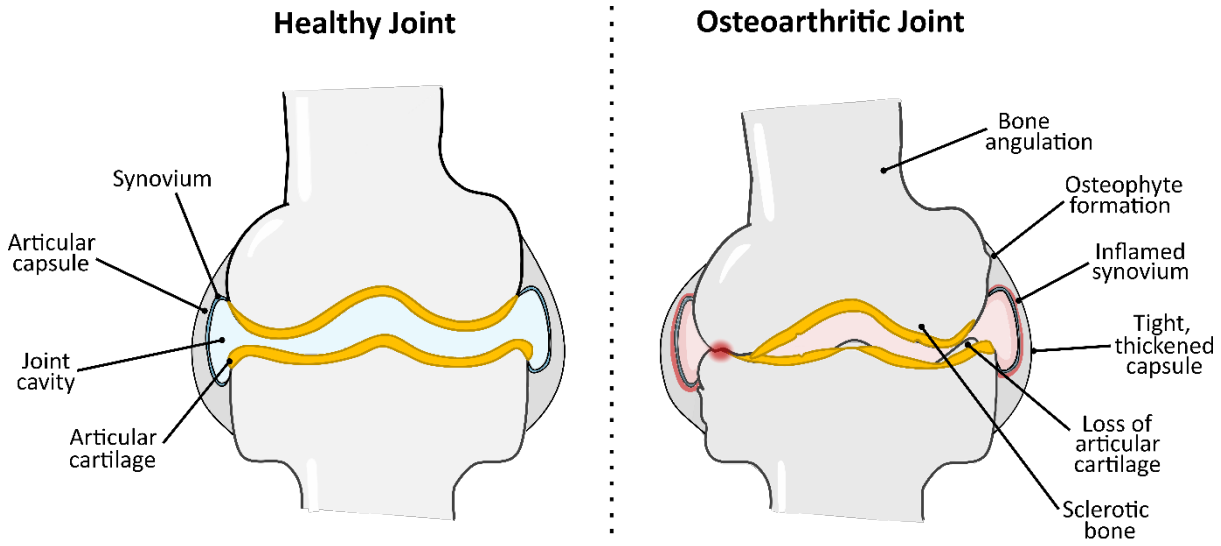

Figure 1.3 – Osteoarthritis causes changes to joint shape and architecture, Schematic showing features of a normal, healthy joint (*left*) compared to a joint with osteoarthritis (*right*). During osteoarthritis, the health of the articular cartilage decreases and starts to degenerate leading to unprotected areas of bone, changes to joint alignment and bone-to-bone contact which can cause pain when the joint is used. Osteophytes (bone protrusions) may also form along the bone edge as the bone becomes sclerotic and more brittle. Inflammation around the joint area and synovium increases, and the joint capsule becomes thickened, reducing joint flexibility.

for protecting the ends of bones, whilst allowing fluid joint movement without friction. It is developed from and maintained by chondrocytes, which secrete collagens (mainly type II collagen), water and proteoglycans to form the extra cellular matrix (ECM) of articular cartilage (103). Chondrocytes help maintain articular cartilage by responding to structural changes in the surrounding cartilage matrix and by managing the dynamic balance between ECM production and its enzymatic degradation (104). In osteoarthritic joints, chondrocytes show increased hypertrophication and apoptosis, and can be characterised by high expression of the hypertrophic markers, type X collagen α1 (Col10a1) and RUNX2, as well as other proteolytic enzymes (105). These enzymes, such as matrix metalloproteinase 13 and aggrecanases, induce cartilage degradation and mineralisation of the ECM, and are thought to cause osteophyte formation at the edge of the articular cartilage (105, 106). Therefore, excessive hypertrophication of chondrocytes is a principal driver behind the development of OA. Due to the low turnover and limited regenerative and repair capabilities of chondrocytes within the articular cartilage, which only declines with age, the maintenance and preservation of healthy chondrocytes is vital for joint health and usability.

Currently, there are no curative or preventative treatments available for OA which is in part due to a lack of understanding of the molecular mechanisms behind the initiation and progression of OA. This is hindered by the complex pathology of OA and its multi-factoral aetiology, involving age, weight, injury and hereditary. Considering the increasing economic and societal burden of OA globally, it is imperative that better preventative methods and curative treatments for OA patients and their families are developed.

1.3.1 Autophagy and osteoarthritis

Joint articular cartilage is retained throughout life, although due to the limited regenerative and repair capabilities of articular cartilage, homeostatic mechanisms such as autophagy are vital for its maintenance and preservation (70, 107). For example, healthy human cartilage shows a high expression of key autophagy factors such as ULK1, Beclin1, and autophagosome-associated MAP1LC3-II, indicating that autophagy is a constitutively active mechanism within cartilage (108). However, in osteoarthritic articular cartilage, expression levels are decreased and decline further as severity of the disease increases (108). Meanwhile, mice with a conditional knock-out of ATG7 in chondrocytes showed increased articular chondrocyte cell death, which escalated with age, and an accumulation of p62 in the articular cartilage, indicating abrogated autophagic flux (58). By 1 year of age, these mice had developed severe OA, with 29% of animals showing complete loss of articular cartilage at joint sites. Alternatively, authors using gene expression data from the Gene Expression Omnibus repository were able to show differential mRNA expression of key autophagy genes in the synovial membrane tissues and chondrocytes of OA patients compared to healthy control patients (109). From real-time PCR analysis, the gene expression of GABARAPL1, GABARAPL2, and ATG13 were shown to be downregulated within OA synovial tissues compared to non-OA synovial tissues.

Together, these results suggest that autophagy plays a protective role against cartilage degradation by maintaining chondrocyte health and survival. Recent data suggest that enhanced autophagy flux could be protective during the early stages of OA and is able to activate an adaptive response to cell stress to promote cell survival (110, 111). Alongside

this, mRNA expression data indicate a role for ATG13 and other ATG8 family members within OA development (109). To date, the molecular mechanisms underpinning the action of OA susceptibility genes within OA development have been poorly described (112). Therefore, this thesis will explore the role that autophagy plays in chondrocyte development and differentiation and seek to understand the mechanisms by which autophagy dysregulation or inactivity affects joint development and formation, using zebrafish as a model.

1.4 Using zebrafish as a model organism

Zebrafish (*Danio rerio*) are being increasingly recognised as a powerful and versatile model organism for the study of vertebrate biology as they are well suited to developmental and genetic analysis (113, 114). Despite some clear differences in morphology and evolutionary history compared to mammals, the zebrafish genome shares 71.4% similarity with the human genome, as well as at least one orthologue for 84% of human disease-related genes (115). Given this high genomic similarity with humans, zebrafish provide a powerful tool in examining the role of different genes in human disease pathology, as well as the opportunity to perform high throughput genetic and chemical screens. Compared to more established vertebrate models, such mice and rats, zebrafish also possess unique advantages for early developmental analysis and live imaging.

Zebrafish first emerged as a potential model organism for biological research in the 1980's, through work by Streisinger *et al.*, who recognised the many experimental virtues inherent within the species (116). Firstly, zebrafish are highly fecund, with a single pair able to lay up to 300 eggs a week, which develop externally as optically translucent larvae (117). This allows for the study of both cellular and gross morphological changes during early development, without the need for invasive experimental techniques or animal sacrifice. Secondly, this optical clarity and external development also enables easy genetic manipulation as through the use of genetic tools such as TALEN (118) and CRISPR-Cas (119), embryos can be injected with constructs at the single cell stage to generate transgenic or genetically altered zebrafish lines. It is through such methods that many knock-out lines and transgenic reporter lines have been developed and used to model specific diseases *in*

vivo, or to visualise and track specific proteins or cell types dynamically and in real-time. As these tools continue to improve, and with access to a fully sequenced genome, it is now possible to efficiently and specifically target multiple genes in a high-throughput manner in zebrafish (120).

Thirdly, from as early as 2 days post-fertilisation (dpf), zebrafish larvae exhibit a wide range of behaviours which from 5dpf are robust and reproducible, and so can be used to study the potential effects of genetic mutations. The behaviour of adult zebrafish can also be easily tracked through clear tanks used to house the zebrafish, allowing for the assessment of neurological differences on behaviour. Lastly, zebrafish are small as adults (~4-5 cm in length), hardy and easy to care for, making them a cheaper alternative to rodents in housing and care costs (116, 121).

1.4.1 Zebrafish as a model to study autophagy

Studies into the autophagy process have shown that the broad molecular machinery involved in its pathway has been evolutionarily conserved from yeast to mammals (25, 122-124). The zebrafish genome itself shares orthologous genes with all core mammalian autophagy-related proteins with the overall amino acid identity between these and their human counterparts ranging between 40 and 96% and an increased identity in functional domains (124). This high degree of conservation indicates that the autophagy pathway operates in a very similar way within zebrafish compared to humans and has enabled the development of many mutant and transgenic autophagy zebrafish lines (Table 1.2).

1.4.2 Transgenic and mutant autophagy zebrafish lines

The first transgenic autophagy reporters generated in zebrafish were the GFP-Map1Lc3 and GFP-Gabarap transgenic lines, with reporters expressed under the control of the constitutive cytomegalovirus (CMV) promoter (125) (Table 1.2). Both Map1Lc3 and Gabarap are homologues of yeast Atg8, and each form a subfamily of proteins in mammals and fish. In mammalian cells, the MAP1LC3 and GABARAP family members act cooperatively to enable autophagosome formation and/or cargo recognition, and as such, are equally useful for measuring autophagy *in vivo* and *in vitro*. However, overall, Map1Lc3 is the most widely used marker for identifying and visualising autophagy activity. During autophagy, GFP-

Table 1.2 - List of transgenic and mutant zebrafish lines that can be used to study autophagy

Gene	Protein description	Effect on Autophagy	Line Name	Ref.
map1lc3b	Marker for autophagosomes	Reporter – Enables visualisation of autophagosomal structures; under high magnification seen as distinct puncta	*Tg(CMV:EGFP-map1lc3b)*	(125)
gabarap	Marker for autophagosomes	Reporter – A functional homologue of Map1lc3; enables visualisation of autophagosomal structures, under high magnification seen as distinct puncta	*Tg(CMV:EGFP-gabarap)*	(125)
map1lc3b	Marker for autophagosomes	Reporter – Tandem fluorescent tag allows for monitoring of autophagic flux and acidity of autolysosomes	*Tg(CMV:EGFP-map1lc3b; CMV:mCherry-map1lc3b)*	(126)
gabarap	Marker for autophagosomes	Reporter – Tandem fluorescent tag allows for monitoring of autophagic flux and acidity of autolysosomes	*Tg(CMV:EGFP-gabarapa; CMV:mCherry-map1lc3b)*	(126)
sqstm1	Autophagy receptor	Reporter - Enables visualisation of autophagosomal structures	*Tg(pT2-mCherry-sqstm1)*	(127)
lamp1	Lysosomal membrane marker	Reporter – Enables visualisation of lysosomes	*Tg(pT2-lamp1-mCherry)*	(127)
atg7	Processes Map1Lc3 ready for conjugation	Mutant – Full protein KO; shows larvae lethality; reduction in Map1Lc3-II and accumulation in p62	*atg7*^{sa14768}	(128, 129)
atg12	Conjugates Map1Lc3 to PE	Mutant – Full protein KO; shows increased p62 accumulation indicative of autophagy inhibition	*atg12*^{ecn3}	(130)
beclin1	Involved in autophagy initiation	Mutant – Full protein KO; shows larvae lethality; reduction in Map1Lc3-II and accumulation in p62	*beclin1Δ8*	(128, 131)
dram1	Localises to lysosomes and promotes autophagic flux	Mutant – Full protein KO; shows accumulation of Map1Lc3 and p62 under induced autophagy; reduced targeting of bacteria to lysosomes	*dram1*^{ibl53}	(132)
epg5	Rab7a effector	Mutant – Full protein KO; shows impaired autophagic flux due to defective degradation of autolysosomes	*epg5*^{ia31}	(133)
lamp2	Lysosomal membrane marker	Mutant – Full protein KO; shows impaired autophagic flux due to disrupted autophagosomal fusion with lysosomes	*lamp2*^{e2}	(134)
optineurin	Autophagy receptor	Mutant – Full protein KO; shows decreased levels of Map1Lc3-II and p62	*optn*^{ibl51}	(135)
spns1	Lysosomal H^+ transporter	Mutant – Full protein KO; shows accumulation of Map1Lc3-I and II; impaired autophagic flux due to improper autolysosomal degradation	*spns1*^{hi891}	(127)
sqstm1	Autophagy receptor	Mutant – Full protein KO; shows decreased levels of Map1Lc3-II and optineurin	*p62*^{ibl52}	(135)

Map1Lc3 – which appears as discrete 0.5-1.0μm puncta during autophagy – acts like endogenous Map1Lc3 and becomes conjugated to PE in the developing phagophore and remains associated with the autophagosome until its full closure (Figure 1.1.1). Using fluorescence microscopy, this lipidated form of GFP-Map1Lc3-II can be visualised as puncta or as ring-like structures (136, 137).

The GFP-Map1Lc3 transgenic zebrafish line has been used in several studies to explore the role of autophagy in bacterial clearance (138), blastema formation following fin amputation (139), and in liver homeostasis (140). With regards to skeletal biology, this line can also be used to explore the expression pattern of autophagy during early skeletal development, and to identify which cells activate autophagy activity and in what context. Given the optical clarity of zebrafish, these organisms can be imaged live under anaesthetic, and the expression of Map1lc3 can be tracked dynamically throughout development in the same fish. For these reasons, the GFP-Map1Lc3 transgenic line, with kind permission from Prof Daniel Klionsky, has been utilised in this thesis for the study of autophagy in cartilage development and maturation.

While expression of GFP-Map1Lc3 can be very useful for identifying where autophagy may be upregulated, its expression alone cannot be used to determine autophagic flux or dynamics. For example, an increase in Map1Lc3 puncta could be due to elevated autophagy activity, and/or due to impaired lysosomal clearance (i.e. impaired autophagic flux) (141). To measure autophagic flux in zebrafish, lysosomes can be labelled with either a dye such as LysoTracker or a fluorescent probe, such as mCherry-Lamp1 or Lamp2 (127). In this way, colocalisation between GFP-Map1Lc3 and a lysosomal marker can be used to assess the level of autophagic activity. Similarly, drugs which block autolysosome formation (e.g., lysosomal H^+-ATPase inhibitors, such as BafilomycinA1), and therefore prevent the turnover of Map1Lc3 puncta, can also be applied to assess autophagic flux (Figure 1.4.2).

1.4.3 Zebrafish as a model to study skeletal development and pathologies

Much has been learnt about the skeletal system and its associated disorders through the use of animal models (142). *In vivo* models offer obvious advantages over *in vitro* cell models for

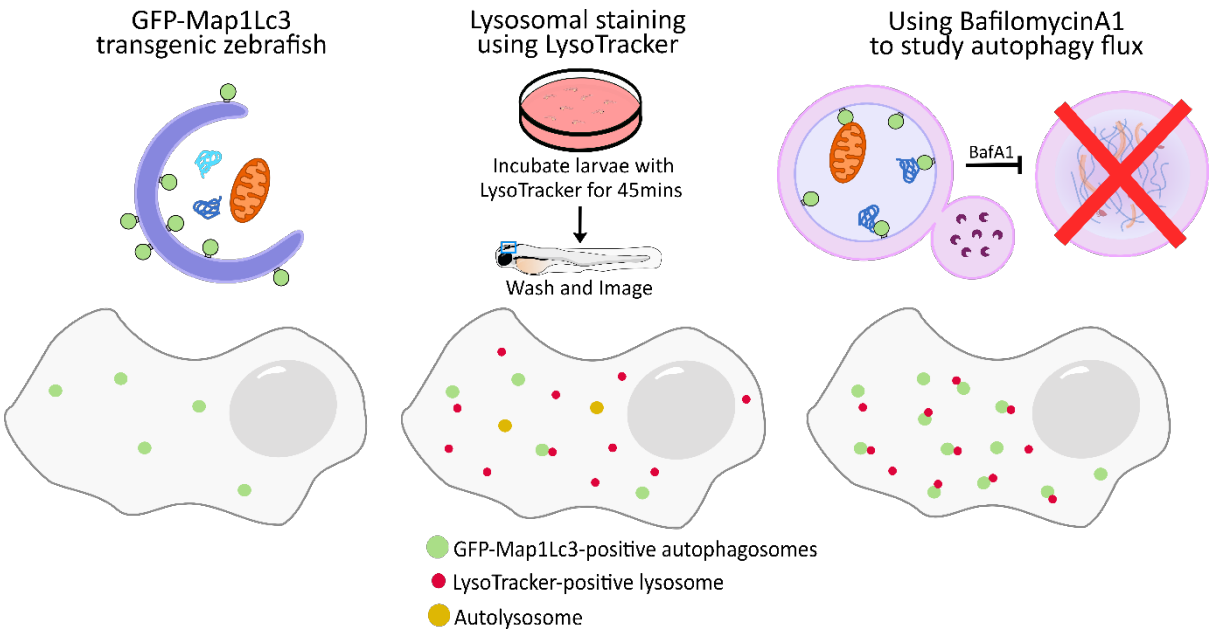

Figure 1.4.2 – Visualising autophagy activity and flux in larval zebrafish cells, Schematic depicting how GFP-Map1Lc3 puncta (*left*), and LysoTracker-positive lysosomes (*middle*) are observed in zebrafish cells by confocal microscopy. Yellow puncta represent LysoTracker-positive lysosome that have fused with GFP-Map1Lc3-positive autophagosomes. Treatment with BafilomycinA1 (*right*) inhibits autolysosomal formation, resulting in an accumulation of GFP-Map1Lc3 puncta.

skeletal research as the complex, moveable, three-dimensional structure of bones and joints cannot be fully recapitulated within an *in vitro* system. Equally, the effects of other cell and tissue types and their related secretions on cartilage and bone cells cannot be recaptured within a unicellular system. Whilst a number of different animals have been used as models for bone research, mouse models remain the most extensively used due to their generally lower husbandry cost, fast generation times, ease of handling and genetic tractability (143). However, despite these advantages, rodent models do have some inherent limitations for bone and autophagy-based research such as, differential bone loading compared to humans, and a lack of visual accessibility at a cellular level and during early developmental stages.

Increasingly, zebrafish are being recognised as a useful alternative to rodent models for skeletal and autophagy research. Skeletogenesis occurs very rapidly in zebrafish, with the initial establishment of specific craniofacial cartilaginous structures occurring as early as 2dpf, and the initiation of joint morphogenesis and movement from 3dpf (144, 145). Alongside this, their transparency at embryonic and larval stages means that the activity of

chondrocytes and osteoblasts during cartilage and bone development can be easily observed and monitored through the use of available transgenic and mutant lines (146, 147). Extending into adulthood, the transparency and easy access of bony fin rays means that long-term *in vivo* imaging is possible for the study of bone growth, repair, and maintenance (148, 149).

Despite clear structural differences, zebrafish share similar skeletal physiology, cell types and development to mammals. In zebrafish, bone cells develop from similar progenitors to mammals, and they share analogous gene expression profiles and signalling pathways (146, 150). For example, it has been demonstrated that in both zebrafish median fin development and tetrapod limb development, the expression patterns of key limb development genes such as, *col2a1, gdf5, noggin3, chordin, bapx1, bmp2b, bmp4* and *sox9a,* are very similar (151). Meanwhile, other studies have shown that key osteogenic transcription factors such as *runx2* and *osterix,* and members of the hedgehog signalling pathway, *indian hedgehog* and *desert hedgehog* are also expressed in zebrafish development indicating conservation across species (152-154). Zebrafish also have the same joint types and joint components as mammals, including the same joint cavities, articular cartilage and synovial membranes (155). This has been most widely shown in the larval zebrafish jaw which has been extensively studied and remains one of the main joint sites used to model joint development. Beyond this, they also have synovial capsules displaying clear fibroblast layers within the inner synovium lining and an external fibrous capsule which surround, although not fully enclosing, certain joints (156).

Many human skeletal disorders can be modelled in zebrafish and can recapitulate the phenotypes seen in higher vertebrates. For example, equivalent models for disorders such as osteogenesis imperfecta, scoliosis, osteoporosis, Stickler syndrome, and OA are available in zebrafish (155, 157-159). Additionally, as zebrafish develop OA naturally during ageing, the pathogenesis of the disease and its common symptoms such as increased spinal deformities, vertebral dislocations, and fractures, and the formation of osteophytes (bone protrusions) can be easily explored (160). Taken together, these data demonstrate that zebrafish are

representative, relevant, and useful models for the study of bone and joint development, the pathology of skeletal disorders, and the genes involved in either processes.

1.5 The role of transcription factors in bone development

Some transcription factors which have a role in regulating autophagy activity have also been found to affect the function and survival of bone cells. Members of the forkhead box O (FOXO) transcription factor family play important roles in cell growth and proliferation, DNA repair, generation of ROS and, maintaining energy homeostasis and glucose metabolism (161). Studies have shown that FOXO3 and FOXO1 work in tandem to cause induction of autophagy activity (162) and that the genetic ablation of FOXOs in osteoblasts causes oxidative stress and increased apoptosis, resulting in an aging phenotype (163). Conversely, the overexpression of FOXO3 in osteoblasts prevents bone loss normally associated with ageing (164). Given the known role of autophagy in protecting against oxidative stress and the link between FOXO activity and autophagy regulation, these data could be linked, although this is yet to be proven.

Activating transcription factor 4 (ATF4), a member of the CREB family, is another example. ATF4 is required for osteoblast function, promoting terminal differentiation and protection against amino acid starvation (165). Changes to ATF4 activity has been implicated within two genetic skeletal disorders: Coffin-Lowry syndrome (166) and neurofibromatosis type I (167), as under expression of ATF4 leads to aberrant mineral deposition and dysfunctional bone formation. However, ATF4 also promotes the transcription of several autophagy genes including MAP1LC3B and ATG5. Therefore, although not conclusive, taken together these data suggest a role for autophagy modulators, such as these and the transcription factor LMX1B, in skeletal cell homeostasis.

1.5.1 LIM homeobox transcription factor 1 (LMX1B)

LMX1B belongs to the LMX group of the LIM-homeodomain family, a diverse family of regulatory proteins which are characterised by the presence of a homeodomain and two LIM domains (LIM-A and LIM-B) (168, 169). The highly conserved helix-turn-helix

homeodomain is located near the C-terminal end of LMX1B and facilitates DNA binding. This is through recognition of A/T-rich (FLAT) elements in genes with a 5′-TAATT-3′ core motif (170), and allows for the modulation of cell type-specific gene expression. The LIM domains are located N-terminally of the homeodomain and are organised in a specialised, tandem zinc-finger structure. They act as an interface for protein-protein interactions and are able to bind to other transcription factors or transcriptional co-factors to form a transcriptional regulation complex (171). These co-factors can determine the transcriptional activity of LMX1B and do so in a tissue-specific manner (170). For example, through its LIM domains, LMX1B interacts with E47, the basic helix-loop-helix transcription factor, to act as a transcriptional activator of insulin gene promoter (172). It is through these different interactions that LMX1B is able to regulate gene activity across a wide range of tissues during development, such as the brain, kidney, and eye (173). Closely related to *LMX1B* is its sister gene, *LMX1A.* As proteins, they share 64% sequence identity, which increases to 65% and 83% amino acid identity for the LIM-A and LIM-B domains, respectively, and 100% amino acid identity for the homeodomain (174). Given this high sequence similarity, they share several common target genes and have overlapping functions in the body.

In vertebrates, LMX1B has several important roles during development and is expressed in a variety of tissues. Meanwhile, mutations in *LMX1B* have been implicated in several diseases including, Parkinson's disease (175), schizophrenia (176), autism (177) and glaucoma (178), and is the only gene associated with the rare genetic disorder, Nail-patella syndrome (179). This disease manifests as defects in the skeleton, kidneys, and eyes, as well as other body systems and will be discussed in further detail in Section 1.5.4 below.

Through work in the Lane lab, LMX1B has also been shown to be involved in regulating the expression of key autophagy and mitophagy genes (180). This regulatory activity of LMX1B is achieved through binding of the homeodomain to FLAT elements within target autophagy-related genes (181). Once bound, LMX1B is believed to act as a transcriptional activator (172). Work by Jiménez-Moreno *et al.,* showed that LMX1B, along with its sister protein LMX1A, regulates the expression of important autophagy genes including ULK1, ATG7, ATG16L1 and TFEB in midbrain dopaminergic neurons (180). The authors showed

that if suppressed, loss of autophagy activation by LMX1B causes a reduction in basal autophagy levels and elevation of mitochondrial reactive oxygen species (ROS) levels within these cells. This is in line with data from Laguna, *et al.* who first demonstrated that LMX1B affects autophagy function in the mid-brain of mice (175). Here, the authors found that the conditional loss of *Lmx1b* in mice caused a reduction in the expression of key autophagy and lysosomal genes as well as genes involved in autophagosome transport and in autophagy gene transcription. Meanwhile, overexpression of LMX1B resulted in an increase in the expression of several of these genes. Alongside this, another study found that both LMX1A and LMX1B are required for dopaminergic neuron survival through their maintenance of mitochondrial function in these neurons (182). Therefore, these data demonstrate a role for LMX1B in autophagy regulation and in helping to protect against cellular stress.

1.5.2 Expression of LMX1B in the body

LMX1B has important roles in the development of a range of tissues. Expression of *Lmx1b* is observed very early during development: from E7.5 in mice and from 16hpf in zebrafish, and can be detected in the early formation of key tissues such as the notochord (183, 184), the brain (185, 186), the inner ear (187), as well as the eye (188) and dorsal limbs (189) (Figure 1.5.2). With regards to early brain development, in mice, *Lmx1b* is seen in the anterior of the embryo by embryonic day (E) 7.5 (186). By E8.5, *Lmx1b* is expressed in the prospective mid-hindbrain boundary (MHB) and in the isthmus by E9.5. By E12.5, *Lmx1b* expression is also observed in the developing spinal cord (184) (Figure 1.5.2B). Meanwhile, in zebrafish larvae, both paralogues of *lmx1b; lmx1ba* and *lmx1bb* are expressed from the 18 somite stage, with both showing strong expression in the MHB and ventral diencephalon. By 24hpf, *lmx1ba* and *lmx1bb* expression can be detected in the diencephalic domain, posterior to TH-expressing neurons, and in the medulla oblongata and hindbrain (190) (Figure 1.5.2D-E).

In murine kidneys, *Lmx1b* has been shown to be expressed only in glomeruli, specifically within podocytes and not within any other nephron segment (173, 191) (Figure 1.5.2C). It has been found that LMX1B activity is essential postnatally to ensure the expression several podocyte-related genes such as, CD2AP, NPHS2, COL4A3 and COL4A4 (191). Expression studies for *lmx1b* in the kidneys have yet to be performed in zebrafish. Meanwhile, during

murine eye development, *Lmx1b* is expressed in the periocular mesenchyme and within adults its expression remains in the trabecular meshwork, corneal stroma, and iris stroma (192). Zebrafish larvae show only *lmx1bb* expression in the otic vesicle, although both paralogues are expressed in optic stalk cells and globe of the eye (188) (Figure 1.5.2D).

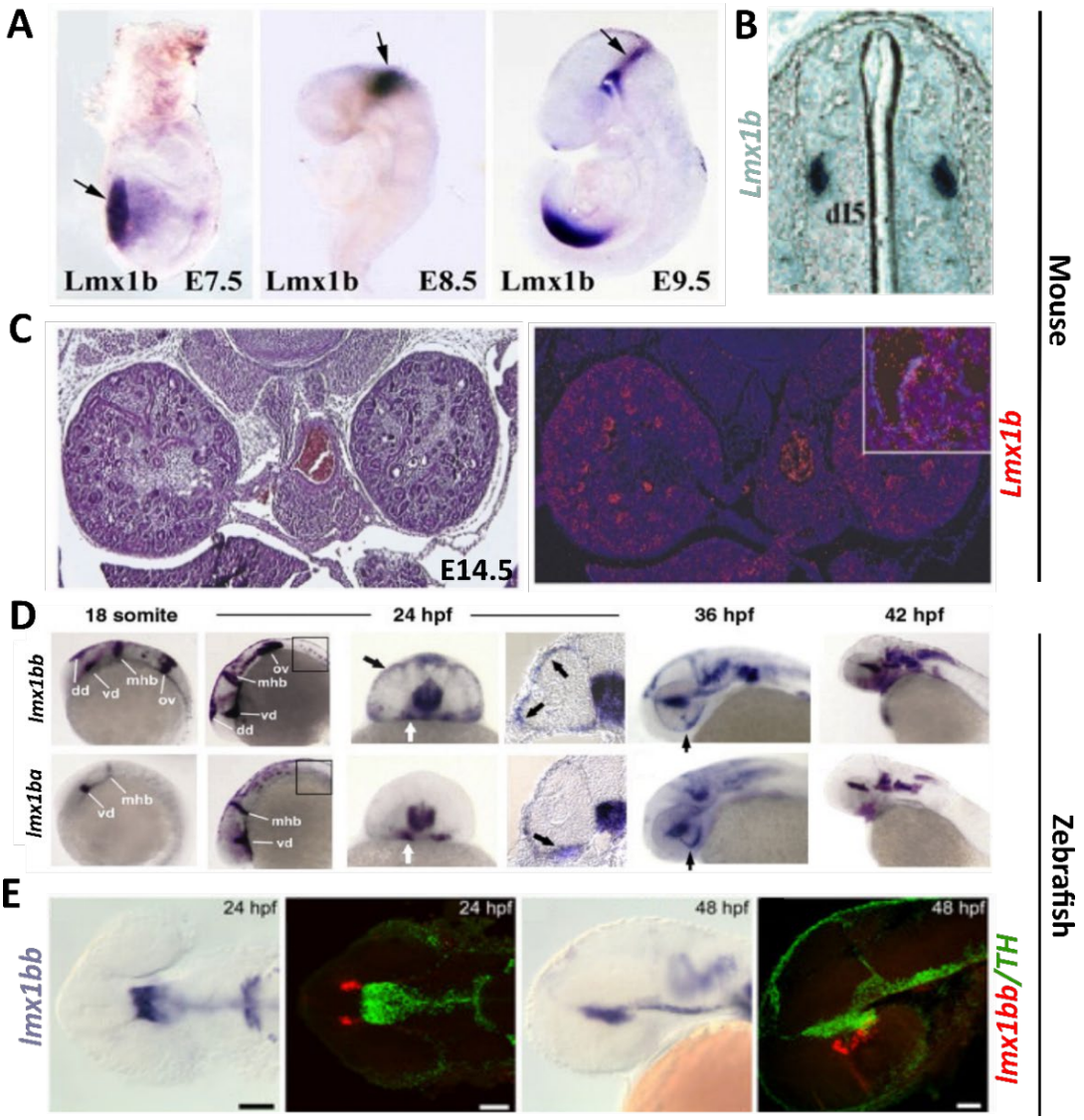

Figure 1.5.2 – Expression of *Lmx1b* in mice and zebrafish embryos during development, (A) Wholemount *in situ* hybridization of *Lmx1b* in mouse embryos from E7.5-E9.5. Black arrows indicate location of *Lmx1b* expression at each stage. Images from Guo *et al.*, 2007 (186). **(B)** In mice at E12.5, *Lmx1b* expression (*grey-blue*) is seen in the developing spinal cord. Image from Chizhikov *et al.*, 2004 (184). **(C)** *Left*, transverse sections of mouse kidney at E14.5 with (*top*) hematoxylin and eosin (H&E) stain and (*bottom*) *in situ* hybridization of *Lmx1b*. Inset shows localisation of *Lmx1b* to visceral epithelium of glomerulus. *(Continued overleaf)*

Images taken from Morello *et al.*, 2001 (173). **(D)** *lmx1ba* and *lmx1bb* expression shown in zebrafish larvae by *in situ* hybridization at 18 somites to 48 hpf. At 18 somites to 24 hpf, both paralogues show strong expression in the MHB and ventral diencephalon (vd). Only *lmx1bb* is detected in the otic vesicle and spinal cord neurons, whilst both paralogues are seen in optic stalk cells (*white arrows*) and globe of the eye (*black arrows*). dd, dorsal diencephalon; ov, otic vesicle; hb, hindbrain. Images from McMahon *et al.*, 2009 (188). **(E)** Expression of *lmx1bb* (*blue or green*) in the brain as analysed by traditional and fluorescent *in situ* hybridisation along with immunostaining for TH (*red*) in 24-48 hpf zebrafish larvae. Expression of *lmx1bb* is detected in the diencephalic domain, posterior to TH-expressing neurons, and in the medulla oblongata and hindbrain. Scale bars = 50 μm; images from Filippi *et al.*, 2007 (190).

1.5.3 Expression and functions of LMX1B in the skeletal system

Expression studies in chicks and analysis of *Lmx1b* mutant mouse models have shown that expression of *Lmx1b* is essential for dorsal limb patterning (193, 194). In both chicks and mice, *Lmx1b* transcripts are found in the dorsal mesoderm of the developing limb bud (193, 194) (Figure 1.5.3). The expression of *Lmx1b* is induced here by wingless-type MMTV integration site family member 7a (*Wnt7a*), which is present on the dorsal ectoderm of the developing limb bud (195). Throughout limb development, *Lmx1b* expression remains restricted to the dorsal side of the limb by expression of engrailed 1 (*En1*), which is triggered by *Bmp* (bone morphogenic proteins) signalling and expands across the ventral ectoderm (196, 197).

As limb development progresses and joints and tendons are formed, *Lmx1b* retains high expression in the distal mesoderm of the developing limb whilst its proximal expression decreases (198). When *Lmx1b* is overexpressed in chicks, it has been shown to cause ventral to dorsal transformation of limb mesoderm (193). Meanwhile, *Lmx1b* mutant mice show loss of dorsal patterning in the hands and feet (autopod level), arms and legs (zeugopod level) during early development, resulting in symmetrical ventral-ventral patterning of footpads, muscles, tendons, and ligaments as well as loss of dorsal hair follicles (194).

Despite the clear role that *Lmx1b* plays in limb patterning, the mechanisms through which *Lmx1b* operates during limb dorsalisation are yet to be determined. Several microarray analysis between *wt* and *Lmx1b* knock-out mice have been used to identify genes that may be regulated by *Lmx1b* during bone and joint formation (199-201). The most recent study by

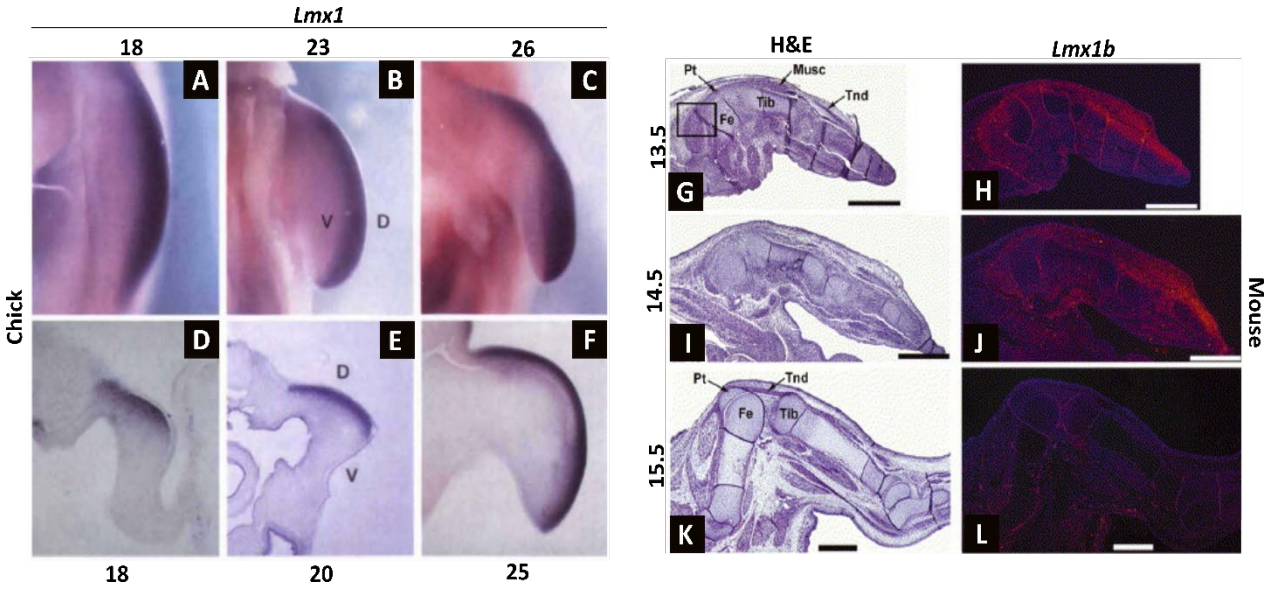

Figure 1.5.3 – Expression of *Lmx1b* in early limb development in chick and mouse embryos, Images showing *in situ* hybridization of *C-Lmxl* mRNA (*dark purple*) in **(A-C),** whole mount embryonic chick limbs, and **(D-F),** limb sections where *C-Lmx1* expression is localised to the dorsal limb mesenchyme. Stage of chick indicated above and below images. V, ventral; D, dorsal; images taken from Vogel *et al.,* 1995 (193). **(G,I,K)** Hematoxylin and eosin (H&E) histological staining shows location of key skeletal and muscle elements in developing mouse limb. **(H,J,L)** *in situ* hybridisation shows expression of *Lmx1b* (*red*) in the proximal limb. Expression of *Lmx1b* seen in the mesodermal condensations forming tendons (Tnd) and joint-associated tissues including the primordial patella (Pt). No *Lmx1b* expression seen in the Femur (Fe) and Tibia (Tib). By 15.5 days post-coitum (dpc), *Lmx1b* expression has decreased whilst muscle and tendon differentiation further mature. Images taken from Dreyer *et al.,* 2004 (198).

Feenstra *et al.,* identified several genes that show reduced expression in the limbs of *Lmx1b* knock-out mice (199). These included the growth/differentiation factor 5 (*Gdf5*), important for skeleton formation, joint development, and chondrogenesis (202), certain proteoglycan genes (*Keratocan*, *Lumican* and *Decorin*) which are involved in connective tissue development, and extracellular matrix genes, *Matrilin-1* and *4*. These findings were further supported by another study, where chromatin immunoprecipitation sequencing (ChIP-seq) against Lmx1b in embryonic mouse limbs was used to identify Lmx1b binding sites in or near potential genes regulated by Lmx1b (189). As each of these genes are known to be important in bone and joint formation, these results highlight a mechanism for how Lmx1b may regulate dorsal limb formation during development. However, disruption to the expression of these genes have been implicated in OA. For example, mutations in *Gdf5*, *Decorin* and *Matrilin-1 and 4* have been shown to lead to OA in human and mouse studies,

respectively (203-206). Whilst changes in the expression of *Keratocan* and *Lumican* can be indicative of late-stage OA (207, 208). Therefore, these results also demonstrate potential mechanisms by which loss of *Lmx1b* expression can induce OA, however, these interactions still require further investigation.

1.5.4 LMX1B in Nail-patella syndrome

As explained above, mutations in *LMX1B* have been shown to cause Nail-patella syndrome (NPS) in humans. Also known as hereditary onycho-osteodysplasia and by several other names, NPS is a rare, autosomal dominant disorder which affects multiple body systems. It is characterised by fingernail dysplasia, the loss or malformation of the patella, iliac horns on the pelvis, and elbow deformities, although renal, ocular, and neurological developmental abnormalities are also observed in most patients (209). NPS has an estimated incidence of 1:50,000, with around 10% of cases being caused by *de novo* mutations. All NPS patients carry heterozygous loss of function mutations in *LMX1B* suggesting that the disorder is caused by haploinsufficiency (181), where a single wild-type allele is unable to compensate for its mutated partner allele, resulting in a disease phenotype.

The clinical manifestations of NPS, in both frequency and severity, can vary greatly from patient to patient, and even within patients from the same family (209). This variance is thought to be due to differences in the penetrance of mutations and therefore, the level of remaining LMX1B expression. Added to this, the ability for co-factors to bind to mutated forms of LMX1B may also play a role in tissue-specific effects. For example, mutations in *LMX1B* have been shown to affect its binding ability with the transcription factor, *PAX2*, a known interactor with *LMX1B*, which along with LMX1B, is involved in kidney and eye development (210).

Although the phenotypes of NPS patients differ, most show symptoms related to the tissues and organs that LMX1B plays a role within. Changes to the nails and patellae are the characteristic symptoms most commonly used to diagnose patients with NPS, as they are present in 95-100% and 74-95% of patients, respectively (209, 211, 212). Other skeletal changes include a loss of flexion around distal joints in the hand, and at the elbows and

knees. This is thought to be caused by the absence or hypoplasia of key muscles and ligaments at these joint sites, and it is not uncommon for patients to develop early degenerative arthritis at the knee (209, 213). Back pain is also reported in around half of patients which is most commonly caused by increased lumbar lordosis: excessive inward curvature of the spine at the lower back (47% of patients), or scoliosis of the spine (23% of patients) (209). Fusions in the lower spine (fifth lumbar and sacral joint), were found in a small proportion of patients as well as degenerative changes to the spine (209). Whether the early development of arthritis seen in these patients is caused directly by loss of *LMX1B* expression or is secondary to skeletal symptoms is yet to be explored, however, it does point to a potential role for LMX1B in OA pathogenesis.

Nephropathies are common in NPS patients, affecting around 40% of patients and are the main influence behind the NPS mortality (211). In NPS patients, the morphology and function of a kidney-specific cell, podocytes are affected. Podocytes are highly specialised, terminally differentiated epithelial cells found within the Bowman's capsule of the kidneys where the glomerulus sits. Here, these cells aid in the process of glomerular filtration, where small molecules migrate from the blood into the kidney filtrate to be excreted. Podocytes wrap around the outer surface of glomerular capillaries and form a filtration barrier by interdigitating their foot processes with neighbouring podocytes (214). These foot processes are connected by the slit diaphragm, a specialised form of intracellular junction, which are critical for stopping the leakage of blood plasma proteins into the urine (known as proteinuria). NPS patients can show a reduction in podocyte foot processes, and loss of slit diaphragm formation, as well as irregular thickening of the glomerular basement membrane (GBM) with some areas appearing 'moth eaten', or electron-lucent under ultrastructural analysis (215). The main renal defect in patients is deficient GBM filtration and in around 10% of cases leads to renal failure (216).

The development of open-angled glaucoma or ocular hypertension are also recognised symptoms of NPS, affecting around a third of patients over 40 years; a rate much higher when compared to the general population (209). From mouse and zebrafish studies, it was found that loss of *Lmx1b* expression causes defective migration and survival of periocular

mesenchymal cells and abnormalities in the formation of key ocular structures (188, 192, 217). Therefore, these diseases are thought to be triggered by malformation of the trabecular meshwork in the eye, a system which helps regulate intraocular eye pressure by controlling fluid flow within the eye (192, 217). Defects to this system can cause impaired fluid outflow and elevated intraocular pressure, leading to a disease state (192).

Some studies describe neurological symptoms experienced by NPS patients, although symptoms are normally mild and only sporadically reported. This is surprising given the role of LMX1B in early brain formation and neuronal cell development. These symptoms include numbness or tingling and diffuse, intermittent pain often at the distal end of limbs, all of which appeared to be idiopathic (209). They are thought to relate to defects in neuronal migration during the dorsal patterning of developing limbs and spinal cord, demonstrating a role *Lmx1b* in dorsal spinal cord neuronal migration (218). There is also preliminary data that attention deficit hyperactivity disorder (ADHD) and major depressive disorder could occur at a higher incidence in NPS patients, linked to the deficits in mesencephalic dopaminergic neuron development (219).

1.5.5 Exploring the role of LMX1B in bone development and OA

Given the role of LMX1B in body patterning and the effects of loss of LMX1B expression on the musculoskeletal system in NPS patients, a role for LMX1B in bone development and disease was explored in this thesis. This work was triggered by two recent genome-wide association studies, where single-nucleotide polymorphisms (SNPs) within *LMX1B* linked to patients with OA or high bone mass density, respectively, were identified, highlighting a potential role for LMX1B expression within joint health and maintenance (220, 221). Using the UK Biobank arcOGEN, a genome-wide meta-analysis was performed on data from participants with hip OA, knee OA, both hip and knee OA, OA diagnosed at any site and healthy controls (455,221 total). The analysis identified 21 novel loci within the participants with hip OA that had reached genome-wide significance (12,850 hospital diagnosed hip OA cases vs 369,983 healthy control cases). Of these 21 loci, one SNP was found within LMX1B (9:129386860_C>T) (221). In this study, the SNP identified in *LMX1B* was found to be significantly associated with patients who have hip OA compared to non-OA affected

participants, which implicates LMX1B in hip OA development, however, functional characterisation is currently lacking. Therefore, altogether these data highlight a potential role for LMX1B in bone and joint development and maintenance, which could be mediated through its activity as a regulator of autophagy.

1.6 Thesis overview

As an essential cellular pathway, the importance of autophagy in skeletal cell functions and homeostasis is not surprising, although the mechanisms of how autophagy dysregulation contributes to skeletal diseases, and in particular OA, is still being investigated. Much work in this area has been achieved using mutant autophagy mouse models, however, these studies have been limited by the neonatal lethality of most murine *Atg* knock-out lines (12). Knock-out zebrafish lines for *Atg* proteins, however, have been shown to survive for longer (41), and due to their external development, they offer the unique advantage of allowing development to be observed from a single cell onwards. Therefore, mutant autophagy zebrafish lines can be used to explore the effect of loss of autophagy on skeletal development from its early stages to completion of the skeletal anlage and its functional use.

Similar to mutant *Atg* models, homozygous *Lmx1b* mutant mouse models show lethality within 24 hours of birth, whilst heterozygous *Lmx1b* mice show a distinctly different phenotype to human NPS patients who carry similar mutations (194). Stable *lmx1b* knock-out zebrafish lines have been previously developed, although a full characterisation of loss of *lmx1b* in zebrafish is yet to be reported. Recent studies have implicated mutations in *LMX1B* in OA, whilst the skeletal symptoms of NPS patients indicate an important role for LMX1B in skeletal system development and maintenance. Cellular studies, meanwhile, demonstrate LMX1B to be a regulator of autophagy activity. Given that both *LMX1B* and autophagy contribute to proper skeletal development, the effect of loss of *LMX1B* on the skeleton could be linked to autophagy dysregulation.

Therefore, the aims of this thesis are to:

- Explore the role of *atg13* and autophagy activity in chondrocyte development and maturation, and in the formation and function of joints, using an *atg13* knock-out zebrafish line.
- Use CRISPR-Cas9 technology to develop *LMX1B* knock-out models in human cells and zebrafish.
- Characterise the phenotype of the *lmx1b* knock-out models, focussing on changes to the skeleton, kidneys, eyes, and brain to establish whether these zebrafish lines can be used as a new model for NPS.
- Explore whether loss of *lmx1b* alters autophagy activity and whether this correlates to changes in skeletal development and maintenance in zebrafish from larvae to adulthood.
- Establish if *lmx1b* plays a role in the pathogenesis of OA.

Chapter 2. Materials and Methods

CHAPTER

2

Materials and Methods

2.1. Materials

2.1.1 Bacterial Strains

Escherichia coli 5-alpha competent cells – genotype: fhuA2 Δ(argF-lacZ)U169 phoA glnV44 Φ80 Δ(lacZ)M15 gyrA96 recA1 relA1 endA1 thi-1 hsdR17 (NEB, #C2987H). These were used for the transformation of intact plasmids.

2.1.2 Plasmids

pX458 SpCas9-2A-EGFP: gRNAs for LMX1B CRISPR in HEK293T cells cloned in at gRNA scaffold site and expressed as fusions to the N-terminus of Cas9-eGFP.

2.1.3 Primers used for qRT-PCR

Table 2.1 – List of primers used for qRT-PCR in HEK293T cells

Gene	Forward Primer	Reverse Primer
LMX1B	5′-GTGTGAACGGCAGCTACGC-3′	5′-TCATCCTCGCTCTTCACGG-3′
GAPDH	5′-TTGAGGTCAATGAAGGGGTC-3′	5′-GAAGGTGAAGGTCGGAGTCA-3′

2.1.4 Sequencing Primers for Zebrafish

Table 2.2 - List of primers used to sequence mutant zebrafish lines, including M13 FAM primer used only in PCR mix for fragment analysis

Gene	Forward Primer	Reverse Primer
Atg13	5′-GGCTCGTGCGACAATGGATAGTG-3′	5′-GACCTCGGGGATGTCCTTTATTGC-3′
O123 Lmx1bb	5′- TGTAAAACGACGGCCAGTCGT AATATTATTCGGACGCCTTT -3′	5′-CGTGCGCATTACACCAATAA-3′
O7 Lmx1ba	5′-TGTAAAACGACGGCCAGTATGT GAAGCCGGAGAAAGG-3′	5′-GGTGGCCAGCTTGTATGACT-3′
Primer for Fragment Analysis		
M13 FAM Primer	Forward: 5'-FAM-TGTAAAACGACGGCCAGT-3'	

2.1.5 gRNA Sequences for CRISPR

Table 2.3 - gRNA sequences used to target LMX1B in HEK293T cells and lmx1ba and lmx1bb in zebrafish. Bold letters in gRNA sequences for HEK293T cells indicate modifications added to gRNA sequences to ensure proper ligation into SpCas9-2A-EGFP vector. Design of CRISPR gRNAs for zebrafish was assisted by Dr Erika Kague (University of Bristol)

	gRNA Name	gRNA sequence
For HEK293T cells (Eurofins Genomics)	**O1 LMX1B**	**FOR:** 5′-**caccg**CAACGAGTCGTCCTGGCACG-3′ **REV:** 5′-**aaac**CGTGCCAGGACGACTCGTTG**c**-3′
	O2 LMX1B	**FOR:** 5′-**caccg**CCGAGTTCGTGATGCGGGCG-3′ **REV:** 5′-**aaac**CGCCCGCATCACGAACTCGG**c**-3′
	O3 LMX1B	**FOR:** 5′-**caccg**CGACGAGTCCGACTCCGGTG-3′ **REV:** 5′-**aaac**CACCGGAGTCGGACTCGTCG**c**-3′
For zebrafish (Merck)	**O1 Lmx1bb**	5′-GAUGGCACUCCGUCCCUGAAGGG-3′
	O2 Lmx1bb	5′-GACGGAGUGCCAUCACCAGGCGG-3′
	O3 Lmx1bb	5′-AGCGGUCGGAUAUCGGCCGCUGG-3′

	O4 Lmx1bb	5′-AGGCUCGGGAGGCACCGGGAAGG-3′
	O7 Lmx1ba	5′-CGGUUUGGACGAGACCUCGAAGG-3′

2.1.6 Primary and Secondary Antibodies

Table 2.4 - List of primary and secondary antibodies used for Western blotting and immunofluorescence in HEK293T cells and zebrafish

1º Antibody	**Supplier**	**Cat. No.**	**Type**	**Dilution**
		For cell staining		
GAPDH	Sigma Aldrich	G8796	Mouse	WB: 1:2000
LC3	Sigma Aldrich	L7543	Rabbit	WB: 1:1000
LMX1B	ProteinTech	18278	Rabbit	WB: 1:1000 IF: 1:400
		For zebrafish staining		
A4.1025	DSHB		Mouse	IF: 1:300
Anti-GFP	Abcam	ab13970	Chicken	IF: 1:200
Anti-mCh	Kerafast	est202	Rat	IF: 1:100
ATG13	Sigma Aldrich	SAB4200135	Rabbit	WB: 1:100
Collagen II	Abcam	ab34712	Rabbit	IF: 1:500
Collagen II	DSHB	II-II6B3-s	Mouse	IF: 1:20
Collagen X	Sigma	SAB4200800	Mouse	IF: 1:100
GAPDH	Protein Tech	10494-1-AP	Mouse	WB: 1:2000
LC3	Abcam	ab51520	Rabbit	WB: 1:300
LMX1B	Abcam	ab66941	Rabbit	WB: 1:400
LMX1B	Prof Ralph Witzgall's lab (173)	-	Rabbit	WB: 1:500
p62	Cell Signalling Technologies	5114	Rabbit	WB: 1:300
Sox9a	Genetex	GTX128370	Rabbit	IF: 1:200

TH	Dr Soojin Ryu's lab (222)	-	Rabbit	IF: 1:500
TH	Millipore	AB152	Rabbit	WB: 1:1000
THBS4	Abcam	ab211143	Rabbit	IF: 1:500
ULK1	Cell signalling	8054S	Rabbit	WB: 1:400

2º Antibody	**Supplier**	**Cat. No.**	**Type**	**Dilution**
Anti-Mouse HRP	SignalChem	G32-62G	Goat Anti-Mouse	WB: 1:10000
Anti-Rabbit HRP	SignalChem	G33-62G	Goat Anti-Rabbit	WB: 1:10000
Dylight 488 anti-mouse	Invitrogen	35502	Goat Anti-Mouse	IF: 1:500
Dylight 488 anti-chicken	Thermofisher	SA5-10070	Goat Anti-Chicken	IF: 1:500
Dylight 647 anti-mouse	Thermofisher	SA5-35500	Goat Anti-Mouse	IF: 1:500
Dylight 650 anti-rat	Thermofisher	SA5-10029	Donkey Anti-Rat	IF: 1:400
Alexa Fluor 488 anti-rabbit	Invitrogen	A21206	Donkey Anti-Rabbit	IF: 1:500
Alexa Fluor 568 anti-rabbit	Invitrogen	A10042	Donkey Anti-Rabbit	IF: 1:500
Alexa Fluor 488 anti-mouse	Invitrogen	A11029	Goat Anti-Mouse	IF: 1:400
Alexa Fluor 488 anti-rabbit	Invitrogen	A11034	Goat Anti-Rabbit	IF: 1:400
Alexa Fluor 568 anti-mouse	Invitrogen	A11031	Goat Anti-Mouse	IF: 1:400
Alexa Fluor 568 anti-rabbit	Invitrogen	A11036	Goat Anti-Rabbit	IF: 1:400

Buffers and Solutions

All buffers and solutions were prepared in ddH_20 (MilliQ, Millipore). Chemicals were purchased from Sigma Aldrich unless otherwise stated.

2.1.7 Media and Solutions for Bacterial Growth and Preparation

Luria-Bertani (LB) broth: 1% (w/v) Tryptone, 0.5% (w/v) yeast extract, 1% (w/v) NaCl - pH 7.4.

LB agar: LB broth with 20 g/L Agar.

Antibiotics: Ampicillin (Sigma, #A0166) and Kanamycin (Sigma, K1637). Stored at 100 mg/ml (-20°C long term) and used at 100 and 50 μg/ml respectively.

S.O.C outgrowth medium: 2% Vegetable Peptone, 0.5% Yeast Extract, 10 mM NaCl, 2.5 mM KCl, 10 mM $MgCl_2$, 10 mM $MgSO_4$ (NEB, #B9020).

2.1.8 Buffers and Solutions for Molecular Biology

Tris-Acetate EDTA (TAE) buffer: 40mM Tris base, 20 mM glacial acetic acid and 1 mM EDTA.

6x DNA loading dye: 2.5% Ficoll®-400, 10 mM EDTA, 3.3 mM Tris-HCl, 0.02% Dye 1, 0.001% Dye 2 - pH 8 (NEB, #B7025S).

DNA ladder: Quick-Load® 100 bp and 1 kb DNA Ladder (NEB, N0467 and N3232 respectively).

10x Restriction digest buffer: CutSmart® Buffer, 50 mM Potassium Acetate, 20 mM Tris-acetate, 10 mM Magnesium Acetate, 100 μg/ml BSA, pH 7.9 (NEB, #7204S).

10x Antarctic Phosphatase Reaction Buffer: 500 mM Bis-Tris-Propane HCl, 10 mM $MgCl_2$, 1 mM $ZnCl_2$, pH 6.0 (NEB, #M0289S).

10x T4 Ligase Reaction Buffer: 660mM Tris-HCl, 50 mM $MgCl_2$, 50 mM DTT, 10 mM ATP, pH 7.5, (Sigma, #10481220001).

Plasmid DNA purification, QIAprep Spin Miniprep kit (Qiagen, #27106)

Buffer P1 (resuspension buffer): 50 mM Tris-HCl, 10 mM EDTA, 100 μg/ml RNase A, 1:1000 LyseBlue (colour pH indicator), pH 8.0.

Buffer P2 (lysis buffer): 200 mM NaOH, 1% (w/v) SDS.

Buffer N3 (neutralization buffer): 4.2 M Gu-HCl 0.9 M potassium acetate, pH 4.8.

Buffer PE (wash buffer): 10 mM Tris-HCl pH 7.5, 80% EtOH.

Buffer EB (elution buffer): 10 mM Tris-HCl pH 8.5.

Plasmid Gel Extraction kit, QIAquick (Qiagen, #28115)

QG buffer: 5.5 M guanidine thiocyanate (GuSCN) and 20 mM Tris-HCl pH 6.6.

Buffer PE (wash buffer): As above.

RNA Extraction kit, RNeasy mini kit (Qiagen, #74104)

RLT lysis buffer: Composition: proprietary. Contains high concentration of guanidine isothiocycanate to supports binding of RNA to the silica membrane.

RW1 wash buffer: Composition: proprietary. Contains ethanol and guanidine salt.

RPE wash buffer: Composition: proprietary. Contains ethanol to remove excess salts from the column.

High-Capacity RNA-to-cDNA™ Kit (Thermo Scientific, #4387406)

20x RT buffer mix: Composition: proprietary. Contains dNTPs, random octamers, and oligo dT-16.

2x RT enzyme mix: Composition: proprietary. Contains MuLV reverse transcriptase and RNase inhibitor protein.

2.1.9 Mammalian Cell Culture Media and Buffers

Fetal Bovine Serum (FBS): EU approved FBS (virus and mycoplasma tested, Gibco, Life Technologies). Aliquoted and stored at -20°C.

Dulbecco's Modified Eagle's Medium (DMEM) high glucose (#D5796): Used for HEK293T cell lines. DMEM with 4.5 g/L glucose supplemented with 10% FBS.

1x Trypsin: 0.05% trypsin and 0.02% EDTA.4Na in Hanks' Balanced Salt Solution (HBSS) with phenol red, pH 7.4.

Opti-MEM® - reduced serum media: Modification of Eagle's Minimum Essential Media buffered with HEPES and sodium bicarbonate supplemented with hypoxanthine, thymidine, sodium pyruvate, L-glutamine, trace elements and growth factors.

FACS buffer: 25 mM HEPES, 2.5 mM EDTA, 2% BSA in PBS, pH 7.

2.1.10 Lysis Buffers

3x protein sample buffer (Laemmli): 10% glycerol, 3% SDS (w/v), 12.5% (v/v) Upper Tris Buffer, pH6.8, Bromophenol Blue + 5% (v/v) β-mercaptoethanol.

Radioimmunoprecipitation assay (RIPA) buffer: 150 mM NaCl, 10 mM Tris, 0.1% SDS, 1% Triton X-100, 1% deoxycholate, 5 mM EDTA, pH 7.2.

Zebrafish tissue lysis buffer: 25 mM NaOH, 0.2 mM EDTA.

Zebrafish tissue neutralisation buffer: 40 mM Tris-HCl, pH 5.

2.1.11 Buffers and Solutions for SDS-PAGE, Immunoblotting and Immunofluorescence

Phosphate Buffered Saline (PBS): 140 mM NaCl, 2.7 mM KCl, 1.5 mM KH_2PO_4, 8.1 mM Na_2HPO_4 (anhydrous), pH 7.4.

Phosphate Buffered Saline with Triton (PBS-T): 140 mM NaCl, 2.7 mM KCl, 1.5 mM KH_2PO_4, 8.1 mM Na_2HPO_4 (anhydrous), 0.01% Triton X-100, pH 7.4.

"Lower" Tris SDS-PAGE buffer (resolving gels): 1.5 M Tris-HCl, 0.4% SDS, pH 8.8.

"Upper" Tris SDS-PAGE buffer (stacking gels): 0.5 M Tris-HCl, 0.4% SDS, pH 6.8.

SDS-PAGE running buffer: 25 mM Tris, 190 mM glycine, 0.1% SDS (w/v), pH 8.3.

3x Protein sample buffer: 10% Glycerol, 0.3% SDS, 12.5% "Upper" Tris buffer, 5% β-Mercaptoethanol

Transfer buffer: 25 mM Tris, 190 mM glycine, 20% (v/v) methanol, 0.02% SDS (w/v).

Ponceau stain: 0.1% w/v ponceau stain, 1% acetic acid.

Tris Buffered Saline (TBS): 20 mM Tris-HCl, 150 mM NaCl, pH 7.7.

Blocking solution for immunoblotting: 1X TBS, 0.1% Tween-20, 5% (w/v) non-fat powdered milk (Marvel).

Protein ladder: PageRuler™ Plus Prestained Protein Ladder, 62.5 mM Tris-H_3PO_4 (pH 7.5 at 25°C), 1 mM EDTA, 2% SDS, 10 mM DTT, 1 mM NaN_3, 33% glycerol (Thermofisher, #26620).

Blocking solution for immunocytochemistry: 5% BSA, 0.3% Triton X-100 in PBS-T.

Mowiol: 2.4g Mowiol l (Sigma, #324590), 6g glycerol, 12mL 0.2 M Tris, pH 8.5 + supplemented with 25 mg/mL of the antioxidant DABCO (1,4-diazabicylo-2-octane).

2.1.12 Solutions for Zebrafish Maintenance and Live Staining

Danieau solution: 500 μM NaCl, 17 μM KCl, 33 μM CaCl and 33 μM $MgSO_4$, with 2 drops per litre methylene blue antifungal agent added.

Tricaine/MS222 (3-amino benzoic acid ethyl ester): 153 mM tricaine powder (Sigma, #A5040), 21 mM Tris at pH 9. Adjust to pH 7.

Alizarin Red (live stain): 0.1% Alizarin Red S, 0.1% HEPES buffer at 1 M, in Danieau solution.

Acridine orange: 1 mg/ml Acridine orange hemi (zinc chloride) salt powder (Sigma, #158550) in Danieau solution.

2.1.13 Solutions for Wholemount Immunostaining of Zebrafish Larvae

Paraformaldehyde for TH staining (PFA+): 4% PFA, 0.15 mM $CaCl_2$, 4% sucrose, 1% DMSO in 0.1 M PO_4 buffer.

PO_4 Buffer: 0.1 M $NaH_2PO_4 \cdot H_2O$. Adjust to pH 7.4.

Proteinase K digestion solution: Proteinase K (Sigma, #4333793) with PBS-T. (Refreshed after 30 minutes at 37°C).

Table 2.5 – Concentration of Proteinase K used to permeabilise zebrafish larvae at different ages

Age of Larvae (days post fertilisation)	Concentration of Proteinase K used	Incubation time @ 37°C
3dpf	10 µg/ml	30 minutes
4dpf	10 µg/ml	40 minutes
5dpf	15 µg/ml	50 minutes
7dpf	15 µg/ml	60 minutes

Blocking buffer: 5% horse serum (ThermoFisher, #16050130) in PBS-T.

2.2. Methods

2.2.1 Molecular Biology Methods

2.2.1.1 Restriction Digestion of Plasmids

Restriction enzymes (New England Biolabs (NEB)) targeting the specific restriction site required were chosen and used to digest plasmid DNA or PCR products. Typically, 5 μg of plasmid DNA or 8 μL PCR product were incubated with 10X CutSmart buffer, 10units of enzyme and H_2O for up to 3 hours at 37°C. For the linearisation of plasmids to be used as ligation vectors, dephosphorylation using Antarctic phosphatase was performed with 5units alkaline phosphatase at 37°C for 30 minutes.

2.2.1.2 Agarose Gel Electrophoresis

For the separation of DNA fragments, agarose gel electrophoresis was used whereby negatively charged DNA migrates through agarose gel matrix towards the positively charged anode, with DNA fragment size determining the rate of migration. Gels were prepared by boiling 1-3% (w/v) agarose (Bioline, BIO-41026) in 1x TAE buffer until fully dissolved. To allow for band detection under UV light, 7.5 μL of 10 mg/mL ethidium bromide (Sigma, E1510) was added once the agarose solution had cooled and gels were cast in trays with removable combs for 30 minutes until set. DNA samples were loaded with 6x loading dye (NEB, B7024S) and 4 μL of either a 100 bp or 1 kb DNA ladder. Electrophoresis was performed in 1x TAE at 95 v for 40 minutes in a circulating-buffer chamber. DNA bands were visualised via a UV transilluminator, and images were acquired using an Olympus Camedia C-5060 digital camera.

2.2.1.3 Agarose Gel Purification

Following separation and visualisation by agarose gel electrophoresis, linearised plasmid fragments were excised from the gel using a blade. DNA was purified from the gel segment

using a QIAquick Gel extraction kit following the manufacturer's instructions. Briefly, gel segments containing DNA were dissolved in Buffer QG at 50°C and passed through a silica spin column by centrifugation at 13,000 *x g* for 1 minute on a benchtop centrifuge. This was followed by two wash steps to purify the DNA and then eluted in ddH_2O. The concentration of purified DNA samples was measured using absorbance spectroscopy.

2.2.1.4 DNA Vector-Insert Ligation

Ligation reactions were prepared following an insert to vector molar ratio of 3:1 in 15 µL reactions. Reaction was formed of 1unit of T4 DNA ligase (Promega, #M1801) with 10x DNA ligase buffer. Reaction was incubated at 16°C overnight.

2.2.1.5 Transformation of Competent E. coli

25 µl DH5-α super-competent cells (Biolabs, #C2987) were thawed on ice and 1 µL DNA or 3 µL ligation reaction were added and incubated on ice for 25 minutes to allow DNA to attach to the bacterial cell wall. Cells were heat shocked at 42°C for 45 seconds then incubated on ice for 5 minutes. 200 µl SOC media was added, and samples incubated at 37.5°C, shaking at 225 rpm for 45 minutes. 200 µl of each sample were then spread onto 20% Agar-LB plates containing the appropriate antibiotic (Ampicillin or Kanamycin) and incubated at 37.5°C overnight. Single colonies were selected and plasmids isolated by mini-prep plasmid growth.

2.2.1.6 Purification of Plasmid DNA

Plasmid DNA was purified from bacterial cells using the Qiagen Miniprep Kit, according to the manufacturer's guidelines. Single colonies were inoculated in 5 mL LB broth containing the appropriate antibiotic (Kanamycin or Ampicillin) and grown overnight at 37.5°C and 225 rpm. Cell growth was checked the following day and cells were pelleted at 4000 *x g* for 5 minutes. Bacterial cell pellets were resuspended in 250 µL cold P1 buffer and lysed in 250 µL P2 lysis buffer for up to 5 minutes. Addition of 350 µL P3 buffer neutralised the reaction and the resulting precipitants were removed by centrifugation at 14,000 *x g* for 10 minutes. Full volume of supernatant was applied to a silica membrane and washed twice with buffer PE by centrifugation at 13,000 *x g* for 1 minute. Purified DNA samples were eluted by direct

addition of 30 μL ddH_2O to the silica membrane which was incubated for 1 minute before a centrifugation at 13,000 *x g* for 1 minute into a fresh 1.5 mL tube.

2.2.2 Culturing of Mammalian Cell Lines

2.2.2.1 Cell Culture

HEK293T (Human Embryonic Kidney) cells were maintained in a tissue culture treated 10 cm dishes (Corning, #430167) in 10 ml of DMEM (Dulbecco's Modified Eagles Medium) supplemented with 10% FBS (termed DMEM complete media hereafter) at 37°C and 5% CO_2 in a humidified incubator. Stocks of HEK293T cells were regularly frozen at low passage numbers (<10 passages) in DMEM complete media plus 10% DMSO at -80°C. Cells were recovered by rapid thawing at 37°C and dilution in DMEM complete media overnight in 10 cm dishes.

2.2.3 Biochemical Techniques in Cells

2.2.3.1 Quantitative Real-time Polymerase Chain Reaction (qRT-PCR)

HEK293T cells were plated on 6-well (Thermo Fisher, #10119831) plates. Following the corresponding treatment, cells were washed once with PBS and then lysed in 350 μL RLT buffer. Total RNA was extracted using a RNeasy kit (Qiagen, #74104) following the manufacturer's instructions. Briefly, cell lysates were passed through a silica spin column by centrifugation for 2 minutes at 13,000 *x g*. Next, 1 volume 70% ethanol was added to homogenised lysate, mixed, and transferred to second silica spin column for centrifugation at 8000 *x g* for 15 seconds. The flow-through was discarded and the silica membrane washed with 700 μL RW1 buffer. Genomic DNA was then digested by incubation with DNase (1 unit/μl in RDD buffer) for 20 minutes at room temperature. The silica membrane was washed once with RW1 buffer and then twice with 500 μL RPE buffer and once without any buffer addition by centrifugation at 8,000 *xg* for 1 minute each. Purified RNA samples were eluted by direct addition of 30 μL RNase-free H_2O (Thermo Fisher, #4415345) to the silica membrane which was incubated for 1 minute before a centrifugation at 13,000 *x g* for 1 minute into a fresh 1.5 mL tube.

RNA samples were reverse transcribed using High-Capacity RNA-to-cDNA™ Kit, according to manufacturer's protocol: 1 μg RNA added (if concentration between 0.1-0.02 μg/μl, 9 μl added), to 10 μl 2x RT buffer and 1 μl 20x enzyme mix and then amplified by real-time polymerase chain reaction (37°C for 60 minutes and 95°C for 5 minutes). The resulting cDNA was then diluted 1:4 in ddH_2O.

For each qRT-PCR experiment, each condition consisted of three distinct triplicates, each run in duplicate. Per sample, 2 μl cDNA was added to 0.5 μl of relevant forward and reverse primers at 5 μM each with 5 μl SYBR™ green PCR mastermix (Life Technologies, #4309155) and 2 μl ddH_2O (10 μl total reaction volume) to one well of a 96-well plate. GAPDH amplified as a control. qRT-PCR was carried out using StepOnePlus System (Applied Biosystems) with the following conditions: initial denaturation at 95°C for 10 minutes, 40 cycles with 95°C for 15 seconds (denaturation), 60°C for 30 seconds (annealing) and 60°C for 30 seconds (elongation). mRNA levels were estimated using the ΔΔCt method, described below (223).

2.2.3.2 Analysis of qRT-PCR Data

A Ct (cycle number) value, which represents the cycle where SYBR green signal is detected above the background and where the PCR product is in the exponential phase, were given for each sample. These Ct values are proportional to initial template levels; thus, lower cDNA template levels give higher Ct values. Any Ct values above 35 were disregarded as these are not distinguishable from background levels.

To calculate mRNA expression levels, first, the mean Ct across each duplicate was calculated then normalized to the control gene, GAPDH by calculating the ΔCt value: mean Ct (gene of interest) – mean Ct (GAPDH). The mean ΔCt was then calculated as the average of the ΔCt values from across the gene triplicate and then relativised to GAPDH as ΔΔCt: Mean ΔCt (gene of interest) - Mean ΔCt (control). The fold of change in mRNA expression relative to GAPDH was calculated as $2^{(-\Delta\Delta Ct)}$. Standard error of mean (SEM) was calculated using propagation of uncertainty when n ≥ 3 as $SEM=\frac{SD}{\sqrt{n}}$.

2.2.3.3 Cell Lysis

Cells grown in 6-well plates were placed on ice and washed once in 2 ml of PBS. Then, 200-250 µl RIPA (Radioimmunoprecipitation assay) buffer plus 10% proteinase inhibitor cocktail (Roche Diagnostics) was added per well and the cells were incubated on ice for 15 minutes with agitation. Cells were removed using a cell scraper and centrifuged at 13,000 rpm for 15 minutes at 4°C. Supernatant was transferred to new tube and 3x Laemmli buffer containing 5% β-mercaptoethanol was added before samples were heated to 95°C for 10 minutes. If not loaded immediately, samples were stored at -20°C.

2.2.3.4 SDS Polyacrylamide Gel Electrophoresis (SDS-PAGE)

Acrylamide gels were prepared using Tris SDS-based buffers and 30% acrylamide/0.8% bisacrylamide (Serva, 10688.03). Polymerization was triggered by the addition of TEMED (Bio-Rad, #1610800EDU) and 10% ammonium persulfate (APS). Resolving gels were prepared at different percentages depending upon the protein(s) of interest (smaller proteins such as LC3-I and LC3-II require a higher 15% gel to ensure sufficient resolution). The stacking gel, poured upon the resolving gel, was prepared in "Upper" Tris-SDS buffer using 4% acrylamide, 0.085% (w/v) APS and 0.25% (v/v) TEMED. Proportions of the resolving gels most commonly used are in Table 2.6.

Gels were poured between two glass plates of the MiniPROTEAN 3 system (Biorad). Once polymerised, gels were arranged into a MiniPROTEAN 3 gasket and placed within the tank filled with 1x Running Buffer. Then, 15-30 µl of sample were loaded per well alongside 5 µl PageRuler Precision Plus Ladder (Thermofisher, #26619). Electrophoresis was performed at 40 mA constant for 1-2 hour, until dye front reached base of the resolving gel.

Table 2.6 – Composition of resolving and stacking gels at indicated percentages (equivalent volumes for 2 gels)

Resolving gel	**10%**	**12%**	**15%**	**Stacking gel**	
Lower buffer	3 ml	3 ml	3 ml	**Upper buffer**	1.5 ml
Acrylamide (30%)	4 ml	4.8 ml	6 ml	**Acrylamide (30%)**	0.8 ml

H_2O	5 ml	4.2 ml	3 ml	**H_2O**	3.7 ml
APS (10%)	50 µl	50 µl	50 µl	**APS (10%)**	25 µl
TEMED	20 µl	20 µl	20 µl	**TEMED**	15 µl

2.2.3.5 Transfer to Nitrocellulose

The wet transfer was performed using the Mini Trans-Blot® Cell system (Biorad). Cassettes were assembled in ice cold 1x Transfer buffer with 20% methanol in the sequence of: sponge (Bio-Rad, 1703933), filter paper x2 (3mm Whatman, Thermofisher, #11330744), polyacrylamide gel, nitrocellulose membrane, filter paper x2, sponge. Proteins on SDS-PAGE gels were electrophoretically transferred at 100 V constant for 70 minutes onto 0.45 µm nitrocellulose membrane (Protran®, #10600015). Following transfer, nitrocellulose membranes were stained with Ponceau for 1 minute and washed thoroughly in ddH_2O to assess the quality of transfer.

2.2.3.6 Immunoblotting

Membranes were first blocked in 5% milk (Marvel) in Tris-buffered saline-triton (TBS-T) solution for 1 hour at room temperature. Primary antibodies (Table 2.4) were diluted in 5% milk/TBS-T to the appropriate dilution and left on membranes overnight at 4°C. The membranes were washed 3 times 5 minutes in TBS-T and then a horseradish peroxidase (HRP) anti-mouse or rabbit antibody (Signal Chem) (made at a 1:10000 dilution in 5% milk/TBS-T solution) was applied for 1 hour at room temperature. The membranes were washed again in TBS-T before incubation in freshly made enhanced chemiluminescence substrate (ECL, GE Healthcare; 1ml per blot) for 1 minute and exposure to photographic film (GE Healthcare) for visual detection of the protein bands. The films were developed in a Curix 60 Chapter 2 55 film processor (AGFA) and GAPDH was used as a protein loading control. Densitometry of the immunoblots was performed using ImageJ software (224).

2.2.3.7 Generation of LMX1B CRISPR Knock-out Cell Line

Generation of Cas9-GFP-gRNA constructs targeting human LMX1B in HEK 293T cells performed following protocol previously described (225). Briefly, the PX458 SpCas9-2A-EGFP vector (gifted from Dr Stephens lab, Bristol; vector map in Section 2.3.1) was linearised

using *BbsI* restriction site and phosphorylated using Antarctic phosphatase, as previously described. CRISPR target gRNA sequences against LMX1B human isoform 1 (Hg38/GRCh38) were selected using the *in silico* gRNA generation tool, CHOPCHOP (226). gRNAs were synthesised externally (Eurofins Genomics) and annealed before ligating into the cut PX458 vector. Following transformation into DH5-alpha cells, ampicillin resistance (1:1000 in LB-agar) was used to select for positive colonies, and single colonies were selected for outgrow in 5 ml LB-media overnight at 37°C and 225 rpm. Cells were pelleted at 4000 x g for 5 minutes and plasmid purification performed using a mini-prep plasmid purification kit. Purified DNA samples were eluted in 35 µl of water and constructs sequenced via Eurofins Genomics using primers for the U6 promoter.

Constructs were transfected into HEK 293T cells using Lipofectamine 2000 (Thermo Fisher, 11668027). Briefly, 24 hours before transfection, $4.5x10^5$ HEK 293T cells per well were seeded onto tissue culture treated 6-well plates in 2 ml of DMEM complete media. Following a 5 minute incubation, 6 µl of Lipofectamine 2000 in 600 µl of Opti-MEM media (Thermofisher, #31985047) was combined with 12 µg of Cas9-GFP-gRNA construct DNA in 600 µl Opti-MEM media and incubated for 20 minutes at room temperature. Next, 200 µl of transfection solution was added dropwise to each well and following an overnight incubation, media was replaced with DMEM complete media. Then, 48 hours after transfection cells were prepared for FACS.

2.2.3.8 Fluorescence Activated Cell Sorting (FACS) for CRISPR-Cas9-positive cells

Cells were rinsed twice in cold, sterile PBS (Sigma, #D8537) before addition of 1 ml cold accutase (Sigma, A6964) and incubated at 37°C for 5 minutes until cells detached and in single cell suspension. Next, 2 ml cold PBS added, and cells centrifuged at 1000 xg for 3 minutes to form cell pellet. Supernatant removed and cells resuspended in cold FACS buffer to give approximately $1x10^6$ cells/ml and placed on ice until FAC sorting.

FACS was carried out at 4°C using a BD Influx Fluorescence Associated Cell Sorter where gating was used to select single, GFP-positive, live cells. Single cells were sorted into 96-well plates (Appleton Woods, #BC015) with 150 ml DMEM complete media. Plates were briefly centrifuged and incubated at 37°C, 5% CO_2. Clones were evaluated 3 days post-sorting to exclude multiple cell contamination. Cells were cultured until confluence and duplicated

until cell number sufficient for analysis of LMX1B expression by fixed cell immunostaining or immunoblotting.

2.2.4 Fluorescence Staining and Imaging

2.2.4.1 Immunocytochemistry

HEK 293T cells were seeded on coverslips to reach 50-70% confluency at time of fixation. Following removal of media, cells were washed once in 2ml PBS and fixed with 4% PFA for 20 minutes on ice and then washed twice in PBS for 3 minutes. Cells were incubated with 5% BSA (in PBS-T) for 1 hour at room temperature. After washing in PBS for 5 minutes, coverslips were placed facedown onto parafilm strips (Bemis, #HS234526C) on top of 40 µL primary antibodies (Table 2.4), diluted in PBS, per coverslip. Coverslips were incubated for 45 minutes and washed thrice in PBS for 5 minutes each. The incubation step was repeated with fluorophore-conjugated secondary antibodies (Table 2.4) then coverslips washed three times in PBS for 5 minutes. Cells were counterstained with 0.1 µg/mL DAPI (4',6-diamidino-2-phenylindole, Thermo Fisher, #62248; prepared in PBS) for 5 minutes, followed by two further 5 minute PBS washes. Coverslips were mounted face down onto glass slides (Academy, #N/A142) with Mowiol (6 µL per 13mm diameter coverslip) and left to dry overnight.

2.2.4.2 Widefield Microscopy

For fixed cell imaging, an Olympus IX-71 inverted microscope (60× Uplan Fluorite objective; 0.65-1.25 NA, oil) with a CoolSNAP HQ CCD camera (Photometrics, AZ) and driven by MetaMorph software (Molecular Devices) was used. As a light source, a xenon lamp for transmitted light and epifluorescence imaging was used.

2.2.5 Zebrafish Husbandry and Lines

2.2.5.1 Zebrafish Husbandry

Zebrafish were raised and maintained under standard conditions in the zebrafish room of the Animal Services Unit (ASU) at the University of Bristol (227). Experiments were performed under a UK Home Office project licence (held by Dr Chrissy Hammond, University of Bristol) and Personal Licence (held by Joanna Moss) under approval by the local ethics committee (the

Animal Welfare and Ethical Review Body of the University of Bristol) and in accordance with the UK Home Office Animals (Scientific Procedures) Act 1986.

Fish above 6dpf were raised and grown at 28.5°C on a 14-hour light:10-hour dark cycle. Embryos bred for the maintenance of lines were obtained from natural spawning at the beginning of the light period. Embryos required for experimental procedures, where careful staging is required, were placed into mating tanks overnight with a divider between males and females. At the beginning of the light period, the divider was removed embryos collected 1 hour later. Embryos were kept in Danieau solution at 28°C in 10cm petri dishes, with Danieau solution refreshed every day until 5 days post fertilisation (dpf) where they were placed in the Zebrafish Facility to grow until adulthood. For larvae not being raised to adulthood, live embryos were killed by anaesthetic overdose in MS222 (0.016%).

2.2.5.2 Zebrafish Lines

All zebrafish referred to as wildtype (*wt*), are non-mutant siblings of the mutant lines (*atg13*, *lmx1ba* or *lmx1bb*) used in this study. All transgenic and mutant lines used in this study are listed in Table 2.7.

The *atg13* mutant fish line was designed and generated using CRISPR-Cas9 mutagenesis by Dr Martina Wirth from Dr Sharon Tooze's lab at the Francis Crick Institute. The line has a 5 base pair (bp) deletion at 92-96 bp (amino acid 31) in the *atg13* gene, producing a premature stop codon 83 bp downstream of the mutation and the insertion of a novel HindIII restriction site at the mutation site. This line was used as an autophagy-null model and used in both the GFP-Lc3 and Col2a1-mCh background.

Table 2.7 - List of transgenic and mutant zebrafish lines used in this thesis

Line Name	Abbr. used	Description	Source and reference
Transgenic lines			
Tg(CMV:EGFP-map1lc3b)	GFP-Lc3	*lc3* gene labelled with eGFP to enable visualisation of autophagosomal structures; under high magnification can be seen as distinct puncta	Klionsky lab, Life Sciences Institute, University of Michigan, USA (125)

Tg(Col2a1aBAC: mCherry)	Col2a1	Type II collagen gene *col2a1* labelled with mCherry; enables visualisation of chondrocytes	Schulte-Merker lab, Hubrecht Institute, Utrecht, The Netherlands (228)
		Mutant lines	
atg13 ^{fci500}	*atg13*$^{-/-}$	Premature stop codon in HORMA domain caused by 5 bp deletion in exon 3; shows reduced autophagy flux	Tooze lab, Francis Crick Institute, London, UK (229)
lmx1ba ^{bsl2962}	*lmx1ba*$^{-/-}$	Premature stop codon in LIM A domain caused by 7 bp deletion in exon 4	Generated as a new line using CRISPR/Cas9 technology
lmx1bb ^{bsl2816}	*lmx1bb*$^{-/+}$	Premature stop codon in Homebox domain caused by 19 bp insertion in exon 3	Generated as a new line using CRISPR/Cas9 technology
lmx1ba ^{bsl2962}***;lmx1bb*** ^{bsl2816}	*dKO*	In-cross of *lmx1ba*$^{-/-}$;*lmx1bb*$^{-/+}$ fish to create full *lmx1b* knock-out line	Studied only as larvae; do not survive to adulthood

2.2.5.3 Survival Assay of atg13 and lmx1b Mutant Lines

For the survival assays, larvae were genotyped before 5dpf and separated into tanks based on genotype. Larvae were monitored twice daily and dead larvae were counted and removed until 18dpf for *atg13* and 15dpf for the *lmx1b* lines. Survival of each line was evaluated using Kaplan–Meier survival curves.

2.2.6 Molecular and Biochemical Techniques in Zebrafish

2.2.6.1 Genotyping

Whole embryos or caudal fin amputations performed on adult zebrafish or larvae at 3-5dpf were used to obtain genomic DNA. For caudal fin amputations, zebrafish were anesthetized in 0.1 mg/mL MS222 and placed laterally on an over-turned petri dish for larvae, or white tape for adult fish. After removing residual water, a microscalpel, or blade for adults, was used to remove the tip of the caudal fin distal to the circulating blood.

Samples were placed in 25 µl of BASE solution for whole embryos and 4-50 µl for larval and adult fin clips respectively and heated at 95^{o}C for 1 hour before addition of equal volume of neutralisation buffer. The genomic DNA was added to a mastermix optimised for

EmeraldAmp GT PCR (Takara Bio, Japan, #RR320B) (Table 2.8) along with the appropriate sequencing primers for each gene (Table 2.2).

For genotyping *atg13, lmx1ba* or *lmx1bb* mutant zebrafish, following the PCR, as detailed in Table 2.8, 8 µl of PCR product was digested with the respective high fidelity restriction enzyme (Table 2.9) by addition of 2 µL of restriction digest solution (0.5 µL restriction enzyme, 1 µl 10x CutSmart buffer, 0.5 µL H_2O water). Samples were incubated for 2 hours at 37^{o}C and then run on a 3% agarose gel for 25 minutes at 95 V.

2.2.6.2 gRNA Design and Microinjection

CRISPR target gRNA sequences were selected using *in silico* gRNA prediction tools, CHOPCHOP (danRer11/GRz11) and CrisprScan track from UCSC Browser (danRer11) (226, 230). gRNAs where selected based on a combination of those having the highest efficiency rating, lowest CFD score (number of off-target gene hits) and being as close to the ATG start codon as possible. gRNA sequences were ordered and synthesised externally (Merck). Primers for each gRNA pair were designed using the web tool, Primer3Plus and ordered from Eurofins Genomics (231) (Table 2.3). Where gRNAs had overlapping target sequences, only one set of primers was designed.

Injection mix was prepared to a final concentration of 20 pmol/µL of gRNA, 20 pmol/µL of SygRNA Tracr RNA (Sigma, #TRACRRNA05N), 600 ng/µL of GeneArt Platinum Cas9 nuclease (Invitrogen) with phenol red and TE buffer and incubated for 15 minutes at room temperature before being placed on ice (Table 2.10). 1 pL of the solution was injected into the cell of eggs at one cell stage. Briefly, a glass capillary (type GC100F-15, Harvard Apparatus, USA) was pulled into a needle using the Intracel system (model P-97m Sutter Instrument Co., USA) with the following settings: heat, 500; pull, 15; velocity, 100; time, 2. The needle was loaded using gel loading tips, with 3 µl of solution and placed onto the injector (Picospritzer II, Parker Instrumentation) with gas pressure output of 30-40 psi, before the end of the needle was broken using tweezers. Only needles with an appropriate drop size of 0.1-1.5 mm (defined by a graticule, embedded in glycerol with 0.1 mm increments) were used. Solution was injected into the cell of embryos at the one-cell stage. Injection-positive embryos were selected by presence of phenol red in cell and kept at 28^{o}C until 5dpf.

Table 2.8 - Details of PCR mastermix and PCR programme used to genotype zebrafish

Standard PCR protocol for genotyping fish	
PCR Mastermix	PCR Programme
1x Mastermix 5 µl EmeraldAmp MAX HS PCR Mix 2x 0.5 µl ddH_2O 0.25 µl Forward primer (20 µM) 0.25 µl Reverse primer (20 µM) 4 µl DNA **Total 10 µl**	1. 95°C for 5 minutes 2. 94°C for 25 seconds 3. 64°C for 25 seconds 4. 72°C for 35 seconds 5. Repeat steps 2-4 x18 (↓ 0.6°C per cycle on step 3) 6. 94°C for 25 seconds 7. 54°C for 25 seconds 8. 72°C for 35 seconds 9. Repeat steps 6-8 x23 10. 72°C for 5 minutes

Table 2.9 – Details of restriction enzymes used to digest PCR products and their resulting digest products to genotype *atg13* and *lmx1b* mutant zebrafish lines

Restriction enzyme	**Cut site**	**Gene**	**Expected digest product**
HindIII	5′…AAGCTT…3′	*atg13*	386 bp for *wt*, 201 bp for homozygote and both bands for heterozygote.
BsaI	5′…GGTCTC $(N)_1{}^{v}$…3′ 3′…CCAGAG $(N)_{5\Lambda}$…5′	*lmx1ba*	170 bp and 175 bp for *wt* (seen as one band), 290 bp for homozygote and all three bands for heterozygote.
DraIII	5′…CACNNN^{v}GTG…3′ 3′…GTG$_{\Lambda}$NNNCAC…5′	*lmx1bb*	400 bp for *wt*, 225 bp and 275 bp for homozygote and all three bands for heterozygote.

Table 2.10 – Concentrations and volumes of reagents required for CRISPR-Cas9 injection into single-cell zebrafish embryos. Injections were assisted by Dr Erika Kague (University of Bristol)

Reagent	**Conc.**	**Vol.**	**Conc.**	**Vol.**
	For 1 gRNA		**For 3 gRNAs**	
gRNA	20 pMol	1 µl	20 pMol (each)	3 µl (total)
TracrRNA (Sigma, 05N)	20 pMol	1 µl	20 pMol	2 µl
Cas9 protein	600 ng/µL	1 µl	600 ng/µL	1 µl
TE buffer	-	1 µl	-	3 µl
Phenol red	-	1 µl	-	1 µl
	TOTAL	**5 µl**		**10 µl**

2.2.6.3 Generation of Stable CRISPR Knock-out Zebrafish Lines

Selected embryos were culled, and their DNA extracted as stated in Section 2.2.6.1. The appropriate lmx1ba or lmx1bb primers, along with a FAM primer, were used to amplify the targeted gene of interest and the PCR products with the FAM tail addition were sent off for sequencing by fragment analysis at the Genomic Facility, University of Bristol (Table 2.11). This helped to determine gRNA efficiency and efficacy whilst remaining siblings were grown to adulthood as a G0 population. G0 adults were genotyped by Sanger sequencing (Eurofins Genomics) using primers designed against gRNA target sequences (Table 2.3) on DNA extracted from tail fin clips, as previously described. CRISPR-Cas9-positive fish were identified and outcrossed to *wt* fish to create a heterozygous G1 population. At 3 months post fertilisation (mpf), fish from G1 population were sequenced using Sanger sequencing to identify the exact mutations carried by each fish. Siblings carrying the same mutation were in-crossed to generate G2 population which should be homozygous for the CRISPR-Cas9 mutation. Final sequencing of G2 population using tail fin clips was performed to determine germline transmission of mutation and to establish stable CRISPR-Cas9 knock-out lines (Figure 2.2.6.3).

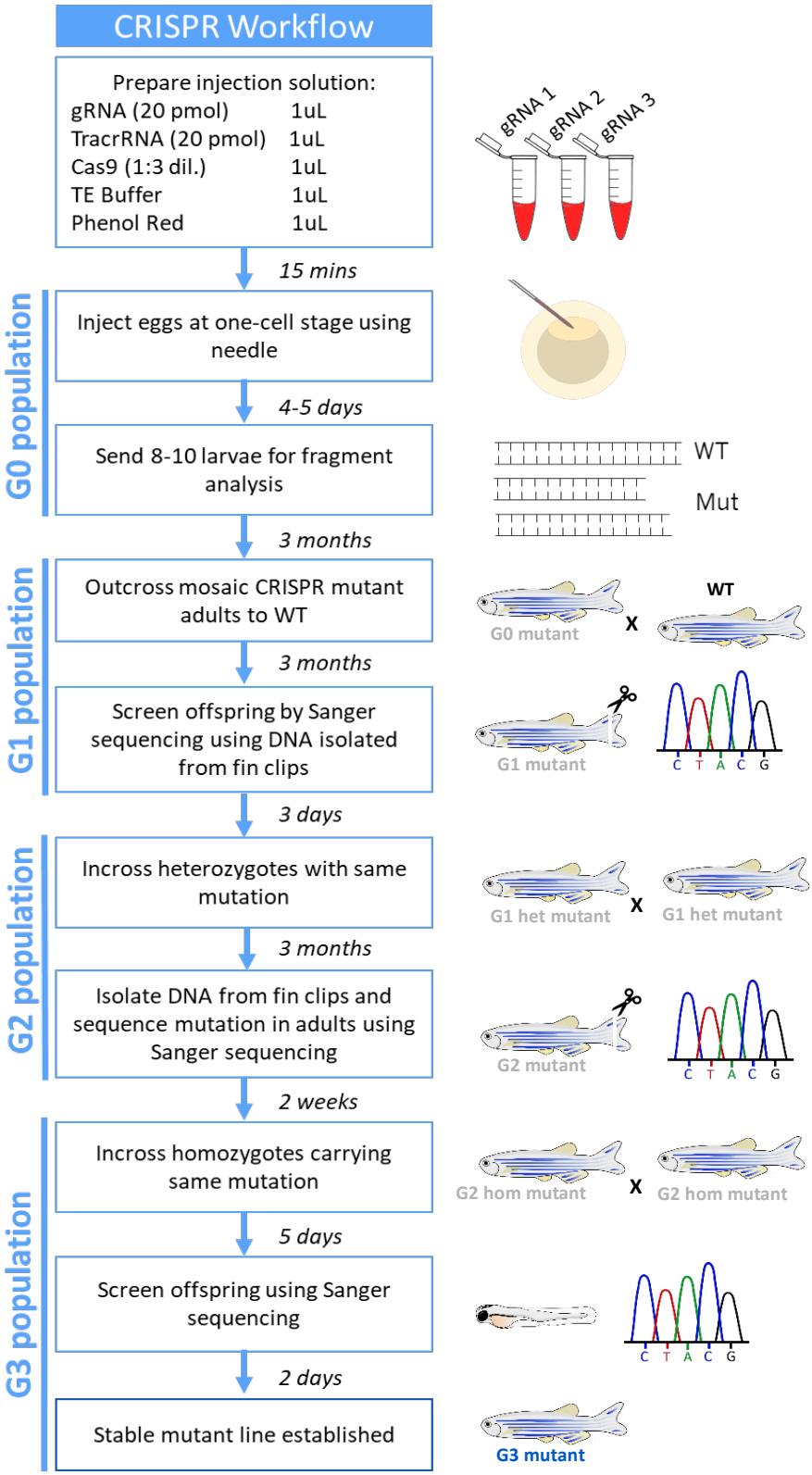

Figure 2.2.6.3 – CRISPR-Cas9 workflow in zebrafish, Schematic detailing the steps involved to generate a stable CRISPR mutant zebrafish line. Het = heterozygote; Hom = homozygote.

Table 2.11 - Concentrations and volumes of reagents required for fragment analysis of CRISPR-Cas9 injected larvae

Reagent	Conc.	Vol.
EmeraldAmp MAX HS PCR Mix	2x	10 µl
FOR primer	20 µM	0.1 µl
REV primer	20 µM	0.25 µl
M13 FAM primer	20 µM	0.2 µl
ddH_2O	-	5.45 µl
DNA	-	4 µl
TOTAL		**20 µl**

2.2.6.4 Protein Extraction from Zebrafish Larvae and Adult Fin Clips

For adults, caudal fin clips were used to collect protein. Fish were anaesthetised in 0.1 mg/mL MS222 and placed laterally onto white tape where a sharp scalpel was used to remove the caudal fin tip. Clips from 1-3 fish were taken per condition/genotype and placed in cold PBS using tweezers. Tissue was macerated with scissors and centrifuged at 13,000 rcf for 4 minutes at room temperature. Pellet was resuspended in 100-200 µL RIPA buffer with 10% protein inhibitor cocktail (Roche, #65892970001) and homogenised with pellet pestle (Sigma, #Z359971) for 40 seconds, moving pestle gently up and down to reach all of tissue. Samples were placed on rocker for 10 minutes at room temperature, then spun at 13,000 rpm for 10 minutes at 4°C. Supernatant placed in new tube with 3x protein sample buffer containing 5% β-mercaptoethanol added before samples were heated to 95°C for 10 minutes. If not loaded immediately, samples were stored at -20°C.

For larval protein extraction, 15-25 larvae per condition were culled at 1-5dpf and the yolk sac manually removed using tweezers. Larvae were collected in 1.5ml Eppendorf tubes and snap frozen using liquid nitrogen. Samples were thawed on ice and the tissue homogenised using a pellet pestle (Sigma, #Z359971) for 45 seconds by gently moving the pestle up and down in solution. Samples were spun briefly at 13,000 rpm for 1 minute and supernatant

reconstituted in a new tube with 100 µl (per 15 larvae) hot 3x protein sample buffer containing 5% β-mercaptoethanol, before being boiled at 95°C for 10 minutes and loaded onto gels. Protein samples were analysed via immunoblotting as described in Section 2.2.3.4

2.2.6.5 Whole-mount Immunohistochemistry on Larvae

Larvae at 3-7dpf were fixed in 4% PFA for 2 hours at room temperature or overnight at 4°C with agitation and then placed at -20°C overnight in 100% methanol. Larvae were re-hydrated with decreasing concentrations of methanol in PBS-T (75% - 50% - 25% - 0%) for 10 minutes each before treatment with proteinase K at 10-15 µg/ml for 35-50 minutes at 37°C. For A4.1025 antibody staining, larvae were instead permeabilised in 0.25% Trypsin for 15 minutes on ice. Larvae were washed 3 times 5 minutes in PBS-T and placed in blocking solution for 2 hours at room temperature. Primary antibodies (Table 2.4) were diluted in PBS-T to the appropriate dilution and left overnight at 4°C with agitation. Larvae were washed 6 times 10 minutes in PBS-T and incubated with secondary antibody, diluted in blocking solution, for 2 hours at room temperature before washing 6 times 10 minutes in PBS-T. For DAPI nuclei staining, larvae were incubated in 1 µg/ml DAPI in PBS-T for 1 hour at room temperature then washed 3 times 10 minutes before imaging.

For staining with the TH antibody, larvae were instead fixed with a modified PFA solution (termed 'PFA+' in this thesis) as adapted from Kastenhuber *et al.* (232). Larvae were fixed in PFA+ at room temperature for 2 hours and then washed 3 times for 5 minutes in PBS. For permeabilisation, proteinase K treatment was used as above, although it was followed by a post fixation in PFA+ at room temperature for 15 minutes. For the remainder of the staining, all other steps were followed as stated above.

2.2.6.6 TUNEL Staining of Larvae

To assess cell death in the *lmx1b* mutants, a TdT-UTP nick end labeling (TUNEL) assay in wholemount larvae was performed using the ApopTag Fluorescein *In Situ* Apoptosis Detection Kit (Chemicon, #S7110; catalogue number for reagents provided by kit listed). Briefly, 1dpf larvae were fixed in 4% PFA for 2 hours at room temperature. After washing in PBS-Triton (0.5% Triton X-100; termed PBS-Tr) for 3 times 5 minutes, samples were permeabilised with 10 ug/ml Proteinase-K for 10 minutes at room temperature. Samples

were then post-fixed in 4% PFA for 20 minutes at room temperature and washed in PBS-Tr before further permeabilization in an ethanol-acetone solution (made at 2:1 ratio) for 10 minutes at -20°C. Following incubation with the Equilibrium buffer (#90416) for 1 hour, the TdT enzyme (#90418), diluted to 30% in the Reaction buffer (#90417, provided by kit) was added to the larvae and left overnight at 37°C.

To stop the enzymatic reaction, Stop/Wash buffer (stock diluted 1:34 in dH_20; #90419) from the kit was added to the larvae for 10 minutes followed by 3 times 5 minute washes in PBS-Tr. Blocking solution (#90425) was added for 2 hours at room temperature and then anti-digoxygenin fluorescein (#90426) added at a 1:1 ratio with the blocking solution and left on overnight at 4°C. Before imaging, larvae were washed 5 times 10 minutes in PBS-Tr and counterstained with DAPI.

2.2.7 Drug Treatments and Live Staining in Zebrafish

2.2.7.1 Treatment with BafilomycinA1

For autophagy flux analysis, larvae were treated at 4dpf or 5dpf with 100 nM BafilomycinA1 (BafA1; Cambridge Bioscience, #14005; dissolved in DMSO, stock at 500 μM) or DMSO in Danieau solution (0.4 μl per 2 ml) for 3 hours at 28°C.

2.2.7.2 Alizarin Red Live Staining

To stain mineralised bone, live fish were incubated for 1 hour or overnight, for larvae and adult fish respectively, in 0.1 % Alizarin Red (Sigma, #A5533) in Danieau solution, before being rinsed twice in Danieau solution for 20 minutes before imaging.

2.2.7.3 Acridine Orange Live Staining

To visualise cell death during development, 1dpf larvae were placed in 10 μg/ml Acridine orange in Danieau solution for 10 minutes at 28°C. Larvae were then washed in Danieau solution three times for 5 minutes each before being imaged using a fluorescent stereomicroscope and the GFP filter in a lateral orientation.

2.2.7.4 LysoTracker Live Staining

For visualisation of lysosomal compartments, LysoTracker Red DND-99 (Invitrogen, #L-7528) was used. Following treatment with DMSO or BafilomycinA1 for 3 hours, larvae at

4dpf were placed in 10 μM LysoTracker Red in Danieau solution for 1 hour at 28°C and then washed three times (3 minutes per wash) in fresh Danieau solution.

2.2.7.5 Cell Proliferation Assay

Proliferation in larvae was measured using the Click-iT EdU imaging kit (Invitrogen, #C10337) according to the manufacturer's instructions. Briefly, *wt* and *atg13* mutant *Tg(atg13;Col2a1aBAC:mcherry)* larvae at 5dpf or *wt* and *lmx1ba* mutant larvae at 4dpf were treated with 400 μM EdU in Danieau solution for 24 hours. Larvae were fixed in 4% PFA for 2 hours at room temperature or at 4°C overnight, then washed in 3% BSA in PBS-T three times for 5 minutes before being permeabilised in either 1% Triton-PBS-T or in proteinase K at the required concentration (listed in Table 2.5) if immunostaining larvae afterwards. The larvae were then washed again for three, 5 minute washes in BSA-PBS-T and then incubated in the Click-iT reaction cocktail (For 1ml: 43 μl Click-iT® reaction buffer, 886 μl H_2O, 20 μl $CuSO_4$, 1 μl Alexa-fluor® 647 azide, 50 μl Reaction buffer additive – added in that order) for 30 minutes. Larvae were washed in PBS for three times 5 minutes before imaging.

For *wt* and *lmx1b* mutant experiments, larvae were immunostained for Col2a1 following EdU staining. The immunostaining protocol was performed as stated in Section 2.2.6.5.

2.2.8 Fluorescence and Live Imaging

2.2.8.1 Stereomicroscope Imaging of Zebrafish

Both fixed and live larval and adult images were obtained using a Leica MZ10 F modular stereo microscope system with GFP and mCherry filters at 1-12x magnification. For live imaging, fish were anaesthetised using 0.1 mg/ml MS222 (Tricaine methanesulfonate) diluted in Danieau solution.

2.2.8.2 Confocal Microscope Imaging of Larvae

For confocal imaging, a Leica SP5-II AOBS tandem scanner confocal microscope attached to a Leica DMI 6000 inverted epifluorescence microscope was used. The dry 10X (0.4 NA), oil immersion 20X (0.7 NA) and oil immersion 40X (1.3 NA) objectives were used and the main laser lines utilised were 50 mW diode laser (for 405 nm excitation), 65 mW Argon laser (488 nm), 20 mW solid state yellow laser (561 nm) and 10 mW Red He/Ne (633 nm). The

microscope was located in the Wolfson Bioimaging Facility, Bristol and run using Leica LAS AF software (Leica, Germany). Maximum projection images were assembled using LAS AF Lite software (Leica) and ImageJ.

Confocal microscopy was used to image both live and fixed larvae. For live imaging, larvae at 3-7 dpf were anaesthetised using 0.1 mg/ml MS222 diluted in Daneaus solution and mounted ventrally in 0.5% LMP agarose (Thermofisher, #16520050). For fixed imaging, larvae were mounted in 1% LMP agarose.

2.2.9 Micro-Computed Tomography and Electron Microscopy

2.2.9.1 Micro-Computed Tomography (µCT)

Adult *lmx1ba* mutant fish were culled at 9mpf and 16mpf and fixed in 4% PFA for 7 days followed by sequential dehydration to 70% ethanol. Fish were wrapped in tissue then parafilm and placed upright within individual tubes in compacted foam (Figure 2.2.9.1). They were scanned using SkyScan 1272 high resolution micro-CT scanner (Bruker) under voxel size of 5µm, x-ray source of 50kV and 200A and 0.5mm aluminium filter. Images were reconstructed using SkyScan CTAn software. Avizo 9.0 was used for 3D volume rendering, segmentation of vertebral segments and image acquisition. For comparison, age matched *wt* fish at 8mpf and 18mpf which had been previously scanned by the Hammond lab, were segmented for analysis here. All scanning of fish in micro-CT scanner was performed by Qiao Tong (PhD student, University of Bristol).

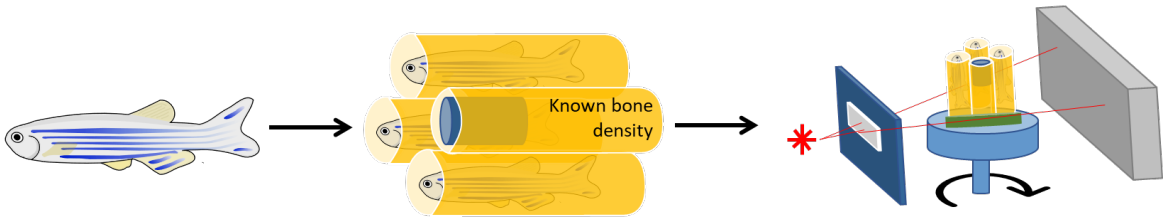

Figure 2.2.9.1 – Micro-CT scanning steps for zebrafish adults, Simplified schematic depicting steps required for micro-computed tomography of zebrafish adults.

2.2.9.2 Transmission Electron Microscopy (TEM) and Analysis

Following any indicated drug treatment, larvae were anesthetised at 3dpf and 5dpf and fixed in 2.5% glutaraldehyde in 0.1 M sodium cacodylate buffer (pH 7.3) overnight at 4°C. For post-fixation, larvae washed 5 times 5 minutes in 0.1 M sodium cacodylate and placed in 0.2 M osmium in sodium cacodylate buffer with 1.5% ferrocyanide for 1 hour at room temperature. They were then washed 3 times 5 minutes in ddH_2O and placed into sample processor using the standard protocol (Table 2.12). Following sample processing, fish were mounted in 100% Epon resin and left to harden for 2 days at 60°C. Sample processing was performed by Dr Chris Neal (Wolfson Bioimaging Facility, University of Bristol).

To cut sections, the Epon blocks were mounted onto a Leica EM UC7 RT ultramicrotome and thick sections were cut using a razor blade until the area of interest was reached. Semi-thin sections (1 μm) were then taken using a glass knife and stained in toluidine blue to enable the plane of interest to be found. From here, ultra-thin serial sections (50 nm) were obtained using a diamond knife (Diatome) and collected on Formvar coated one-hole copper grids (Agar Scientific, #AGS162). Sections were dried overnight at room temperature before being used for imaging. Transverse sections of *wt* and *atg13* mutant samples were taken by Dr Sally Hobson (Wolfson Bioimaging Facility, University of Bristol), whilst the *wt* and *lmx1ba* and *lmx1bb* mutant samples were sectioned transversely for cartilage analysis and medially for kidney analysis by Dr Chris Neal.

The sections were observed using a Tecnai 12-FEI 120kV BioTwin Spirit transmission electron microscope. Images of chondrocytes within the ethmoid plate were taken from 3 larvae per genotype, per condition using an FEI Eagle 4k × 4k CCD camera and analysed using ImageJ. Briefly, the outer membrane of chondrocytes were outlined using the polygon tool and their area measured. For cytoplasmic area, the area of the nucleus was subtracted from total chondrocyte area. For autophagosomal counts, the number of vacuole structures were counted and normalised to chondrocyte number in the ethmoid plate per fish. Exocytosing vesicles were classified as having a portion of their membrane fused with the chondrocyte cell plasma membrane and counted per chondrocyte. Vesicle number were counted as any enclosed membranous structure present in chondrocyte cytoplasm that could not be identified as an organelle (i.e., mitochondria, endoplasmic reticulum, nucleus,

or Golgi apparatus). Lastly, for chondrocyte intercalation, chondrocytes orientated perpendicular to the central stack of chondrocytes or having at least 50% of their cell volume out of the central line of the stack were counted as not intercalating properly and were calculated as a percentage of the total chondrocyte number per ethmoid plate, per fish.

For serial block face scanning EM (SBFSEM) larvae were postfixed in reduced osmium, treated with thiocarbohydrazide refixed with osmium tetroxide, stained en bloc with uranyl acetate and then lead aspartate, dehydrated with ethanol, infiltrated with propylene oxide Durcupan mixtures and Durcupan and then polymerised at 60°C for 48 hours.

Table 2.12 - Standard protocol for electron microscopy (EM) tissue processing in Leica TP EM

Solution	**Agitation setting**	**Time (hh:mm)**	**Temp. (°C)**
0.1M sodium cacodylate	AG3	00:10	4
0.1M sodium cacodylate	AG3	00:10	4
1% OsO4 in0.1M sodium cacodylate	AG3	01:00	4
0.1M sodium cacodylate	AG3	00:10	4
Deionised H_2O	AG3	00:30	4
Deionised H_2O	AG3	00:10	10
3% Uranyl Acetate	AG3	04:00	10
30% EtOH	AG3	00:10	10
70% EtOH	AG3	00:10	15
80% EtOH	AG3	00:10	15
95% EtOH	AG3	00:15	20
100% EtOH	AG3	00:15	20
100% EtOH	AG3	00:15	20
100% EtOH	AG3	00:20	20
100% EtOH	AG3	00:20	20
100% propylene oxide	AG3	00:10	20
100% propylene oxide	AG3	00:10	20

100% propylene oxide	AG3	01:30	20
50% propylene oxide/50% Epon	AG1	01:00	20
100% Epon	AG1	01:00	20
100% Epon	AG1	02:00	20
100% Epon	AG1	03:00	20
100% Epon	AG1	06:00	20

2.2.10 Adult Swim Behaviour

2.2.10.1 Recording Behaviour of Adult Zebrafish

To monitor the behaviour of *wt* and *lmx1b* mutant fish, individual adults were placed in an 8 L tank (Techniplast) to be recorded for 10 minutes. All recordings were performed in the same location in an isolated room to minimize any disruptive audio or visual stimuli which may affect the behaviour of the fish. White paper was placed beneath the tank and a white board behind the tank, and the videos taken in black and white to enhance image quality for automated analysis. Before recording, fish were placed into the room for 30 minutes to allow for climatisation before being put into recording tank. Videos at 15 frames per second were taken in unison from the side and top of the tank using two cameras whose position from the tank were maintained for all videos. A sheet with black dots of a known size were placed beside the tank to allow for scale calibration.

2.2.10.2 Analysis of Adult Body Curvature

To analyse body movements, the videos of individual fish swimming filmed from above the tank from Section 2.2.10.1 were used. A freely available Modular Image Analysis plugin developed by Dr Stephen Cross (v0.5.17) (Cross, 2018) for Fiji which can track the location and body curvature of fish was utilised. All MIA plugins used in this thesis which have been designed by Dr Stephen Cross can be downloaded from his Github page (Link in Chapter 7.2, Appendix B). Initially, the software identified the tank region and then binarized the image using the intermodes threshold (233). Objects which appeared to move location frame to frame were identified and a size threshold set to eliminate any noise falsely detected as 'fish'. Fish were tracked frame to frame using the Apache HBase implementation of the

Munkres algorithm (234), allowing for the calculation of instantaneous speed (measured from frame-to-frame).

Body curvature was measured by the skeletonization of the binarized objects (fish) and addition of a spine-line (termed spline) curve along the backbone of the fish using the Apache Math3 library (235). From this spline curve, the local curvature of the fish was measured in correlation to the length of the background where right-sided bends had a maximum value of +1 and left-sided bends a maximum value of -1. The location of the bend was defined as where along the spline the bend originated, with head end given a value of 0 and the tail end a value of +1. Due to processing power restrictions, for each video, 500 frames (~33 seconds) were analysed. The top three highest positive (right-sided bends) or negative (left-sided bends) values for body curvature were taken along with an average instantaneous swim speed, calculated as the mean across the values given for each frame.

2.2.10.3 Adult Swim Behaviour Analysis

To analyse the effect of the *lmx1b* mutations on risk aversion and anxiety, the position of the fish in the tank, their average swim speed and percentage of time spent frozen was quantified. These behaviours were assessed as they have been shown to be affected by loss of dopaminergic signalling (236-239). To quantify the vertical position of the fish in each video, a neural network developed by Yushi Yang (PhD student, University of Bristol) was used. Firstly, the tank is split horizontally into four equal zones: zone 1 (bottom of the tank), zone 2, zone 3 and zone 4 (top of the tank). The zone location of the fish is then recorded for each frame so the time proportional time spent in each zone can be calculated across the 10 minute recording which was graphed for each genotype. To analyse average swim speed and freezing behaviour a Modular Image Analysis program (MIA; version v0.18.7) workflow automation plugin for Fiji developed by Dr Stephen Cross (Wolfson Bioimaging Facility, University of Bristol) was used (240). Instantaneous speed is measured as the pixel distance between the location of the fish in one frame to the next frame, measured from the central point of the fish. These values were converted to cm/second (calculated as (1cm / ((distance/pixel)/average speed)*frames per second) where distance/pixel is 23.01844 and frames per second is 15) and an average speed for each fish taken. Freezing was assessed as the percentage of time spent across the first and last 90 seconds where the fish moved less

than 0.8cm/second (239). Due to the high computer power and time requirements of this plugin to analyse these videos, only 3 minutes of each video (the first and last 90 seconds) was analysed for the quantification of swim speed and percentage freezing time.

2.2.11 Image Analysis

2.2.11.1 Larval Measurements and Phenotype Analysis

Following anaesthetisation, lateral images of larvae at 1-7dpf were taken using a stereomicroscope for whole body measurements, eye diameter measurements and phenotype analysis. Measurements were taken manually using the line tool in ImageJ following scale calibration. For whole body length larvae were measured from the tip of the mouth to the end of the tail, whilst for eye diameter, a diagonal measurement across the centre of the eye was taken. Whole body length and eye diameter measurements, and phenotype analysis of *lmx1ba* and *lmx1bb* mutant larvae only were assisted by Elizabeth Blyth and Jan Stanka (Undergraduate project students, University of Bristol).

2.2.11.2 LysoTracker Analysis

LysoTracker-positive and GFP-Lc3 puncta were counted using the 'Analyze Particles' command in ImageJ. Briefly, single z-slices from three independent fields of a set size per larvae were selected and the channels separated. Images were converted to 8-bit images, the colour inverted and then a threshold set for each channel (185 for LysoTracker (red channel); 180 for GFP-Lc3 (green channel); Figure 2.2.11.2). Only particles above 4 pixel units and a circularity between 0.5-1.0 were counted as specified in the 'Analyze Particles' menu. For each independent field, the number of LysoTracker and GFP-Lc3 particles counted were averaged by the number of cells present in the field of view.

2.2.11.3 Measurement of Jaw Movement Frequency

Larvae were anaesthetised and mounted laterally in 1% agarose. Agarose was cut away from the proximal end to expose the head and neck, and Danieau solution was added to remove the anaesthetic. High-speed movies of 1000 frames were made of jaw movements of *wt* and *atg13* mutants. The number of mouth movements was recorded per 1000 frames for 5

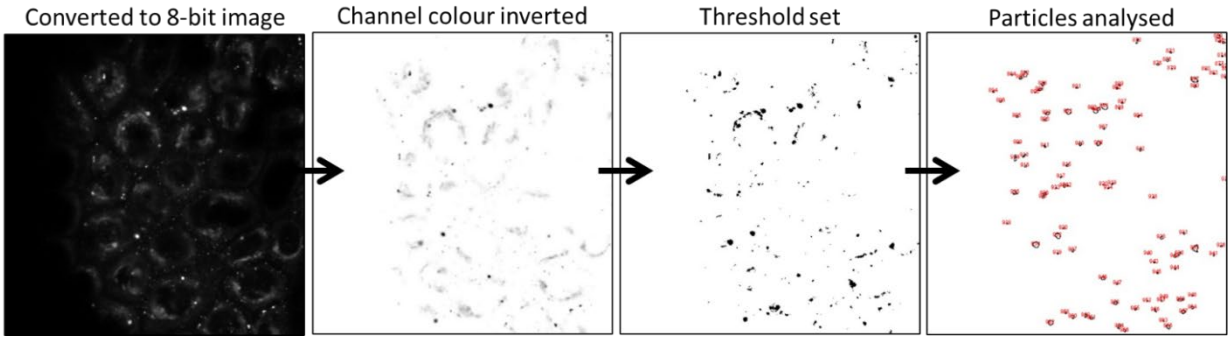

Figure 2.2.11.2 – Workflow for analysis of LysoTracker and GFP-Lc3-positive puncta, Example images showing steps involved in analysis of LysoTracker-positive fluorescent particles from a selected single z-stack slice using the 'Analyze Particles' command in ImageJ.

wt and *atg13* mutants respectively. Frames displaying maximum jaw opening were selected, imported into ImageJ and the width in jaw opening calculated in μm using the straight line tool. Schematic showing where measurements taken from is shown in the corresponding figure. Acquisition of high speed movies was assisted by Emma Case (Undergraduate summer student, University of Bristol).

2.2.11.4 Jaw Measurements

Whole jaw measurements and jaw muscle fibre number and length measurements were taken manually in ImageJ from max projections of confocal z-stacks of *wt* and *atg13* mutant and *lmx1ba, lmx1bb* and *dKO* mutant larvae immunostained with Collagen Type II or A4.1025 antibodies, respectively, at 3-7dpf. All measurements were made using the straight line tool. Location of where measurements were taken from is shown in the corresponding figures.

Cell analysis on larval jaws was performed using an MIA program (version 0.11.26) developed by Dr Stephen Cross (Wolfson Bioimaging Facility, University of Bristol) (224, 241). The program requires input of confocal z-stacks of larval jaws, labelled with Collagen Type II and Lc3, at 3-7dpf to allow for the calculation of cell number and volume, jaw element volume and distance, and inter-element volume. Data are collated into a Microsoft Excel document for analysis.

2.2.11.5 Sox9a Analysis

To quantify Sox9a expression, the Seg3D program was used (a custom script written in MATLAB (version 2015a; Mathworks) developed by Dr Stephen Cross) whereby the volume of Sox9a positive expression within the Col2a1 positive cells is calculated using confocal z-stacks in specified regions of interest which are selected via a freehand tool within the program (Figure 2.2.11.5A). Briefly, in selected regions of interest, Sox9a expression is segmented from 3D z-stacks following the principle of Otsu's threshold (242). After setting a threshold value, all voxels within the ROI which show an intensity value above the threshold are set as a single object (Figure 2.2.11.5B) and an alpha shape calculated (243). The volume of the alpha shape is calculated using the method provided by the MATLAB alpha shape class (244). The same threshold value was used each individual sample and calculated by averaging the mean of the automatic threshold value given for each stack for *wt* and *atg13* or *lmx1b* mutants, respectively.

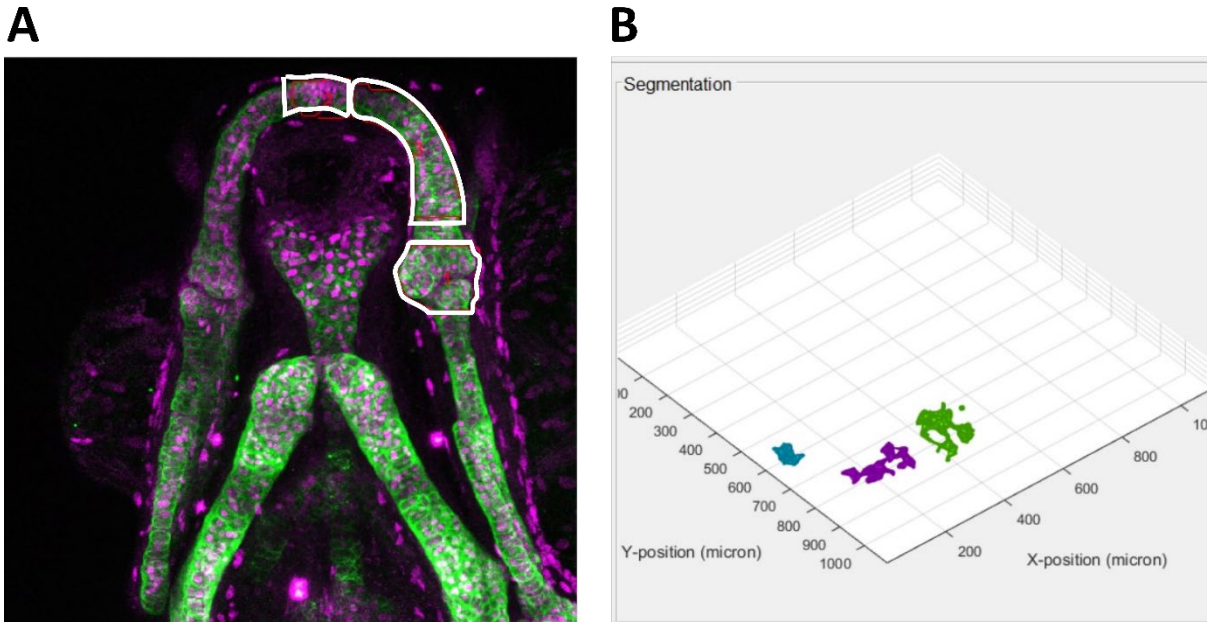

Figure 2.2.11.5 – Images from SoxQuant program showing identification of regions of interest for analysis in the jaw and 3D plot of Sox9a fluorescence volume (A) Example image of compiled z-stack max projections for each channel (Col2a1 in green, Sox9a in magenta) showing where the three regions of interest were drawn (*white lines*). **(B)** Example 3D segmentation of Sox9a fluorescence detected in the three regions of interest. Different colours of segmentations represent each region of interest. Volume of each segmentation taken and used for quantification in analysis. Example images taken as screenshots from SoxQuant program.

2.2.11.6 Brain Ventricle Measurements

Lateral images of anaesthetised larvae at 1dpf were taken on a stereomicroscope, zoomed in on the head region. Larvae were turned until the eyes overlapped each other to ensure all images were taken at the same angle. Following scale calibration, ventricle height was measured per larvae using the line tool in ImageJ, with the measurement being taken 60 μm from the edge of the midbrain-hindbrain boundary (MHB), stretching from the base of the ventricle to the top of the head.

Abnormalities in MHB formation were observed from the same images and categorised by severity. Briefly, no abnormality in MHB formation was determined by a clear distinction of the midbrain and hindbrain with clear fold in the middle. Where the fold was only part formed or where the distinction between the midbrain and hindbrain was less clear, this was determined as a mild abnormality. Where only ventricle constriction could be seen, this was classed at a moderate abnormality. Severe abnormality was categorised by complete loss of MHB fold. Analysis of MHB development and abnormalities was assisted by Elizabeth Blyth (Undergraduate project student, University of Bristol).

2.2.11.7 Analysis of Tyrosine Hydroxylase (TH) immunostaining

Following immunostaining with TH, confocal z-stacks of the heads of larvae, mounted ventrally were taken at 3dpf. TH-positive cells were identified in the forebrain and midbrain and counted using the multi-point tool in ImageJ by going through each sequential z-slice per fish.

2.2.11.8 Larval Trunk Muscle Analysis

Confocal images of trunk muscle, immunostained with A4.1025 and counterstained with DAPI, were taken at 3dpf and 5dpf for *wt* and *dKO* mutants, and at 5dpf for *lmx1ba* and *lmx1bb* mutants. Measurements for somite area, muscle fibre length and percentage muscle coverage per somite were taken manually in ImageJ from max projections of confocal z-stacks. For each fish, measurements from three individual somites were taken and an average calculated from these. For somite area, somites were drawn around using the polygon tool and for fibre length, the length of one muscle fibre per somite (fourth muscle fibre in somite from centre of fish) was measured using the straight line tool. For percentage

muscle coverage, somites were drawn around using the polygon tool, a threshold applied between 10-45 depending on image brightness and value for percentage area taken. Schematics showing location and method of measurement collection is shown in the corresponding figure.

2.2.11.9 Statistical Analysis

All statistical analyses were performed using Graphpad (Prism, v.8 and above). The number of biological replicates per experiment is indicated in the figure legend as the n number, along with the type of statistical test used and relevant *P* values. D'Agostino and Pearson tests for normality were performed on all datasets prior to further statistical analysis. Error bars on all graphs represent the mean ± standard deviation.

Chapter 3. Exploring the role of *atg13* in coordinating chondrocyte development and maturation in zebrafish

At a glance…

In this first chapter of results, a novel autophagy mutant zebrafish line is characterised, and the methods used to monitor autophagy flux in zebrafish are reported. In the second part of this chapter, it is demonstrated how loss of autophagy activity affects chondrocyte development and maturation in this zebrafish model, which consequently leads to a reduction in joint mobility.

CHAPTER

3

Exploring the role of *atg13* in coordinating chondrocyte development and maturation in zebrafish

The majority of results in this chapter have been published as a research article in The FASEB Journal (229). Text and all figures and figure legends from the publication have been adapted for this thesis, as noted in the figure legends where appropriate. For this publication, I was first author and performed all experiments and data analysis, excluding only the generation of the *atg13* mutant zebrafish line, which was designed and created by Dr Martina Wirth at the Francis Crick Institute. I also was also responsible for writing and editing the manuscript, generating all figures and figure legends, and responding to the reviewers' comments. The contribution of colleagues for specific techniques is acknowledged in the Materials and Methods section where relevant (Chapter 2) and highlighted in figure legends in this chapter where appropriate.

3.1. Introduction

ATG13 is an autophagy factor required within the initial stages of autophagy induction. In vertebrates, autophagy initiation requires the formation of the ULK complex, comprising the serine/threonine protein kinase ULK1/2, and its adaptors, ATG13, FIP200, and ATG101 (44). Upon autophagy induction, the ULK complex translocates to discrete foci dispersed

throughout the cell, typically associated with endoplasmic reticulum (ER) membrane, where it phosphorylates components of PI3KC3, triggering recruitment of the remaining core autophagy machinery (63). Along with FIP200, ATG13 has been shown to play a vital role in both the localised activation of the ULK kinase and its recruitment at the isolation membrane of the nascent autophagosome (245, 246). Here, ATG13 helps form a building scaffold for other proteins within the autophagy pathway to bind and be stabilised (16). These roles require the two key domains that comprise ATG13: the C-terminal HORMA (Hop1/Rev7/Mad2) domain, and the N-terminal IDR (Intrinsically Disordered Region) (247, 248). In particular, the highly conserved HORMA domain is essential for autophagy induction and the recruitment of PI3KC3 via ATG14 (249). The HORMA domain aids in complex formation as it dimerises with ATG101, via its HORMA domain (247). This dimerisation interface within ATG101 is highly conserved and studies have shown that disruption to this interaction results in severe autophagy defects (250). Meanwhile, the IDR helps in both ULK1/2 recruitment, through the presence of the C-terminal microtubule-interacting and transport (MIT)-interacting motif (MIM), and in forming a protein scaffold, as the flexibility of the IDR allows ATG13 to act as a disordered assembly component (16, 251). In a range of vertebrate models and cell lines, loss of ATG13 expression has been shown to block autophagy activity ((31, 252-256); see Table 3 in (17)). Meanwhile, mouse knock-out models for Atg13 are embryonic lethal, a result consistent with the targeting of other autophagy genes in murine knock-out models, including Fip200, and Atg7 (23, 257, 258).

As previously mentioned in Section 1.1.3 of the Introduction, extensive studies have established the importance of autophagy in a range of housekeeping pathways (20, 259, 260), many of which are essential for chondrocyte development and survival, and for chondrogenesis (49, 52, 53). Correspondingly, autophagy dysregulation has been implicated in several skeletal disorders, including the degenerative joint disorder, osteoarthritis (OA) (47, 49, 58, 261, 262). Although often characterised as a disease of ageing, recent studies have highlighted the effect of improper joint shape formation during skeletogenesis on OA development in later life (263-266). Therefore, determining the impact of cellular processes, such as autophagy, on the co-ordination of cartilage and joint development is essential for

deepening our understanding of the pathogenesis of OA and how this disease can be best treated.

The process of chondrogenesis begins with the condensation and differentiation of mesenchymal stem cells at sites of future skeletal formation (Figure 3.1). These cells differentiate into cartilage forming chondrocytes which secrete a characteristic extracellular matrix (ECM) formed largely of Type II collagen α1 (termed Col2a1 here) and specific proteoglycans, such as aggrecan, generating a cartilage matrix (267). As chondrocytes develop, they pass through a well-characterised set of maturation steps. These include intercalation and proliferation, where cells flatten and separate into a narrow, single-cell stacked column, followed by hypertrophication, as cells exit the cell cycle, become enlarged, and switch from secreting Col2a1 to type X collagen α1 (termed Col10a1 here) (268-270). Hypertrophy is considered the terminal stage of differentiation for chondrocytes. During intermembranous bone development, many hypertrophic chondrocytes will undergo apoptosis with their lacunae subsequently being occupied by osteoblasts which replace the cartilage matrix with bone.

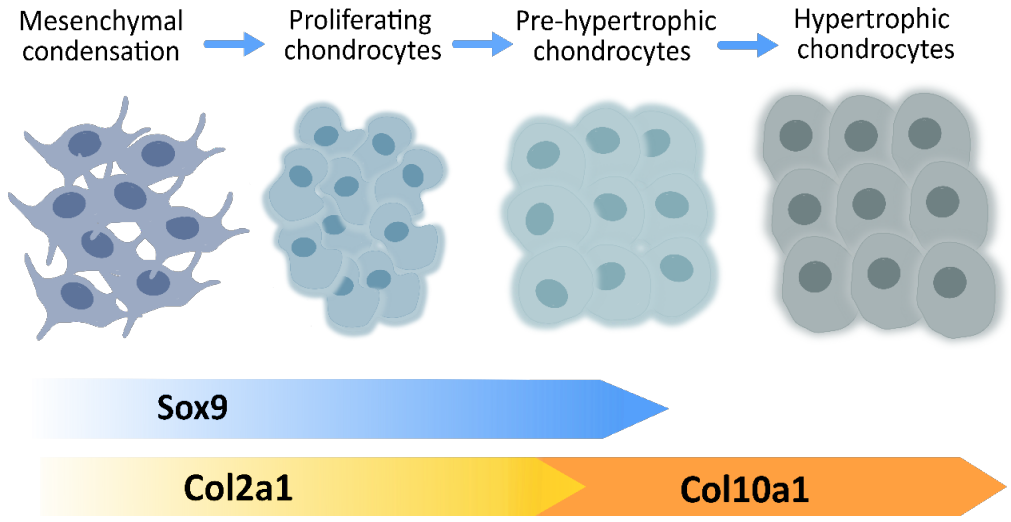

Figure 3.1 – Process of chondrogenesis during vertebrate skeletal development, Simplified schematic showing key steps involved in chondrogenesis which includes the differentiation of mesenchymal stem cells into early chondrocytes, which mature into hypertrophic chondrocytes. Arrows below highlight the time frame for the expression or secretion of key factors during chondrogenesis, which can be used to stage chondrocyte maturity. Sox9 expression occurs during early differentiation, along with the secretion of Type II collagen α1 (Col2a1) to form part of the extracellular matrix (ECM). As chondrocytes become hypertrophic, secretion of Col2a1 decreases as Type X collagen α1 (Col10a1) secretion into the ECM increases.

Several studies have identified important roles for autophagy throughout chondrogenesis. In the early stages of this process, *in vitro* studies have shown a positive correlation between autophagy activity and chondrocyte proliferation and differentiation (69), whilst maturing chondrocytes show high MAP1LC3 expression (81). In mice, during early chondrogenesis, chondrocyte autophagy is induced in the growth plate postnatally (82), and the conditional loss of *Atg5* or *Atg7* during chondrogenesis has been shown to reduce growth plate activity and cause growth retardation (69), which is likely triggered by ER stress within chondrocytes (271). Additionally, conditional knock-out of *Atg7* in mouse chondrocytes causes enlarged ER cisternae, extracellular matrix (ECM) disorganisation and retention of procollagen 2 (a preform of Col2a1 – a major component of cartilage matrix), as well as reduced chondrocyte proliferation and survival (82, 271). If autophagy is disrupted later in chondrogenesis, chondrocytes in the proliferative stage show an accumulation of glycogen granules, severe growth retardation, and increased apoptosis (52). Meanwhile, looking beyond early development, reduced autophagy activity via a chondrocyte-specific *Atg5* deletion causes the premature onset of OA development in mice from 6 months (58). Together these studies demonstrate a key role for autophagy in chondrocyte proliferation and cartilage growth; and highlight how disruption to this process can lead to the premature development of degenerative joint disease. However, the role of the autophagy pathway within chondrocyte differentiation is still incompletely understood.

Here, a novel autophagy mutant zebrafish *atg13* line is used to characterise the role of Atg13, and consequently autophagy, during cartilage and joint development. Through this investigation it is found that suppression of autophagy accelerates chondrocyte maturation, leading to improper chondrocyte intercalation and disruption to jaw joint formation and movement. Arguably, it is this developmental defect that contributes to the lethality of the *atg13* mutants at around day 17, due to a failure of these mutants to thrive at free-feeding stages. The disruption to joint function seen in this model indicates an important role for autophagy in supporting the regulation of chondrocyte development to ensure proper joint formation and highlights an important pathway through which autophagy dysregulation may contribute to OA development.

3.2. Results

Characterisation of the *atg13* mutant zebrafish line

3.2.1 Protein structure of Atg13 is highly conserved from humans to zebrafish

Atg13 is a key component of the core autophagy machinery and is part of the first complex formed during autophagy initiation known as the ULK complex. The protein sequence and structure of ATG13 in humans is known to be formed of an ordered region and intrinsically disordered region. Using phylogenetic analysis of human and zebrafish Atg13 proteins, these regions were identified within the zebrafish form of Atg13 and their sequence similarity compared. In zebrafish, the protein coding sequence for Atg13 is 14 amino acids (aa) shorter compared to the human form (517aa compared to 503aa) although there is a strong sequence homology between the two species (75%) and between the key domains within the protein (Figure 3.2.1). The key HORMA (Hop1/Rev7/Mad2) domain and MIM (MIT-interacting motif) motifs showed especially high sequence similarity between zebrafish Atg13 and human ATG13 proteins (93% for the HORMA domain, and 100% and 88% for the respective MIM motifs, Figure 3.2.1A), suggesting that in both species, Atg13 is likely to carry out the same roles during autophagy initiation. Therefore, any changes in Atg13 expression seen in this zebrafish model will likely be indicative of what would occur in humans with reduced ATG13 expression

3.2.2 Site of atg13 mutation causes full knock-out in zebrafish

An *atg13* mutant zebrafish line created using CRISPR-Cas9 mutagenesis was kindly gifted to the Hammond lab. The line has a targeted 5 bp (base pair) deletion in exon 3 of the zebrafish *atg13* gene and results in a premature stop codon 97 bp succeeding the mutation site and introduction of a novel HindIII restriction site (Figure 3.2.2A). The mutation occurs in the HORMA domain of Atg13, near the N terminus, which is a region highly conserved across multiple species (Figure 3.2.2B) and is essential to the role of Atg13 within the ULK1 complex. This suggests that changes to the amino acid sequence at this site are likely to be

B

```
Hs ATG13 NP_001192049.1   METDLNSQDRKDLDKFIKFFALKTVQVIVQARLGEKICTRSSSSPTGSDWFNLAIKDIPE  60
Dr Atg13 NP_956727.1      MDSDLSPQDKKDLDKFIKFFALKTVQVIVQARLGEKISTCSSSSPTGSDWFNLAIKDIPE  60
                          *..**..**.****************************.*.********************

Hs ATG13 NP_001192049.1   VTHEAKKALAGQLPAVGRSMCVEISLKTSEGDSMELEIWCLEMNEKCDKEIKVSYTVYNR  120
Dr Atg13 NP_956727.1      VTHEAKKALAGQLPGIGRSMCVEISLKTSEGDSMELETWCLEMNEKCDKDIKVSYTVYNR  120
                          **************..**********************.***********.**********

Hs ATG13 NP_001192049.1   LSLLLKSLLAITRVTPAYRLSRKQGHEYVILYRIYFGEVQLSGLGEGFQTVRVGTVGTPV  180
Dr Atg13 NP_956727.1      LSLLLKSLLAITRVTPAYKLSRQQGHDYVILYRIYFGDVQLTGLGEGFQTVRVGIVGTPI  180
                          ******************.***.***.**********.***.************.****.

Hs ATG13 NP_001192049.1   GTITLSCAYRINLAFMSTRQFERTPPIMGIIIDHFVDRPYPSSSPMHPCNYRTAGEDTGV  240
Dr Atg13 NP_956727.1      GTITLSCAYRTNLALVSSRQFERTGPIMGIIIDHFVERPFTNMAHTHPCSYRAPGEDDGG  240
                          **********.***..*.******.***********.**.......***.**..***.*.

Hs ATG13 NP_001192049.1   IYPSVEDSQEVCTTSFSTSPPSQLSSSRLSYQPAALGVGSADLAYPVVFAAGLNATHPHQ  300
Dr Atg13 NP_956727.1      TYAGIEDSQEVCTTSFSTSPPSQLYSSRLSYQTPPLGT--VDLCHPT---ACTGAAHPHQ  295
                          *...*******************.*******...**....**..**....*...*.****

Hs ATG13 NP_001192049.1   LMVPGKEGGVPLAPNQPVHGTQADQERLATCTPSDRTHCAATPSSSEDTETVSNSSEGRA  360
Dr Atg13 NP_956727.1      MVVPGKDGGIPQVPAQPNHGTGAEQGRIPSCPTGQPPQLPPPTSC--------SSEVKTV  347
                          ..****.**.*..*.**.***.*.*.*...*...........*..........*.....

Hs ATG13 NP_001192049.1   SPHDVLETIFVRKVGAFVNKPINQVTLTSLDIPFAMFAPKNLELEDTDPMVNPPDSPETE  420
Dr Atg13 NP_956727.1      SPSDVLETTFTRKVGAFVNKATTQVTTTGLDLPFAAFAPRSYDMEENDPMVHPPPSPIPS  407
                          **.*****.*.*********...***.*.**.***.***.....*..****.**.**...

Hs ATG13 NP_001192049.1   SPLQGSLHSDGSSGGSSGNTHDDFVMIDFKPAFSKDDILPMDLGTFYREFQNPPQLSSLS  480
Dr Atg13 NP_956727.1      SPLQGSLHSNNSS-HSGGQPNDDFVMVDFKPAFSKDDLLPMDLGTFYREFQNPPQLASLS  466
                          *********..**..*.*...*****.**********.******************.***

Hs ATG13 NP_001192049.1   IDIGAQSMAEDLDSLPEKLAVHEKNVREFDAFVETLQ                       517
Dr Atg13 NP_956727.1      IDVSAQSMAEDLDSLPEKLAVYEKNIDEFDAFVDTLQ                       503
                          **..*****************.***..******.***
```

Figure 3.2.1 – Key protein domains in Atg13 show high sequence alignment in humans and zebrafish, (A) Schematic showing key protein domains, their amino acid position and their sequence similarity between human and zebrafish Atg13. The HORMA domain is coloured orange, the LIR (LC3-interacting region) motif yellow and the MIM motifs in blue. **(B)** Multiple sequence alignment by Clustal Omega (EMBL-EBI), between human and zebrafish Atg13 proteins. Colours correlate with (A) and indicate locations of key domains (HORMA, LIR and MIM motifs). Green indicates sequence similarity; black line indicates sequence divergence and numbers show amino acid position. Relevant accession numbers for each sequence given, Hs = *Homo sapiens*; Dr = *Danio rerio*.

deleterious and result in a loss of protein function. Additionally, the early location of the mutation within the protein sequence and the resulting premature stop codon indicate that protein translation will be halted by this mutation, resulting in the formation of a truncated, non-functional protein within the *atg13* mutant fish.

The introduction of a novel HindIII restriction site in the CRISPR mutant fish allows for easy identification of heterozygous and homozygous mutant siblings after digestion as both display smaller DNA fragment at ~200 bp compared to *wt* DNA fragment at 386 bp (Figure 3.2.2C). When analysing Atg13 protein expression in the *atg13* mutants compared to *wt*, complete loss of Atg13 expression in the homozygous mutants was observed along with minimal loss of expression within the heterozygotes compared to *wt* (Figure 3.2.2D). These data confirm that the mutation causes a full knock-out of Atg13 in the homozygous mutants but that this presumed loss of expression is a least partially rescued in the heterozygotes by the elevated expression of the remaining *wt* allele. Given this, the homozygous *atg13* mutants will be used for the majority of this study and they will be termed '*atg13* mutants'.

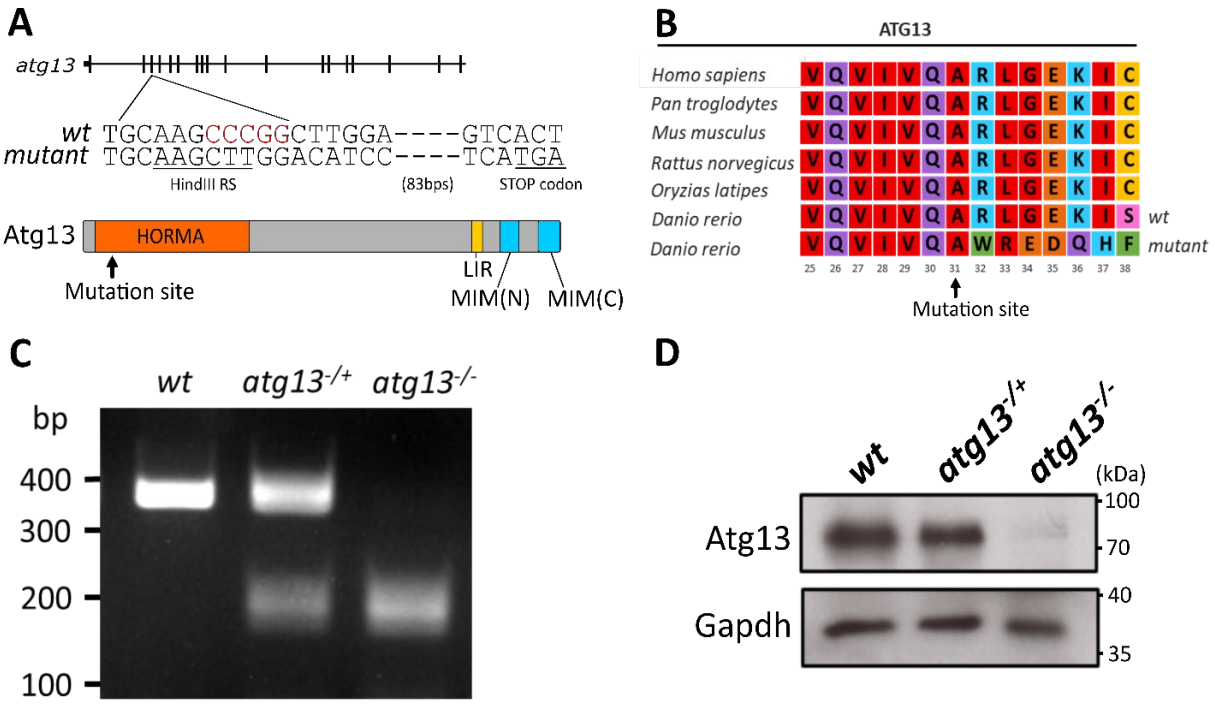

Figure 3.2.2 – Gene and protein location of *atg13* mutation and identification of *atg13* mutant fish, (A) *top*, schematic diagram of *atg13* exon structure in zebrafish with *wt* and mutant nucleotide sequence at the site of the mutation. Red indicates the 5 bp deletion in the mutant. *Bottom,* protein structure of zebrafish Atg13 with location of mutation in HORMA domain. **(B)** Multiple protein *(continued overleaf)*

Figure 3.2.2 continued - sequence alignment of amino acid position 31 showing high sequence conversation across multiple species and the effect of the mutation on protein sequence in zebrafish. Amino acids with similar physiochemical properties share the same colour. **(C)** Representative agarose gel showing HindIII restriction digest of PCR product obtained from wild type, heterozygous and homozygous *atg13* mutant fish. **(D)** Representative Western blot of *atg13* larvae, probed for Atg13. Gapdh used as a loading control. Proteins from 25 larvae per genotype were loaded in each well. Figure adapted from (229).

3.2.3 Loss of atg13 leads to decreased survival and phenotypic changes compared to wild-type fish

Following the confirmation of full protein knock-out in the *atg13* mutant fish, the effect of loss of Atg13 on early development and survival was explored. Mutant embryos were viable and born at the expected Mendelian ratio. At 24hpf (hours post-fertilisation), larvae showed no phenotypic differences between *atg13* mutants and *wt,* although by 3dpf (days post-fertilisation) certain developmental differences were observed (bent body axis, oedema; Figure 3.2.3A). By 5dpf, *atg13* mutants were significantly shorter in length and all displayed at least one phenotypic difference compared to *wt* and *atg13* heterozygotes such as oedema, bent body axis and a failure to fully use the yolk sac (indicated by higher yolk sac mass) or inflate the swim bladder, the latter being indicative of a delay in normal development (Figure 3.2.3B *orange arrows*, C). However, despite phenotypic variabilities, no *atg13* mutant survived beyond 17dpf which is consistent with other mouse and zebrafish knock-out models for key autophagy-related genes which also die prematurely (Figure 3.2.3D) (41, 272). Taken together, these results confirm that Atg13 is essential for zebrafish survival into adulthood and that loss of Atg13, although not vital for early developmental stages, disturbs larval developmental rate and morphology. These data also demonstrate that partial loss of Atg13, as seen in the *atg13* heterozygotes, has only a slight effect on larval development and survival, confirming a minimal loss in Atg13 expression as shown in Figure 3.2.2D.

3.2.4 Measuring autophagy flux in zebrafish using Bafilomycin A1

To confirm that autophagy is functionally disrupted in the *atg13* mutants, GFP tagged map1lc3 (GFP-Lc3) zebrafish (125) in the *atg13* mutant background were generated

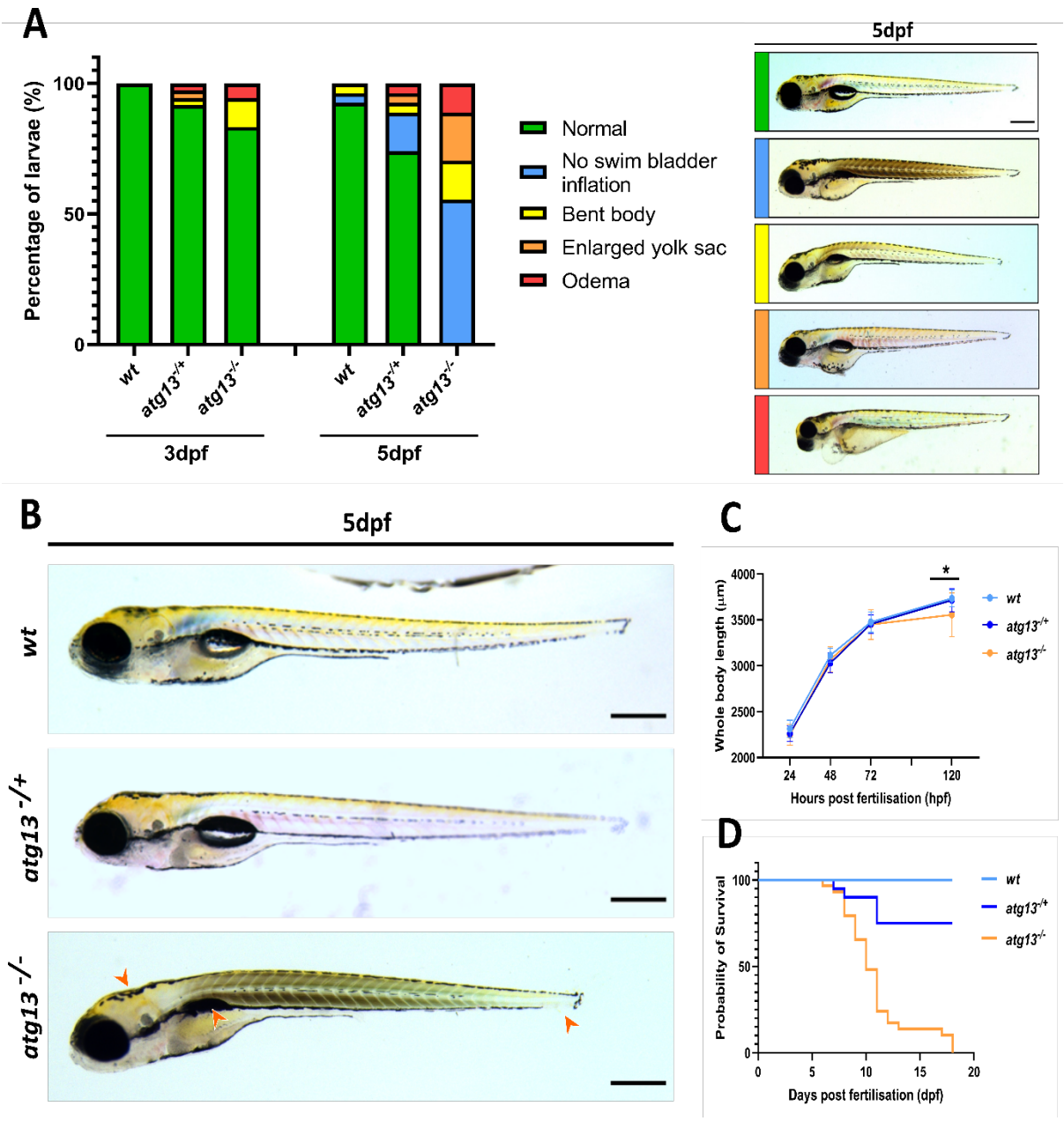

Figure 3.2.3 – Atg13 is required for zebrafish larval development and survival, (A) Phenotypic differences observed from 1-5dpf and categorised depending upon severity (green = mild, to red = severe). Representative brightfield images taken at 5dpf, n= 24 for all ages and genotypes. Scale bar = 500 µm. **(B)** Representative brightfield images of *wt*, heterozygous and homozygous *atg13* mutant larvae at 5dpf. Arrows indicate phenotypic differences in *atg13* mutant compared to *wt*. Scale bar = 500 µm. **(C)** Full ventral length measured from brightfield images at 1-5dpf. Student's unpaired t test performed where *P<0.05. n =13 for *wt*, 12 for heterozygote and 17 for mutant. **(D)** Survival rate of each genotype recorded until 17dpf. Data collated from 3 separate experiments. Figure adapted from (229).

(*Tg(atg13^{fci500};cmv:gfp-map1lc3b))*. Following autophagy initiation, cytosolic Lc3-I is conjugated to phosphatidylethanolamine, a constituent of the autophagosome, forming lipidated Lc3-II which has greater mobility on SDS-PAGE gels and can be detected in GFP-Lc3 zebrafish as discrete GFP-positive puncta using fluorescence microscopy (141).

To test autophagy flux, the vacuolar-type H^+-ATPase inhibitor, Bafilomycin A1 (BafA1) was used. As an inhibitor of lysosomal acidification, BafA1 prevents the formation of autolysosomes, and thus causes accumulation of Lc3-II and autophagic cargo primarily by blocking the degradation of autophagosomes. By comparing protein expression of lipidated Lc3 and of the autophagy receptor protein p62 (SQSTM1), which is degraded by the autophagy machinery, under basal and BafA1 treated conditions, autophagic flux rates can be assessed. To determine the most appropriate concentration and duration of BafA1 to be used, several drug titrations were performed. A range of BafA1 concentrations were selected from the literature (124, 139, 273) and tested over a range of incubation times (Figure 3.2.4). Initially, the behaviour of the larvae was monitored to assess for any adverse reactions to BafA1 (Figure 3.2.4A, *column 4*). The longer incubation time of 6 hours caused a reduction in response to stimuli (i.e., startle response to light, movement of water or end of tail being touched), even at the lowest tested concentration of 50 nM. Meanwhile, treatment of larvae at 5dpf for 3 hours with BafA1 showed no adverse effect on behaviour at the 50 nM and 100 nM concentrations but caused a similar effect to stimuli responses at 200 nM as the 6 hour treatments.

Alongside the assessment of BafA1's effects on larval behaviour, it was also important to demonstrate what concentration of BafA1 is required to cause an observable effect on autophagy flux. To determine this, analysis of Lc3 lipidation levels and of p62 expression was measured using immunoblotting (Figure 3.2.4B). An increase in Lc3-II levels was seen across all treatment groups indicating that the lowest concentration of 50nm BafA1 is sufficient to block autophagy flux in larvae at 5dpf. However, the 50 nM treatment showed only a modest increase in Lc3-II and p62 levels. Therefore, moving forward, the concentration of 100 nM BafA1 for an incubation of 3 hours will be used, as this provides a sufficient block to autophagy flux and has no adverse effects on the larvae.

3.2.5 There is reduced autophagy flux in atg13 mutants

After determining the most appropriate dose of BafA1 for treating larval zebrafish, autophagy flux assays were performed on the *wt* and *atg13* mutants. By applying LysoTracker Red, a vital lysosomal dye, the abundance of autophagosomes and lysosomes in *wt* and *atg13* mutants at 4dpf were measured by counting the number of GFP-Lc3 and

A

Condition	BafA1 conc.	Incubation	Effect on larvae
1 (Control)	0 nm	6 hrs	Responsive and free swimming
2	200 nm	3 hrs	Less responsive
3	100 nm	3 hrs	No effect
4	50 nm	3 hrs	No effect
5	100 nm	6 hrs	Not responsive to stimuli
6	50 nm	6 hrs	Less responsive

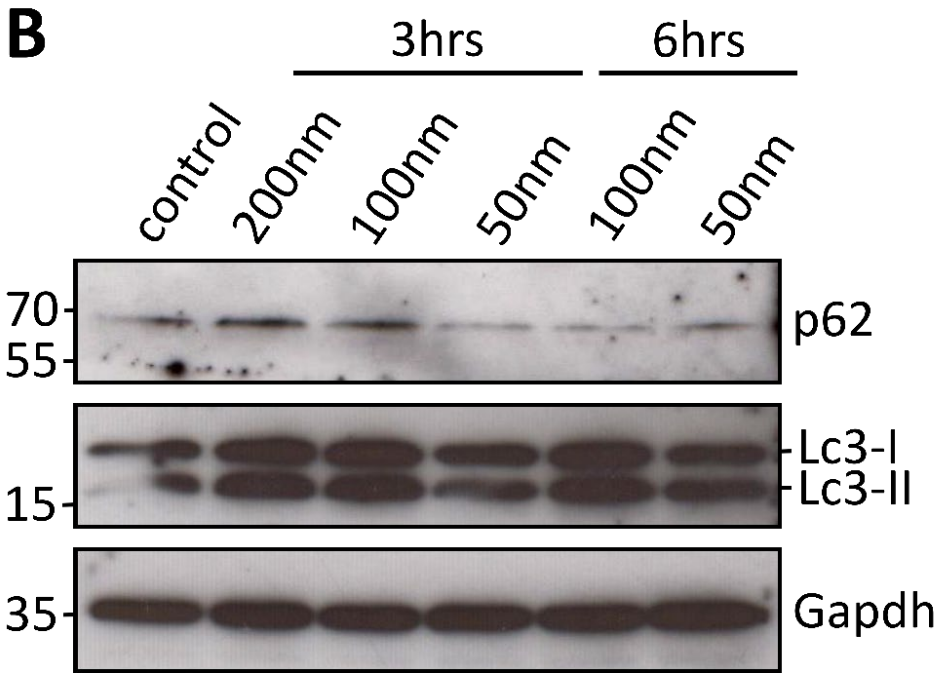

Figure 3.2.4 – Drug titration of BafA1 to determine the incubation time and concentration required to block autophagy flux in 5dpf larvae, (A) Table showing the concentrations and incubations times selected for BafA1 treatment and their effect on larval behaviour. **(B)** Immunoblot of *atg13 wt* larvae, probed with antibodies against p62, Lc3 and Gapdh as a loading control. Labels indicate BafA1 concentration and incubation time performed on each larval group. Proteins from 15 larvae per genotype were loaded per each well.

LysoTracker positive puncta per cell (Figure 3.2.5A). Under basal conditions (DMSO treatment), *atg13* mutants showed no differences in lysosome abundance compared to *wt*, with a non-significant decrease in GFP-Lc3 puncta numbers (Figure 3.2.5A and B). Though loss of *atg13* is expected to prevent autophagosome formation through inhibiting early autophagic signalling (245), GFP-Lc3 positive puncta were present in *atg13* mutants. GFP-Lc3-positive aggregates have previously been observed in the mouse *atg13* mutant model (257) and in *C. elegans atg13*/*epg1* mutant embryonic cells (274, 275) and we propose are also occurring in this *atg13* mutant zebrafish model.

To analyse the rate of autophagy flux, larvae were treated with BafA1, whereupon *wt* zebrafish showed a significant increase in GFP-Lc3 puncta numbers compared to basal conditions, indicative of high autophagic flux, as expected (Figure 3.2.4A and B). However, there was a dramatically reduced accumulation of GFP-Lc3 puncta in *atg13* mutants, indicating attenuated autophagic flux (Figure 3.2.5A and B).

Immunoblot analysis of endogenous Lc3 did not reveal clear differences in the abundance of lipidated Lc3-II between *wt*, heterozygous and homozygous *atg13* mutants under basal conditions and in response to BafA1 treatment (Figure 3.2.5C). However, analysis of the autophagy receptor protein p62 (Sqstm1), which is degraded by the autophagy machinery, showed a strong accumulation of p62 and defect in autophagic flux in the *atg13* mutants (Figure 3.2.5C). Taken together, these results demonstrate that loss of *atg13* causes the expected deficiencies in autophagy, correlating with reduced turnover of autophagic substrates, and that under basal conditions, *atg13* mutants are close to maximal autophagy levels. Therefore, under a stress phenotype, *atg13* mutants have a significantly reduced capacity for an autophagy response.

Exploring the role of autophagy in joint and cartilage development

3.2.6 The atg13 mutant fish show decreased jaw function

Once it had been established that the *atg13* mutant is a full knock-out and does cause defects to autophagy, the role Atg13 and autophagy plays in skeletal development was investigated next.

Given the role of autophagy in key skeletal processes, the effect of the *atg13* mutation on cartilage development in the context of joint formation was examined first. In zebrafish, skeletal formation begins as early as 2dpf with initial establishment of specific craniofacial cartilaginous structures (144). Zebrafish skeletal physiology is comparable to that of mammals, as they share the same joint types and components such as joint cavities, articular cartilage and synovial membranes (155). This has been most extensively shown in the larval zebrafish jaw, which has a synovial joint and is often used to model joint development.

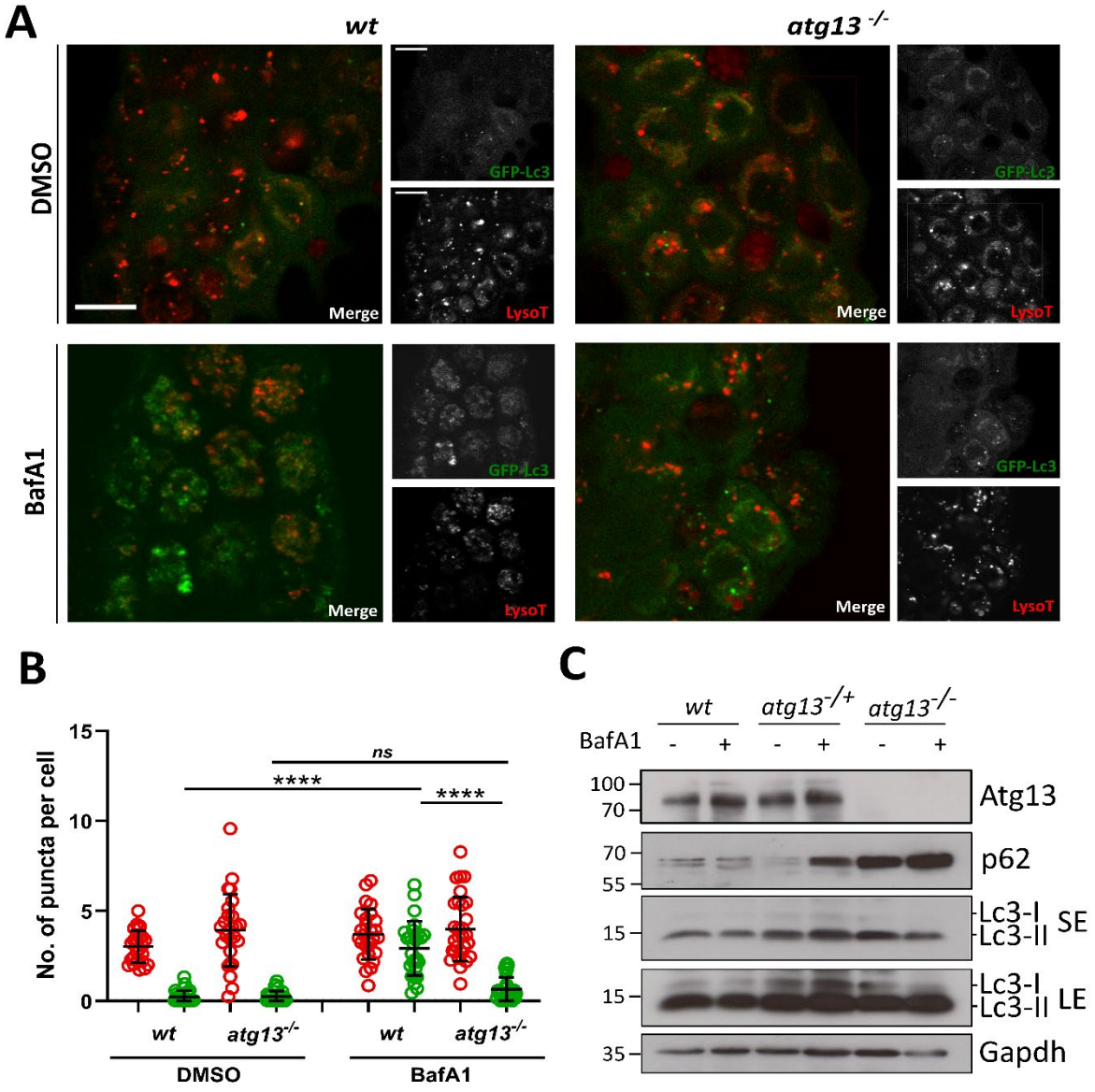

Figure 3.2.5 – The *atg13* mutants show reduced autophagy flux, (A) Representative single confocal z-slices of cells in the epidermis from LysoTracker stained *Tg(cmv:gfp-map1lc3;atg13) wt* and mutant larvae, at 4dpf following treatment with DMSO or 100 nM Bafilomycin for 3 hours. Scale bar = 10μm. **(B)** Quantification of number of lysosomal (red) and GFP-Lc3 (green) puncta per cell. 2-way ANOVA performed for each; **** *P*<.0001. **(C)** Representative immunoblot of *atg13 wt*, heterozygous and mutant larvae at 5dpf following treatment with DMSO or 100 nM Bafilomycin for 3 hours. *SE* = short exposure, *LE* = long exposure. Molecular weight markers indicated on right hand side of immunoblots. Figure adapted from (229).

Therefore, lower jaw elements in zebrafish larvae were used to compare the development of the cartilaginous skeleton template between *wt* and *atg13* mutants.

Zebrafish make two distinct jaw movements for feeding and for breathing, which are here described as mouth and buccal jaw movements, respectively (Figure 3.2.6A; red for mouth movements and yellow for buccal movements) (276). For more detailed analysis, videos of jaw movements were taken at 5dpf, and the numbers of movements at either joint were measured alongside the displacement distance between the upper and lower jaw (Figure

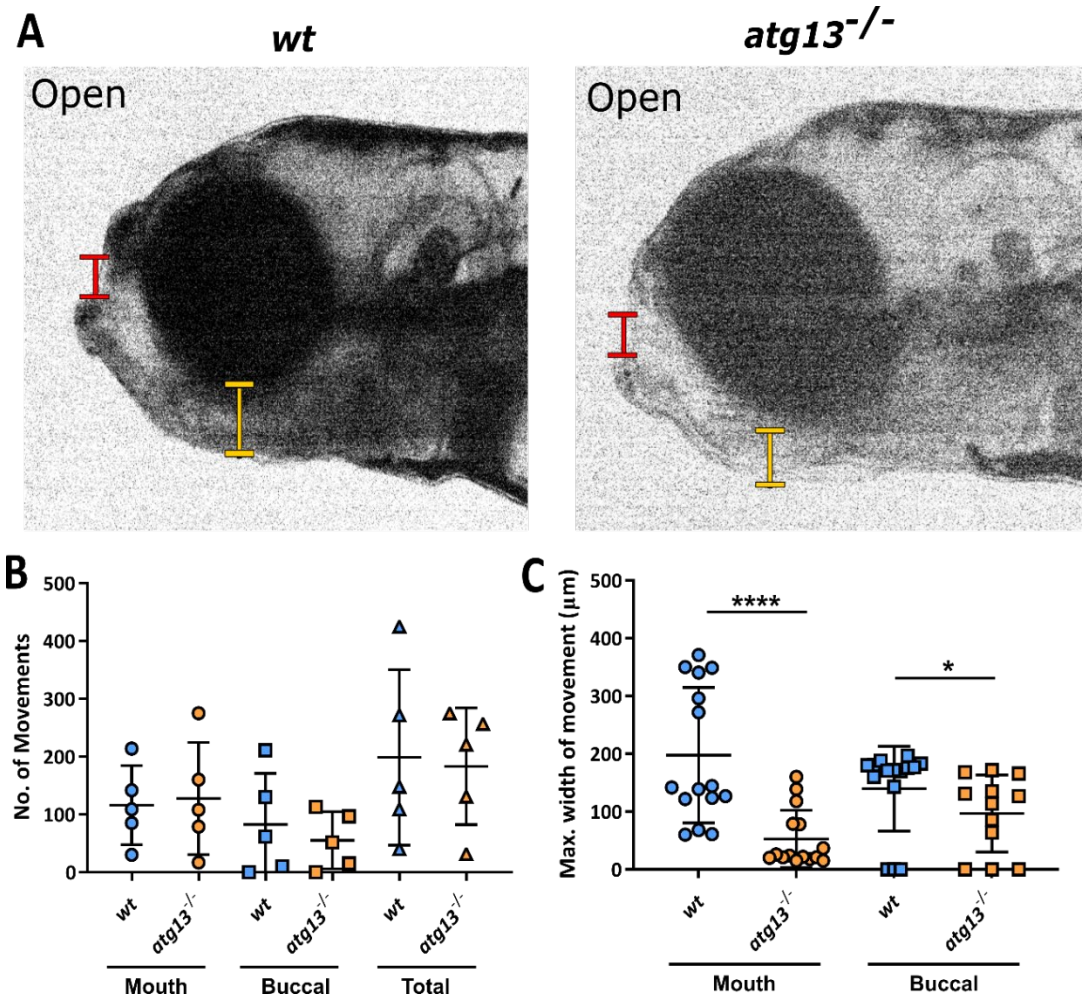

Figure 3.2.6 – The *atg13* mutants show altered jaw movements, **(A)** Stills from videos of larval jaw movements taken at 5dpf of *wt* and *atg13* mutant fish. Red and yellow lines indicate where mouth and buccal width measurements taken from, respectively. Quantification of number **(B)** and displacement **(C)** of jaw movements at the mouth and buccal joint. n = 5 for each genotype; three widest jaw openings taken per larvae. Student's unpaired t test performed for C, **** *P*<.0001, * *P*=.0129. Figure adapted from (229).

3.2.6; Chapter 7.3, Appendix C for videos). It was observed that the *atg13* mutants did indeed have a significantly reduced range of motion at both joints compared to *wt*, although the total number of movements remained unaffected (Figure 3.2.6B and C). The jaw joint showed the greatest reduction in movement compared to *wt*, indicating that the mutants cannot open their mouths as wide which could impede feeding.

3.2.7 Muscle development and patterning is not affected in atg13 mutant fish

To establish whether the different ranges of jaw movements were caused by defects in the jaw muscle architecture, muscle fibre number, and the width and length of muscle fibre bundles in the lower jaw was quantified in the *atg13* mutants and *wt* at 5dpf (Figure 3.2.6). Using immunostaining against heavy chain skeletal myosin (using an antibody against A4.1025), the intermandibularis posterior (IMP) and interhyal (IH) muscles, and the intermandibularis anterior (IMA) muscles were analysed as together these help control ventral jaw opening and closing respectively (Figure 3.2.6A) (144). Crucially, the *atg13* mutants showed no differences in muscle fibre number compared to *wt* (Figure 3.2.6B), whilst the width and length of the IMP, IH and IMA muscles were also comparable (Figure 3.2.6C; width and IMA data not shown). These data indicate that the changes to jaw movements are not being caused by changes to muscle patterning but are due to altered joint formation and function.

3.2.8 Gross jaw morphology is unaffected in atg13 mutant fish

Given that changes to jaw movement are not due to aberrant muscle development, it was next investigated whether these were due to the loss of autophagy activity affecting the overall growth and formation of the jaw. At 3, 5 and 7dpf, the length and width of lower jaw dimensions were measured using immunostaining of Col2a1 (Figure 3.2.7A). From this analysis, it was evident that no changes in Meckel's cartilage length and width (the front

cartilage element of the lower jaw; measurement 1 and 3), or in the full length of the lower jaw (measurement 2) were observed between the *wt* and *atg13* mutant fish (Figure 3.2.7B-D). From this, it was inferred that changes to cartilage development at these stages caused by the absence of *atg13* appear to be limited to the joint site only and to the cells forming this region.

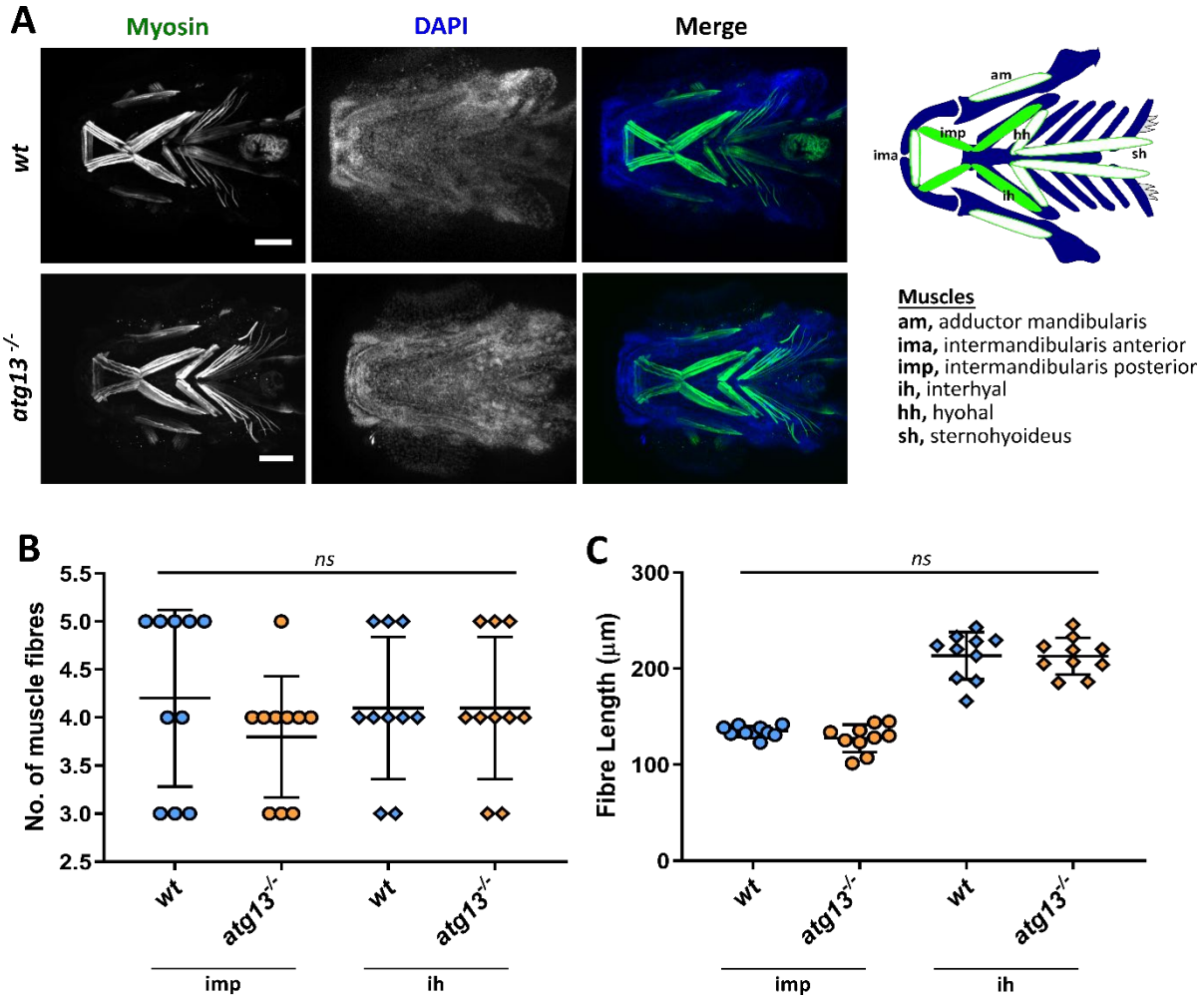

Figure 3.2.7 – The *atg13* mutation does not affect muscle development in the lower jaw, (A) *Left,* representative confocal z-stack projections of the lower jaw at 5dpf in *wt* and *atg13* mutant larvae, immunostained for muscle (green) and counterstained with DAPI (blue). Scale bar = 100µm. *Right,* schematic showing key muscle groups (green) within the lower jaw at 5dpf. Quantification of muscle fibre number **(B)** and muscle length **(C)** of IMP, IH and IMA muscles of *wt* and *atg13* mutant fish, n = 5 for all, right and left side counted separately per fish. *IMP* = intermandibularis posterior, *IH* = interhyal, *IMA* = intermandibularis anterior. Figure adapted from (229).

3.2.9 Expression of GFP-Lc3 is observed at joint sites within the jaw during development

Using the transgenic *CMV:EGFP-map1lc3b* zebrafish line, the expression of Lc3 during development can be observed. Bright expression of GFP-Lc3 was observed in the jaw joints and at the mandibular symphysis at the tip of the jaw where the Meckel's cartilage meets which is where the most immature chondrocytes are (Figure 3.2.9A). At a higher magnification (100x; Figure 3.2.9B) expression of GFP-Lc3 within individual cells at the joint interface can be seen, suggesting that autophagy activity may be being upregulated at the

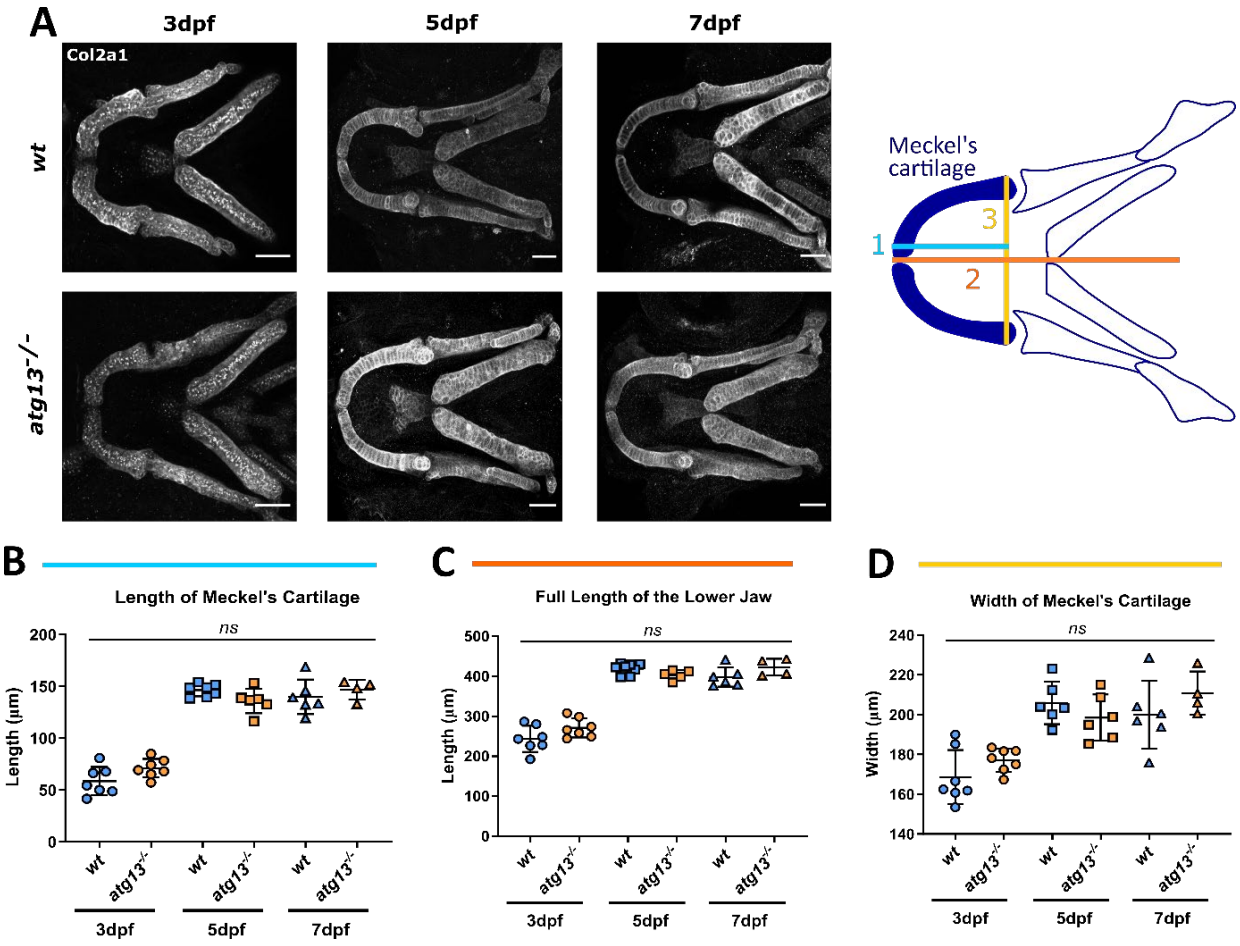

Figure 3.2.8 – Loss of *atg13* does not affect size of lower jaw in development, (A) *Left,* representative confocal z-stack projections of the lower jaw at 3, 5 and 7dpf in *wt* and *atg13* mutant larvae, immunostained for collagen Type II (Col2a1). Scale bar = 50µm. *Right,* schematic showing where 3 measurements taken within lower jaw of larvae. (B-D) Quantification of three measurements; **(B)** length of Meckel's cartilage, **(C)** length of lower jaw, **(D)** width of Meckel's cartilage. N = 7 for 3dpf, n = 6 for 5dpf and n = 6 and 4 at 7dpf for *wt* and *atg13* mutant, respectively. Student's unpaired t test performed for each age, ^{ns} P>.05. Figure adapted from (229).

joint site during development. It is at the joint interface where mesenchymal cells differentiate into one of the several cell populations which form the joint, such as myocytes, chondrocytes or fibrocytes. Therefore, these data imply that GFP-Lc3, and by extension autophagy activity, could be being upregulated as these cells undergo differentiation and establish their cell fate.

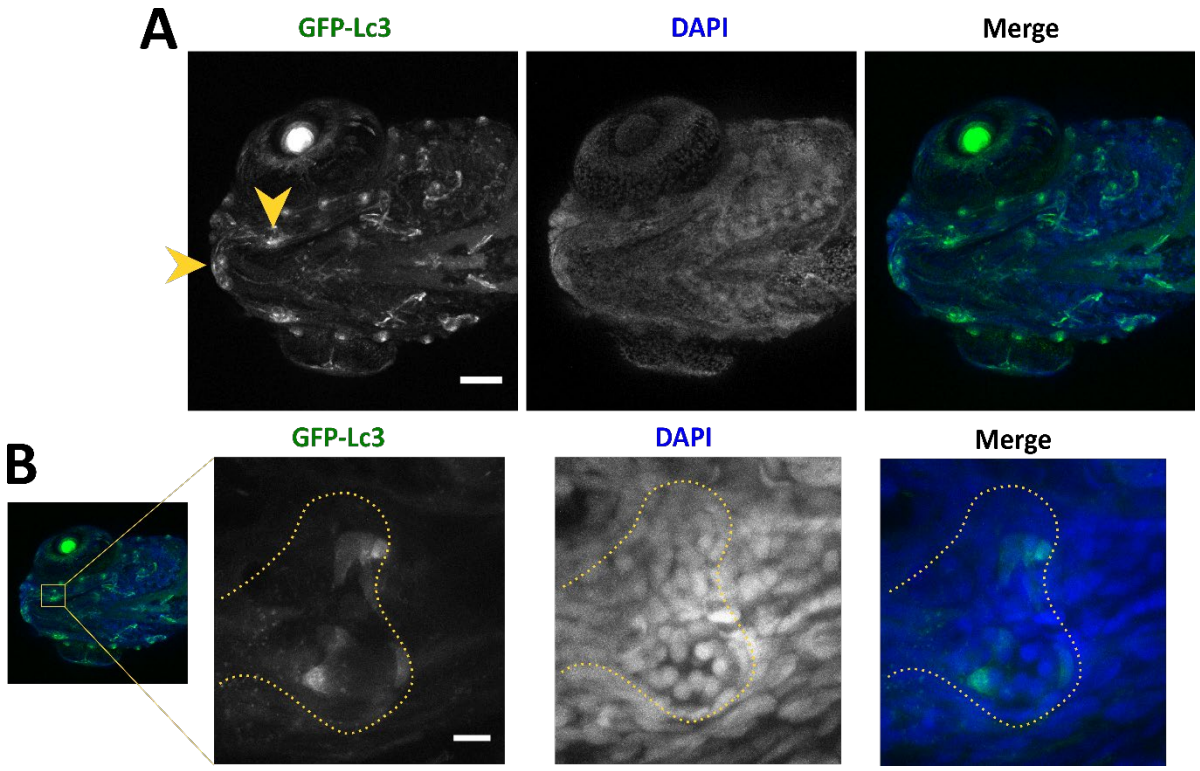

Figure 3.2.9 – GFP-Lc3 expression can be seen at joint sites during early development, (A) Representative max projection image of transgenic *CMV:EGFP-map1lc3b wt* zebrafish jaw at 4dpf for GFP-Lc3 (green), counterstained with DAPI (blue). Orange arrowheads indicate GFP-Lc3 expression at site of Meckel's symphysis (left arrow) and lower jaw joint (right arrow). Scale bar = 100 μm. **(B)** Representative max projection image of zebrafish lower jaw joint. Yellow dotted line indicates outline of cartilage element forming the joint. Scale bar = 10 μm.

3.2.10 Morphology of GFP-Lc3-postive cells at jaw joint site is altered in atg13 mutant fish compared to wild-type

To explore the role of autophagy within the developing skeleton, *wt* and *atg13* mutant transgenic GFP-Lc3 larvae were immunostained for Col2a1 from 3-7dpf and their lower jaws were imaged using confocal microscopy. As observed previously, GFP-Lc3-positive cells were still present in the *atg13* mutants, which is likely due to cells continuing to express

genes associated with autophagy, such as Lc3. Similar to *wt*, the *atg13* mutants showed increased GFP-Lc3 expression specifically at the lower joint site and at the Meckel's symphysis (Figure 3.2.10A).

To investigate whether loss of *atg13* has any effect on GFP-Lc3-expressing cells in the mutants, GFP-Lc3-postive cell number and volume within the joint element and within the inter-joint zone was calculated. This was achieved by utilising a Modular Image Analysis (MIA) program which can identify and outline individual Col2a1-positive cells and GFP-Lc3-positive cells that form the lower jaw joint during development (241). In this instance, GFP-Lc3-positive cells within the inter-joint zone (Figure 3.2.10B, *top*) and within the lower joint (Figure 3.2.10B, *bottom*) were outlined and measured (Figure 3.2.10C).

No difference in cell number within the joint interface was seen at any time point between either genotype, although cell number did increase from 5dpf to 7dpf in both *wt* and mutant (Figure 3.2.10D). However, there was a significant increase in the volume of GFP-Lc3-postive cells within the joint space at 5dpf and 7dpf in the *atg13* mutant compared to *wt* (Figure 3.2.10E). No differences in cell number or volume were seen in the GFP-Lc3-postive cells found within the cartilage elements (Figure 3.2.10F and G).

As cells within the joint interzone are differentiating and deciding cell fate, an increase in cell volume here may indicate a stalling in differentiation. Also, the increasing number of GFP-Lc3-positive cells in the joint interface from 3dpf-7dpf further points to a role for autophagy within cell differentiation as more cells differentiate as the joint is formed.

Therefore, to fully understand the role of autophagy on cell differentiation within the joint, the cell types are expressing GFP-Lc3 at the joint interface will need to be identified. This could potentially be achieved by FACS of GFP-LC3-positive cells, and single cell sequencing to characterise their expression profiles more definitively. From this, the impact of loss of autophagic activity upon the development and proliferation of these cell populations could be established.

3.2.11 GFP-Lc3-positive cells within joint interzone show no change to proliferation in the atg13 mutants and are Sox9a positive

Using an EdU proliferation assay kit, potential differences in the proliferation of GFP-Lc3-positive cells in the *atg13* mutant were explored. Larvae were treated with EdU for 24 hours from 5-6dpf and after counting the number of GFP-Lc3 and EdU-positive cells within the joint elements and at the inter-joint zone, no difference in the proliferation of GFP-Lc3-positive cells between *wt* and the *atg13* mutants was found (Figure 3.2.11A). This is in line with data from the modular cell analysis in 3.2.10 which showed no change to GFP-Lc3 cell number at the inter-joint space between *wt* and *atg13* mutants. This indicates that the loss of autophagy in the *atg13* mutants does not affect the proliferation of these GFP-Lc3-positive cells.

To explore the identity of the GFP-Lc3-positive cells within the inter-joint zone, larvae at 5dpf were immunostained with Sox9a. Sox9a is a transcription factor that is expressed in cells forming mesenchymal condensations and is essential for the differentiation of these cells into chondrocytes (277). In these images, all GFP-Lc3-positive cells at the inter-joint space, of both *wt* and *atg13* mutants, show strong co-expression of Sox9a indicating that these cells are of mesenchymal origin and could later differentiate into chondrocytes forming the joint (Figure 3.2.11B).

Due to time constraints, the biology of these GFP-Lc3-positive cells within the joint region was not explored further and instead the effect of the *atg13* mutation on chondrocytes was examined in more detail.

Figure 3.2.10 – *atg13* mutant fish show differences in GFP-Lc3-postive cell volume within inter joint space, (A) Representative confocal slices of lower jaw joint at 3, 5 and 7dpf in transgenic *atg13;CMV:EGFP-map1lc3b wt* and mutant fish, immunostained for Col2a1 (red) and GFP for GFP-Lc3 (green). **(B)** Example slices from confocal images showing GFP-Lc3 cells outlined by program in joint space (top) and in cartilage elements (bottom). **(C-F)** Quantification of GFP-Lc3 cell number and volume from joint space (C, D) and cartilage elements (E, F) for *wt* and *atg13* mutant. Cell number normalised to cartilage element volume (right). Each data point = one larvae, data are mean with SD. Student's t test performed where *** *P*=.0003, * *P*=.0115. Scale bars = 20μm. Figure adapted from (226). *Figure overleaf.*

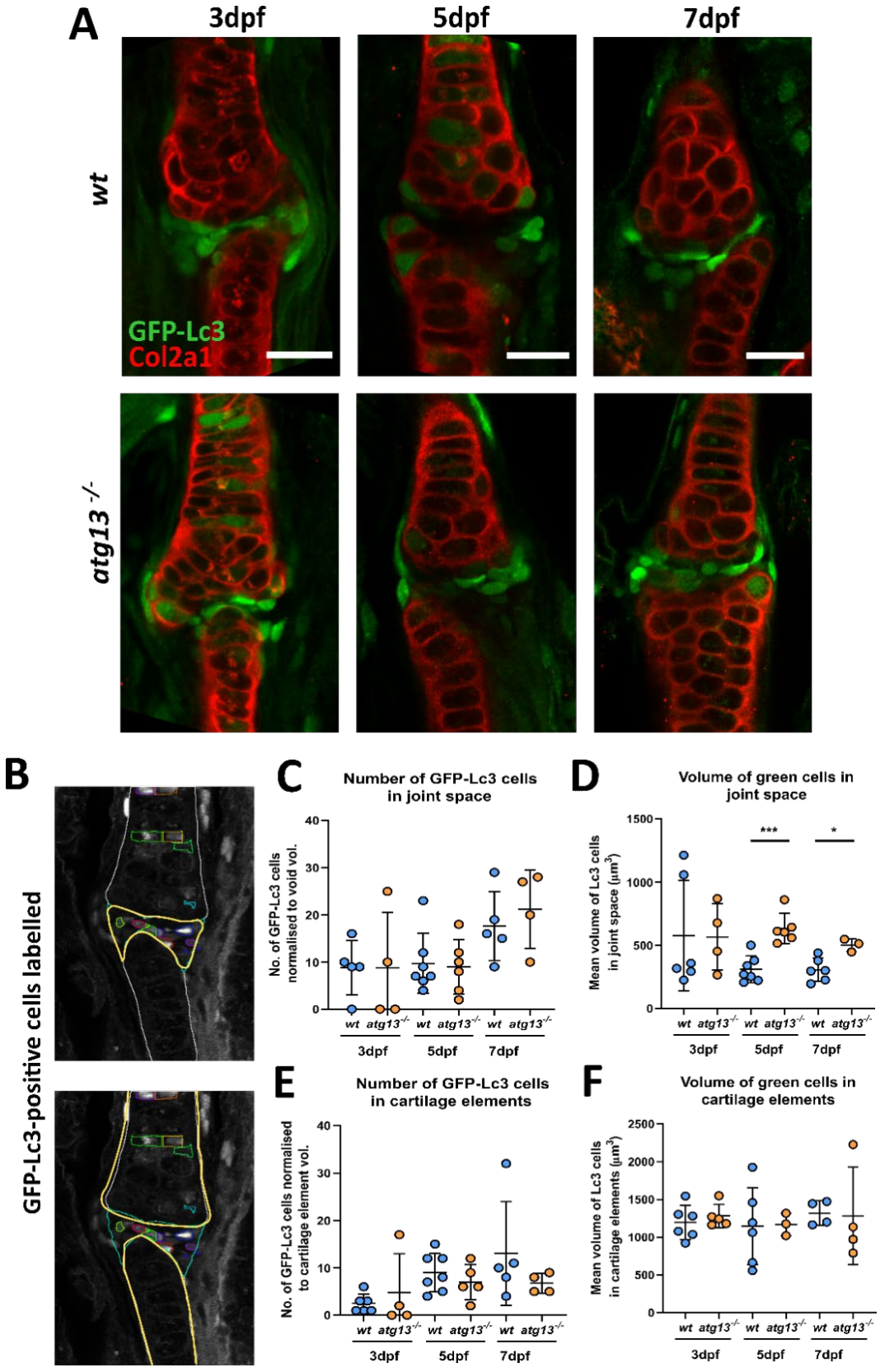
A
3dpf
5dpf
7dpf
wt
atg13 -/-
GFP-Lc3
Col2a1
B
GFP-Lc3-positive cells labelled
C
Number of GFP-Lc3 cells in joint space
No. of GFP-Lc3 cells normalised to void vol.
D
Volume of green cells in joint space
Mean volume of Lc3 cells in joint space (µm³)
***
*
E
Number of GFP-Lc3 cells in cartilage elements
No. of GFP-Lc3 cells normalised to cartilage element vol.
F
Volume of green cells in cartilage elements
Mean volume of Lc3 cells in cartilage elements (µm³)
wt atg13-/-
3dpf
5dpf
7dpf

3.2.12 The atg13 mutants show changes to cartilage cell number within the jaw joint

Using confocal images of larval jaws labelled for Col2a1 at 3, 5 and 7dpf, the number and volume of all cells from within the cartilage elements forming the joint site was quantified to indicate any differences in rate of cell proliferation and cell differentiation as chondrocytes increase in size as they become mature and become hypertrophic (Figure 3.2.8). This analysis was achieved using the same Modular Analysis Program from 3.2.10, whereby individual Col2a1-positive cells forming the lower jaw joint during development are identified and outlined (Figure 3.2.12B, *left*). Analysis of the collated data showed that at 5dpf and 7dpf, the number of Col2a1-positive chondrocytes forming the cartilage elements was decreased in the *atg13* mutant compared to *wt* when normalised to total element volume (Figure 3.2.12B, *left graph*). However, cell volume remained unchanged (Figure 3.2.12B, *right graph*). This could indicate decreased cell proliferation as cell volume is unaffected.

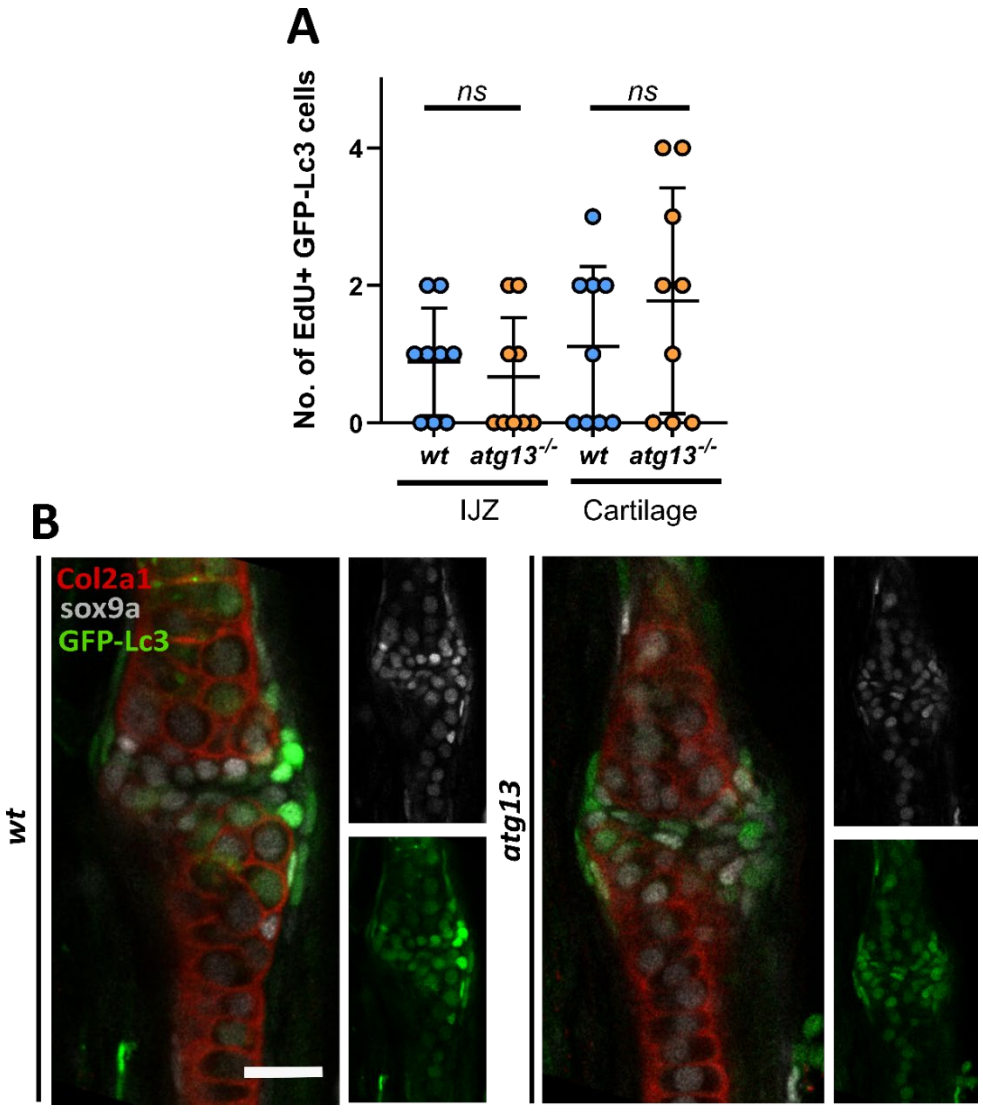

Figure 3.2.11 – *atg13* mutation does not affect GFP-Lc3 cell proliferation at joint site but does cause decreased Sox9a expression at inter-joint zone, (A) Quantification of number of EdU-GFP-Lc3-positive cells within the cartilage of the lower jaw joint (determined as region at 5x zoom on 20x objective, when joint in middle of image plane) and at inter-joint zone (IJZ) in *wt* and *atg13* mutant larvae at 6dpf. EdU-positive cells colocalised to GFP-LC3-positive cells were counted by going through z-stack. N = 9 for both genotypes; Student's unpaired t-test performed where ^{ns} P>.05**. (B)** Representative confocal slices of lower jaw joint at 5dpf in transgenic *atg13;CMV:EGFP-map1lc3b wt* and mutant fish, immunostained for Col2a1 (red), GFP for GFP-Lc3 (green) and sox9a (grey). Scale bar = 20μm. **(C)** Quantification of volume of sox9a expression at IJZ in *wt* and *atg13* mutant larvae at 5dpf as measured using modular image analysis program (SoxQuant). N = 6 for wt and 5 for *atg13* mutants; Student's unpaired t test performed, **** P<.0001. Figure adapted from (229).

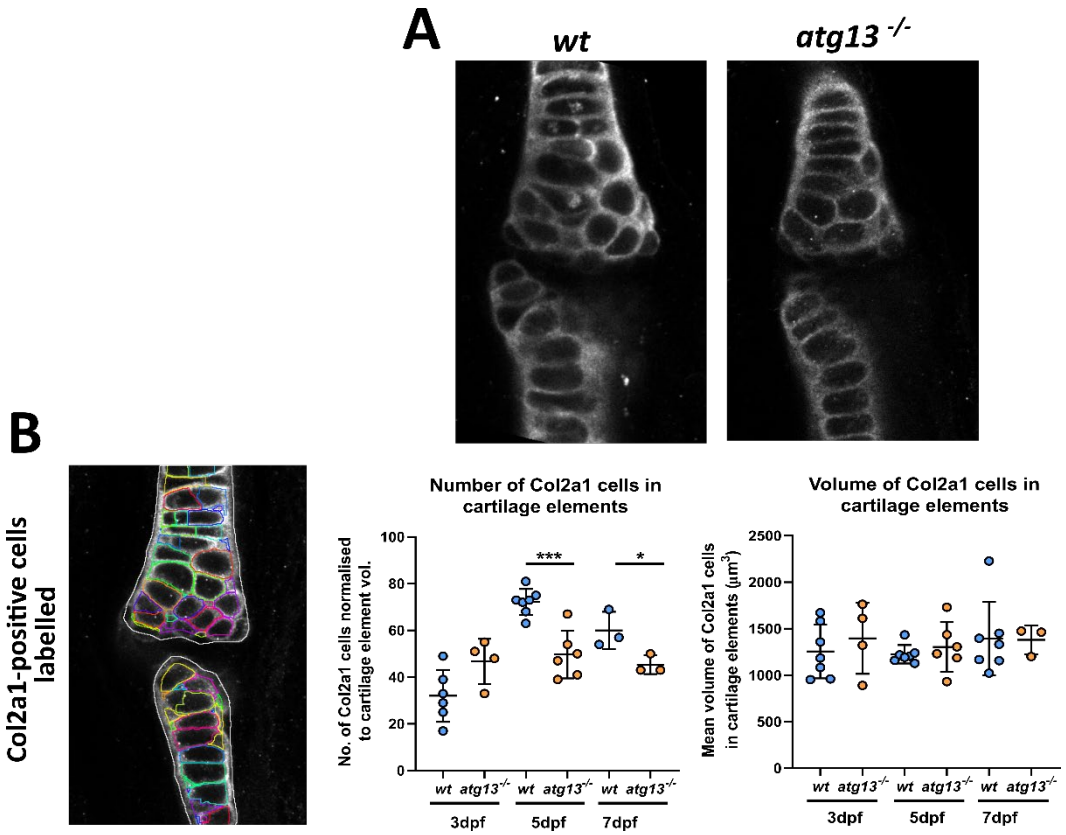

Figure 3.2.12 – *atg13* mutant fish show decreased number of cartilage cells at joint site, (A) Representative confocal slices of lower jaw joint at 5dpf in transgenic *atg13;CMV:EGFP-map1lc3b wt* and mutant fish, immunostained for Col2a1 (white). **(B)** *Left,* example slice from confocal image showing Col2a1-positive cells outlined by modular image analysis program run in ImageJ. *Right,* quantification of Col2a1 cell number normalised to cartilage element volume (right) and volume of Col2a1 cells within cartilage element (left) for *wt* and *atg13* mutant. Each data point = one larvae, data are mean with SD. Student's unpaired t test performed where *** P=.0004, * P=.0463. Scale bars = 20μm. Figure adapted from (229).

3.2.13 Changes to chondrocyte cell number in atg13 mutants due to reduced proliferation

To investigate whether the decrease in chondrocyte number at the joint site is caused by changes to proliferation rates, an EdU proliferation assay was performed on larvae from 5-6dpf (Figure 3.2.13A). By analysing the number of EdU-positive chondrocytes at the joint site, it was found that the *atg13* mutants showed a 66% decrease in the number of proliferating cells within the joint compared to *wt* (Figure 3.2.13B). This implies a role for autophagy in chondrocyte development and maturation. This is of particular significance at joint sites where pre-chondrogenic cells are beginning to differentiate and mature as they are pushed up the element into the intercalation zone. Therefore, changes to differentiation and maturation here will have the biggest impact upon joint morphology.

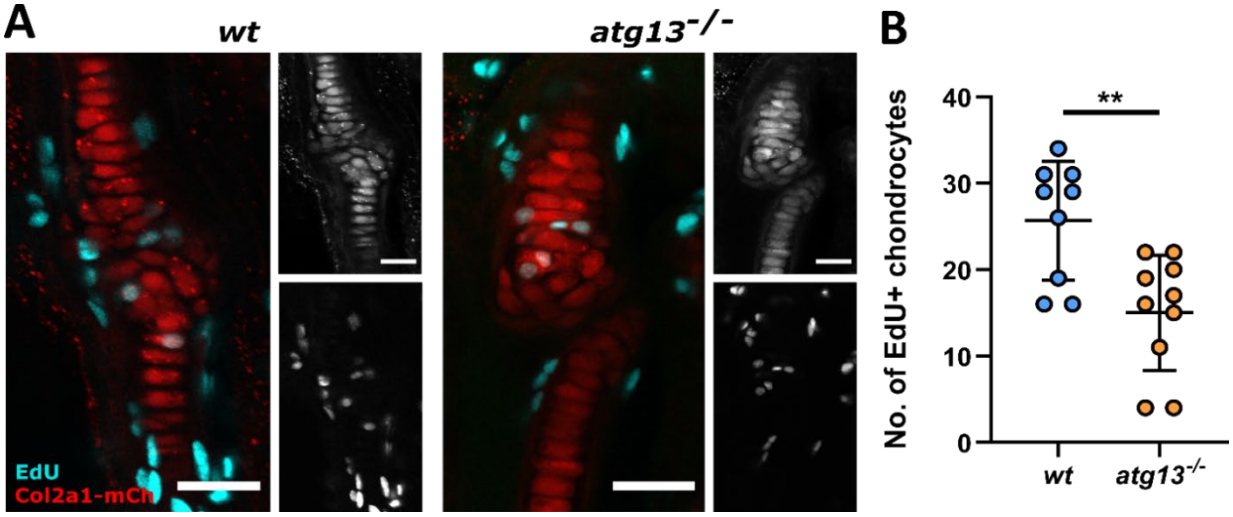

Figure 3.2.13 – *atg13* mutant fish show reduced proliferation at joint site, (A) Confocal max projections of larval jaw joint in *Tg(atg13;Col2a1aBAC:mcherry) wt* and *atg13* mutants at 6dpf following 24 hour treatment with EdU Click-iT (EdU in cyan and mCherry-Col2a1 positive cells (chondrocytes) in red). Scale bars = 25μm; 20μm for inset. **(B)** Quantification of number of EdU positive chondrocytes within jaw joint region (determined as region at 5x zoom on 20x objective, when joint in middle of image plane). EdU positive chondrocytes colocalised to mCh-Col2a1 positive cells were counted by going through z-stack. N = 9 for wt and 10 for *atg13* mutants; Student's unpaired t test performed, ** *P*=.0032. Figure adapted from (229).

3.2.14 Chondrocytes show increased maturation within atg13 mutants

SOX9 is one of the first transcription factors expressed within the chondrocyte maturation pathway, and is essential for chondrocyte differentiation and subsequent cartilage formation (278). Larvae at 5dpf were immunostained for Col2a1 and Sox9a, an ortholog of tetrapod

SOX9 (279), and the volume of Sox9a expression within chondrocytes was measured using a modular image analysis program called 'SoxQuant'. Using this program, Sox9a expression within a specified region of interest is calculated as the volume of Sox9a fluorescence present through an image z-stack. Here, the *atg13* mutants show a significant decrease in the expression of Sox9a, at three regions within the lower jaw: at the joint site, within the intercalation zone of the Meckel's cartilage, and at the Meckel's cartilage symphysis (Figure 3.2.14A-D), thus, indicating an overall reduction in Sox9a across chondrocytes forming the lower jaw. As chondrocytes mature and become hypertrophic, Sox9a expression decreases, therefore, a reduction in Sox9a expression comparative to *wt* is indicative of premature progression of immature chondrocytes into hypertrophic chondrocytes.

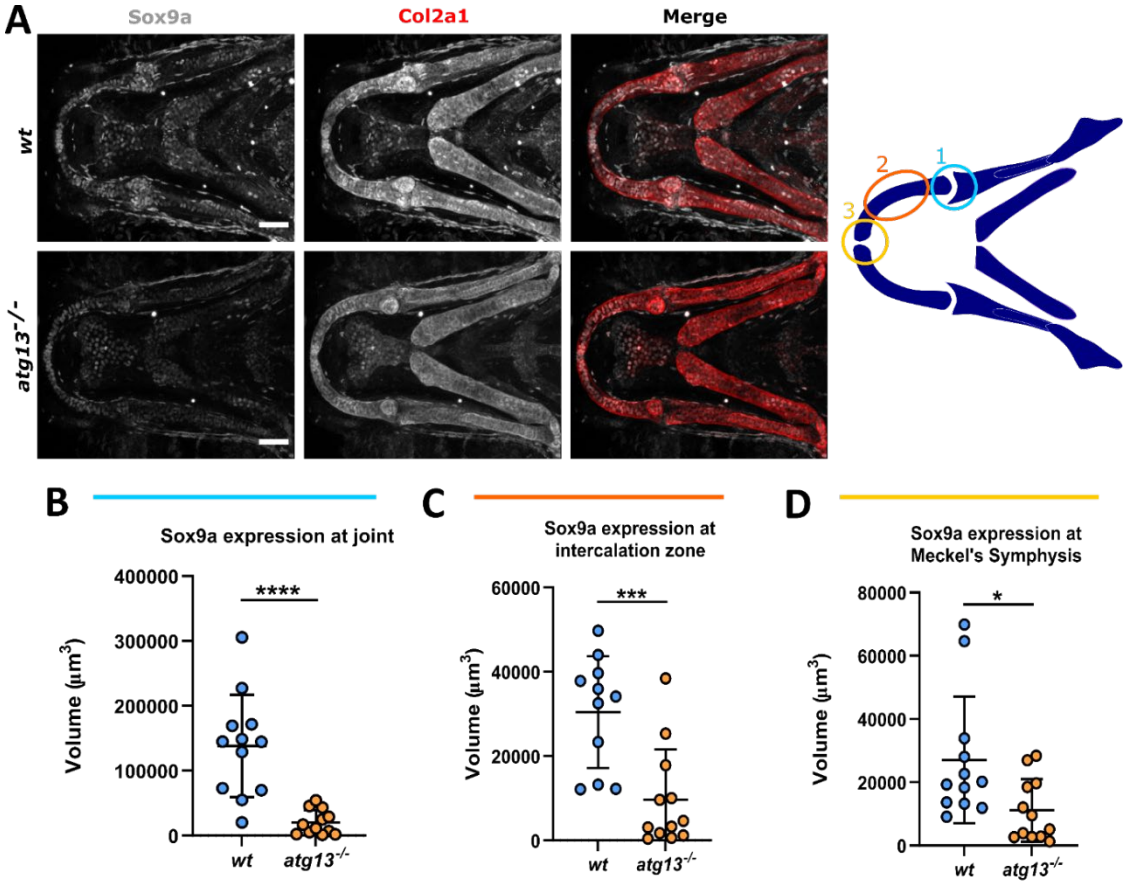

Figure 3.2.14 – *atg13* mutation affects expression of Sox9a in chondrocytes, (A) *Left,* confocal max projections of lower jaw at 5dpf in *wt* and *atg13* mutant fish, immunostained for Sox9a (grey) and Col2a1 (red). Scale bars = 50µm. *Right,* schematic showing regions of interest selected within lower jaw in modular image analysis program (SoxQuant). Colours correspond to graphs below. **(B-D)** Quantification of Sox9a expression measured as volume of Sox9a within Col2a1 positive cells from confocal z-stack. Student's unpaired t test performed where **** $P<.0001$, *** $P=.0007$, * $P=.0173$; n = 12 for both. Figure adapted from (229).

3.2.15 Chondrocytes show premature hypertrophication within atg13 mutants

To confirm that the chondrocytes in the *atg13* mutants are maturing more rapidly, the expression of type X collagen α1 (Col10a1) was assessed via immunostaining (Figure 3.2.15). Col10a1 can be used as a marker for hypertrophic chondrocytes, as well as early osteoblasts, cartilage maturation chondrocytes switch collagen expression from Col2a1 to Col10a1 (270). At 7dpf, it was found that the *atg13* mutants had an elevated Col10a1-positive chondrocyte population compared to *wt*, indicating that these cells are maturing more rapidly. Along with evidence of reduced Sox9a expression, these data indicate that loss of autophagy activity disrupts the rate of chondrocyte maturation and causes chondrocytes to become prematurely hypertrophic.

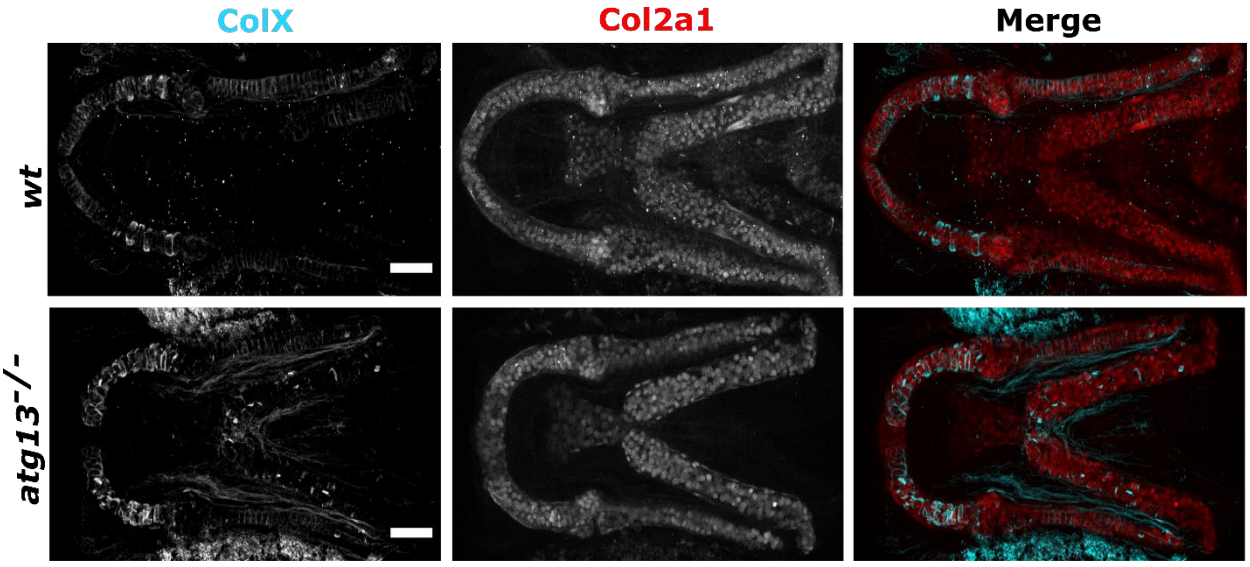

Figure 3.2.15 – Loss of *atg13* increases expression and production of Col10a1 in cartilage development, Confocal max projections of the lower jaw at 7dpf in *Tg(atg13;Col2a1aBAC:mcherry)* *wt* and *atg13* mutant larvae, immunostained for collagen Type X (ColX) (cyan) and mCherry (for Col2a1, red). N = 6 for both genotypes; scale bars = 50μm. Figure adapted from (229).

3.2.16 The atg13 mutant chondrocytes show alterations to chondrocyte organisation and ECM formation

To explore how these changes to chondrocyte maturation manifest within the developing tissue, ultrastructural analysis was performed on chondrocytes of the ethmoid plate at 5dpf (Figure 3.2.16). Under basal conditions, *wt* chondrocytes appeared elongated, were arranged in a stacked formation along the length of the cartilage and were surrounded by a dense and

organised ECM (Figure 3.2.16A). In contrast, the *atg13* mutant chondrocytes were more disorganised with increased numbers of immature and non- or partially intercalated chondrocytes observed at the cartilage edge, resulting in a non-uniform and bumpy appearance along on the cartilage border (Figure 3.2.16B, 3.2.16D *orange arrowheads,* and 3.2.12G). Compared to *wt,* the *atg13* mutant chondrocytes were less electron dense (Figure 3.2.16D), indicative of late stage hypertrophication. These data, together with the changes to Sox9a and Col10a1 expression, indicate that the *atg13* mutant chondrocytes undergo an altered maturation process which inhibits proper cell placement and intercalation, leading to disorganisation of cartilage structure.

Focusing on the intracellular contents of the chondrocytes, in *wt* fish, vesicles containing low-electron dense material, predicted to be type II collagen fibrils were evident within the cytoplasm, with a substantial population fusing with the plasma membrane during exocytic events (Figure 3.2.16C, *red asterisks*). Although similar vesicles could be observed in the *atg13* mutants (Figure 3.2.16C and D), very few of those vesicles were found to be undergoing fusion with the plasma membrane (Figure 3.2.16H). This suggests that loss of autophagy affects vesicle exocytosis in chondrocytes. To explore the effect of these changes on ECM formation, modular analysis of the ECM structure and organisation from the ultrastructural images was attempted by using an automated measure of Haralick's texture features (280).

Haralick's texture features were developed in the 1970's as a way to analyse differences in intensities between different regions within an image (281). The system involves comparing differences in the grey level distribution between neighbouring voxels (volumetric pixels) found within the selected region of an image (ROI; region of interest). These differences in grey level values between neighbours are then collated within a GLCM (grey level cooccurrence matrix) which can be used to assess the texture or 'roughness' of an image. In this instance, the GLCM was used to measure differences in image between ROI variance (a measure of the distribution of voxel grey values about the mean), entropy (the orderliness of the grey level distribution across voxels in an ROI) and the angular second moment (a measure of the homogeneity of grey values within an ROI) (282). Haralick's texture features have been used in several studies as a way to measure the uniformity, variance, and coarseness of the ECM within cartilage samples. For example, they have been used to

analyse the textural and organisational changes of the ECM during development (283), and to compare ECM organisation and structure between healthy and osteoarthritic patients as a potential diagnostic tool (284). Unfortunately, although the analysis program could detect differences in ECM organisation between different ROI's, these results were not comparable across separate images due to differences in image contrast which could not be standardised across images. Therefore, differences in ECM density and structure between *wt* and *atg13* mutant chondrocytes were qualitatively inferred from election micrograph images. Notably, the ECM surrounding the chondrocytes appeared sparser and less well organised in the *atg13* mutants (Figure 3.2.16C and D, *inset*), which is predicted to be related to a reduction in vesicle exocytosis, as these vesicles are predicted to contain collagens required for ECM formation.

To explore whether these effects were specific to loss of autophagy caused by the *atg13* mutation, larvae were treated with BafA1 for 3 hours at 5dpf (Figure 3.2.16E and F). Similar to the effect of the *atg13* mutation, it was found that BafA1 treatment abrogated vesicle exocytosis in wt fish (Figure 3.2.16H), causing an increase in the number of vesicles within the cytoplasm of wt chondrocytes (Figure 3.2.16E). This supports the hypothesis that blocking or stalling of the autophagy pathway has a role in vesicle exocytosis within chondrocytes. The *wt* treated larvae also showed an increase in the number of chondrocytes not intercalating (Figure 3.2.16G), with more cells present at the outer edges of the cartilage, perpendicular to the main stack, as also seen in the mutants. These data demonstrate a role for autophagy in the control of chondrocyte differentiation and in ECM formation.

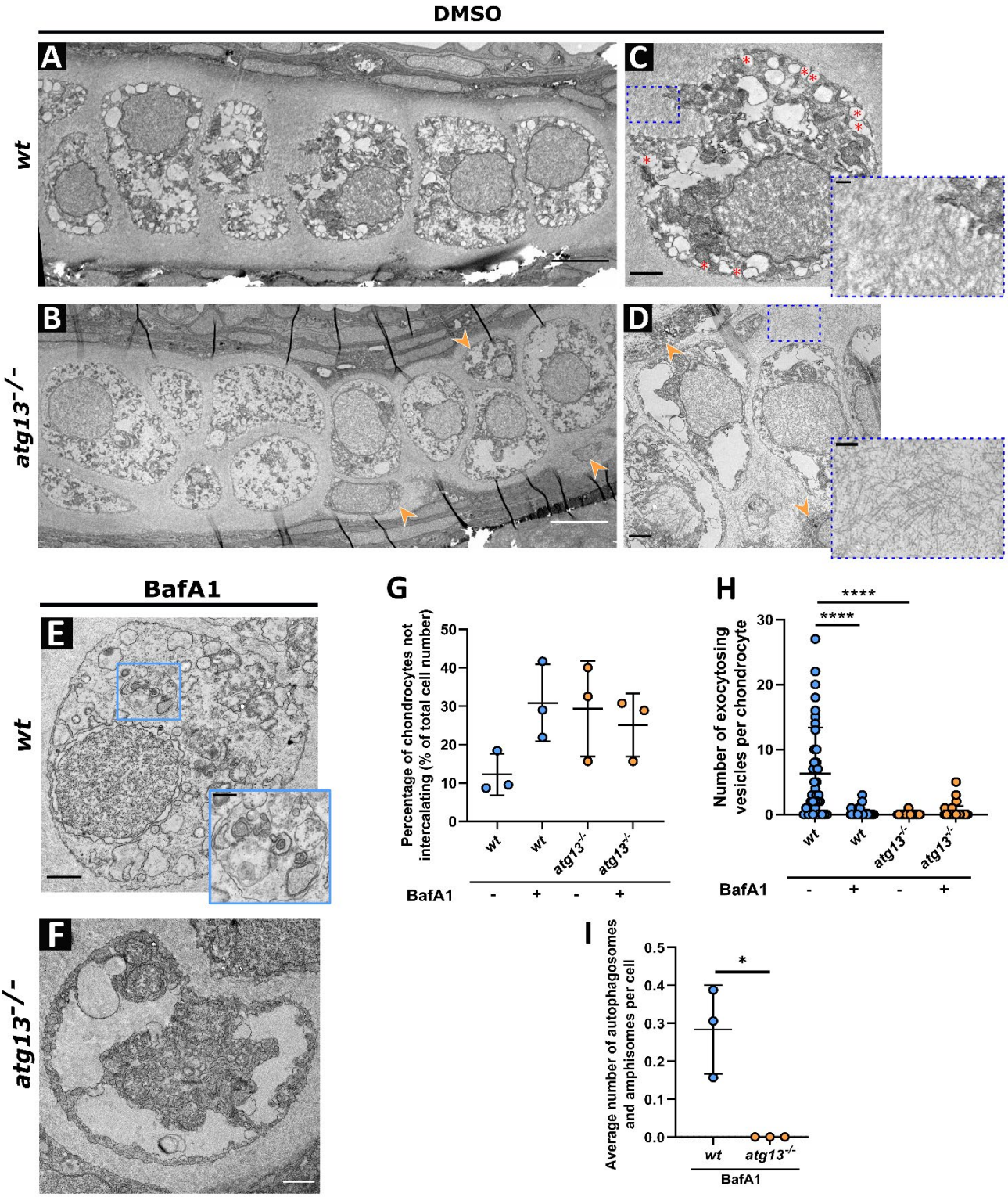
DMSO
A
C
wt
B
D
atg13-/-
BafA1
E
F
G
Percentage of chondrocytes not intercalating (% of total cell number)
wt
wt
atg13-/-
atg13-/-
BafA1
H
Number of exocytosing vesicles per chondrocyte
****
****
I
Average number of autophagosomes and amphisomes per cell
*
wt
atg13-/-
BafA1

Figure 3.2.16 – Ultrastructure and organisation of chondrocytes affected in *atg13* mutants, (A-D) Electron microscopy of ethmoid plate in *wt* and *atg13* mutant fish at 5dpf following DMSO or **(E, F)** BafA1 treatment for 3hrs. **(B, D)** Orange arrow heads highlight areas of non-uniformity and non-intercalating chondrocytes in *atg13* mutant cartilage. **(C)** Red asterisks show vesicles fusing with outer membrane in *wt,* not present in *atg13* mutant. Blue dotted boxes and inset show differences in ECM organisation and density between *wt* and *atg13* mutants. **(E, F)** BafA1 treatment increases number of vesicles in both *wt* and *atg13* mutants and ablates vesicle-membrane fusion events. Blue box and inset in **(E),** shows an autophagosome in BafA1 treated *wt* chondrocyte, not present in *atg13* mutants. Scale bars A, B = 5μm; C, D, E, F = 1.5μm; C', D', E' = 0.5μm. **(G)** Number of chondrocytes on periphery of cartilage and not aligning down central line of stack. Calculated as percentage of total cell number along ethmoid plate in one section. N = 38 chondrocytes total from 3 larvae, per condition and genotype. **(H)** Number of vesicles fusing with outer cell membrane quantified per cell following DMSO or BafA1 treatment. 2-way ANOVA performed for each; **** $P<.0001$. **(I)** Average number of autophagosomal structures per chondrocyte in bafilomycin A1 treated fish, calculated as average of all chondrocytes per individual fish. Student's unpaired t-test performed; * $P=.0138$. Larval samples for TEM were processed by Dr Chris Neal (School of Biochemistry, University of Bristol) and samples were sectioned by Dr Sally Hobson (School of Biochemistry, University of Bristol). Figure adapted from (229).

3.3. Discussion

In this chapter the role of autophagy in chondrocyte development and maturation has been explored. These results have shown that loss of a key autophagy protein, Atg13, affects cartilage formation, joint function and is detrimental to zebrafish larval survival.

Through studying the *atg13* zebrafish model, it has been found that loss of Atg13 affects early larval development, causing reduced growth and loss of swim bladder inflation, and juvenile lethality by 17dpf. These data demonstrate that expression of *atg13* is essential for zebrafish survival, and that Atg13 may play both autophagic and non-autophagic roles in development. This is in line with data from a previous study that showed that loss of Atg13 in zebrafish affects swim bladder inflation and causes larval lethality (41). In a murine *Atg13*$^{-/-}$ model, Kaizuka *et al*. demonstrated that mutant mice die by embryonic day 17.5 (E17.5) and show growth retardation, as well as myocardial defects (257). Here, no obvious changes to cardiac development were seen in the *atg13* mutants and therefore, it is hypothesised that the delayed growth and eventual lethality of these mutants is in part due to reduced yolk sac metabolism from 1-5dpf and reduced free feeding beyond 5dpf due to altered jaw morphology and function. Similarly, Mawed *et al.* demonstrated that following yolk absorption at 5dpf, *becln1* and *atg7* knock-out zebrafish mutants were unable to cope with metabolic stress and died at 9dpf and 15dpf, respectively (272). Defects in hepatic glycogen and lipid metabolism, and within intestinal architecture were also observed in both mutants, indicating that autophagy is critical for energy metabolism during early zebrafish development.

Through its interaction with ULK1 and FIP200, ATG13 is a vital element of the ULK1 protein kinase complex which is a key signalling node and the first protein complex within the autophagy pathway and is essential for initiating autophagosome formation (285, 286). These data show that under basal conditions, the *atg13* mutant has limited autophagy activity, as indicated by an accumulation of p62. As an adaptor protein, p62 helps deliver cargo to the autophagosome by binding to ubiquitinated substrates and Atg8 family

members, and is mainly degraded by autophagy (287). Therefore, an accumulation of p62 indicates autophagy inhibition. The results also show a reduction in GFP-Lc3 puncta compared to *wt,* indicative of reduced autophagy activity, however, it could be anticipated that an autophagy-null model would show a complete loss of GFP-Lc3 puncta. Although surprising, the presence of GFP-Lc3 puncta have been observed in other *atg13* null mouse and *C. elegans* models, and therefore, are predicted to be due to LC3 aggregation or activation of a non-canonical autophagy pathway, such as LAP (LC3-associated phagocytosis), where LC3 lipidation can occur independently of the ULK1 preinitiation complex (288, 289). This could also account for the presence of lipidated Lc3 shown by immunoblot in the *atg13* mutants. Upon review of the literature on Lc3 protein expression in zebrafish larvae, there are several papers which show a difference in Lc3-I and Lc3-II levels by immunoblotting in *wt* zebrafish compared to murine or human models during development (125, 126, 140, 290, 291). These data indicate that the observed response to increasing or blocking autophagy flux normally seen in mammalian models (e.g., lower Lc3-II levels at basal levels and higher Lc3-II levels when starved or stressed, (292)), is not replicated in zebrafish models when immunoblotting and therefore, is less able to be used in an identical manner to assess autophagy flux. For this reason, p62 expression has been used in conjunction to Lc3 expression to assess autophagy activity in the *atg13* mutant in immunoblots.

Following treatment with BafA1, the *atg13* mutants also showed impaired autophagic flux as demonstrated by the minimal increase in GFP-Lc3 puncta and p62 protein levels. Using electron microscopy, autophagosomes and amphisomes present in BafA1 treated *wt* chondrocytes were detected which were completely absent in *atg13* mutant cells, further demonstrating a loss of autophagic activity caused by the *atg13* mutation (Figure 3.2.16E, *blue box inset* and 3.2.16I). Therefore, despite the presence of GFP-Lc3 puncta within the *atg13* mutant and differences in Lc3-I lipidation in zebrafish compared to murine and cell models, taken altogether these results still demonstrate a reduction in autophagy flux within the *atg13*$^{-/-}$ model which is in line with the expected outcome of this mutation.

As mentioned, previous studies using mice have identified roles for autophagy in cartilage development and growth; however, the effect of these changes on joint formation and

function has not been discussed. Here it has been shown that *atg13* mutant zebrafish have reduced jaw function at 5dpf, which is not caused by alterations to jaw muscle development or gross jaw morphology, but instead correlates with changes to chondrocyte number at the jaw and reduced proliferation of joint precursors (Figure 3.3). These results are consistent with those from other autophagy-null murine models which also show decreased chondrocyte proliferation during development, leading to a reduction in long bone length and overall body size from birth to adulthood (52, 69, 271). Sox9a staining of the chondrocytes forming the lower jaw joint showed decreased expression in the *atg13* mutants compared to *wt*. Taken together with the increased expression of Col10a1 in *atg13* mutants, these data suggest that autophagy, and specifically Atg13, has a role in regulating the rate of chondrocyte maturation.

This disruption to chondrocyte maturation was confirmed by ultrastructural analysis as chondrocytes in the *atg13* mutants were more disorganised and had a reduced cellular density. Additionally, in the *atg13* mutants an increase in the number of chondrocytes failing to fully intercalate into the cartilage element was observed; a phenotype which could be induced in *wt* following treatment with BafA1, indicating that these changes may be specifically due to loss of autophagy activity. Sox9 is a key factor in early chondrogenesis and chondrocyte differentiation (277), and heterozygous deletion of *Sox9* in mice has been shown to cause premature chondrocyte hypertrophy and accelerated ECM mineralisation (293), whilst *sox9* null zebrafish show reduced chondrocyte numbers and absence of proper chondrocyte intercalation (294). Meanwhile, in undifferentiated mesenchymal cells, *Sox9* has been shown to be regulated by the serine/threonine protein kinase mTORC1 (295), which is also a master regulator of autophagy (296). Therefore, it could be hypothesised that the effects on chondrocyte maturation and intercalation seen in the *atg13* mutants are due to dysregulation of *sox9a* expression, and that this dysregulation could be mediated by loss of autophagy activity. To explore this, mTOR activity in *wt* and *atg13* mutants could be measured via immunoblotting for phosphorylated S6-kinase 1 (p-S6K1), a substrate of mTOR which is commonly used to assess mTOR activity. If the hypothesis is correct, the *atg13* mutants should show a decrease in p-S6K1 protein expression compared to *wt*.

Ultrastructural analysis revealed a decrease in ECM density and organisation in the *atg13* mutants which could be observed, but not measured from the ultrastructure images (Figure 3.3). This is similar to the ECM phenotype seen in mice with conditional loss of *Atg7* in chondrocytes, which is caused by retention of procollagen 2 within the ER, as demonstrated by the enlarged and highly electron dense ER cisternae in the *Atg7* mutant mice (82). In this *atg13* mutant model, no obvious changes to ER structure and distribution are seen, but a drastic reduction in the number of vesicular exocytosis events is observed. Therefore, it is hypothesised that the changes to ECM formation are due to a reduction in the secretion of collagens required for ECM formation via exocytosis. This decrease in collagen secretion could be due to two reasons: dysregulation of the autophagy pathway affecting vesicle exocytosis within chondrocytes; or their accelerated maturation, as chondrocytes reduce collagen production as they become more hypertrophic (297, 298). Alongside this, *Sox9* expression is required for expression of *Col2a1*, along with other collagens (299, 300), and therefore, its decreased expression in the *atg13* mutant could affect collagen production, leading to reduced secretion and a sparser ECM. To confirm this hypothesis, the contents of these chondrocytic vesicles could be explored using immunogold labelling for collagen fibrils. This would help determine whether these vesicles are secreting collagen for ECM formation and if there are any differences in collagen quantity between *wt* and *atg13* mutant vesicles.

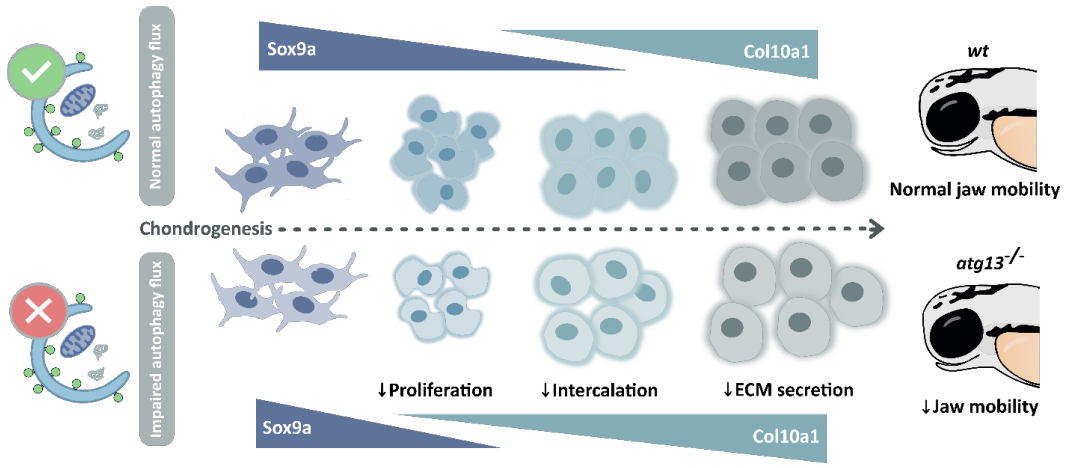

Figure 3.3 – Autophagy is required for timely chondrocyte maturation and proper jaw function in zebrafish larvae, Impaired autophagy flux in *atg13* mutant chondrocytes causes a reduction in Sox9a expression and increased Col10a1 expression compared to *wt*, indicative of premature chondrocyte hypertrophy. This disrupts chondrocyte proliferation and intercalation, and reduces extracellular matrix (ECM) secretion, resulting in reduced jaw mobility in 5dpf larvae.

Expression of GFP-Lc3-positive cells at the joint interzone were also observed in both *wt* and the *atg13* mutants, indicating that autophagy might be upregulated at joint sites during their formation. In the *atg13* mutants, these cells at the inter-joint zone appeared larger but showed no change to proliferation, and were Sox9a-positive, identifying them as early mesenchymal cells. Unfortunately, further analysis of these cells to determine their fate and role in joint development, and how autophagy may affect these processes was not possible within this thesis. Looking ahead, the monitoring of GFP-Lc3 expression within these cells would be useful to understand the activity profile of autophagy during joint development. This could be achieved through using the Kaede system whereby selected Kaede-expressing cells can be photoconverted to an alternate colour to allow for the tracking of their migration. Using this system, mosaic Kaede *atg13* mutant, GFP-Lc3-positive fish could be generated by mRNA injection of the Kaede protein, or permanent transgenic fish could be generated using the UAS-Gal4 system (301). Alternatively, Zebrafish Brainbow system could also be used where adjacent cells are labelled with different colours through microinjection of Brainbow plasmid DNA (302). This enables multiple cells to be followed through development, including their migration patterns and cell morphology changes over time. From this, the most critical time for autophagy activity during joint development could be identified.

Furthermore, it would be interesting to use markers for joint-specific components, such as proteoglycan 4 (surface marker for articular chondrocytes) or thrombospondin 4 (tendon marker) to investigate the identity of these GFP-Lc3-positive cells at the inter-joint zone. Using the *atg13* mutants, any differences in the differentiation or migration of these cells could be observed to understand the effect that loss of autophagy has at the inter-joint zone and subsequently, on joint formation. Together, these experiments could help support the findings shown here by exposing further the roles autophagy plays in cell differentiation during joint development.

Together these results show that Atg13 has a role in cell differentiation during skeletal development and that changes to autophagy activity have an impact upon how joints are formed and maintained, and function. Given the link between autophagy and OA, these data highlight three possible mechanisms for increased OA risk following loss of *atg13* and

dysregulation of autophagy. Firstly, perturbations to chondrocyte maturation can alter joint function leading to impairments in joint loading throughout life. Secondly, premature maturation of chondrocytes could cause increased hypertrophy of articular cartilage, resulting in increased cartilage mineralisation, and thirdly, reduced cartilage matrix secretion could lead to cartilage that is less able to withstand physiological load and is at higher risk of breakdown. Therefore, these results identify potential links between specific autophagy proteins and cartilage health which can be used to improve our understanding of joint diseases such as OA.

Chapter 4. Development of *LMX1B* knock-out cell and zebrafish lines using CRISPR-Cas9 technology

At a glance…

In this chapter, we encounter the highs and lows experienced using CRISPR-Cas9 technology in our mission to generate an LMX1B knock-out model. Whilst a stable knock-out of LMX1B in HEK293T cells proved elusive, the process used to successfully generate two lmx1ba and lmx1bb knock-out zebrafish lines is demonstrated and the methods utilised to identify each knock-out mutation shown.

CHAPTER

4

Development of *LMX1B* knock-out cell and zebrafish lines using CRISPR-Cas9 technology

4.1. Introduction

The genetic modification of genomes to remove or edit genes is one of the most useful molecular tools for understanding the role that specific genes play in normal development and homeostasis, and disease. To that end, gene knock-outs in model organisms and the study of their consequent phenotypes have played an essential role in uncovering the function of genes and their involvement in certain diseases. *LMX1B* has already been established as the gene responsible for the Mendelian disorder, Nail-patella syndrome (NPS), as well as being involved in normal body patterning, eye, and kidney development (179, 189, 214, 217). Additionally, mutations in *LMX1B* have also been implicated in hip OA and increased bone mineral density (221). A recent study has also shown a role for LMX1B in autophagy regulation (180). Therefore, to study the role of LMX1B in skeletal development and autophagy regulation, and to test whether there is a connection between the two, *LMX1B* knock-out models in human cells and zebrafish were generated using CRISPR-Cas9 genome editing.

The CRISPR-Cas system is a molecular tool used to manipulate genetic sequences in model organisms and was appropriated from bacteria and archaea where it originally evolved as a

microbial nuclease defence system. CRISPRs (clustered regularly interspaced short palindromic repeats) are repetitive loci found in bacterial and archaeal genomes which are separated by spacer sequences (sections of variable genetic code) and usually adjacent to Cas (CRISPR-associated) genes. The spacer sequences were discovered to correspond to sequences from plasmids and viruses and therefore, are used by the host as marker sequences to detect invading pathogens (303). When transcribed, these spacer sequences, known as CRISPR RNA (crRNA) pair with Cas proteins, a family of enzymes and nucleotide-binding proteins which can cleave nucleic acids, to form CRISPR-Cas complexes which can locate, bind to, cut and silence invading nucleic acids.

Although there are now six identified types of CRISPR-Cas systems, the Type II system is the one most commonly used for genetic engineering as it is one of the simplest systems, requiring only one protein Cas protein, Cas9 (304, 305). Cas9 is a large multidomain protein comprising of two nuclease domains, a RuvC-like (RNase H fold) domain and an HNH (McrA-like fold) domain which together enable the cleavage of target DNA (306). Along with the Cas9 protein, the type II system is formed of two parts: CRISPR RNA (crRNA) and transactivating crRNA (tracrRNA). The crRNA is formed usually of a 17-24 nucleotide sequence which is complementary to the target DNA and helps guide the Cas nuclease to the right area for editing. Meanwhile, the tracrRNA forms a binding scaffold for the Cas endonuclease protein. Once directed to the target site by the crRNA, the Cas protein will typically cause a double-stranded break in the DNA. Once a double-stranded break is made, the cell will try to repair the break via non-homologous end joining (NHEJ), an error prone process which can introduce insertions or deletions (indels) into the cut site, causing a mutation and potential loss of gene function. This system has been successfully appropriated for biological research and applied in a multitude of cell and animal models with significant success. This includes zebrafish where it has been widely used to produce stable knock-out lines, cementing its value as a central tool for reverse genetic screening (307).

CRISPR-Cas9 technology, along with other molecular tools, have already been used to generate several murine *Lmx1b* knock-out models (173, 194, 217, 308, 309). These models have been pivotal for showing the role and requirement of Lmx1b in dorsal limb patterning,

establishment of the midbrain-hindbrain boundary and cerebellum (310), and other neuronal types (218, 309, 311), podocyte development in the kidneys (173, 194) and anterior segment eye formation (217) and maintenance (308). Comparable with humans, homozygous loss of *Lmx1b* in mice is neonatally lethal with mutant mice dying within 24 hours after birth (194). Conversely, heterozygous loss of *Lmx1b* in mice does not cause a mutant phenotype indicating that the haploinsufficiency seen in NPS patients is not present in mice (194, 312). This points to a difference in dose sensitivity to *Lmx1b* expression in mice which may affect how good a model it is for studying LMX1B function and the impact of its lost expression.

In zebrafish, full knock-down of *lmx1b* is complicated by the presence of two paralogues for *lmx1b: lmx1ba* and *lmx1bb* (also known as *lmx1b.2* and *lmx1b.1,* respectively). This is due to a genome-wide duplication event which was thought to have occurred before the divergence of zebrafish, pufferfish, and medaka lineages (185, 313, 314). In other studies, genome editing tools have been used to make two knock-out zebrafish, with each targeting one of the paralogues (183, 315, 316), however, little work has been performed on these models and there is no characterisation of a full *lmx1b* knock-out of both paralogues in zebrafish. Instead, most studies in zebrafish have utilised morpholino's (short RNA constructs injected directly into the yolk of embryos at the single-cell stage) to temporarily knock-down *lmx1ba* or *lmx1bb* expression during early development (185, 188, 190, 214, 316). These models have been useful for demonstrating the expression pattern and role of both *lmx1b* paralogues in zebrafish which appear very similar to mammalian models (188). Given the neonatal lethality of mouse *Lmx1b* knock-out models and the lack of a full *lmx1b* knock-out zebrafish model, a stable *lmx1b* knock-out zebrafish line was generated here.

Using the *lmx1ba* and *lmx1bb* zebrafish knock-out lines, the role of each paralogue will be characterised and defined from development through to adulthood. Zebrafish have the advantage of developing externally from the mother. This means that even if the mutant lines show early lethality, as seen in mice carrying homozygous mutations for *Lmx1b,* the effect of this mutation on early development can still be analysed. Alongside these zebrafish models, the *LMX1B* knock-out HEK293T cell line would be useful to explore the role of LMX1B as a regulator of autophagy, and the effect of its loss on autophagy activity and

autophagy protein expression. In comparison to the zebrafish lines, this cell model could be used to explore the mechanistic action of LMX1B as an autophagy regulator and the genes that it helps to regulate.

4.2. Results

Development of an *LMX1B* knock-out cell line

4.2.1 Development of CRISPR-Cas9-GFP system and design of gRNAs

Previous data from the Lane lab has identified a role for the transcription factor LMX1B as a regulator of autophagy (180). Given the success and widespread use of the CRISPR-Cas9 system to mutate or knock-out genes, thereby removing their function, the development of an *LMX1B* knock-out cell model in HEK293T cells was attempted. For this, a modified version of the type II CRISPR nuclease system developed by Cong *et al.* was used, which can be used to modify mammalian cells. Within this system, the bacterial Cas9 nuclease (fused to GFP to allow for cell sorting) is co-expressed in cells alongside the gRNA following transfection (Figure 4.2.1A) (303).

A web tool for selecting potential target sites for CRISPR-Cas9, 'CHOPCHOP' (version 3) (317), was used to identify seven target sites in the human *LMX1B* gene (chromosome 9 from hg38/GRCh38 genome). Three target sites which showed the highest predicted gRNA efficiency, a G/C content between 65-70% and each targeted key domains within *LMX1B* were selected, designed, and sequenced *in vitro* by Eurofins Genomics (Figure 4.2.1B).

These gRNAs were then annealed and ligated into the SpCas9-2A-EGFP vector each and transfected into HEK293T cells (gRNAs termed O1, O2 and O3, respectively) (Figure 4.2.1C). CRISPR-Cas9-positive cells were selected based upon GFP-Cas9 fluorescence and sorted via FACS into 96-well plates, where one single cell colony was added to each well. These colonies were cultured and confluent colonies for each gRNA were selected and tested for LMX1B expression.

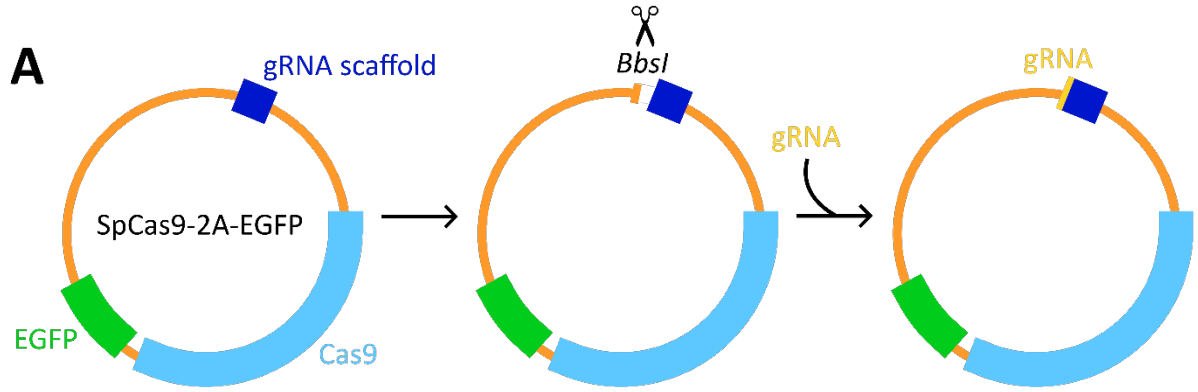

B

gRNA name	Target site seq.	Exon	Location in LMX1B	G/C content	gRNA efficiency
Oligo 1	CAACGAGTCGTCCTGGCACG	2	LIM1 domain	65%	60%
Oligo 2	CGCCCGCATCACGAACTCGG	3	LIM2 domain	70%	63%
Oligo 3	CACCGGAGTCGGACTCGTCG	3	Between LIM2 and homeobox domain	70%	64%

C

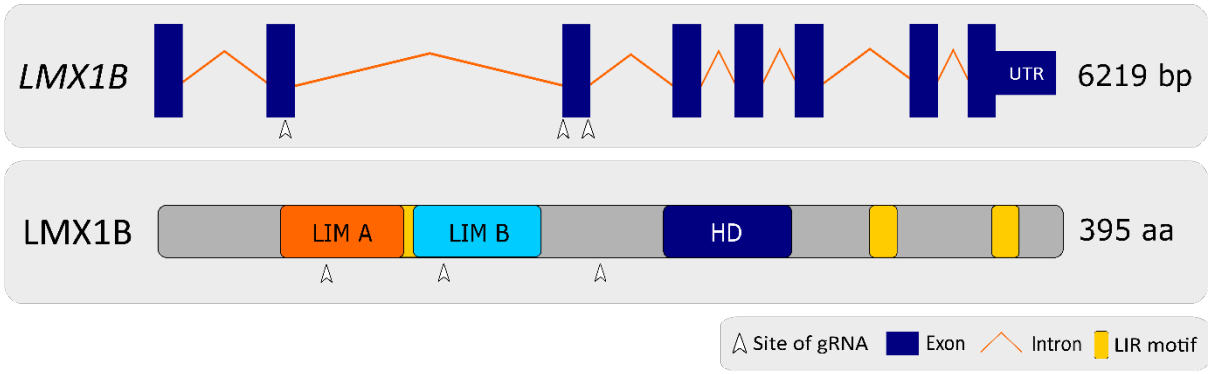

Figure 4.2.1 – Design and generation of gRNA constructs against *LMX1B* using SpCas9-eGFP vector, (A) Schematic depicting cloning steps performed to generate gRNA constructs for transfection into HEK293T cells. **(B)** Table showing three target site sequences selected for CRISPR-Cas9 modification. Table highlights G/C content of target sequences, predicted gRNA efficiency, and target location within *LMX1B* gene. **(C)** Simplified schematic of gene and protein structure of LMX1B in humans showing the exons and protein domains targeted by three selected gRNAs.

4.2.2 Validation of LMX1B expression in LMX1B knock-out HEK293T colonies

Immunoblotting and immunofluorescence was used to validate LMX1B expression within selected colonies. From 96 single cell colonies, between 6-9 confluent colonies were grown

up and selected for each gRNA. Analysis of LMX1B expression by immunoblot was inconclusive due to poor antibody availability (multiple non-specific bands around expected band size (~55kDa) were detected using two separate LMX1B antibodies) (Figure 4.2.2A). Instead, fixed cell immunofluorescence was used to determine CRISPR-Cas9 efficiency. In WT cells (i.e., cells transfected with empty SpCas9-eGFP vector) under basal conditions, LMX1B is localised to the nucleus as distinct puncta (Figure 4.2.2B, *left panel, top row*). Initially, some of the selected clones for each gRNA showed clear changes in LMX1B expression by immunofluorescence (30% of clones infected with O1 gRNA, 50% of clones infected with O2 gRNA and 25% of clones infected with O3 gRNA) (Figure 4.2.2B, *left*). In these clones LMX1B puncta number was decreased, and the puncta appeared more diffuse and cytosolic (non-nuclear) which is indicative of decreased LMX1B expression. However, when the immunofluorescence was repeated at a later date (7 days from first immunofluorescence staining), the location and number of LMX1B puncta had largely returned to WT conditions with LMX1B puncta more present in the nucleus compared to the cytoplasm (Figure 4.2.2B, *right*). Subsequent qRT-PCR analysis on three select clones, one for each gRNA, revealed that only one clone showed reduced LMX1B expression (O1G5; 52% of WT), whilst clones O2G5 and O3F5 showed almost normal LMX1B expression (O2G5, 83% of WT; O3F5, 81% of WT; Figure 4.2.2C). These data indicate that expression of LMX1B has been rescued within these cells, likely by clonal expansion of higher expressing cells within each colony, resulting in the death of LMX1B knock-out or knock-down cells and re-establishment of LMX1B expression. Therefore, these cell lines were not pursued further within this thesis.

Development of *lmx1b* knock-out zebrafish lines

4.2.3 Examining the structure and conservation of LMX1B orthologs in zebrafish

To study the role of *LMX1B* within a whole organism, a CRISPR-Cas9 *Lmx1b* knock-out zebrafish line was generated. As an important gene in early development, for patterning of embryos, and in neuronal development, *LMX1B* is strongly conserved across vertebrates, including mammals and fish. As mentioned in the introduction to this chapter, zebrafish contain two paralogues of *lmx1b*: *lmx1ba* and *lmx1bb* (185). Using multiple sequence alignment of human and zebrafish Lmx1b amino acid sequences, their sequence similarity

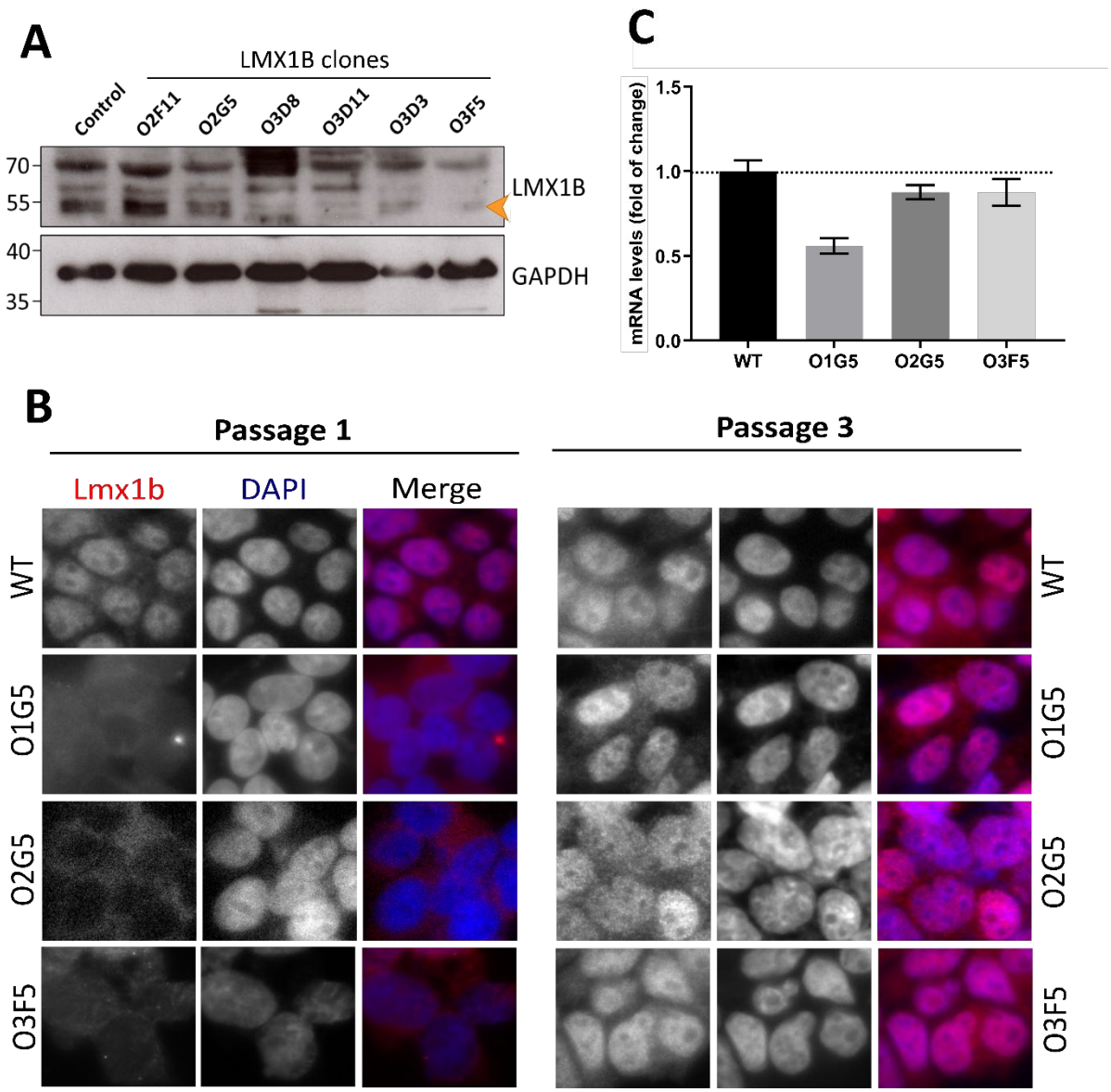

Figure 4.2.2 – Targeted knockdown of *LMX1B* in HEK293T cells using CRISPR-Cas9, (A) Representative immunoblot for LMX1B from CRISPR-Cas9-positive cell clone lysates, orange arrowhead indicates predicted size for LMX1B. GAPDH used as a loading control **(B)** Representative immunofluorescence images from fixed CRISPR cell clones labelling LMX1B (red) and counterstained with DAPI (blue). Images taken from same cells following first passage (left), and third passage (right). 'O1', etc., refers to oligo number; 'G5', etc., refers to well number clone was first grown in. **(C)** mRNA levels of LMX1B in selected CRISPR clones determined by qRT-PCR and normalised to GAPDH levels.

---

was compared, and the locations of key domains (LIM domains A and B and Homeobox domain) were identified (Figure 4.2.3). In zebrafish, the protein coding sequences for lmx1ba and lmx1bb are 20 amino acids (aa) shorter compared to the human protein (375 aa to 395 aa), but overall, they show high sequence similarity; 82% and 87% between human LMX1B

and lmx1ba, and lmx1bb, respectively. They also show full conservation of the homeodomain region which is the main functional DNA binding domain of the protein (Figure 4.2.3A and B). The two LIM domains which form the protein interacting regions, share 76% and 81% identity, respectively, whilst other functional domains such as LIR motifs also show high conversation (Figure 4.2.3B).

These results demonstrate that the protein sequence structure of LMX1B is highly conversed from humans to zebrafish, indicating conservation of function between the two species. Given the high similarity between the two zebrafish paralogues, *lmx1ba* and *lmx1bb* may be genetically redundant and share similar roles within the body. Therefore, a double knock-out of both *lmx1ba* and *lmx1bb* may be required to establish a zebrafish line with no functional lmx1b activity.

A

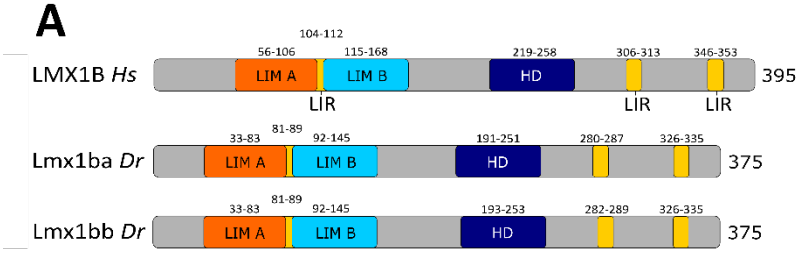

B

Domain	Seq. similarity
LIM A	76%
LIM B	81%
Homeobox	100%
LIR 1	88%
LIR 2	86%
LIR 3	100%

	Seq. similarity
LMX1B to Lmx1ba	82%
LMX1B to Lmx1bb	87%
Lmx1ba to Lmx1bb	84%

C

```
Hs LMX1B    sp|O60663-2      MDIATGPESLERCFPRGQTDCAKMLDGIKMEEHALRPGPATLGVLLGSDCP-HPAVCEGC  59
Dr Lmx1ba   NP_001349521.1   ----------------------MLDGIKIED-QFRTGAETLGVMLGADCAHHQSVCEGC  36
Dr Lmx1bb   NP_001020338.2   ----------------------MLDGIKIEDHPLRSGQATLGVMLGTECH-HQAVCEGC  36

Hs LMX1B    sp|O60663-2      QRPISDRFLMRVNESSWHEECLQCAACQQALTTSCYFRDRKLYCKQDYQQLFAAKCSGCM  119
Dr Lmx1ba   NP_001349521.1   HRPISDRFLLRMNDSSWHEECLQCSVCQQLLTMSCYSRDHKLYCKHDYQQLFATKCSGCL  96
Dr Lmx1bb   NP_001020338.2   QRPISDRFLMRVNESSWHEECLQCAVCQQPLTTSCYFRERKLYCKYDYQQLFATKCSGCL  96

Hs LMX1B    sp|O60663-2      EKIAPTEFVMRALECVYHLGCFCCCVCERQLRKGDEFVLKEGQLLCKGDYEKEKDLLSSV  179
Dr Lmx1ba   NP_001349521.1   EKISPTELVMRALESVYHLSCFCCCVCERRLCKGDEFVLKEGQLLCKTDYEREKDLA---  153
Dr Lmx1bb   NP_001020338.2   EKIAPTEFVMRALECVYHLNCFCCCVCDRQLRKGDEFVLKDGQLLCKSDYEREKDLLGSV  156

Hs LMX1B    sp|O60663-2      SPDESDSVKSEDEDGDMKPAKGQGSQSKGSGDDGKDPRRPKRPRTILTTQQRRAFKASFE  239
Dr Lmx1ba   NP_001349521.1   SPDLSDSDKSEDEDLDVKPEKGAGGQGKGS-DDSKDPRRPKRPRTILTTQQRRAFKASFE  212
Dr Lmx1bb   NP_001020338.2   SPDDSDSEKSEDEELDIKPEKGSGG--TGKGDDGKDPRRPKRPRTILTTQQRRAFKASFE  214

Hs LMX1B    sp|O60663-2      VSSKPCRKVRETLAAETGLSVRVVQVWFQNQRAKMKKLARRHQQQQEQQNSQRLGQEVLS  299
Dr Lmx1ba   NP_001349521.1   VSSKPCRKVRETLAAETGLSVRVVQVWFQNQRAKMKKLARRQQQQQEQQNSQRLGQDVMS  272
Dr Lmx1bb   NP_001020338.2   VSSKPCRKVRETLAAETGLSVRVVQVWFQNQRAKMKKLARRQQQQQEQQNSQRLGQEVMS  274

Hs LMX1B    sp|O60663-2      SRMEGMMASYTPLAPPQQQIVAMEQSPYGSSDPFQQGLTPPQMPG-------NDSIFHDI  352
Dr Lmx1ba   NP_001349521.1   SRMENLMSSYTPLAPPPPHALVSMESSGYSTDPFQQGLTPPQMPGDHMNPYGNDSIFHDI  332
Dr Lmx1bb   NP_001020338.2   NRMEGMMNSYTPLAPAQQQMVALENG--YSTDPFQQGLTPPQMPGDHMNPYGNDSIFHDI  332

Hs LMX1B    sp|O60663-2      DSDTSLTSLSDCFLGSSDVGSLQARVGNPIDRLYSMQSSYFAS                  395
Dr Lmx1ba   NP_001349521.1   DSDTSLTSLSDCFMSASDAAALQSRVGNPIDRLYSMQSSYFTS                  375
Dr Lmx1bb   NP_001020338.2   DSDTSLTSLSDCFMASSDAGSMQARVGNPIDRLYSMQSSYFAS                  375
```

Figure 4.2.3 – Protein structure of LMX1B is highly conserved from humans and zebrafish and shows high sequence similarity, (A) Simplified schematic depicting protein structure of human (*Hs*) and zebrafish (*Dr*) LMX1B, highlighting location of key domains. Numbers indicate amino acid position of each domain (HD, homeobox domain). **(B)** Percentage amino acid sequence similarity of LMX1B orthologs comparing full protein sequences and key domains between humans and zebrafish. **(C)** Multiple amino acid sequence alignment of LMX1B from humans and zebrafish using Clustal Omega (EMBL-EBI). Colours correlate with (A) and indicate location of key domains (LIM A, LIM B and HD). Green indicates sequence similarity; black line indicates sequence divergence and numbers show amino acid position. Relevant accession numbers for each sequence shown; Hs = *Homo sapiens*; Dr = *Danio rerio*.

4.2.4 Design of gRNAs and injection into zebrafish embryos

For the design and selection of gRNAs against *lmx1ba* and *lmx1bb,* two different web tools were used; CHOPCHOP and CRISPRscan (230). This was done to allow for the comparison of predicted gRNA efficiencies, as each tool utilises a different algorithm to score potential gRNA sequences. Therefore, where possible, gRNAs with equally high predicted efficiencies across the two programs were chosen to maximise the probability of genome editing success. Predicted efficiencies were rated as: ideal = 70-80%; good = 60-70%; average = 50-60%; poor = <50%.

As above, gRNAs which showed the highest predicted gRNA efficiency, a good G/C content and which targeted key domains, were selected for against the *lmx1ba* and *lmx1bb* genes (chromosome 5 and 8, respectively, using the GRCz11/danRer11 genome assembly). In the majority of patients with Nail-patella syndrome (NPS), mutations within LMX1B are concentrated within the two LIM domains (present in exons 2 and 3) and in the homeodomain, encoded by exons 4-6 (181, 211, 318-321). To date, no NPS patients with mutations in exons 7 or 8 have been found indicating that mutations in these exons do not lead to an NPS phenotype (322). Therefore, only gRNAs targeting regions in exons 1-6 were selected for and tested.

Overall, seven gRNAs were selected, designed, and synthesised *in vitro* by Merck (Sigma); O5, O6 and O7 for *lmx1ba* and O123 (formed of three gRNAs injected together) and O4 for *lmx1bb* (Figure 4.2.4A). Due to the close target proximity of gRNAs O1, O2 and O3, these were selected to be injected together as this has been shown to help increase overall gRNA efficiency (323). Each gRNA, or gRNA group targets a different exon and protein-coding

domain within each gene, increasing the likelihood of at least one gRNA causing a loss of function mutation (Figure 4.2.4B).

For CRISPR-Cas9 editing, the 'crRNA: tracrRNA two-part system' by Merck was utilised. Here, crRNA (CRISPR RNA) refers to a 20 nucleotide sequence which is complementary to the target DNA which, in this thesis is termed gRNA. Meanwhile, the tracrRNA (trans-activating crRNA) forms the binding scaffold for the Cas9 nuclease protein. The gRNA and trans-activating crRNA (tracrRNA) were synthesised separately *in vitro* and injected together with the Cas9 protein, phenol red and TE buffer into zebrafish embryos at the single cell stage (Figure 4.2.4C). Direct injection of Cas9 protein has been shown to induce a greater number of genome modifications compared to the injection of Cas9 mRNA (324, 325). This is likely due to the increased speed of complex assembly and function as translation of the Cas9 protein is not required. Phenol red was used within the injection mix as this is a coloured dye which can remain within injected cells for up to 24hpf. Therefore, it was used as a marker for successful cell injection, with red-positive embryos being selected for either gRNA validation by fragment analysis or grown into adults as part of the founder populations for *lmx1ba* and *lmx1bb* (Figure 4.2.4C).

4.2.5 Identification of CRISPR-positive fish within generation zero (G0)

The gRNA efficiency following single-cell injection was determined by fragment analysis whereby the frequency of mutated genomic forms of *lmx1ba* or *lmx1bb,* which have either lost or gained nucleotides due to CRISPR-Cas9 mutagenesis, is measured per larvae. A single peak indicates no mutation or wild-type gene sequence, as all transcript copies are of the same length (Figure 4.2.5B, *top graph*). Whereas multiple smaller peaks indicate successful CRISPR-Cas9 activity as multiple transcript copies have been mutated and lost or gained nucleotides, changing their length (Figure 4.2.5B, *bottom graphs*). Of the five gRNAs injected, three showed high CRISPR-Cas9 activity and overall good efficiency (O123, O4 and O7; 83%, 100% and 80%, respectively) whilst the remaining two gRNAs showed no CRISPR-Cas9 activity (O5 and O6; 0% each) (Figure 4.2.5C). These results are largely in line with the predicted gRNA efficiencies in Figure 4.2.4A, as the gRNAs with the lowest average predicted efficiency score performed less well compared to those that were rated higher. This supports the use of these online tools to select gRNAs and the reliability of the

A

gRNA name	Target site sequence (gRNA)	Exon	Location in *lmx1b*	G/C content	Predicted efficiency (CRISPRscan)	Predicted efficiency (CHOPCHOP)
		lmx1ba				
O5	GAACGACAGCTCGTGGCATG	2	LIM A domain	50%	56%	61%
O6	AGCCCAGACCTCTCCGACTC	3	After LIM B domain	55%	56%	48%
O7	CGGTTTGGACGAGACCTCGA	4	Homebox domain	53%	71%	66%
		lmx1bb				
O1	GATGGCACTCCGTCCCTGAA	3	LIM A domain	39%	65%	67%
O2	GACGGAGTGCCATCACCAGG	3	LIM A domain	39%	72%	71%
O3	AGCGGTCGGATATCGGCCGC	3	LIM A domain	39%	61%	51%
O4	AGGCTCGGGAGGCACCGGGA	5	After LIM B domain	48%	82%	50%

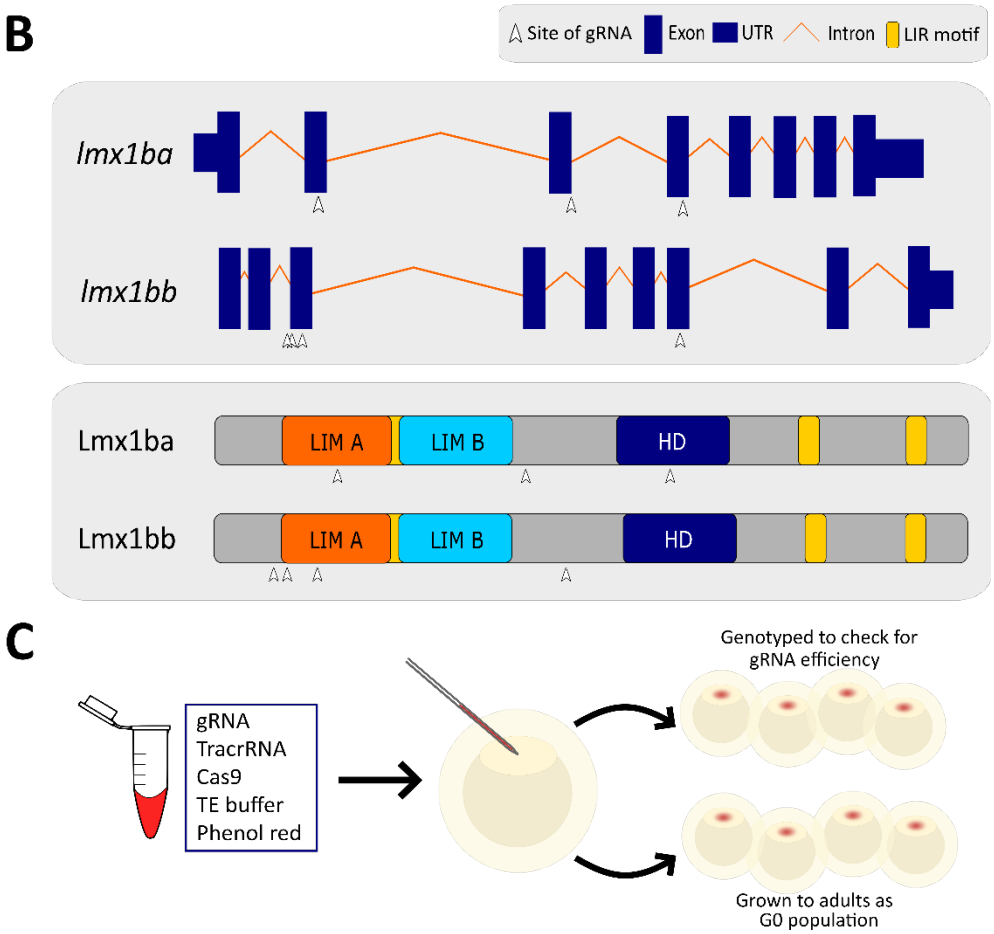

Figure 4.2.4 – Design and generation of gRNAs for the targeted mutation of *lmx1ba* and *lmx1bb* in zebrafish, (A) Table showing seven target site sequences selected for CRISPR-Cas9 modification. Table highlights G/C content of target sequences, predicted gRNA efficiencies, and location within *lmx1ba* and *lmx1bb* genes. **(B)** Schematic indicating exon and protein domains targeted by gRNAs in *lmx1ba* and *lmx1bb*. **(C)** Schematic showing the components within the gRNA injection solution and the injection site location within single-cell zebrafish zygotes and steps following successful injection (indicated in zygotes as presence of red dye in cell).

efficiency scores they generate. Therefore, larvae injected with gRNAs O123 and O4, and O7 showing mutations in *lmx1bb* and *lmx1ba,* respectively, were grown to adulthood to form the first generation (G0) populations of *lmx1ba* and *lmx1bb* knock-out fish.

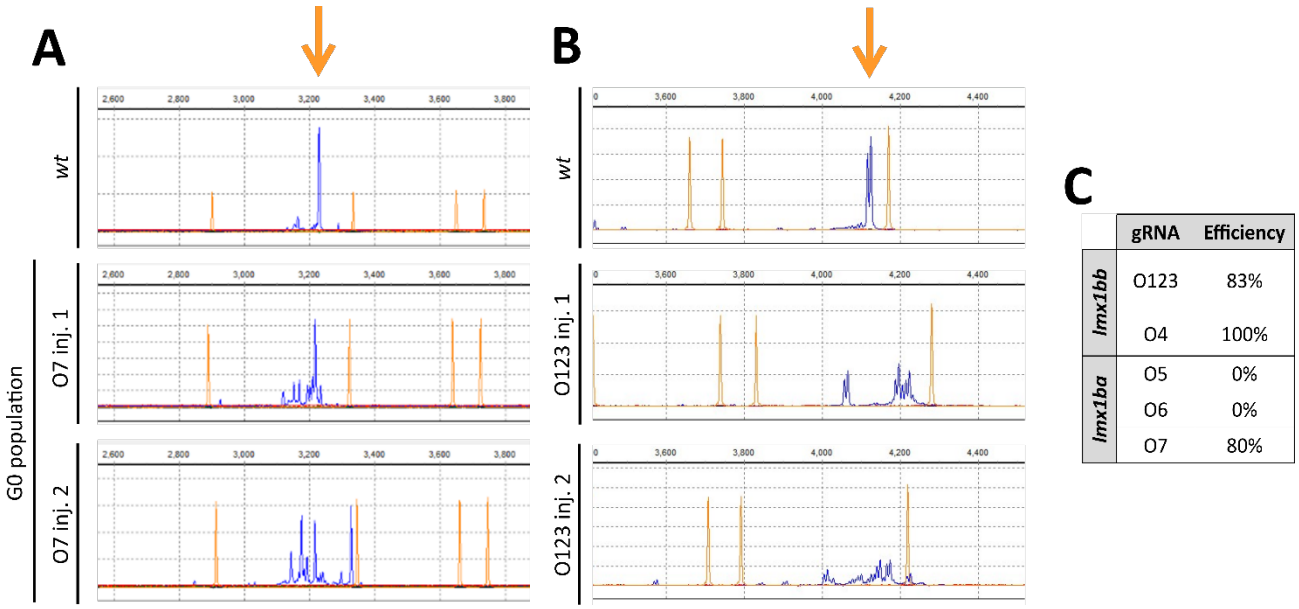

Figure 4.2.5 – Three gRNAs cause genetic mutations in *lmx1ba* and *lmx1bb* genes, (A) Representative fragment analysis charts showing positive mutant readings following injection with O7 gRNA and **(B)** O123 gRNA (inj. = injected zygote). Top graphs show single *wt lmx1ba* or *lmx1bb* fragment peaks at ~3225 bp and ~4175 bp, respectively, as indicated by orange arrows. Bottom two graphs show multiple fragment peaks ~3200 bp and ~4200 bp indicating mosaic gene expression. G0 = Generation zero. **(C)** Table showing gRNA efficiency following injection. Percentages calculated as proportion of CRISPR-Cas9 mutated fish per 20 fish genotyped by fragment analysis per gRNA.

4.2.6 Identification of mutations in lmx1ba and lmx1bb in G1 populations

Following on from the establishment of the G0 populations, three individual adult fish from two of the G0 populations (O7 and O123) were selected and outcrossed to wild-type fish to create heterozygous G1 populations (Figure 4.2.6A, *G0-G1 stage*). These populations were termed, O7.1, O7.2 and O7.3; O123.A, O123.B and O123.C for *lmx1ba* and *lmx1bb,* respectively. Performing an out-cross to wild-type (*wt*) at this stage reveals whether germline transmission of the genetic modifications has occurred, whilst also allowing for the isolation of the exact mutations within individual fish forming the G1 population. To identify the specific genetic modifications caused by CRISPR-Cas9 in *lmx1ba* and *lmx1bb*

respectively, Sanger sequencing was performed on DNA extracted from G1 adults. Here, CRISPR-Cas9-positive adults can be identified by a double set of DNA traces starting from the gRNA target sequence site (Figure 4.2.6B, *orange arrows*). Two DNA traces indicates a heterozygous genotype, where one allele shows the *wt* gene sequence and the other a mutated form. By comparing the two sequences to the *wt* sequence, the mutant sequence for each fish was elucidated. A variety of mutations in *lmx1ba* or *lmx1bb* were observed within the G1 populations as expected from the heterogenic or mosaic cell expression of either gene in the G0 populations. Mutations which would cause a frame shift in the codon sequence and result in a premature stop codon as homozygous mutants were selected for. For each gene, two different mutant sequences were selected from two G1 populations each: fish from O7.2 and O7.3 for *lmx1ba*, and fish from O123.A and B for *lmx1bb* (Figure 4.2.6A, *orange boxes at G1 stage*). Fish carrying the same heterozygous mutation were in-crossed to create the G2 populations (Figure 4.2.6A, *G1-G2 stage*).

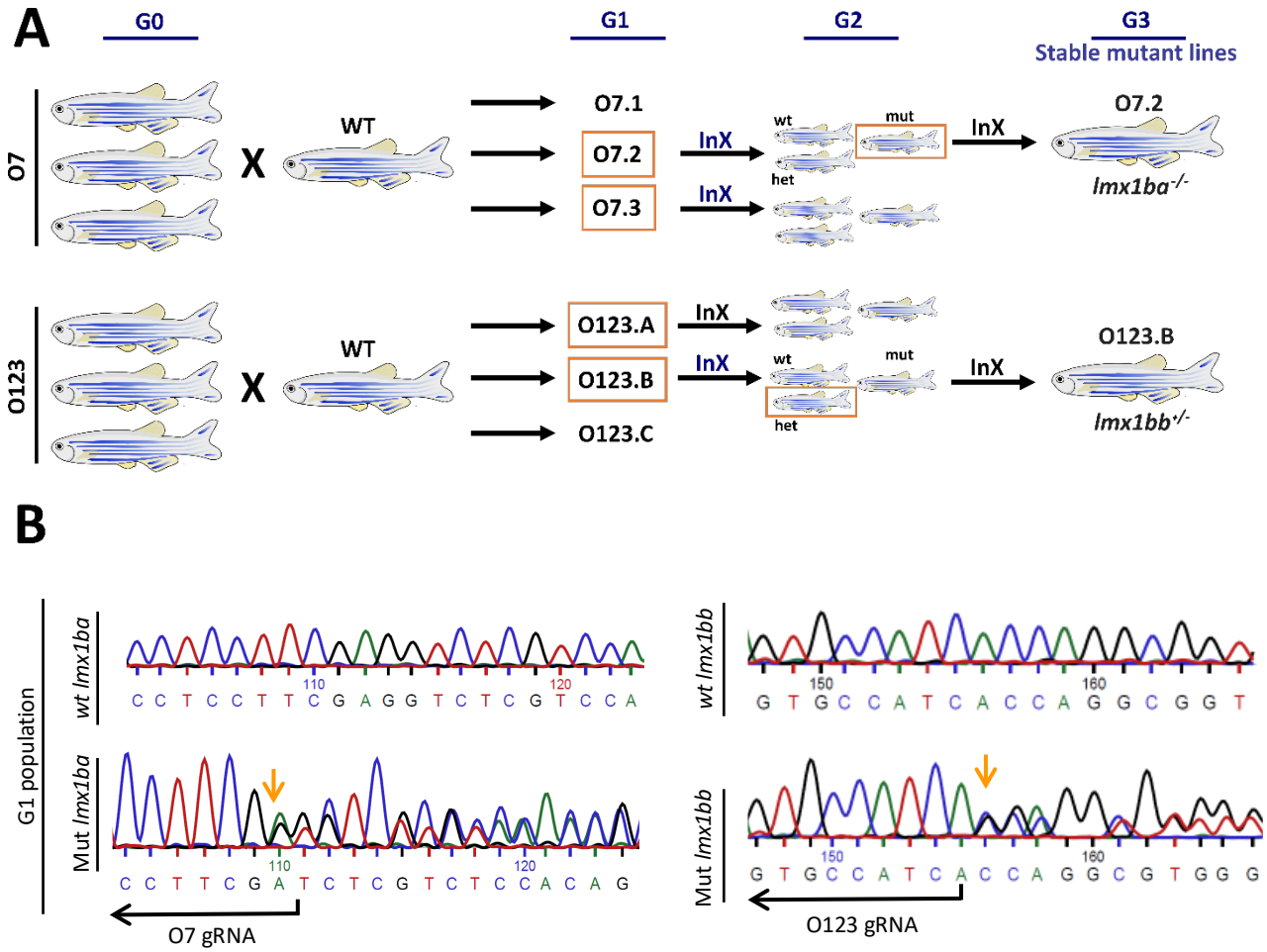

Figure 4.2.6 – Heterozygous mutations in *lmx1ba* and *lmx1bb* genes identified in G1 populations, (A) Schematic demonstrating the steps involved in creating G0 populations to G3 stable mutant lines. Orange boxes indicate the G1 and G2 populations selected at each stage. G = generation; InX = in-cross. **(B)** Representative *wt* and heterozygous mutant DNA traces from Sanger sequencing of DNA from G1 populations of *lmx1ba* and lmx1bb-CRISPR zebrafish**.** Orange arrows show mutation start site, black arrows show target site of gRNA.

4.2.7 Generation of stable lmx1ba and lmx1bb knock-out zebrafish lines

Following a heterozygous in-cross of G1 population adults, Sanger sequencing on whole larvae was used to identify the presence of *wt*, heterozygous mutants and homozygous mutants in each population (Figure 4.2.7A). Due to reduced germline transmission of the O7.3 *lmx1ba* mutation and an issue with sequencing the O123.A *lmx1bb* mutant sequence, it was decided that only fish from the O7.2 and O123.B populations would be carried forward for further investigation.

Based on the *wt* and heterozygous sequences obtained from the G1 populations, the homozygous mutant sequences for *lmx1ba* and *lmx1bb* were predicted and then verified by Sanger sequencing of the G2 populations (Figure 4.2.7B). Restriction sites either created or lost by the CRISPR-Cas9 mutations were also identified in the homozygous mutant sequences and were utilised to genotype the G2 populations (Figure 4.2.7C). Thus, the *lmx1ba* homozygous mutants (*lmx1ba*$^{-/-}$) have a 19 nucleotide insertion which results in a premature stop codon 27 nucleotides from the insertion start site. They also show loss of a *BsaI* restriction site which results in no restriction digestion when treated with *BsaI* and a single band at ~300 bp when run on a DNA electrophoresis gel (Figure 4.2.7C, *left*). Meanwhile, the *lmx1bb* mutants have a 7 nucleotide deletion which also results in a premature stop codon just 13 nucleotides downstream of the deletion start site. The mutant *lmx1bb* sequence also shows insertion of the *DraIII* restriction site which when cut results in two distinct bands at ~275 and ~225 bp (Figure 4.2.7C, *right*). Therefore, moving forward, restriction digest of PCR products for *lmx1ba* and *lmx1bb* will be used to genotype these lines and identify heterozygous and homozygous mutant fish in each population.

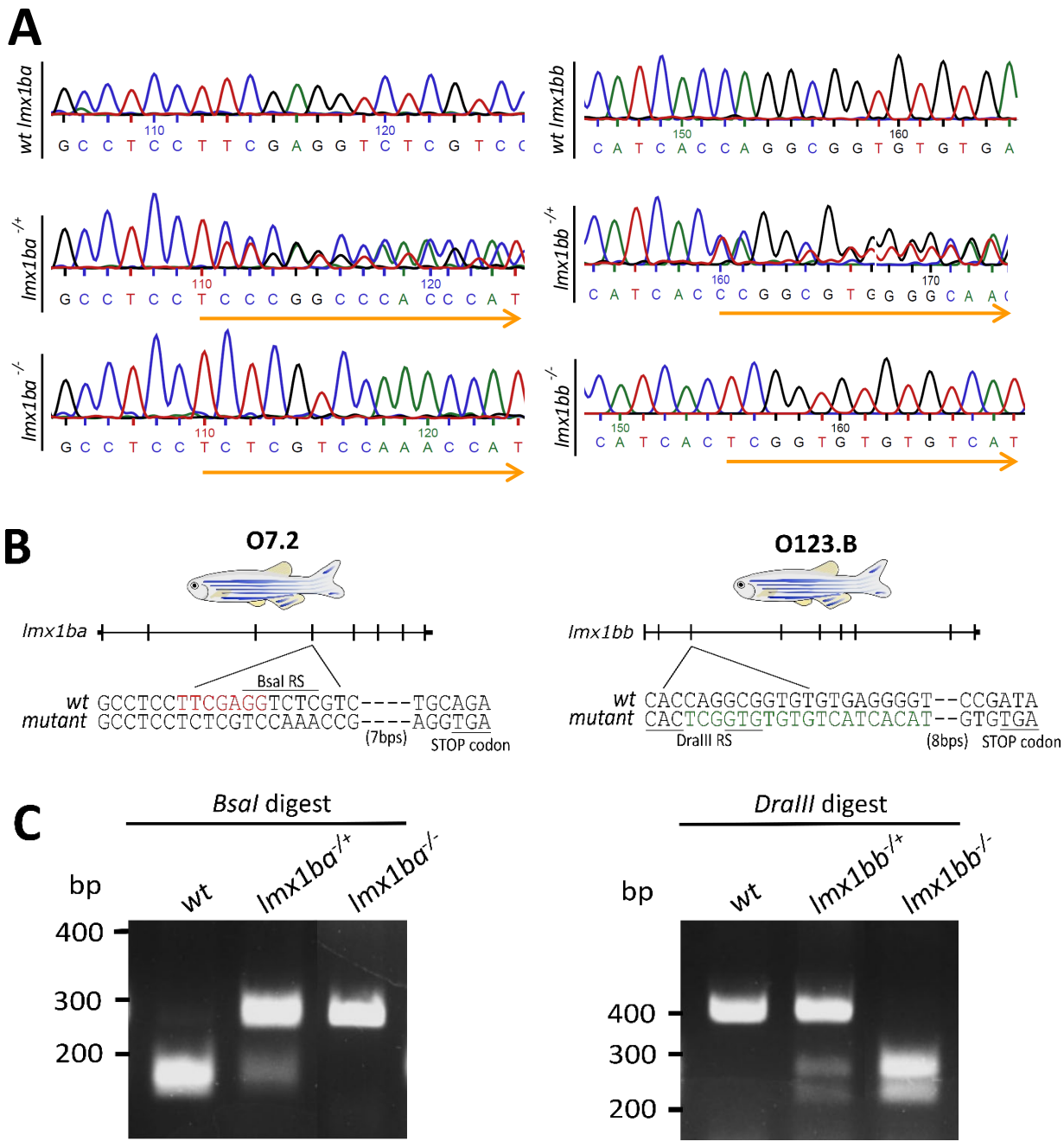

Figure 4.2.7 – *lmx1ba* and *lmx1bb* null fish lines generated using CRISPR-Cas9, (A) Representative *wt*, heterozygous and homozygous DNA traces of *lmx1ba* and *lmx1bb* from Sanger sequencing of DNA from G2 population larvae**.** Beginning of mutated sequences highlighted by orange arrow. **(B)** Schematic showing exon position of selected mutations in both O7.2 and O123.B populations, with resulting nucleotide deletion or insertion depicted in red and green, respectively, and position of stop codon highlighted. Location and sequence of restriction sites used to genotype each population highlighted. RS, restriction site. **(C)** Example gel images of restriction digest of O7.2 and O123.B DNA with *BsaI* and *DraIII* restriction enzymes, respectively, to separate genotypes of each population.

4.2.8 Mutants show differences in survival beyond early development

Following the successful identification of homozygous mutants within the O7.2 and O123B lines, the remaining larvae for each population were grown up to be genotyped as adults. At 3mpf, the two lines were genotyped using DNA extracted from adult fin clips. It was found that whilst the *lmx1ba* mutant line showed the expected Mendelian ratio of *wt*, heterozygote and homozygote mutants, the *lmx1bb* mutant line showed only the presence of heterozygote mutants and *wt*.

To investigate this, the survival of each line was monitored from 1dpf (Figure 4.2.8). As expected, due to their largely normal development into adults, the *lmx1ba* mutants showed no difference in lethality compared to *wt*. However, the *lmx1bb* mutants could not survive beyond larval stages, with all larvae dying by 13dpf. Therefore, *lmx1bb*, but not *lmx1ba,* is required for zebrafish survival, indicating that *lmx1bb* has greater functional significance compared to *lmx1ba*. Following these results, a stable *lmx1ba* homozygous mutant line and a stable *lmx1bb* heterozygous mutant line were generated and established. Therefore, the *lmx1ba* mutants were studied as larvae and adults, and *lmx1bb* mutants as larvae only.

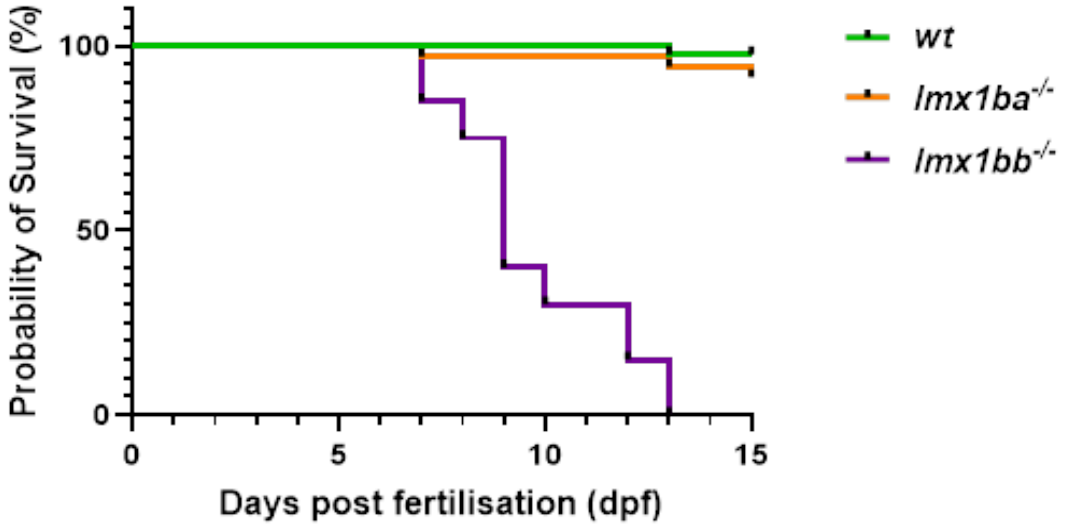

Figure 4.2.8 – *lmx1bb* homozygous fish do not survive beyond larval stages, Graph showing survival rate of the *lmx1ba* and *lmx1bb* homozygote populations compared to *wt*, recorded until 15dpf. For *wt* and *lmx1ba* mutants, n = 44; for *lmx1bb* mutants, n = 20.

4.2.9 Generation of full lmx1b knock-out fish

Once stable *lmx1ba* and *lmx1bb* mutant lines were established, these lines were crossed to try and generate full *lmx1b* knock-out fish (Figure 4.2.9A). As the *lmx1bb* homozygous mutants cannot survive beyond larval stages, it was clear that *lmx1b* knock-out fish would not survive to adulthood. Instead, a stable *lmx1ba*$^{-/-}$;*lmx1bb*$^{-/+}$ line (termed KO;Het) was generated. Firstly, the *lmx1ba* homozygous and *lmx1bb* heterozygous lines were crossed to generate *lmx1ba*$^{-/+}$;*lmx1bb*$^{-/+}$ fish (termed dHet for double heterozygous; Figure 4.2.9A, *orange box at G4 stage*). Unfortunately, once these fish had reached sexually maturity by around 3mpf, the entire population was male, so these were out-crossed with *lmx1ba* homozygous mutants. This allowed for the generation of the *lmx1ba*$^{-/-}$;*lmx1bb*$^{-/+}$ line (KO;Het), which survived to adulthood and were in-crossed to create mutants homozygous for both *lmx1ba* and *lmx1bb* (*lmx1ba*$^{-/-}$;*lmx1bb*$^{-/-}$, Figure 4.2.9, *blue box at G6 stage*). These *lmx1b* knock-out fish (termed dKO for double knock-out), were followed as larvae. As expected, they did not survive beyond larval stages and died by 10dpf (Figure 4.2.9B, *pink line*).

Following the successful establishment of two single mutant *lmx1b* lines and dKO *lmx1b* larvae, in the next results chapter, Chapter 5, these lines will be investigated further to characterise the effect of loss of *lmx1b* on zebrafish development, focussing especially on any effects to the skeletal system.

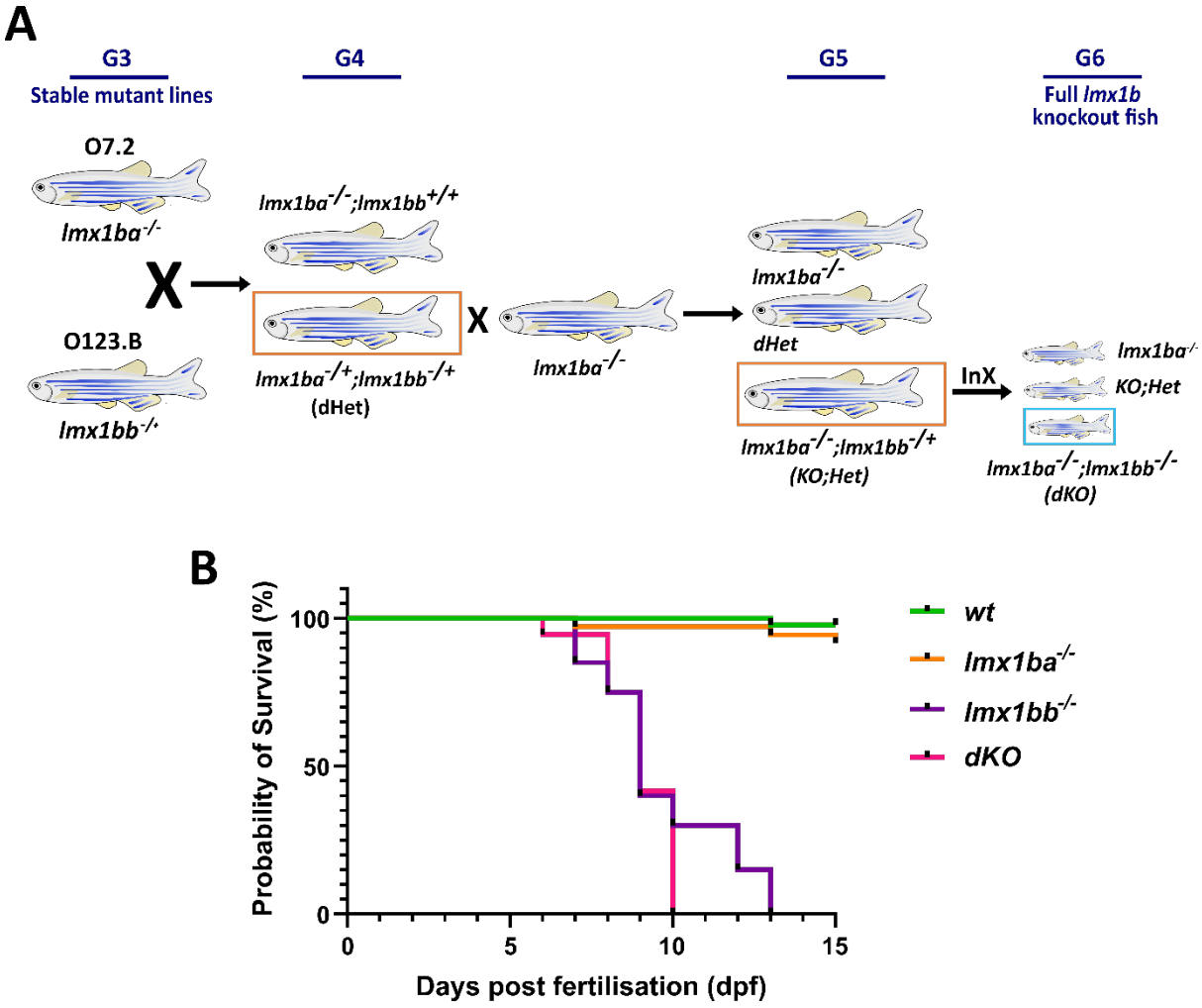

Figure 4.2.9 – Generation of full *lmx1b* knockout fish, (A) Schematic showing the generation steps involved to create fish homozygous for both *lmx1ba* and *lmx1bb* (dKO; blue box). Orange boxes indicate genotype selected to cross for next stage; G = generation; InX = in-cross. **(B)** Graph showing survival rate of dKO fish compared to *lmx1ba* and *lmx1bb* homozygote fish and *wt.* Survival recorded until 15dpf. For *wt* and *lmx1ba* mutants, n = 44; for *lmx1bb* mutants, n = 20; for dKO mutants, n = 36.

4.3. Discussion

In this chapter, CRISPR-Cas9 technology was used to generate two *LMX1B* knock-out models, in human cells and zebrafish. Although a stable *LMX1B* knock-out cell line could not be generated, greater success was seen in the *lmx1b* zebrafish models as two mutant *lmx1ba* and *lmx1bb* lines were generated and their separate mutations characterised by Sanger sequencing.

It has been established that complete loss of *Lmx1b* is neonatally lethal in mice, which is also thought to be the case in humans as the genotype is yet to be described (194). Similarly, through this work, it was found that *LMX1B* is required for HEK293T cell survival. Following transfection with CRISPR-Cas9, Cas9-eGFP-positive clones survived and were able to grow into confluent colonies. Through immunofluorescent staining of these colonies, it was found that some showed decreased LMX1B expression compared to WT. The expression of LMX1B was also altered in these clones, with LMX1B being expressed largely in the cytosol compared to its more usual nuclear location. However, despite these initial observations, these same cells showed increased LMX1B expression over subsequent passages and a return of LMX1B expression to the nucleus. These results were further confirmed by qRT-PCR which showed minimal loss of LMX1B in all but one clone, which showed 52% *LMX1B* expression compared to WT.

This loss and then increase in expression is indicative of clonal expansion whereby the colony is taken over by cells expressing higher levels of LMX1B. This indicates that LMX1B is vital to cell function and that without it, cells have a growth disadvantage and are less likely to survive. Given that CRISPR-Cas mutagenesis is irreversible, cells with mutations to *LMX1B* and potential loss of its expression would not be able to regain it. However, clonal expansion and takeover could have occurred if errors were made when sorting colonies into single cells. As single cell sorting is determined by cell size, it is possible that two small cells together or two cells attached longitudinally could be incorrectly counted as a single cell.

Therefore, if one of these cells had higher or WT LMX1B expression, it would be able to out-compete its neighbour's daughter cells. However, filtering of the cells using a cell strainer was performed before FACS to help remove cell clumps and ensure a single-cell suspension. Addition of EDTA to the FACS sorting buffer was also done to minimize cell stickiness, and single cell gates on the FACS machine were used to regulate droplet size to only a single cell. Therefore, steps were taken to minimize the risk of this happening and although still possible, it seems unlikely that multiple cells could have been incorrectly sorted for all the clones that were tested.

Alternatively, CRISPR-Cas9 efficiency could have been affected by the heterogenous karyotype of HEK293 cells (326). The HEK293 cell line, and its derivatives, including HEK293T, are considered to be pseudotriploid (327). This means that most cells have three sets of chromosomes although the chromosomal number, organisation and arrangement are altered from the normal human karyotype (326). HEK293 lines have also been shown to have a high copy number variation, which is where the number of gene copies varies from line to line, and even, cell to cell (326, 328). Therefore, it could be possible that the HEK293T cells used here have multiple copies of the *LMX1B* gene and that the CRISPR-Cas9 system was unable to cut all copies of the *LMX1B* gene in each cell. Additionally, it is possible that the impact of the CRISPR-Cas9 induced mutations may have differed across the copies, resulting in a loss of function to some copies but not others. In either scenario, these cells could have upregulated expression of the remaining *LMX1B* genes, to promote survival, resulting in an increase in expression over time. This hypothesis may also help explain why these cells were able to survive initially and showed some LMX1B expression via immunofluorescence. Any cells with full loss of *LMX1B* may have failed to divide and survive as single clones which could be possible given the low survival rate of the clones for each gRNA (~9% for gRNA 1, ~7% for gRNA 2 and ~6% for gRNA 3). To explore this further, CRISPR-editing of *LMX1B* could be performed in alternative cell lines with more stable karyotypes, such as HeLa cells or RPE cells. By monitoring the efficiency and stability of any of these knock-out cell lines, the effect of the variable karyotype of HEK293T cells on CRISPR-editing could be examined.

To overcome these obstacles, an alternative CRISPR-Cas system could be selected to improve CRISPR-Cas9 efficiency whilst maintaining cell survival. To this end, the Lane lab are currently developing an inducible CRISPRi *LMX1B* cell line where the expression of the *LMX1B* gene can be inhibited at will by addition of doxycycline through a doxycycline-induced Tet system. This system utilises a catalytically dead Cas9 enzyme (dCas9) which, in the presence of doxycycline, can bind to the target DNA sequence but instead of cutting, simply remains bound to the target DNA (329). Thus, binding of RNA polymerase or transcription factors is disrupted leading to gene repression without any alteration to the genomic sequence. As this system allows for the expression of LMX1B to be restored, this would help ensure cell survival thereby allowing a stable line to be maintained and used for multiple experiments.

Similar to the HEK293T cell model results, development of the *lmx1b* knock-out lines in zebrafish showed that *lmx1bb*, but not *lmx1ba*, is required for zebrafish survival. The homozygous *lmx1bb* mutants died by 13dpf, however, the *lmx1ba* homozygous mutants did not show larval lethality and were able to survive until adulthood with a survival rate comparative to *wt*. This demonstrates some divergence in the function of each paralogue and suggests that *lmx1bb* may be the predominantly expressed paralogue.

Compared to the survival of the *lmx1ba* mutants, the lethality of the *lmx1bb* mutants matches much more closely with the *Lmx1b* knock-out mice which are neonatally lethal. *Lmx1bb* also shows higher sequence similarity to human LMX1B compared to *lmx1ba* (87% compared to 82%), including within the functional LIM A and B domains. Therefore, taken together, these results may suggest that *lmx1ba* has a redundant gene function. This is most commonly the case for duplicated genes, where the outcome for one paralogue is loss-of-function (330). However, in some cases both copies are retained, and neo-functionalisation (one paralogue develops a new gene function) or sub-functionalisation (splitting of current gene function between the paralogues) can occur (331). In the next chapter, phenotypic comparison of the *lmx1ba* and *lmx1bb* lines will be useful for determining this and showing whether there are any differences in paralogue expression and function. From this, it can be ascertained whether *lmx1ba* carries any different functions to *lmx1bb* or is indeed a redundant gene. However, from the initial results of the *dKO* line, which have an earlier lethality compared

to the *lmx1bb* mutants (dying at 10dpf compared to 13dfp), this would suggest that *lmx1ba* does have a role during early development. This will be explored further in the following chapter.

When analysing the phenotype of these lines, it will be important to consider the risk of off-target effects which may influence the phenotype and therefore affect its reliability as a model for *lmx1b* knock-down. For the generation of the *lmx1ba* and *lmx1bb* knock-out zebrafish lines, microinjection of ribonucleoproteins (RNP) into the cell nucleus was performed. This approach was selected as it has been shown to have the highest editing efficiency in zebrafish (332). RNPs have been shown to be less stressful for cells and have decreased off-target effects compared to other delivery methods (333, 334). This is because RNPs can assemble quickly and cleave DNA very soon after delivery (335). They are also degraded rapidly by the cell, reducing the risk of off-target binding and cleavage (333). This is aided by microinjection, which helps ensure a controlled delivery of RNPs into the cell, reducing the risk of off-target effects due to excess Cas9 expression and activity (334). gRNAs with low predicted off-target effects (identified using CHOPCHOP) were also selected. Therefore, several steps were taken to minimize the risk of off-target effects. Moving forward in the next chapter, comparison of these models to current murine knock-out and zebrafish knock-down models will be useful for confirming their reliability and potential use as models for NPS.

After the generation of these lines, further in-crossing was performed to generate double knock-out fish which show frameshift mutations and premature stop codons in both *lmx1b* paralogues. As expected, given the lethality of the *lmx1bb* knock-out, these double *lmx1b* mutants did not survive beyond larval stages, dying by 10dpf. Despite this low survivability, the double mutant fish remains a useful *lmx1b* knock-out model as the effect of loss of *lmx1b* on full body development, including on skeletal, renal and brain formation, can be observed. Something which cannot currently be achieved in any other *Lmx1b* knock-out model.

Following the successful generation of three *lmx1b* zebrafish models in this chapter, the succeeding chapter will utilize these lines to explore the role of *lmx1b* and its two paralogues in skeletal development and autophagy activity, and as a potential model for NPS.

Chapter 5. Investigating the role of *lmx1b* in musculoskeletal and neuronal development in zebrafish

At a glance…

In the final chapter of results, the lmx1b mutant zebrafish lines are characterised and the effect of these mutations on zebrafish development and behaviour is explored. Initially, the focus of the chapter is on the individual phenotypes of each line, looking at the effect of loss of lmx1bb on kidney development; of lmx1ba on skeletal and neuronal development, and then the consequences of these effects as adults. Finally, the phenotype of the lmx1b mutants is investigated, concentrating on the musculoskeletal phenotype of this mutant.

CHAPTER

5

Investigating the role of *lmx1b* in musculoskeletal and neuronal development in zebrafish

Initially, this project aimed to understand if the effects of loss of *lmx1b* on neuronal, renal, and skeletal development are linked to its role as a regulator of autophagy and by consequence, autophagy dysregulation. Unfortunately, this could not be achieved due to constraints of time and reagent and antibody availability. Delays to the delivery of reagents, such as antibodies and qRT-PCR primers, and a reduction in access to microscopy facilities due to the COVID-19 pandemic also hindered the progression of experiments. Therefore, the focus of this chapter is on the characterisation of the *lmx1b* zebrafish lines as a potential model for NPS, and the contribution *lmx1b* makes to the formation and maintenance of the musculoskeletal system. The contribution of colleagues for specific techniques shown in this chapter are highlighted in the figure legends where appropriate.

5.1. Introduction

During development, LMX1B has been shown to play an important role in the formation and specification of several cell types across a diverse range of tissues. Animal studies have

shown that expression of Lmx1b is present in the limbs, eyes, kidneys, brain and spinal cord, and that loss of *Lmx1b* significantly affects the formation and function of these structures (183, 185, 186, 188, 189). These data correlate well with the phenotype observed in patients with NPS (209). Indeed, it was through the comparison of *Lmx1b* knock-out mice to the NPS phenotype that *LMX1B* was discovered to be the causative gene behind NPS (336). This chapter will characterise the phenotypes of the three mutant *lmx1b* lines, looking at the key organs where *lmx1b* is known to be important during development: the skeletal system, the brain, and the kidneys. Additionally, data are presented that suggest a potential new role for *lmx1b* in muscle formation.

As described in Section 1.5.2 of Chapter 1, a clear role for *LMX1B* in limb dorsalisation has already been identified. The most common skeletal abnormalities found in NPS patients, such as nail dysplasia, hypoplastic patellae and pelvic iliac horns, can be linked to this loss of dorsal patterning in the limbs. However, other skeletal defects, such as scoliosis of the spine, spinal fusions, and premature OA, have also been identified in NPS patients (209), which may have a primary cause beyond defective dorsal body patterning. Alongside this, homozygous *Lmx1b* mutant mice show abnormalities in skull formation with reductions in calvaria bone size (bones forming top part of skull) and abnormal suture formation between these bones (337). Together these findings highlight roles for *LMX1B* in skeletal development that are beyond regulating limb dorsalisation and indicate a potential consequence for defective *LMX1B* activity in adult skeletal maintenance.

In mammals, both foetal and adult kidneys show high expression of LMX1B (42). In particular, this expression is primarily restricted to podocytes within the Bowman's capsule of the kidneys. In murine knock-out studies, loss of *Lmx1b* inhibits podocyte development, abrogating formation of foot processes and the slit diaphragm and causing splitting of the glomerular basement membrane (GBM) (338, 339). These defects have been shown to be detrimental to kidney function and in *Lmx1b*$^{-/-}$ mice, all pups are born exhibiting severe nephropathies and die within 24 hours of birth (194, 340). Meanwhile, mice with a conditional, podocyte-specific *Lmx1b* knock-out are able to survive for longer but show loss of podocyte foot processes and dysregulation to the formation of podocyte actin cytoskeleton (173, 214). These defects affect GBM filtration, resulting in proteinuria and

renal failure within 14 days after birth (173). Alongside these phenotypic observations, several studies have shown that Lmx1b regulates the expression of key renal genes, including genes essential to podocyte development and maintenance, such as *Nphs2*, *Col4a4*, *Abra*, *Arl4c* and *Wt1* (191, 214, 312, 341). Therefore, these results show that Lmx1b is essential for podocyte development and differentiation, as well as for their maintenance in adults to ensure healthy kidney function and homeostasis.

Compared to mammals, the renal system of teleost fish such as zebrafish is much less complex (342). However, the development and structure of the kidneys is a fairly well conserved process within vertebrates, with numerous cell types and structures found in mammalian kidneys such as, podocytes, proximal and distal tubule segment epithelial cells, and nephrons also being found in zebrafish (343). In zebrafish larvae, the kidney is comprised of one central glomerulus from which two pronephric tubules project down the midline of the fish (344) (Figure 5.1A). Analogous to the mammalian system, these tubules consist of a nephron, proximal and distal tubules, and a distal duct which connects to the cloaca for urinary secretion (342) (Figure 5.1B). The glomerulus is where blood filtration occurs, and as explained in Section 1.5.2 of Chapter 1, the glomerulus contains specialised podocyte cells which aid in the filtration process (214). From the glomerulus, the blood filtrate passes through the bilateral nephrons and along the tubules to the cloaca. Epithelial

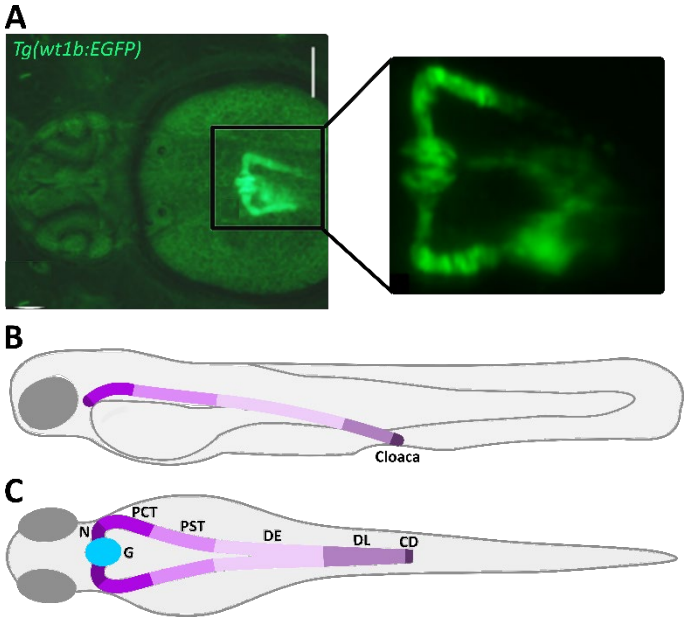

Figure 5.1 – Organisation of the zebrafish pronephros at larval stages, (A) Image of *Tg(wt1b:EGFP)* larvae at 2dpf showing glomerulus and bilateral extension of the pronephric tubules. Scale bar = 80µm. Image taken from Ding *et al.* (344). Schematics showing basic structure of the larval kidney at 3dpf. **(B)** Lateral view showing segmented pronephric tubule running along length of larva to the cloaca. **(C)** Pronephric tubules are separated into discrete segments: G = glomerulus; N = nephron; PCT = proximal convoluted tubule; PST = proximal straight tubule; DE = distal early; DL = late distal; and CD = collecting duct. Schematic adapted from Drummond *et al.* (342).

cells line the length of the tubules, allowing the contents of the blood filtrate from the glomerulus to be altered before its secretion (345).

Expression studies of *lmx1ba* or *lmx1bb* in zebrafish podocytes have yet to be performed, although morpholino knock-down of both paralogues has been shown to cause oedema and reduced kidney function, indicating a similar role for lmx1b in zebrafish kidney development and function (214). Here, the phenotypes of the *lmx1ba* and *lmx1bb* mutants will be compared to determine the role of both in zebrafish kidney development and function.

Comparatively, the role of *lmx1b* in brain development has been characterised to a greater extent in both mice and zebrafish. In the developing brain, Lmx1b is required for the proliferation, specification, and differentiation of dopaminergic (DA) and serotonergic (5-HT) progenitors into neurons (311, 346). Along with other co-factors, Lmx1b helps regulate key genes required for DA neuron specification such as, *En-1* and *En-2,* (347) and *Ngn2, Corin* and *Slit2* (346). It is also essential for the induction and maintenance of the Isthmic Organiser (IsO), a critical signalling centre found in the isthmus (186, 347). The isthmus sits at the midbrain-hindbrain border during early development, and through the IsO, is responsible for regulating and patterning the development of neuronal subtypes (such as DA neurons) as well as key brain regions, such as the tectum and cerebellum (348). This is achieved through the secretion of key transcription factors and signalling molecules by the IsO, such as *Fgf8, Pax2* and *Wnt1*, whose expression is regulated by Lmx1b (186, 349). In both mice and zebrafish, *Lmx1b* shows high expression in the isthmus and loss of *Lmx1b* in either model causes abrogation of IsO activity and secretion, leading to abnormal brain morphology and a significant reduction in DA neuronal number in embryos (185, 186, 218, 349). The similarities in *Lmx1b* null model phenotypes indicates conservation of Lmx1b activity across species and further demonstrates that it is essential for early vertebrate brain development and formation. This conservation means that zebrafish are a good model for studying vertebrate neuronal development and indicates that they would be comparable to mammalian models for the study of NPS.

As mentioned previously, mutations in *LMX1B* have been implicated in several neurological diseases, including Parkinson's disease (175) and schizophrenia (176). Studies have also

indicated behavioural disorders, such as attention deficit hyperactivity disorder (ADHD) and major depressive disorder within the clinical spectrum of NPS, although these data are still preliminary (219). Each of these disorders can be linked to defects in dopaminergic or serotonergic signalling where *LMX1B* plays a key role. Given the early lethality of *Lmx1b* knock-out animal models, it is not possible to study the effects of loss of *Lmx1b* on adult behaviour. To overcome this, some studies use mice with a conditional *Lmx1b* knock-out in DA or 5-HT neurons (175, 350, 351). These mice show loss of their respective neuronal populations (175, 351), and impairments to motor co-ordination and memory recall in the case of DA neuron-specific knock-out mice (175), which is similar to the symptoms displayed in Parkinson's patients. However, the conditionality of these models means that the effect of loss of *Lmx1b* on the whole brain, and any resulting changes to behaviour, cannot be explored. Therefore, in this chapter, the *lmx1ba*$^{-/-}$, *lmx1bb*$^{-/+}$ and *lmx1ba*$^{-/+}$;*lmx1bb*$^{-/+}$ (double heterozygote, *dHet*) mutants were used to study the effect of reduced *lmx1b* expression on adult behaviour as these lines can survive to adulthood.

Although not considered a part of the standard phenotype of NPS, the abnormal development of the proximal musculature has been observed in NPS patients, with some showing decreased muscle mass in the upper arms and legs (209). Mouse knock-out models for *Lmx1b* also show muscle abnormalities in their limbs, especially in the paws where patterning of the muscles and ligaments is disrupted; although it is likely that these abnormalities are secondary to defects in skeletal patterning (308). However, these phenotypes have yet to be described in detail, and the functional impact of these patterning defects have not been investigated. Here, the effect of loss of *lmx1b* on muscle development and formation was explored, specifically within the *dKO* mutants as they showed a significant reduction in body growth as larvae.

Following on from the successful generation of three *lmx1b* zebrafish lines, this chapter explores the phenotype of these lines with a particular focus on the effect of loss of *lmx1ba, lmx1bb* or both paralogues on the musculoskeletal system. Similar to mouse knock-out models for *Lmx1b*, these zebrafish mutant lines were found to show abnormalities in skeletal formation, early brain development and in kidney function. Distinct differences between the larval phenotypes of the *lmx1ba* and *lmx1bb* mutants was observed, indicating a degree of

functional divergence between the two paralogues. Interestingly, the *dKO* mutants showed a strikingly different body phenotype compared to the single mutants and significant changes to the trunk muscle formation and structure which were explored. Given the association of mutations within *LMX1B* in hip OA (352), the effect of loss of *lmx1b* on skeletal maintenance in adult fish was also investigated and *lmx1ba* mutants were shown to have signs of premature OA. Altogether, these results demonstrate the potential use of these zebrafish lines as a model for NPS and highlight a role for mutations within *lmx1b* in the onset of OA.

5.2. Results

Characterisation of the gross phenotype of *lmx1ba*, *lmx1bb* and *dKO* mutant lines during early development

5.2.1 Loss of lmx1b affects body length and eye diameter in larvae

Given the role of LMX1B in dorsoventral patterning of the body during embryogenesis (179), the effect of the single and double mutations on gross body formation during early development was explored. The whole body length of larvae, from nose to tail, was measured using lateral images taken from 1dpf-7dpf (Figure 5.2.1A, *pink line*). Heterozygotes crosses of each mutant meant that *lmx1ba* and *lmx1bb* mutant larvae were compared to their corresponding *wt* and heterozygote siblings (Figure 5.2.1B-E), whilst *dKO* mutants were compared to the homozygous single mutants and their *wt* siblings (Figure 5.2.1F and G). Both single mutants showed no significant difference in body length compared to siblings at any age, although the growth of the *lmx1ba* mutants does appear to be slightly delayed until 7dpf where their average body length once again matches sibling averages (Figure 5.2.1B). The *dKO* mutants however, showed a significant stalling in growth from 2dpf onwards, resulting in larvae that are 40% shorter in length at 7dpf compared to *wt* and either homozygous single mutant (average *dKO* length of 2500 μm compared to an average length of ~3500 μm for the other genotypes) (Figure 5.2.1F). This failure to grow beyond 1dpf is startling and results in a very truncated body phenotype which will be explored further below in Section 5.2.3.

The eye diameter of the larvae was also measured (Figure 5.2.1A, *blue line*) as studies have indicated a role for both transcripts in eye development (188, 217). The *lmx1ba* mutants showed no changes to eye diameter (Figure 5.2.1C), whilst the *lmx1bb* mutants showed a significant decrease in diameter from 6-7dpf compared to *wt* siblings (Figure 5.2.1E). In the

dKO mutants, a reduction in eye diameter was seen from 2dpf onwards, following a similar but more significant trend as the *lmx1bb* mutants (Figure 5.2.1G).

These results indicate potential differences in expression between the two *lmx1b* genes and highlight a possible role for *lmx1bb,* but not *lmx1ba,* in eye development and formation. The significant change in whole body growth present in the *dKO* mutants is surprising, especially given the lack of a similar trend in the single mutants. The cause behind this reduced body size will be explored later in this chapter.

5.2.2 Loss of lmx1ba and lmx1bb have differing effects on body morphology during development

Analysis of body formation was also performed on each mutant from 1-7dpf to identify any other body systems where *lmx1b* may play a role. This was first performed on the single *lmx1ba* and *lmx1bb* mutants to allow for comparison between corresponding homozygous and heterozygous siblings. At 1dpf, both mutants showed no obvious phenotypic differences in development compared to *wt* siblings. This is in line with morpholino studies against *lmx1ba* and *lmx1bb,* where knock-down of one paralogue was not sufficient to affect early development up to 2dpf (185). However, by 3dpf, both the *lmx1ba* and *lmx1bb* homozygous mutants showed observable developmental differences such as the presence of oedema and bent body axis, although the penetrance of these phenotypes was much stronger in the *lmx1bb* mutants (data not shown). For example, with the presentation of oedema, 14% *lmx1ba* homozygous mutants developed severe oedema from 3dpf, whilst the majority of *lmx1bb* mutants (84%) had mild to moderate oedema by 5dpf which worsened in severity with age (Figure 2.2.2A-C), until all *lmx1bb* mutants developed oedema by 7dpf (Figure 2.2.2D). In the *lmx1bb* mutants, oedema of the yolk sac was most prominent first (Figure 2.2.2A, *white arrowhead*), followed by pericardial oedema and oedema of the eye by 4-5dpf (Figure 2.2.2A, *blue arrowhead and navy arrowhead, respectively*).

Inflation of the swim bladder is known to be a key indicator of healthy development in zebrafish, with the majority of zebrafish expected to have an inflated swim bladder by 5dpf (353, 354) (Figure 2.2.2E). In these results, a similar proportion of *lmx1ba* mutant larvae to *wt* and heterozygous siblings showed an inflated swim bladder by 5dpf (60% *wt* to 77%

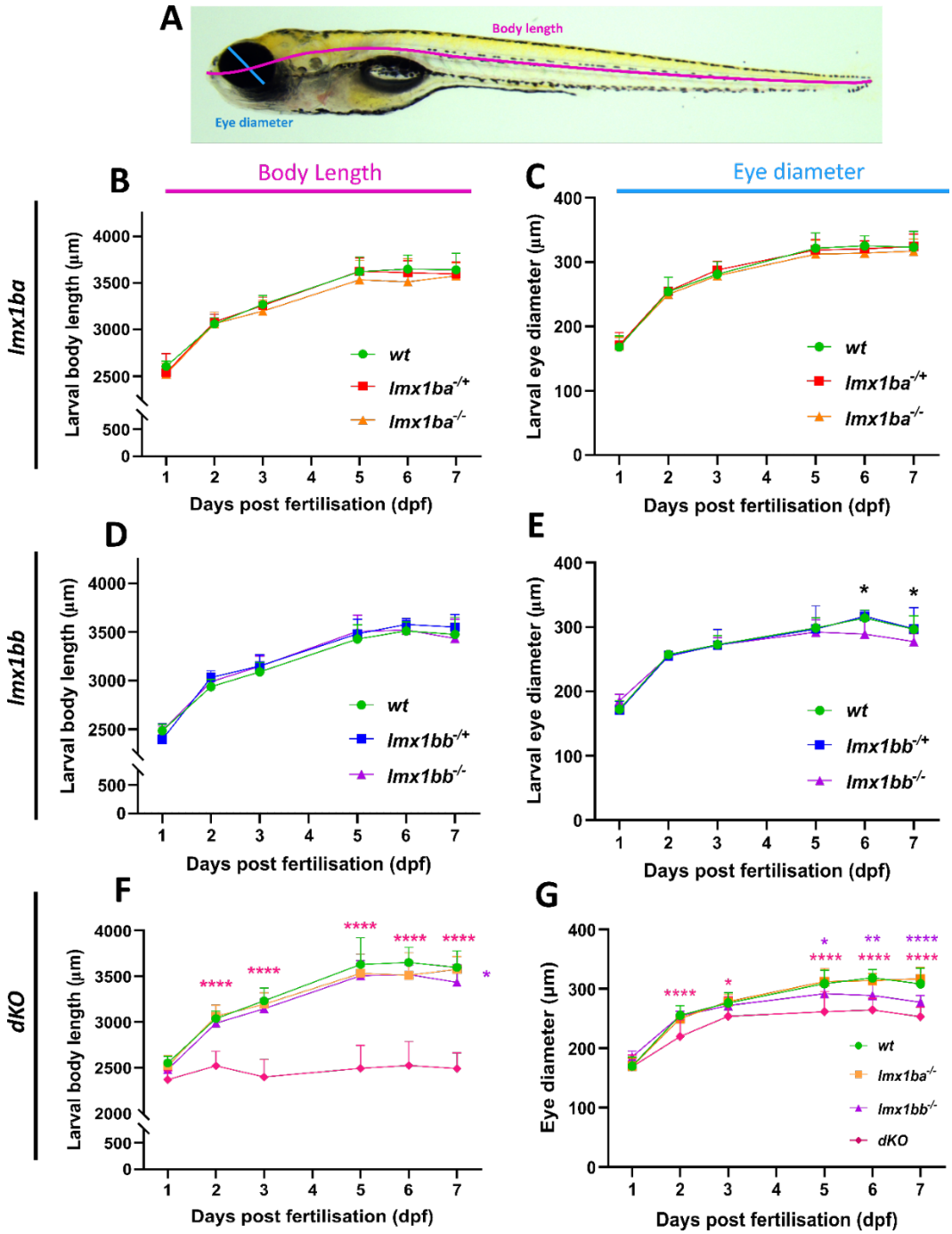

Figure 5.2.1 – Single and collective loss of *lmx1ba* and *lmx1bb* has differing effects on larval growth and eye development, (A) Lateral image of larvae at 5dpf showing lines of measurement used to measure body length (*pink line*) and eye diameter (*blue line*). Graphs showing measurements for **(B, D, F)** body length, and **(C, E, G)** eye diameter taken from *wt,* heterozygous and homozygous mutant larvae at 1-7dpf. **(F and G)** Pink asterisks refer to statistical significance between *wt* and *dKO,* and purple asterisks between *wt* and *lmx1bb* mutants. For graphs **(F and G),** the same data for *lmx1ba* and *lmx1bb* homozygous mutants as plotted in graphs **(B-E)** is used, and the *wt* data is collated from both single mutants. N = 10 larvae for *wt* and heterozygous, 19 larvae for *lmx1ba* and *lmx1bb* homozygous mutants and 28 larvae for *dKO* mutants. A Mixed-effects analysis was performed for all graphs where, **** *P*<.0001, *** *P*<.001, ** *P*<.01 and * *P*<.05.

homozygous *lmx1ba* mutants), meanwhile only 11% of *lmx1bb* homozygous mutants had an inflated swim bladder at 5dpf (Figure 5.2.2F and G). A failure to inflate the swim bladder is indicative of a delay in normal development and along with the high prevalence of oedema suggests that the *lmx1bb* mutants are struggling to thrive in early development. Studies in *atg*-mutant zebrafish have also shown that autophagy is required for swim bladder inflation through its role in lamellar body maturation (41). Therefore, changes to autophagy activity caused by a reduction in *lmx1b* expression could also be influencing this process.

Given the full penetrance of oedema incidence in the *lmx1bb* mutants, this is hypothesised to be the cause of their larval lethality. In zebrafish, oedema can be a sign of defective kidney function as the kidneys play a key role in excreting water and maintaining proper osmoregulation (345, 355). A lack of proper fluid filtration can cause oedema as water accumulates in the body. Therefore, it is likely that loss of *lmx1bb,* and to a lesser degree *lmx1ba,* has an effect on kidney function, which manifests in oedema. In a later section, this will be investigated further by ultrastructural analysis on *wt* and *lmx1bb* homozygous mutants.

5.2.3 Complete loss of lmx1b significantly affects body development

The development of *dKO* mutants was also monitored from 1-7dpf and compared to *wt* and the *lmx1ba* and *lmx1bb* homozygous mutants. In line with the result from Section 5.2.1, from 3dpf onwards, the *dKO* mutants are smaller than *wt* larvae and have a truncated body phenotype (Figure 5.2.3A-B) which persists until they die at ~10dpf. The heads of the *dKO* mutants are a comparable size to *wt,* with the trunks being significantly shorter. This correlates with the phenotype observed in NPS patients where some patients have a proportionally larger head and shorter distal limbs (209). Therefore, the spine and trunk muscle of the *dKO* mutants will be explored in Section 5.2.16 to elucidate the cause behind this body truncation.

The majority of *dKO* mutants show some form of oedema by 5dpf (72%, Figure 5.2.3C), with 40% of mutants showing severe oedema by 7dpf (Figure 5.2.3D). Similar to the *lmx1bb* mutants, oedema presented in the yolk sac and heart first, before appearing in the eye by

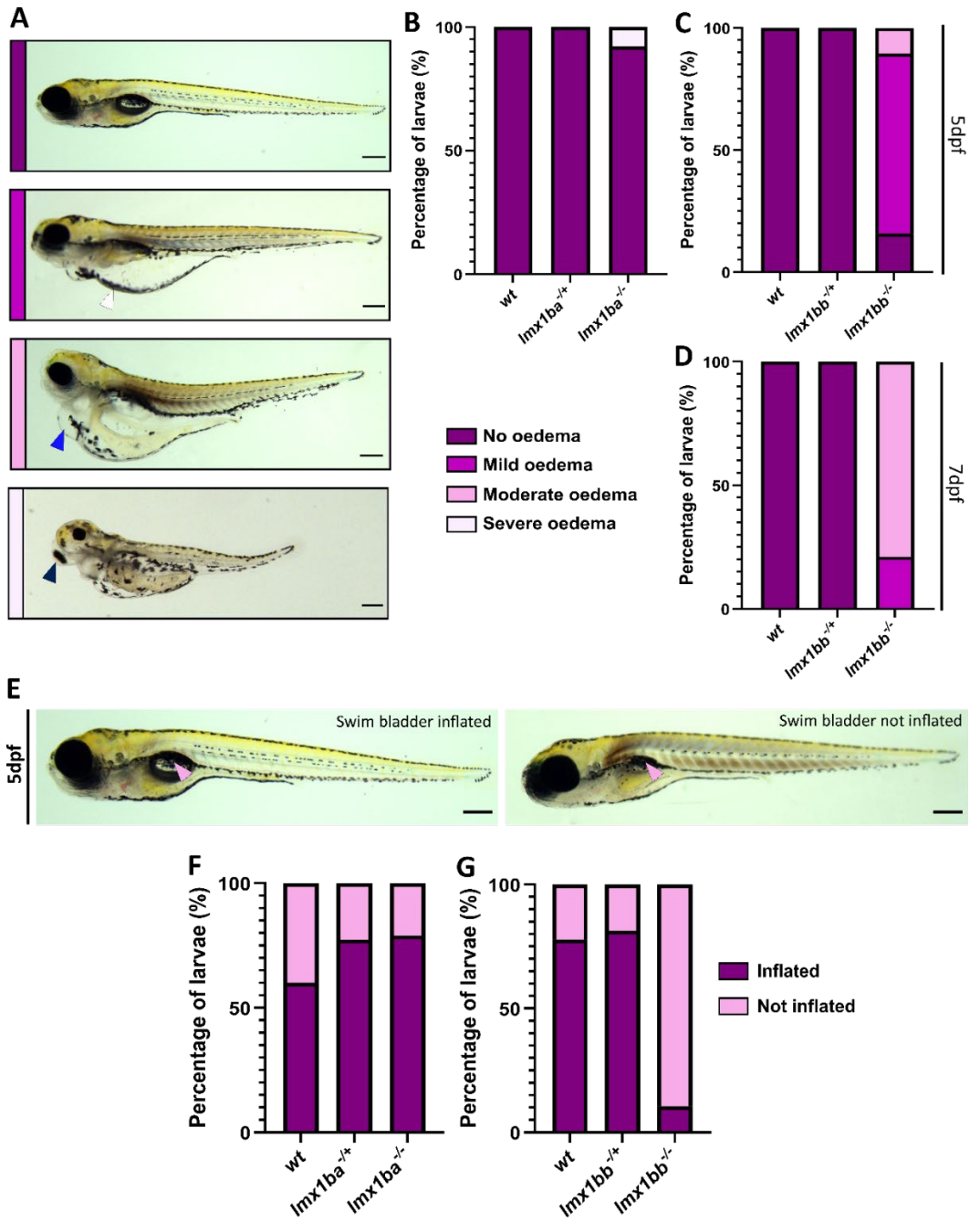

Figure 5.2.2 – Loss of *lmx1bb* but not *lmx1ba* causes a delay in larval development and body oedema in all mutants by 7dpf, (A) Representative images of levels of oedema severity in *lmx1ba* and *lmx1bb* larvae at 5dpf. Mild oedema detected primarily as yolk sac oedema (*white arrowhead*); moderate oedema classified by onset of pericardial oedema (*blue arrowhead*); severe oedema indicated by addition of eye oedema (*navy arrowhead*). **(B)** and Graphs showing percentage of larvae within each oedema classification at **(C)** 5dpf and **(D)** 7dpf for only the *lmx1bb* mutants and siblings. Colours in key (*middle*) correspond to colours used in graphs **(B-D). (E)** *lmx1ba wt* and mutant larvae at 5dpf showing swim bladder inflation (*left image*) and non-inflation (*right image*). Location of swim bladder shown by pink arrowhead. Quantification of number of larvae at 5dpf showing swim bladder inflation or non-inflation for **(F)** *lmx1ba* and **(G)** *lmx1bb*. For *lmx1ba*, n = 10 for *wt*, 22 for heterozygotes and 38 for homozygous mutants. For *lmx1bb*, n = 9 for *wt*, 16 for heterozygotes and 19 for homozygous mutants. Scale bar = 250μm for all.

7dpf (Figure 5.2.3A and B). Although the proportion of *dKO* mutants with no oedema is higher than the *lmx1bb* homozygous mutants at both 5 and 7dpf, there is a greater incidence of severe oedema in the *dKO* mutants. From Section 5.2.1 it is clear that loss of *lmx1bb* has the greatest effect on oedema compared to *lmx1ba* and therefore, is more likely to have a role kidney development. However, these results suggest that *lmx1ba* also retains some function in regulating kidney development as loss of *lmx1ba,* along with *lmx1bb* increases oedema severity.

At 5dpf, 100% of *dKO* mutants fail to inflate their swim bladders and just under 50% have a bend in their body axis (Figure 5.2.3B, *blue arrowhead,* and E). A smaller proportion (28%) show defects in eye size, which may be due to oedema around the eye area (Figure 5.2.3B, *pink arrowhead*), which is in line with data from Section 5.2.1 which showed that the *dKO* mutants have smaller eyes compared to *wt*. Despite some phenotypic similarities between the single mutants and the *dKO* mutants, this analysis shows that the *dKO* mutants have a distinct body phenotype compared to the single mutations, which appears by 3dpf. Given the absence of this phenotype in either single mutant, it is possible that each paralogue compensates for the loss of the other.

As demonstrated in patients with NPS and from studies in murine *Lmx1b* knock-out models, mutations in *LMX1B* can affect a variety of body systems including the renal system, skeletal system, and specific neuronal populations and brain structures. Therefore, to fully characterize these lines and to explore any differences in expression or function of these paralogues, each of these body systems, along with the trunk musculature were studied in turn.

For the remainder of this study, all three mutants were compared to the same *wt* (bred from siblings of a *lmx1bb* heterozygous line in-cross), as *wt* siblings from both lines appear to show no comparable differences in development to each other. As the heterozygous siblings for each of the single knock-out genotypes also show a similar phenotype to *wt*, they were also not studied any further at larval stages.

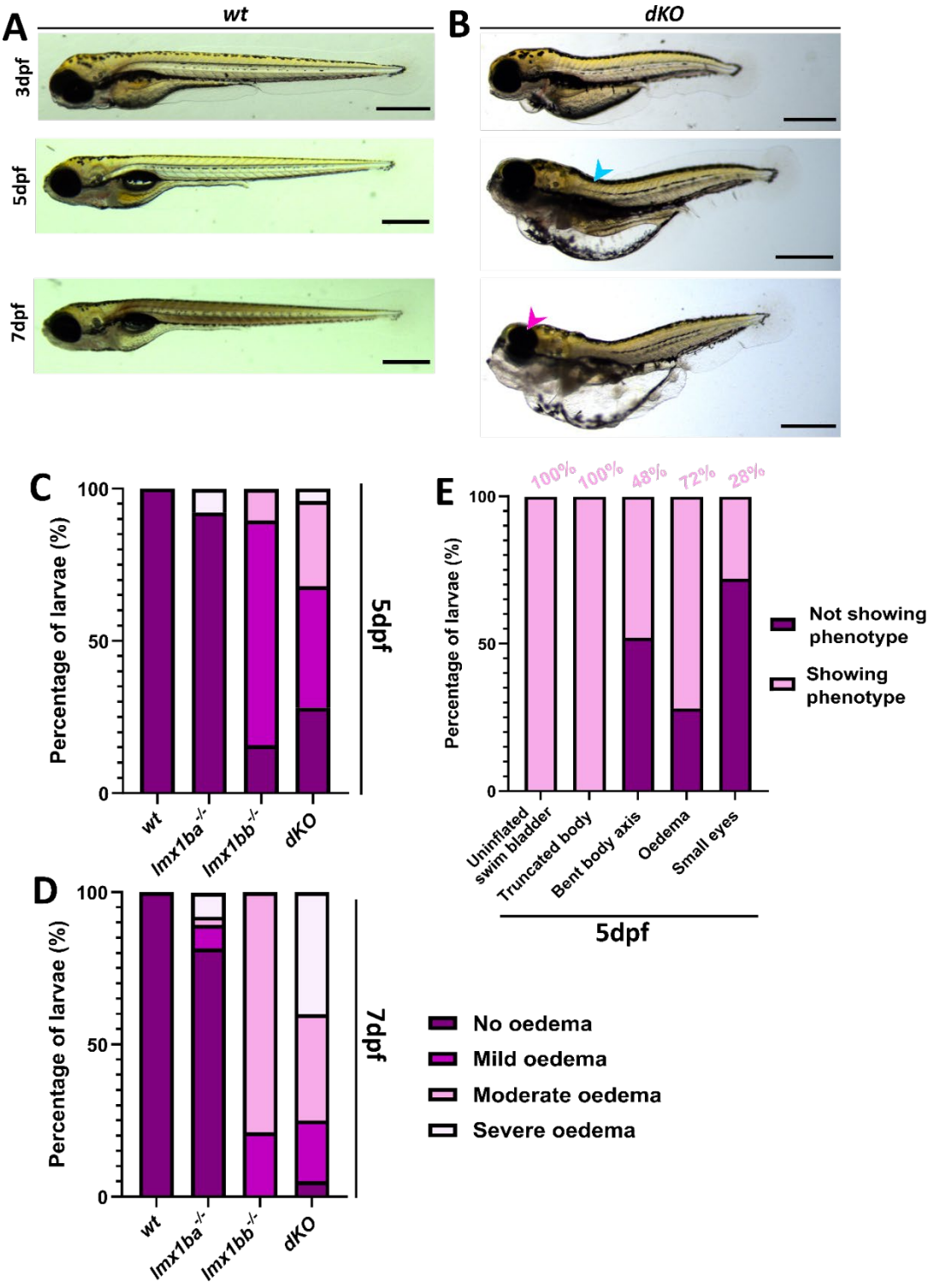

Figure 5.2.3 – *dKO* mutants show changes to body morphology during development and high oedema incidence by 5dpf, Representative stereomicroscope images of **(A)** *wt* and **(B)** *dKO* mutants from 3-7dpf. Blue arrowhead indicates bend in body axis; pink arrowhead, decreased eye size and eye oedema. Scale bar = 250μm. Graphs showing percentage of larvae within each oedema classification at **(C)** 5dpf and **(D)** 7dpf. Colours in key (*right of* **(D)**) correspond to colours in graphs for **(C, D). (E)** Graph showing the incidence of body abnormalities in *dKO* mutants at 5dpf.N = 19 for *wt;* 38 for *lmx1ba*$^{-/-}$; 19 for *lmx1bb*$^{-/-}$ and 25 for *dKO* at 5dpf, and 22 at 7dpf.

Investigating the role of *lmx1bb* in kidney formation

5.2.4 Kidney glomerulus morphology is disrupted in lmx1bb mutants

Given the high incidence of an oedemic phenotype in the *lmx1bb* mutants and the strong association of *Lmx1b* with kidney development and formation, ultrastructural analysis was used to explore the structure of the renal system in *lmx1bb* mutants and *wt* (Figure 5.2.4). By 2dpf, glomerular filtration begins in zebrafish, although it is leaky (342). By 4dpf, all common features of the kidney glomerulus, such as fenestrated endothelial cells, a glomerular basement membrane, and podocytes can be seen via transmission electron microscopy, suggesting establishment of the filtration barrier (356).

Looking within the glomerulus of *wt* larval kidneys at 6dpf, key structures forming the filtration barrier can be easily identified and show a clear organisation (Figure 5.2.4A and B). Surrounding blood vessels and endothelial cells, a dark, electron dense line can be seen indicating formation of the glomerular basement membrane (GBM) (Figure 5.2.4A and B, *white dashed line*). On the urinary side of the GBM, podocyte foot processes appear as tall columnar-like structures along the edge of the GBM (Figure 5.2.4A and B, *white arrowheads*), with interdigitation between foot processes present in some areas (Figure 5.2.4A, *IDP, pink and white arrowheads*). On the blood side of the GBM, fenestrations in the endothelium, which allows for the filtration of low-molecular-weight waste products from circulation, can be seen next to the GBM (Figure 5.2.4A and B, *F, pink asterisks*). Meanwhile, in the *lmx1bb* mutants, the cells and structures forming the glomerulus appear much less organised, with some areas showing no discernible pattern or structure (Figure 5.2.4C). In these areas, the mitochondria appeared round and swollen, indicative of mitochondrial dysfunction and a sign of kidney disease (357), and there is an appearance of swollen compartments (Figure 5.2.4C). With the lack of structural organisation in these mutants, it is difficult to determine the identity of these structures, although they might be podocyte foot processes. Other areas do show more organisation, and a GBM surrounding blood vessels can be identified in some locations (Figure 5.2.4D). However, in the *lmx1bb* mutant, the line distinguishing the GBM appears thickened (Figure 5.2.4D), a phenotype observed in both *Lmx1b*$^{-/-}$ mice and in NPS patients with renal disturbances (336, 358). The formation of podocyte foot processes or endothelial fenestrations along the GBM are harder to identify and the structures present

near the GBM appear more swollen and disordered (Figure 5.2.4D, *black arrowheads*). Altogether, these changes indicate a disruption to kidney structure, and GBM and podocyte formation in the *lmx1bb* mutants, which is likely to be impacting kidney function and the filtration of substrates from circulation.

Unfortunately, due to time constraints, this kidney phenotype could not be evaluated any further. However, these initial results implicate the *lmx1bb* paralogue in podocyte development and indicate that the larval lethality seen in these mutants is likely due to kidney failure. This may also be the case for the *dKO* mutants however, this will require further investigations to be determined. Next, the effect of the *lmx1ba*, *lmx1bb* and *dKO* mutations on the skeletal system were explored.

Determining the role of *lmx1ba* and *lmx1bb* in skeletal development

5.2.5 Lower jaw development is affected in lmx1ba and dKO mutants but not lmx1bb mutants

Given the established roles of LMX1B in regulating dorsal limb patterning and the skeletal changes observed in NPS patients (359, 360), the effect of loss of *lmx1ba* and/or *lmx1bb* on skeletal formation in zebrafish was explored. Larvae were immunostained with Col2a1 (Figure 5.2.5A) and the lower jaws from each line was measured at 3dpf and 5dpf (Figure 5.2.5C, E and G, *left and right hand graphs, respectively*). Three measurements were taken, including full length of the lower jaw, length of the Meckel's cartilage and width of the Meckel's cartilage (Figure 5.2.5B, D and F). The *lmx1bb* mutants showed minimal variances in jaw length and width compared to *wt* at both ages (Figure 5.2.5C, E and G, *purple data points*), apart from the length of the Meckel's cartilage, where a significant difference compared to *wt* was seen. However, from 3dpf to 5dpf this difference reverses from being significantly longer, to shorter indicating that *lmx1bb* may be having a specific effect on cartilage growth but this effect becomes overwhelmed by a secondary influence, potentially a failure to thrive, which leads to a reduction in overall growth. The lower jaws of the *lmx1ba* mutants, however, were significantly shorter in length compared to *wt* and show a consistent trend in decreased length and width at 3dpf and 5dpf (Figure 5.2.5C, E and G,

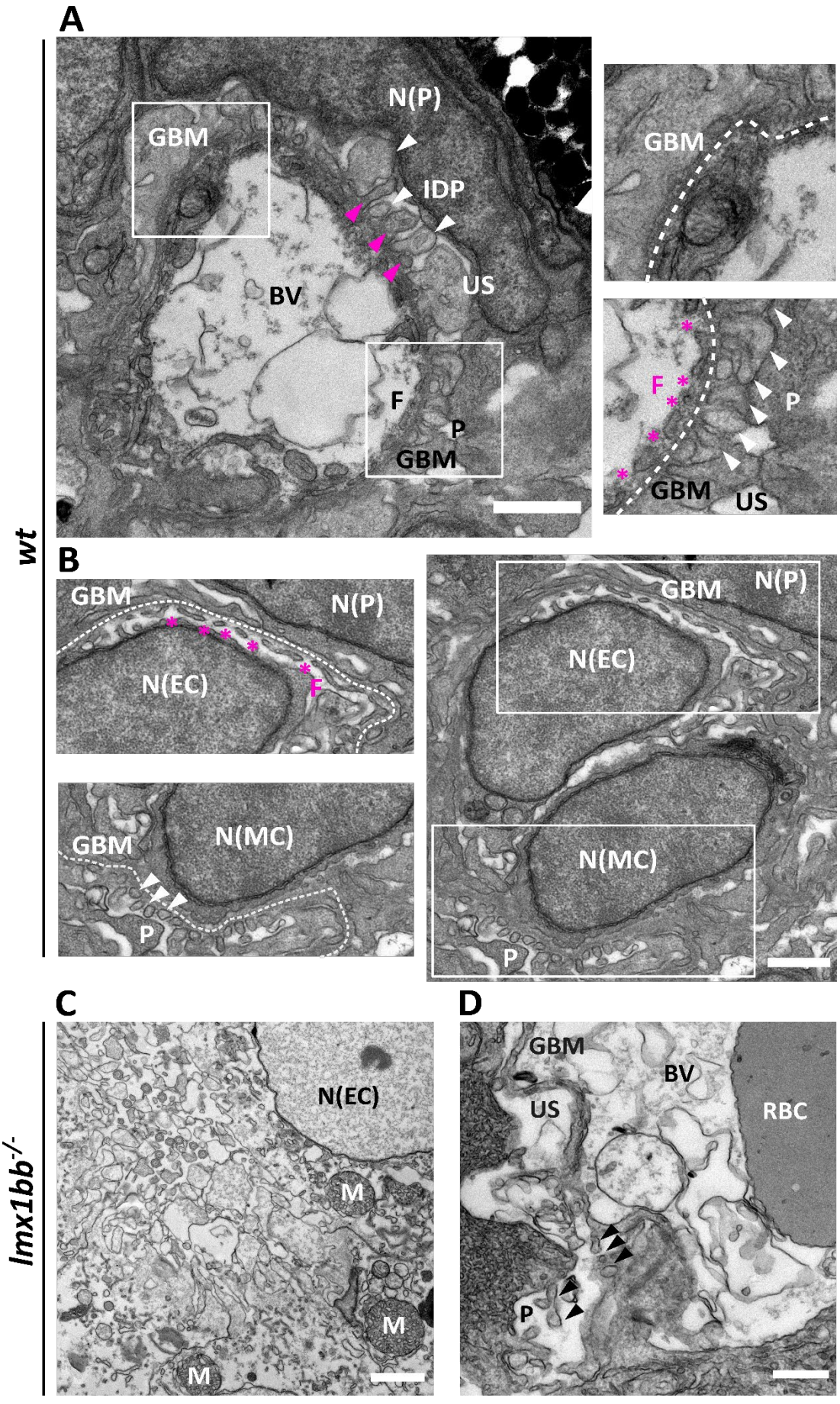
A
GBM
N(P)
IDP
BV
US
F
P
GBM
GBM
F
P
GBM
US
wt
B
GBM
N(P)
N(EC)
F
GBM
N(P)
N(EC)
GBM
N(MC)
P
N(MC)
P
C
N(EC)
M
M
M
lmx1bb-/-
D
GBM
BV
US
RBC
P

Figure 5.2.4 – Disruption to kidney structure and the formation of glomerular basement membrane and podocytes in the *lmx1bb* mutants compared to *wt* at 6dpf, Representative electron micrograph images of the glomeruli of **(A,B)** *wt,* and **(C,D)** *lmx1bb* mutants at 6dpf. White and black arrowheads indicate podocyte foot processes, and white and pink arrowheads together show interdigitating podocyte foot processes. White dashed lines show GBM, and pink asterisks indicate fenestrations. BV = blood vessel; F = fenestrations; GBM = glomerular basement membrane; IDP = interdigitating podocyte foot processes (indicated by alternating foot processes of different electron densities); M = mitochondria; N(EC) = nucleus of endothelial cell; N(MC) = nucleus of mesenchymal cell; N(P) = nucleus of podocyte cell; P = podocytes; RBC = red blood cell; US = urinary space. Scale bars = 1μm for A-C; 500nm for D. N = 3 for *wt* and 2 for *lmx1bb* mutant. Samples were sectioned and imaged by Dr Chris Neal (University of Bristol).

orange data points). This consistent difference in length and width at both ages indicates reduced jaw growth, however, only the Meckel's cartilage shows a reduced rate of growth from 3dpf to 5dpf compared to *wt.* This indicates that either the reduced rate of growth occurs before 3dpf or that the decreased whole jaw length is solely due to the Meckel's cartilage being shorter.

Compared to the *lmx1ba* mutants, the *dKO* mutation had an opposite effect on lower jaw length and width at 3dpf, showing a higher average value for all three measurements compared to *wt* (Figure 5.2.5C, E and G, *pink data points*). By 5dpf, the length of the lower jaw and Meckel's cartilage was similar to *wt*, although *dKO* jaw width remained significantly wider than *wt* or either single mutant (Figure 5.2.5D, F and H). This suggests that the growth rate of the *dKO* mutants normalises after 3dpf and that the increased jaw width may be due to a separate factor. Later in this chapter, changes to musculature in the jaw will be explored to determine whether they may be affecting jaw development and structure.

Taken altogether, these results indicate a role for *lmx1ba* in skeletal development which is not replicated in the *lmx1bb* mutants. Given the results of the *dKO* mutant, it would appear that complete loss of *lmx1b* accelerates the early growth rate of zebrafish jaws, although this normalises close to *wt* levels beyond 3dpf.

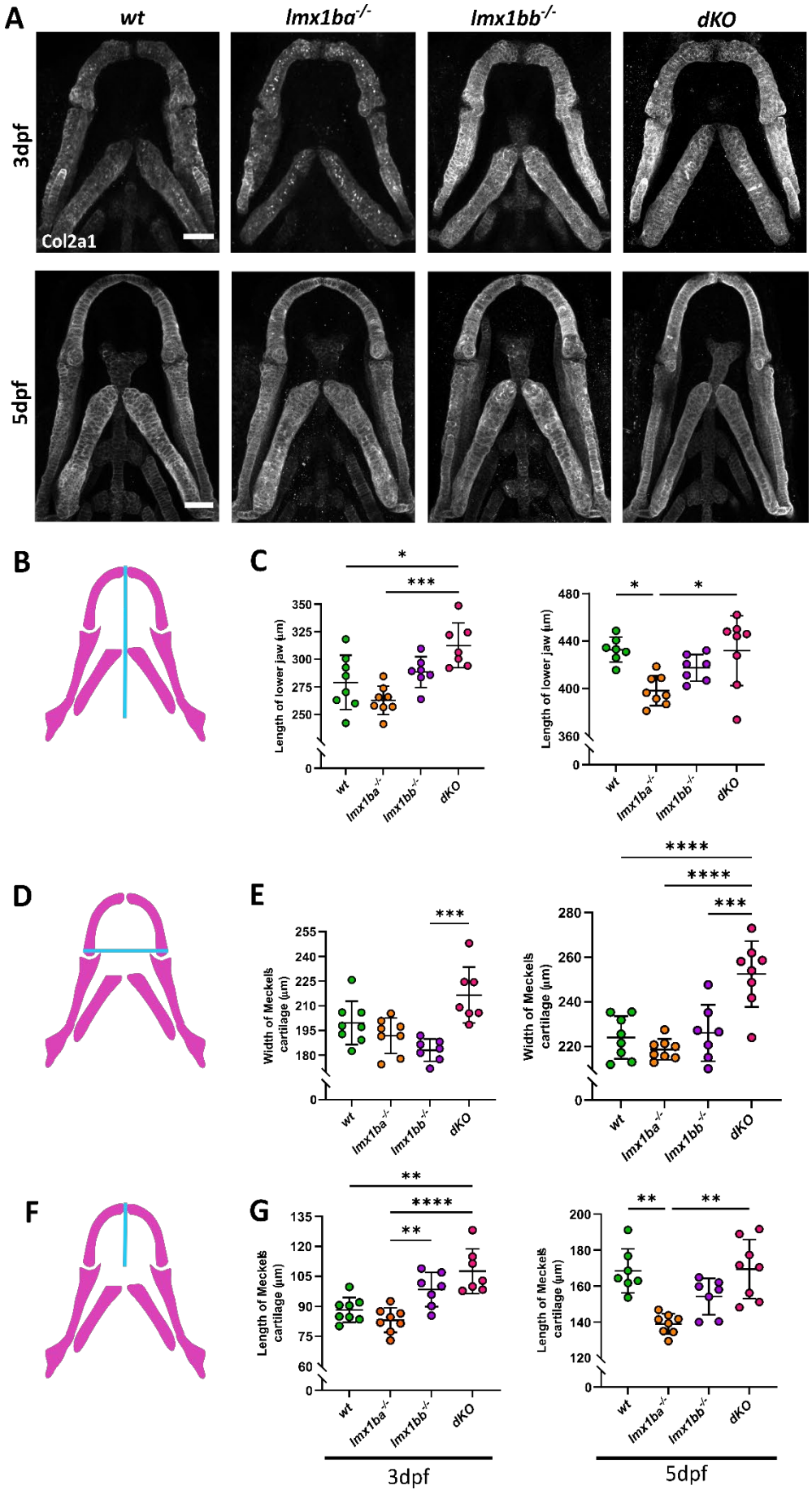
A
wt
lmx1ba-/-
lmx1bb-/-
dKO
3dpf
5dpf
Col2a1
B
C
Length of lower jaw (µm)
D
E
Width of Meckel's cartilage (µm)
F
G
Length of Meckel's cartilage (µm)
3dpf
5dpf

Figure 5.2.5 – *lmx1b* mutants show differences in lower jaw size compared to *wt* in larval development, (A) Representative confocal z-stack projections of the lower jaw at 3dpf and 5dpf in *wt* and *lmx1ba, lmx1bb* and dKO mutant larvae, immunostained for Col2a1 (white). Scale bars = 50μm. Schematics indicating where measurements were made for **(B)** length of lower jaw, **(D)** width of Meckel's cartilage and **(F)** length of Meckel's cartilage. **(C), (E)** and **(G)** Graphs showing quantification of results at 3dpf (*left*) and 5dpf (*right*). For 3dpf, n = 8 for *wt,* 8 for *lmx1ba* mutants, 7 for *lmx1bb* and 7 for dKO mutants. For 5dpf, n = 7 for *wt,* 8 for *lmx1ba* mutants, 7 for *lmx1bb* and 8 for dKO mutants. One-way ANOVAs performed for all where **** $P<.0001$, *** $P<.001$, ** $P<.01$ and * $P<.05$.

5.2.6 Reduced proliferation of chondrocytes forming the jaw joint in lmx1ba mutants

To explore whether the changes in jaw size seen in the *lmx1ba* and *dKO* mutants is due to a change in chondrocyte proliferation, an EdU assay was performed. This was followed by immunostaining for Col2a1 to highlight the chondrocytes forming the jaw and jaw joint (Figure 5.2.6A and B). Cells positive for both EdU and Col2a1 were counted across the whole jaw and at the site of the lower jaw joint (Figure 5.2.6C and D). Both areas were analysed as a change in gross jaw size was seen in both mutants, however, the joint site is one of the main sites where cartilage growth occurs as chondrocytes proliferate and are pushed into the intercalation zone of the cartilage.

The *lmx1ba* mutants show a reduction in the number of proliferating cells within the whole jaw compared to *wt*, although this difference was not significant (Figure 5.2.6C). However, at the joint site, there was a significant decrease in EdU-Col2a1-positive chondrocyte number, indicating that there is reduced chondrocyte proliferation in the *lmx1ba* mutants (Figure 5.2.6D). From this, it is hypothesised that this decrease in proliferative capacity is responsible for decreased jaw size in the *lmx1ba* mutants. Previous studies have shown a role for *Lmx1b* in regulating the proliferation of midbrain dopaminergic neurons (346), as well as glioma and oesophageal cancer cells (361, 362), therefore, *lmx1ba* could be a regulator for chondrocyte proliferation. This decrease in proliferation could also be due to loss of *lmx1ba* perturbing chondrocyte differentiation and maturation, which will be explored later using ultrastructural analysis.

The same proliferation assay was also performed on *dKO* larvae as they showed an increase in growth rate of the lower jaw from 3-5dpf. The assay was initially performed on *dKO* larvae at 2-3dpf to capture any changes to proliferation which may help explain the

increased jaw size at 3dpf. Unfortunately, accurate results from these experiments could not be obtained as the larvae failed to take up the EdU reagent. At 5dpf, the *dKO* mutants showed a slight decrease in chondrocyte proliferation within the whole jaw (Figure 5.2.6C). However, at the jaw joint, there was no difference in EdU-Col2a1-positive cell number compared to *wt*, indicating that chondrocyte proliferation is not affected in the *dKO* mutants at 5dpf (Figure 5.2.6D). As lower jaw length in the *dKO* mutants becomes comparable to *wt* size by 5dpf, this result is not surprising. Although why loss of *lmx1ba* alone reduces jaw growth and chondrocyte proliferation, but loss of both *lmx1b* paralogues does not, is harder to understand. This could be due to compensatory mechanisms in the *dKO* mutants which are absent when one paralogue is expressed.

5.2.7 The lmx1ba mutants show no changes to Sox9a expression

Next, to explore whether changes to chondrocyte proliferation in the *lmx1ba* mutants are linked to changes in chondrocyte maturation and differentiation, the expression of Sox9a, a chondrocyte transcription factor, was analysed. As detailed earlier, Sox9a is an early chondrocyte marker whose expression is essential for chondrocyte differentiation and subsequent cartilage formation. Using the same SoxQuant program, the volume of Sox9a fluorescence in z-stacks of 5dpf larval jaws was measured (Figure 5.2.7).

At three sites within the lower jaw, there was no significant change in the volume of Sox9a fluorescence measured between *wt* and the *lmx1ba* mutants (Figure 5.2.7B and C). With the changes to cartilage growth and chondrocyte proliferation in the jaw seen in the *lmx1ba* mutants, this is a surprising result. However, changes to chondrocyte maturation might still be occurring as will be explored further next.

5.2.8 The lmx1ba mutants show reduced chondrocyte maturation and altered chondrocyte organisation

In Chapter 3, the maturation state of chondrocytes in the jaw was further assessed by immunostaining with a Col10a1 antibody. Unfortunately, due to this antibody no longer working, this experiment could not be performed here. Therefore, to ascertain whether the changes to cartilage growth in the jaw and chondrocyte proliferation are due to a disruption

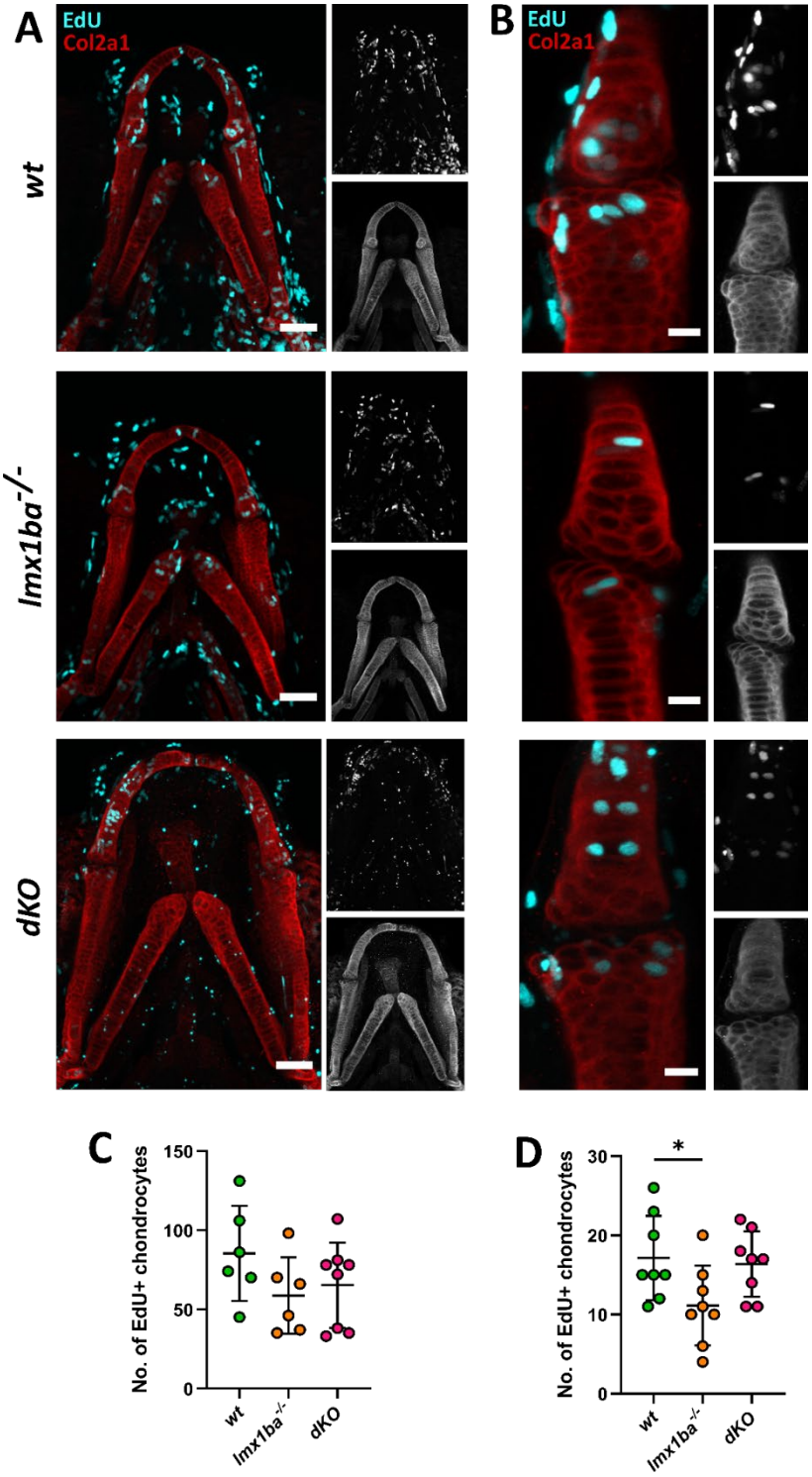

Figure 5.2.6 – Proliferation of chondrocytes at the joint site is decreased in *lmx1ba* and *dKO* mutants, Representative confocal z-stack projections of the **(A)** lower jaw and **(B)** lower jaw joint at 5dpf in *wt*, and *lmx1ba* and *dKO* mutants, immunostained for EdU (cyan) and Col2a1 (red) following 24 hour treatment with EdU Click-iT. Scale bars = 50μm for the jaws and 10μm for the joints. Number of EdU-Col2a1-positive cells quantified for **(C)** the whole lower jaw and **(D)** jaw joint. N = 6 and 8 for *wt* and *lmx1ba* mutants, and 8 for *dKO* mutants. One-way ANOVA performed for both where * *P*=.0406.

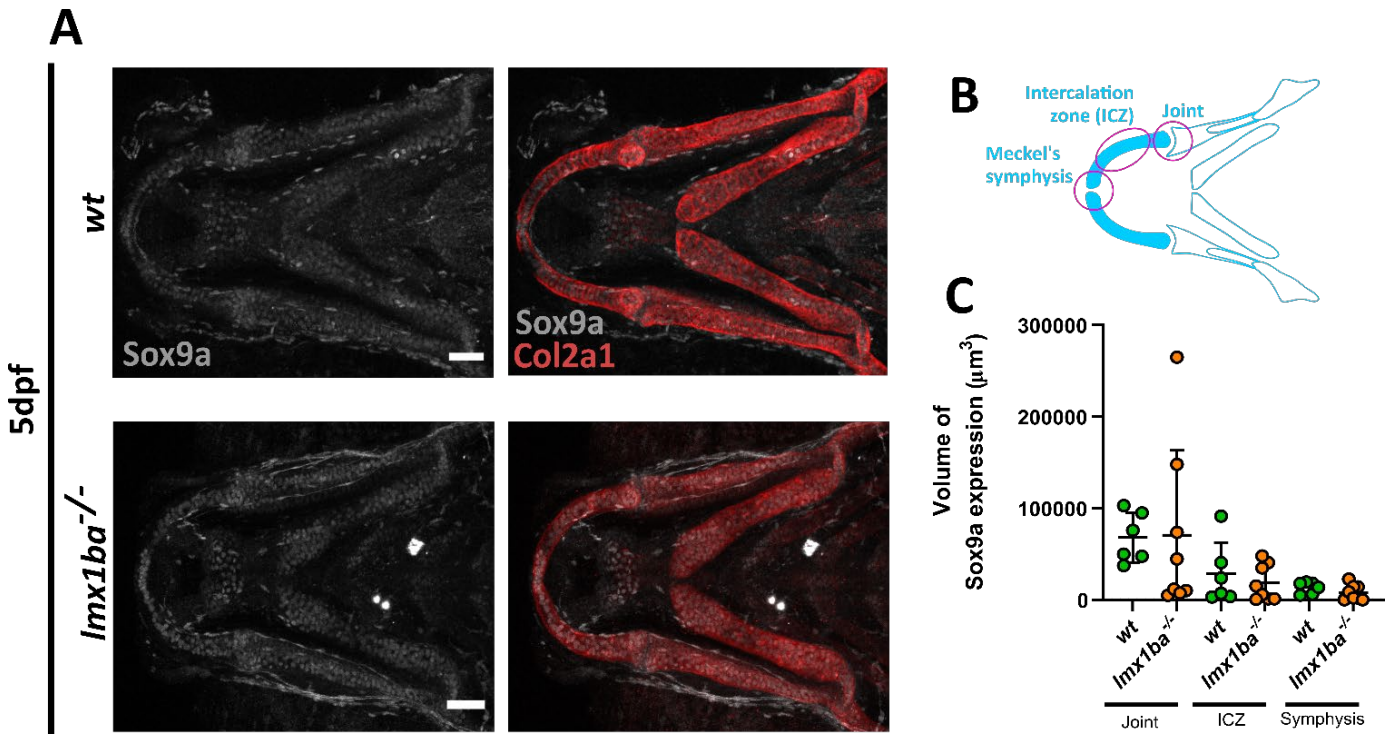

Figure 5.2.7 – Sox9a expression largely unaltered in *lmx1ba* mutants compared to *wt*, (A) Representative confocal z-stack max projections of Sox9a (grey) and Col2a1 (red) immunostained lower jaws of *wt* and *lmx1ba* mutant fish at 5dpf. Scale bars = 50µm. **(B)** Schematic showing the three locations (pink circles) where Sox9a expression was analysed using the SoxQuant software (designed by Dr Stephen Cross, University of Bristol). **(C)** Quantification of Sox9a expression. ICZ = intercalation zone. N = 6 for *wt* and 8 for *lmx1ba* mutants. Student's unpaired t-test or Welch's t-test performed for all.

in chondrocyte maturation and differentiation, ultrastructural analysis of *wt* and *lmx1ba* mutant chondrocytes at 5dpf was performed (Figure 5.2.8).

Similar to the *atg13 wt* larvae in Section 3.2.16, the *lmx1b wt* chondrocytes appeared elongated and had sparsely filled cytoplasm (Figure 5.2.8A and B), which is an indicator of late-stage hypertrophication in chondrocytes. Along the length of the cartilage, the majority of *wt* chondrocytes were neatly stacked in a column, giving the cartilage a smooth border along its edge (Figure 5.2.8A). In comparison, the *lmx1ba* mutant chondrocytes were smaller and more electron dense, showing a significantly greater number of vesicles per chondrocyte compared to *wt* (Figure 5.2.8B, D, E and F). The *lmx1ba*$^{-/-}$ chondrocytes also showed disrupted organisation, with an increase in the number of chondrocytes not intercalating properly and being present on the edge of the cartilage stack, resulting in a bumpy appearance to the cartilage (Figure 5.2.8B, *pink arrowheads*, and G). However, no

observable differences in ECM structure, organisation or density could be seen in the *lmx1ba* mutants compared to *wt.*

Taken together, these results indicate that at 5dpf, *lmx1ba* mutant chondrocytes are less hypertrophic than their *wt* counterparts. This suggests that loss of *lmx1ba* affects the rate of chondrocyte maturation, causing a delay in their differentiation. Given that these results are opposite to the effect seen in autophagy-deficient *atg13* mutant zebrafish, this suggests that this is not simply due to dysregulation in autophagy activity caused by loss of *lmx1ba.* Instead, this suggests that this is due to the loss of *lmx1ba* itself within the chondrocytes.

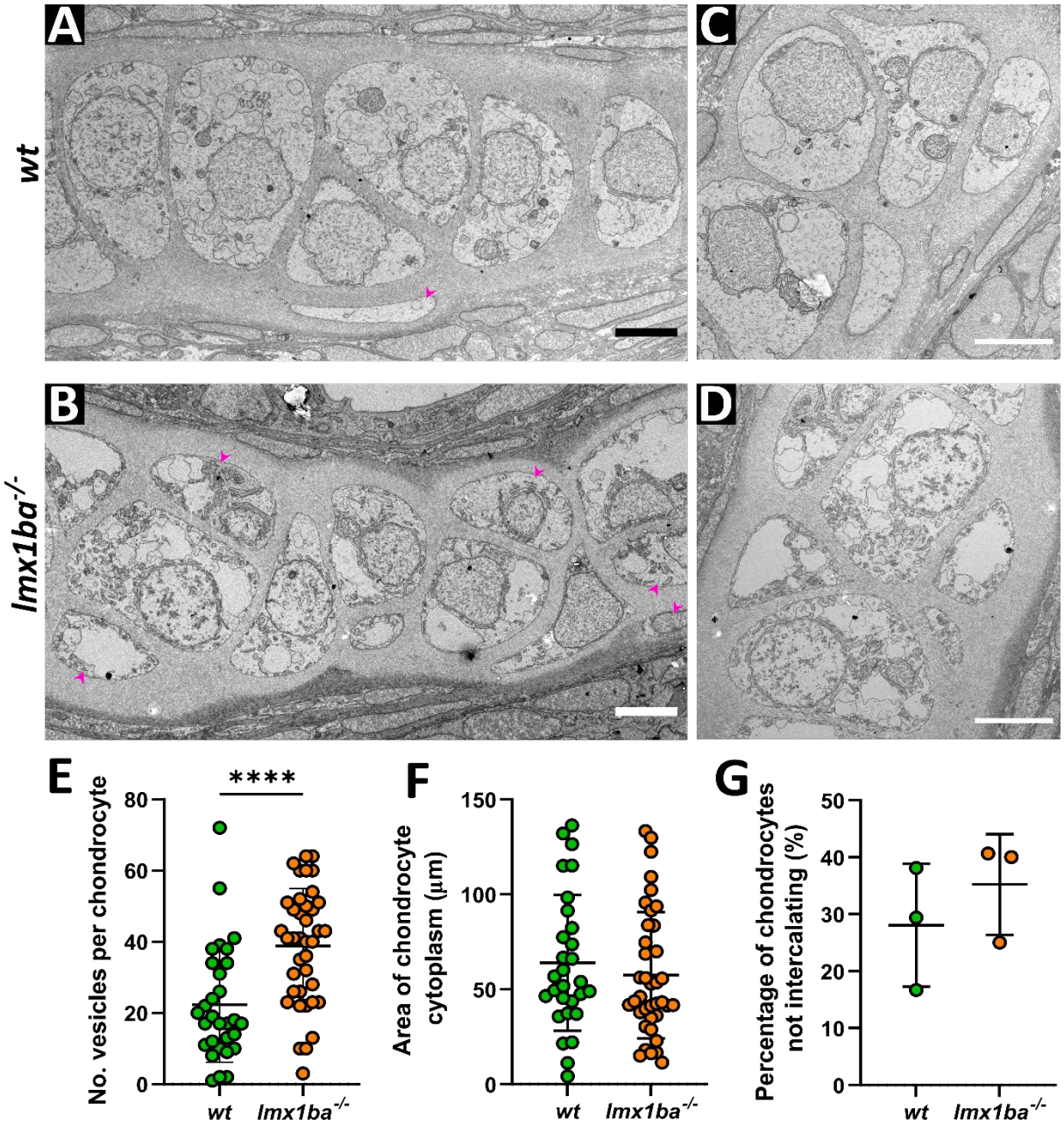

Figure 5.2.8 – Ultrastructure and organisation of chondrocytes affected in *lmx1ba* mutants, (A-D) Electron microscopy of ethmoid plate in *wt* and *lmx1ba* mutant fish at 5dpf. **(A, C)** Pink arrowheads highlight areas of non-uniformity and non-intercalating chondrocytes. Scale bars = 5μm for all. **(E)** Number of vesicles present per chondrocyte. Mann-Whitney unpaired t-test performed where, **** *P*<.0001. **(F)** Area of chondrocyte cytoplasm calculated by subtracting nuclear area from total chondrocyte area. **(G)** Number of chondrocytes on periphery of cartilage that are not aligning down central line of stack. Calculated as percentage of total cell number along ethmoid plate in one section per fish. N = 30 chondrocytes total from 3 larvae per genotype. Larval samples for TEM were processed and sectioned by Dr Chris Neal (School of Biochemistry, University of Bristol).

5.2.9 Rate of bone mineralisation is decreased in lmx1ba mutants

To see if the *lmx1ba* mutation affects other parts of the skeletal system, the rate of bone mineralisation in *lmx1ba* mutants was explored. Alizarin red is a calcium dye that can be used to detect mineralised bone in developing organisms by live staining. Here, it was used to stain the vertebrae of *wt* and *lmx1ba* mutant larvae at 5dpf, 7dpf and 10dpf. The mineralisation of zebrafish vertebrae begins between 4-5dpf (149), and can offer an insight into how well the early processes of bone formation are being performed.

At 5dpf, *wt* larvae showed partial mineralisation of the first few vertebral centrae (Figure 5.2.9A, *pink arrowheads*), whilst the *lmx1ba* mutants showed no mineralisation (Figure 5.2.9A and D). By 7dpf, *wt* larvae showed full mineralisation of several vertebrae (Figure 5.2.9B, *white arrowheads*), which increased in number by 10dpf (Figure 5.2.9C and D). Meanwhile, the *lmx1ba* mutant larvae showed significantly fewer mineralised vertebrae at 7dpf, with the majority of larvae having only 1 vertebrae mineralised, compared to an average of 4 in *wt.* By 10dpf, the *lmx1ba* mutants showed an increase in bone mineralisation rate, although they still had fewer vertebrae mineralised compared to *wt* (an average of 18 in *wt* compared to 13 in the *lmx1ba* mutants; Figure 5.2.9D). Therefore, the rate of bone mineralisation is decreased in *lmx1ba* mutants and suggests that loss of *lmx1ba* causes delays to the maturation and development of cells within the skeletal system. This is in line with the previous results which suggests that loss of *lmx1ba* delays chondrocyte maturation. As the *lmx1ba* mutants do survive to adulthood their skeletons must become mineralised, albeit at a slower rate compared to *wt.* The effect this delay has on skeletal formation and maintenance will be explored next.

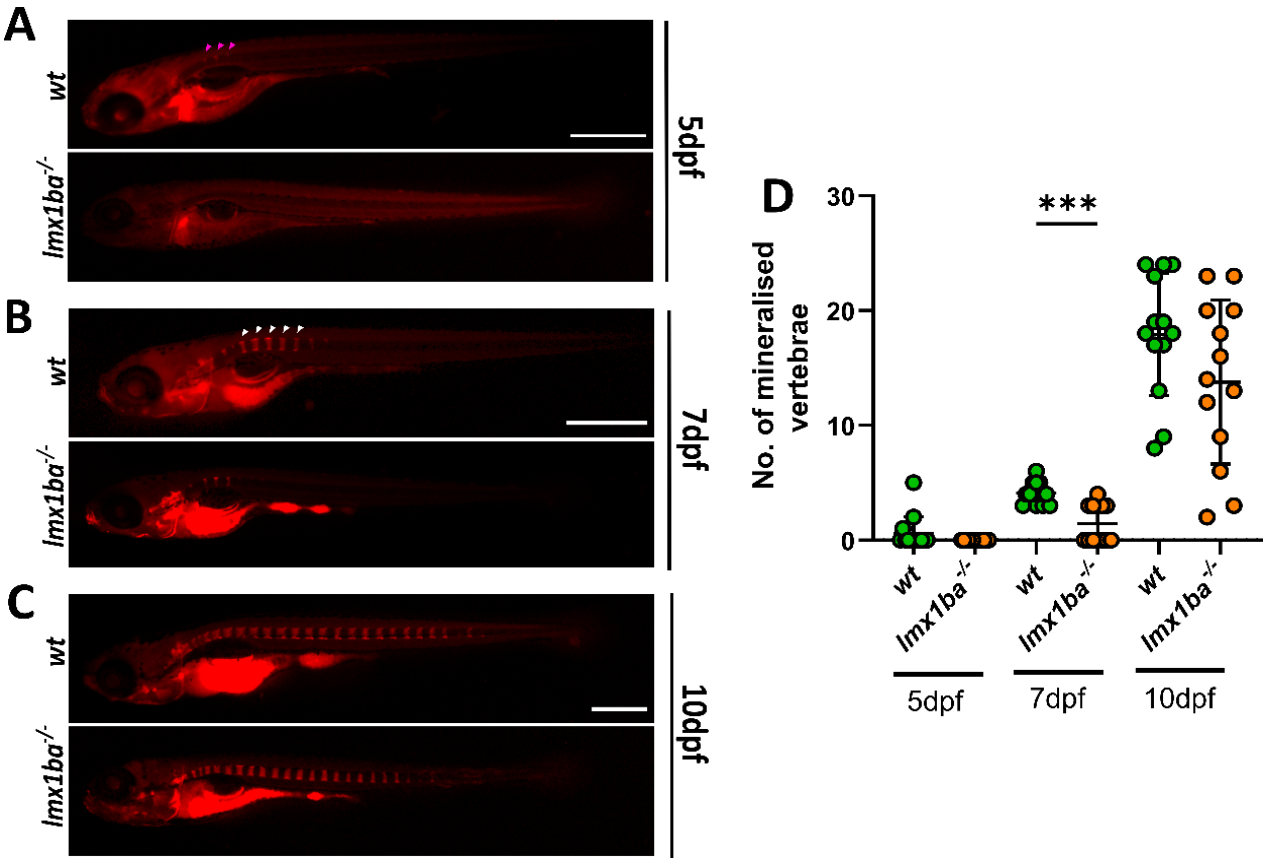

Figure 5.2.9 – The *lmx1ba* mutants show a delay to bone mineralisation in the spine, (A) Representative lateral stereomicroscope images of *wt* and *lmx1ba* mutant larvae at **(A)** 5dpf, **(B)** 7dpf and **(C)** 10dpf following live staining with Alizarin red for 1 hour. Pink arrowheads show example of partially mineralized vertebrae; white arrowheads show example of fully mineralized vertebrae. Scale bar = 500μm for all. **(D)** Graph showing the number of mineralized vertebrae per fish at each time point. N = 13 for both genotypes and all ages. Mann-Whitney u test performed where *** *P*=.0002.

5.2.10 Adult lmx1ba mutants show signs of premature ageing in the spine compared to wt

To analyse whether changes to early skeletal development and maturation seen in the *lmx1ba* mutants has any effect on the adult skeletal system, the skeletons of adult *wt* and *lmx1ba* mutants were analysed via micro-computed tomography (μCT) (Figure 5.2.10). Age matched siblings were not available for analysis and therefore, pre-scanned *wt* fish from the Hammond lab database were used instead. Fish at 8-9mpf and 16-18mpf for *wt* and *lmx1ba* mutants, respectively, were scanned and segmented. Once segmented, the skeleton can be analysed in 3D for changes to bone morphology and for signs of degeneration.

As they age, zebrafish naturally develop signs of bone degeneration and characteristics associated with OA, such as osteophytes (bone spurs), vertebral fusions and spinal curvature (160). These typically progress after 1 year of age where few abnormalities are seen; then increase by 2 years, with more frequent and severe abnormalities by 3 years (160). For this thesis, changes to spinal morphology and the vertebrae were largely focussed on, as these give the best indication for OA onset.

In the 8mpf *wt* fish, almost no spinal abnormalities were seen, with only one fish showing signs of vertebral calcification (Figure 5.2.10A and E). By 18mpf, the number of abnormalities had increased with around 10% of vertebrae showing either osteophytes or vertebral fusions (Figure 5.2.10B and F). In the *lmx1ba* mutants, a significantly increased number of spinal abnormalities were seen from 9mpf, with all *lmx1ba* mutants showing signs of premature OA in their spines (Figure 5.2.10C and D). The most common defect was vertebral fusions seen in over 20% of vertebrae (*pink arrowheads*), followed by osteophytes (11%; *pink asterisks*) and vertebral calcifications (6%; *white asterisks*) (Figure 5.2.10C and G). A small number of dislocations between vertebrae were also seen, creating bends in the spine (Figure 5.2.11C, *white arrowheads*). By 16mpf, the majority of *lmx1ba* mutant vertebrae had defects, with over 30% showing fusion between vertebrae (Figure 5.2.10D and H). Bends in the spine were also more severe, occurring both in the middle and tail end of the spine (Figure 5.2.10D). Therefore, degenerative changes to the spine are accelerated in the *lmx1ba* mutants, with younger adults showing signs of OA much earlier than *wt* fish.

5.2.11 Analysis of swim behaviour reveals changes to spinal curvature in lmx1ba mutants

To assess whether these premature signs of spinal degeneration have any impact on movement and swim ability in the *lmx1ba* mutants, videos of *wt* and *lmx1ba* mutant fish swimming in an open tank were taken at 6mpf and 3mpf, respectively (Figure 5.2.11A). Individual fish were placed into a tank and filmed for 10 minutes from above. A modular image analysis (MIA) program, which can outline the body of the fish and track it's movements within the tank, was used to analyse the videos (Figure 5.2.11A, *fish body outlined in red; orange line shows tracking line*). The analysis works by determining how far from the central line of their body (termed 0), a fish bends either to the right or left, giving a measurement of up to +1 for the

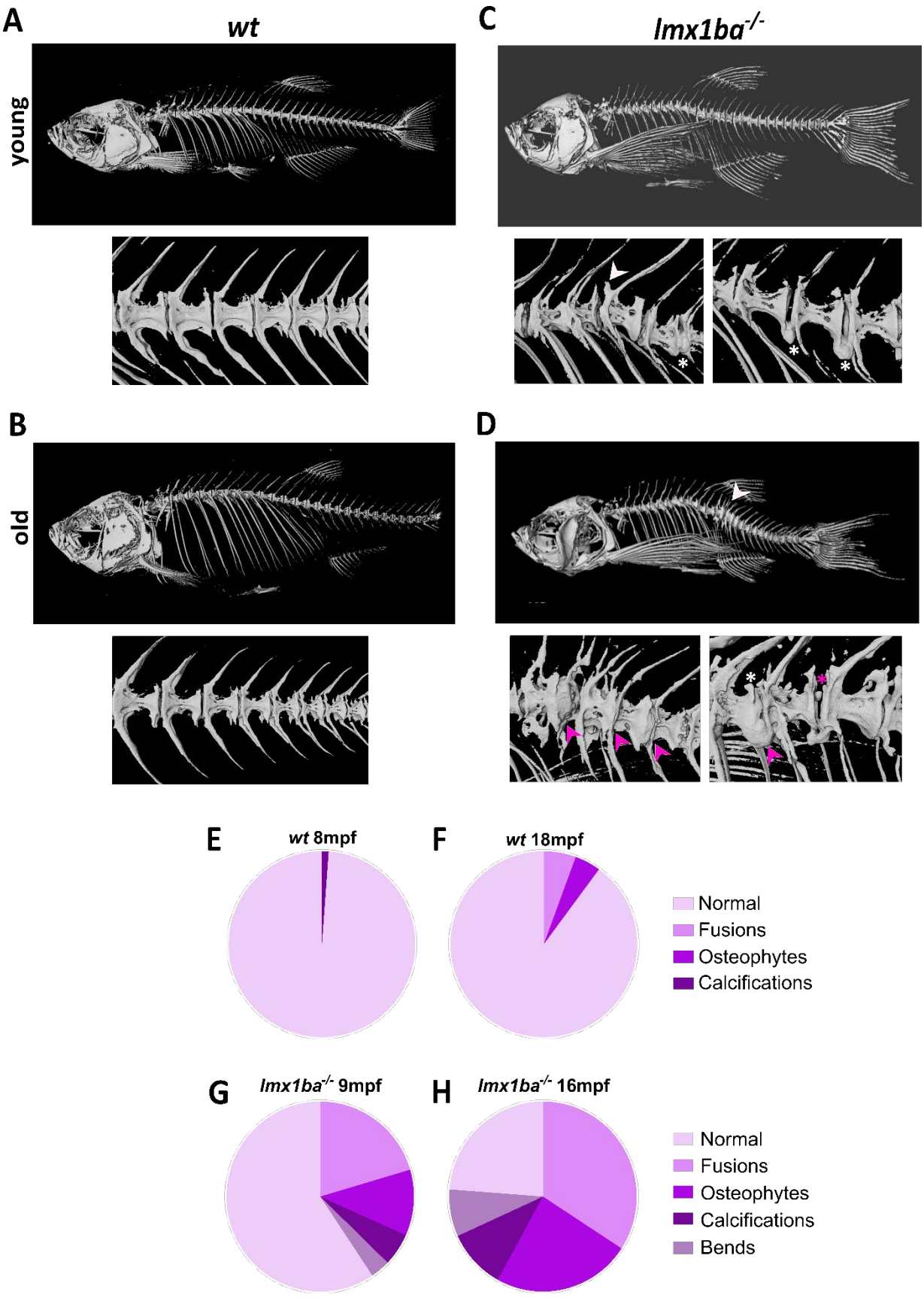
A
wt
C
lmx1ba-/-
young
B
old
D
E
wt 8mpf
F
wt 18mpf
Normal
Fusions
Osteophytes
Calcifications
G
lmx1ba-/- 9mpf
H
lmx1ba-/- 16mpf
Normal
Fusions
Osteophytes
Calcifications
Bends

Figure 5.2.10 – Signs of premature OA can be seen in spines of aged *lmx1ba* mutants, Representative 3D volume renderings of **(A, B)** *wt* and **(C, D)** *lmx1ba* mutant spines taken from μCT images at 8mpf and 18mpf for *wt,* and 9mpf and 16mpf for *lmx1ba* mutants. For 18mpf *wt* fish, the tail was cut off prior to μCT scanning. White arrowheads highlight vertebral dislocations; pink arrowheads show vertebral fusions; white arrows show osteophytes; white asterisks show calcifications, and pink asterisks highlight spinal bends. μCT scans and skeletal segmentations performed by Qiao Tong, PhD student, University of Bristol. Quantification of spinal abnormalities at **(E)** 8mpf in the *wt,* **(F)** 9mpf in the *lmx1ba* mutants, **(G)** 18mpf in the *wt,* and **(H)** 16mpf in the *lmx1ba* mutants. Measured as the average number of vertebrae showing each, or no, abnormality as a percentage of total vertebrae number. N = 3 for all ages and genotypes.

right-sided bends, and of up to -1 for the left-sided bends (Figure 5.2.11B). Looking at the maximum spine curvature movement made to both the right and left for each fish, it was found that the *lmx1ba* mutants do not bend as much in either direction as the *wt* fish (Figure 5.2.11C). Similarly, when looking at the three highest curvature events going right or left, the *lmx1ba* mutants showed a decreased range of bending at the spine compared to *wt* (-0.16 – 0.15 mm^{-1} in the *lmx1ba* mutants compared to -0.39 – 0.27 mm^{-1} in the *wt*; Figure 5.2.11D). However, no change to where along the fish these bends were being made was seen in the *lmx1ba* mutants compared to *wt* (Figure 5.2.11E). For this analysis, the lower down within the body of the fish the bend occurs, the higher the value given, with the values ranging from 0 (the head), to +1 (the tip of the tail) (Figure 5.2.11E, *schematic on right*). On average, per fish, the *lmx1ba* mutants were bending in the same location as the *wt* fish. However, given the changes to spine curvature in the *lmx1ba* mutants and early signs of spinal degeneration, it is likely that this would change as the fish age.

Overall, these results show that the *lmx1ba* mutants are consistently bending less than *wt* fish as they swim and that their maximal range of movement at the spine is reduced. Although these results are not significant, they show a trend towards the *lmx1ba* mutants having a decreased level of spinal curvature compared to *wt*, which given that the *lmx1ba* mutants are only 3mpf in this analysis, this difference would be expected to increase as they age.

Taken altogether, these data indicate that loss of *lmx1ba* affects cartilage and skeletal development, causing changes to skeletal morphology which affects their movement as adults. The increasing incidence of skeletal abnormalities in the older *lmx1ba* fish also indicates a role for *lmx1ba* in skeletal maintenance, although these changes could also be due to abnormal and deficient bone formation in development, leading to a weaker skeleton that

is more prone to damage from increasing mechanical load and ageing. Therefore, further investigations are required to determine whether the loss of *lmx1ba* affects only early development, or if it is required in skeletal maintenance into adulthood, however, these results point to a clear role for *lmx1ba* in skeletogenesis and as a gene of interest in OA development. Moving forward, the role of *lmx1b* in zebrafish brain and neuronal cell development will be explored next.

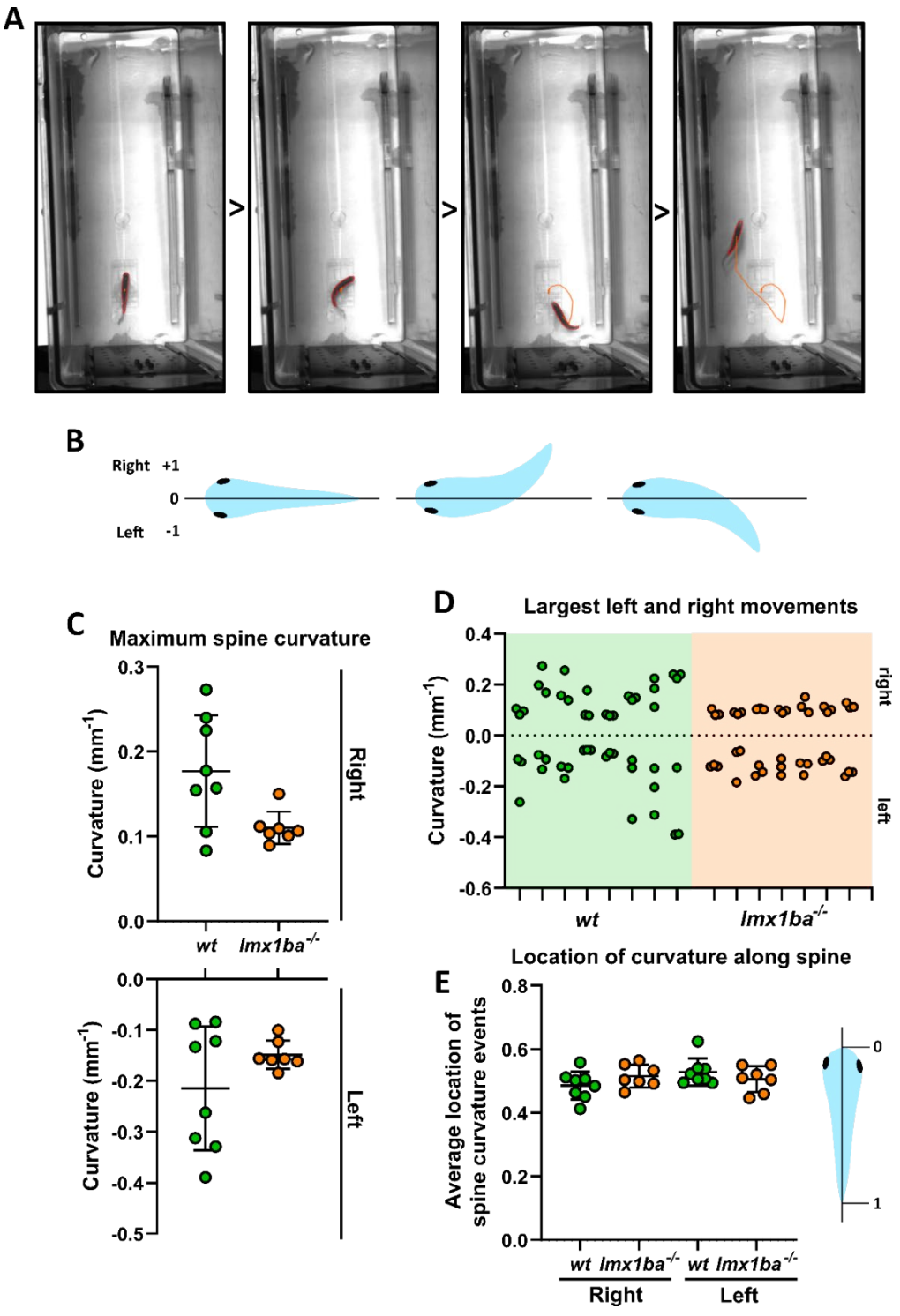

Figure 5.2.11 – Decreases in spine curvature seen by 3mpf in *lmx1ba* mutants, (A) Sequential individual stills taken from video showing tracking of adult fish as it swims. Tracking performed over 500 frames (33 seconds) per video; videos taken at 15 frames per second. Fish body outlined in red and orange line behind fish shows tracking of fish movement in each individual frame. Videos analysed using modular image analysis software developed by Dr Stephen Cross (University of Bristol). **(B)** Schematic showing how body curvature is measured by the modular image analysis (MIA) program, developed by Dr Stephen Cross (University of Bristol). When fish is straight, value of 0 given; when fish bends right, value up to 1 given; when fish bends left, value up to -1 given. Measurements given per frame of video. **(C)** Graph showing maximum spine curvature made to the right and left. One datapoint per fish. **(D)** Graph showing largest 3 movements each fish made to the right and left. Each downward dash on x-axis indicates total of 6 measurements from one fish. **(E)** Graph showing average location of spine curvature events per fish (*left*), where movements made closer to head are given a value between 0-0.5 and movements made closer to tail are given a value from 0.5-1 (*right*).

Exploring the effect of loss of *lmx1b* on neuronal development and adult behaviour

5.2.12 Complete loss of lmx1b affects gross brain morphology in early development

To investigate whether loss of *lmx1ba* or *lmx1bb* expression has an effect on brain development, lateral images of larval heads were taken at 1dpf and analysed (Figure 5.2.12). Firstly, the height of the ventricle space was measured (Figure 5.2.12A, *red lines*). The brain ventricular system is highly conserved in vertebrates and is one of the earliest structures to form during brain development. (363). It forms as cavity deep within the brain and is responsible for developing the neuronal circulatory system (364, 365). Therefore, ventricle height can be used as a measure of normal early brain development. Neither single mutant showed any changes to ventricle height compared to *wt* (Figure 5.2.12B). However, ventricle height could not be measured in the *dKO* mutants (Figure 5.2.12B, *red asterisk*), as no clear ventricle outline could be observed. This indicates abnormalities in early brain formation in the *dKO* mutants.

To analyse this further, midbrain-hindbrain boundary (MHB) formation was observed as an indicator for healthy brain formation. The MHB is a highly conserved fold in early vertebral brains (Figure 5.2.12C), which functions as an embryonic organizing centre (185), later forming the cerebellum and part of the tectum (366, 367). By observing the degree of MHB formation, a severity scale was designed: no abnormality indicating full formation (as shown in *wt*, *lmx1ba*$^{-/-}$ and *lmx1bb*$^{-/-}$ in Figure 5.2.12A); mild abnormality as partial MHB formation;

moderate as early ventricle constriction, and severe as an absence of clear MHB formation (shown by *dKO* in Figure 5.2.12A). The *lmx1bb* mutants showed a slighter greater number of larvae at 1dpf with mild abnormalities in MHB formation, but overall, both single mutants showed comparable MHB formation to *wt* (93% and 84% of *lmx1ba* and *lmx1bb* mutants, respectively, showed normal MHB formation compared to 93% in *wt*; Figure 5.2.12D). However, as indicated by the results in Figure 5.2.12B, the *dKO* mutants showed abnormalities in MHB formation, with the majority of larvae having either a moderate or severe abnormality (70% together), and none showing normal MHB formation (Figure 5.2.12D).

Together, these results indicate that *lmx1b* plays a very important role in early brain development and formation, although loss of both *lmx1b* paralogues is required to see this phenotype. The minimal disruption to MHB formation and ventricle height seen in the *lmx1ba* and *lmx1bb* mutants is consistent with data from morpholino experiments in zebrafish, where a single knock-down of either *lmx1ba* or *lmx1bb* was not sufficient to affect MHB formation (185). This suggests that either paralogue is compensating for the other, indicating overlapping functions for these paralogues within the brain.

5.2.13 Increased cell death found in brain region of lmx1b mutants

Despite only the *dKO* mutants showing a change to early brain development, cell death assays were performed to explore whether loss of *lmx1b* is affecting cell survival in the brain region. Initially, this was done using the live dye, acridine orange which is a nucleic binding agent. When intercalated with double stranded DNA, acridine orange emits a green fluorescence. In healthy cells this appears as a diffuse green stain whilst apoptotic cells are displayed as bright green puncta. Larvae were incubated with acridine orange at 1dpf and then imaged in the head region (Figure 5.2.13). As expected during early developmental stages, some green puncta were visible in *wt* at 1dpf (Figure 5.2.13A). However, the *lmx1ba, lmx1bb* and *dKO* mutants showed a greater accumulation of green puncta mainly in the brain region around the ventricles (Figure 5.2.13A). This indicates an increase in cell death in the *lmx1b* mutants, with loss of *lmx1ba* or both paralogues together having the greatest effect on cell death.

To explore this further, TUNEL staining was used next. TUNEL (terminal deoxynucleotidyl

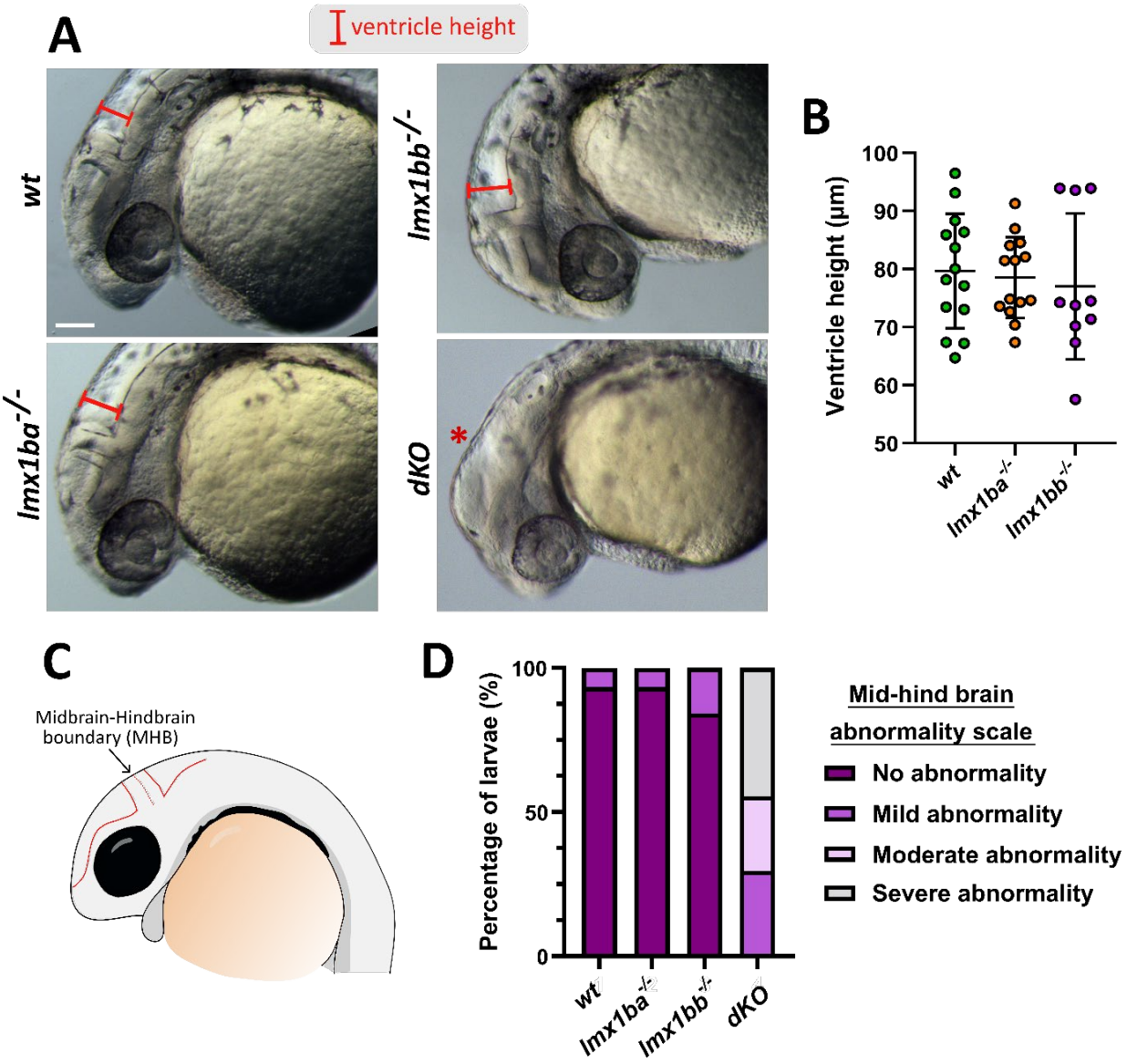

Figure 5.2.12 – Only *dKO* mutants show differences in overall brain morphology at 1dpf compared to *wt*, (A) Representative stereomicroscope images of *wt,* and *lmx1ba, lmx1bb* and *dKO* mutant larvae at 1dpf. Red lines indicate where ventricle height measurements were taken from. Red asterisk indicates no ventricle height measured due to lack of discernible ventricles. Scale bar = 100µm. **(B)** Quantification of ventricle heights; n = 14 for *wt* and *lmx1ba* mutants and 10 for *lmx1bb* mutants. **(C)** Schematic outlining boundary between the midbrain and hindbrain within larvae at 1dpf. **(D)** Quantification of percentage of larvae showing normal or abnormal mid-hind brain boundary formation across *wt* and mutant genotypes. N = 30 for *wt* and *lmx1ba* mutants, 19 for *lmx1bb* mutants and 27 for *dKO* mutants.

transferase dUTP nick end labelling) staining works by attachment of a fluorescently labelled antibody to the ends of DNA breaks via the enzyme, terminal deoxynucleotide transferase (TdT). These DNA breaks occur during DNA fragmentation in the final stages of

apoptosis. Therefore, this assay is a more sensitive detector of apoptotic cells compared to staining with acridine orange and allows for the number of apoptotic cells to be more accurately quantified.

TUNEL staining was performed at 1dpf on *wt* and *lmx1ba* mutant larvae as they showed the greatest increase in cell death compared to the *lmx1bb* mutants (Figure 5.2.13B). Unfortunately, due to time constraints, TUNEL staining could not be performed on the *dKO* mutants. Overall, the *lmx1ba* mutants showed an increase in the number of TUNEL-positive cells compared to *wt*, with puncta being found along the length of the brain, from the forebrain to hindbrain and around the eye (Figure 5.2.13C). Without a co-stain it is difficult to pinpoint the cell types that are showing increased cell death, although the location of the acridine orange and TUNEL-positive puncta would suggest that these include neuronal and retinal cell populations. To explore this further, immunostaining was performed on the *lmx1ba* and *dKO* mutants using a neuronal cell marker.

5.2.14 Expression of TH-positive dopaminergic (DA) neurons is reduced in lmx1ba and dKO mutants

LMX1B is known to help regulate the expression and differentiation of mesencephalic dopaminergic neurons in early development (346). As mentioned, loss of *Lmx1b* expression during early development has been shown to significantly reduce DA neuronal number in mouse embryos (218). To explore the effect of the *lmx1ba* and *dKO* mutations on DA neuron development and survival, larvae were immunostained for tyrosine hydroxylase (TH) at 3dpf and their brains imaged (Figure 5.2.14). TH is an enzyme which helps convert tyrosine to L-DOPA in DA neurons and therefore, is a commonly used marker for detecting DA neurons in the central nervous system (368, 369).

Compared to *wt*, both the *lmx1ba* and *dKO* mutants showed a decrease in the average number of TH-positive neurons found within the forebrain and midbrain (Figure 5.2.14A-C). The *dKO* mutants showed the greatest average decrease in TH-positive cell number in the forebrain: an average of 17 versus 27 in the *wt*, and 21 in the *lmx1ba* mutants. Whilst in the midbrain, both mutants showed a similar reduction (Figure 5.2.14C). However, none of these results were statistically significant and instead indicate more of a trend in decreased TH cell number in the *lmx1b* mutants compared to *wt.*

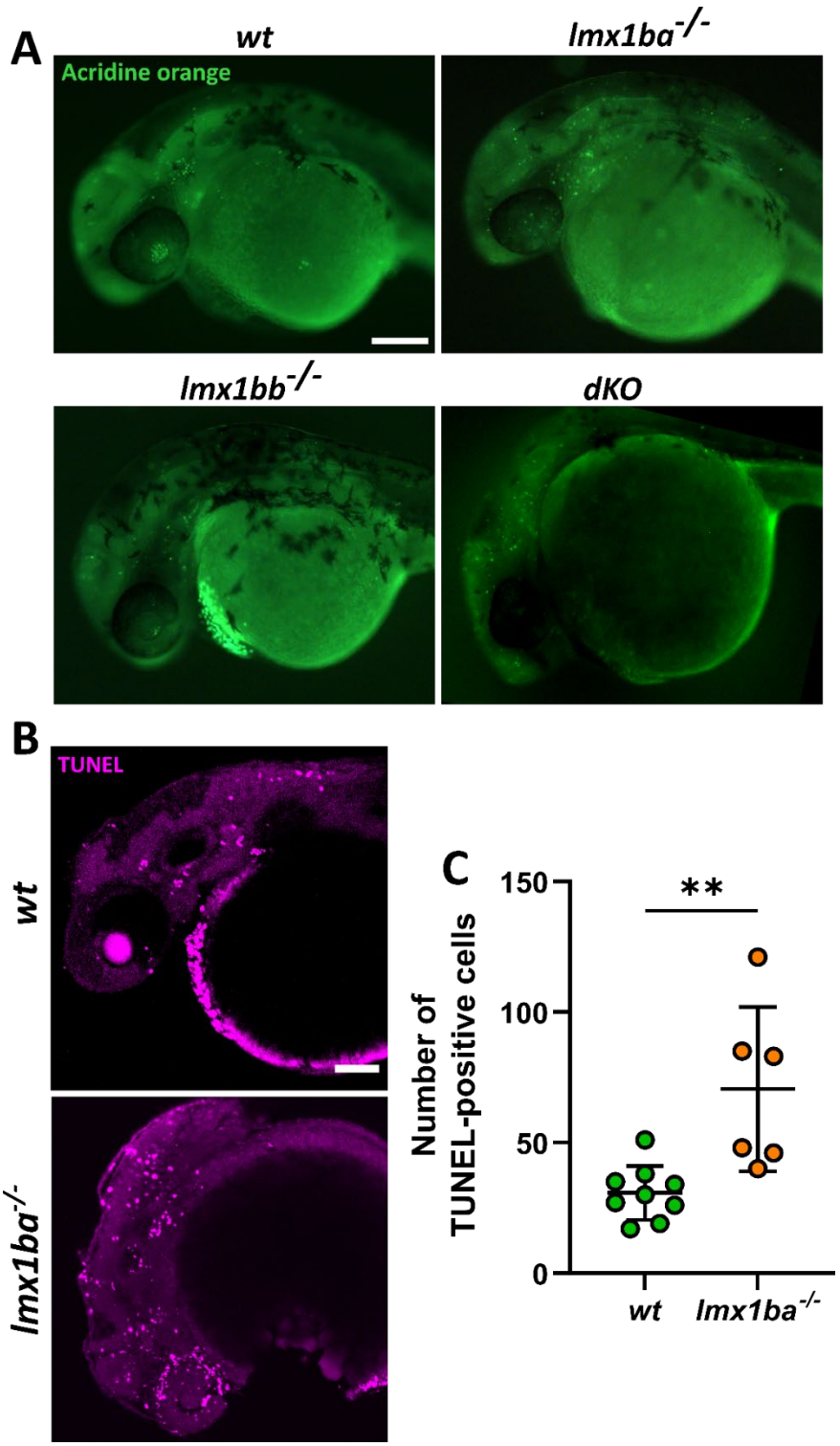

Figure 5.2.13 – The *lmx1b* mutants show an increase in cell death around the brain region at 1dpf compared to *wt*, (A) Representative stereomicroscope images of *wt,* and *lmx1ba, lmx1bb* and *dKO* mutant larvae at 1dpf stained with acridine orange (green). Scale bar = 100μm. **(B)** Representative max projections of TUNEL stained (magenta) *wt* and *lmx1ba* mutant larvae at 1dpf. Scale bar = 100μm. **(C)** Quantification of number of TUNEL puncta present in each fish within the head region. N = 9 for *wt* and 6 for *lmx1ba* mutants. Student's unpaired t-test performed where ** *P*=.0035.

Taken together with the results from the cell death assays in Section 5.2.13, these data suggest that this decrease in neuronal number in the *lmx1ba* and *dKO* mutants is due to increased cell death. Therefore, loss of *lmx1b* affects the survival of DA neurons causing a decrease in the number of TH-positive cells by 3dpf.

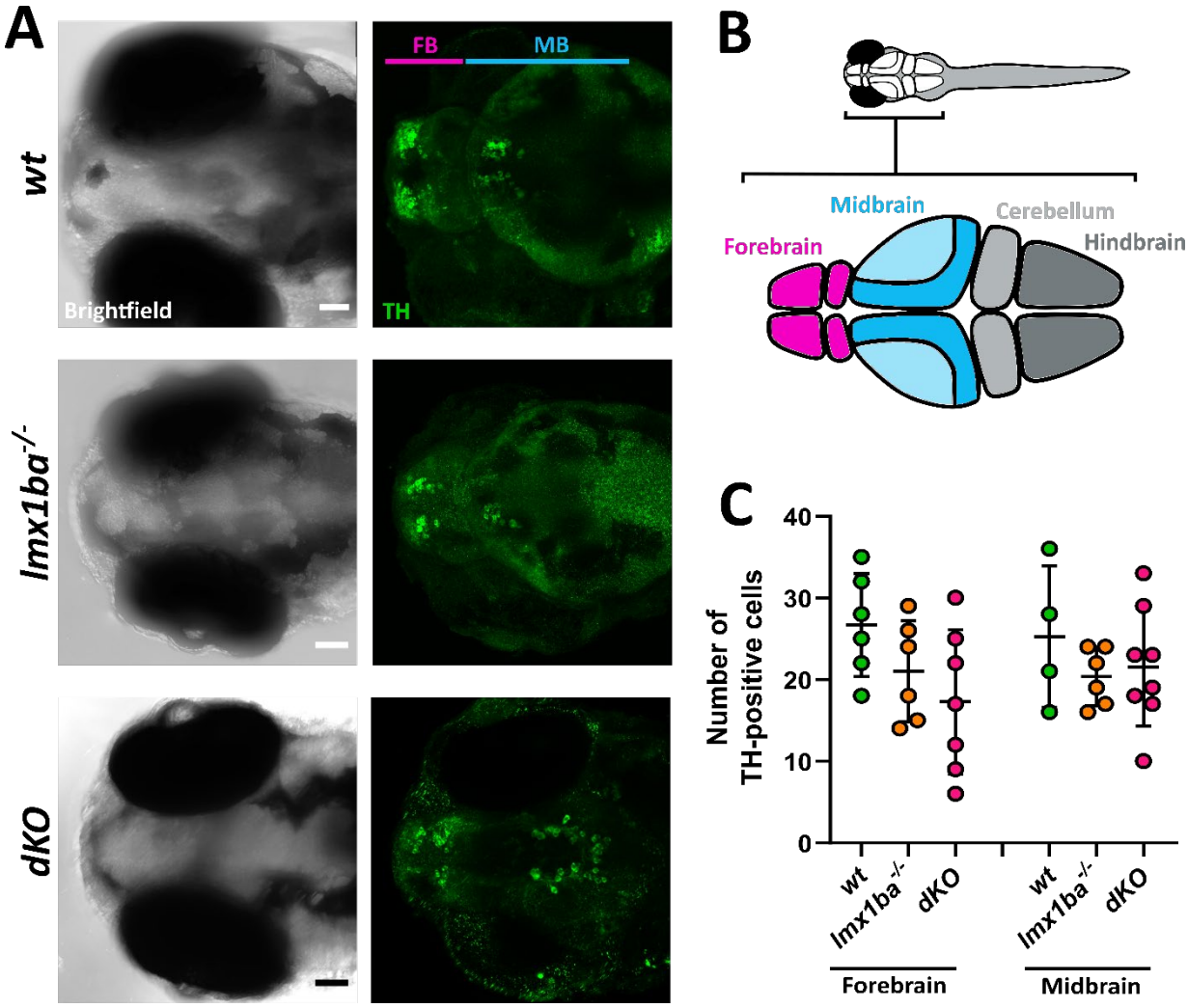

Figure 5.2.14 – *lmx1ba* and *dKO* mutants show a reduction in TH-positive cell number within the forebrain and midbrain at 3dpf, (A) Representative confocal max projections of brightfield images and TH immunostaining (green) in *wt,* and *lmx1ba* and *dKO* mutant larvae at 3dpf. Forebrain (FB) and midbrain (MB) regions highlighted by pink and blue lines, respectively. Scale bars = 50µm. **(B)** Schematic showing the basic brain morphology in zebrafish larvae and locations of key brain structures. Schematic adapted from Society of Neuroscience, eNeuro blog. **(C)** Quantification of number of TH-positive cells in the forebrain and midbrain in each genotype. N = 6 and 4, respectively for *wt;* 6 for both for *lmx1ba* mutants; and 7 and 8, respectively for *dKO* mutants. One-way ANOVA performed for each brain region.

5.2.15 Mutants show no changes to swim speed but are less risk adverse compared to wt

Given the observed changes to the survival of DA neurons in the *lmx1ba* and *dKO* mutants, the effect of these changes on adult behavioural patterns was explored on adult fish at 3-6mpf. Dopamine activity is known to regulate a variety of behaviours including risk awareness and anxiety, among others (370). Meanwhile, degeneration of the mesencephalic DA system, a region whose development is regulated by LMX1B, has been shown to significantly affect behaviour and movement control as highlighted in patients with Parkinson's disease (218). Therefore, it was hypothesised that a reduction in DA neurons might affect the behaviour of the mutants compared to *wt.* To test this, individual fish were placed into a new tank and their behaviour was recorded over 10 minutes. When placed in a novel environment, standard *wt* behaviour would be to remain at the bottom of the tank (the 'safest' area in the new environment) and exhibit periods of 'freezing' or zero movement. As the fish acclimatizes to the new environment, their behaviour would become more exploratory as they perceive no new threats or risks and swim further and into higher areas of the tank more frequently (239).

Freezing moments and the average speed of the fish was measured using an automated modular image analysis (MIA) program which can track fish from frame to frame (designed by Stephen Cross, University of Bristol). These measured were made during the first and last 90 seconds over a 10 minute period to assess differences in habituation over the test time. Due to the lethality of certain homozygous mutants, only certain genotypes could be tested as adults, including, *wt, lmx1ba*$^{-/+}$ and *lmx1ba*$^{-/-}$ mutants, *lmx1bb*$^{-/+}$ mutants and *lmx1ba*$^{-/+}$;*lmx1bb*$^{-/+}$ mutants (double heterozygotes, termed *dHet*). *KO;Het* mutant fish were not added to this analysis as they were not old enough when the experiment was performed.

For both measures, the results were very variable between individual fish of the same genotype and no significant difference was seen between genotypes or time points, except for the decreasing average speed of *lmx1ba* homozygous adults from the first to last 90 seconds (Figure 5.2.15A and B). Given the variability of the data, it is difficult to draw a conclusion and suggests that more fish may need to be analysed to reveal any patterns in behavioural response between genotypes. The lack of a pattern between the two time points also suggests

that these may not be the best measurements for tracking fish behaviour or that an extended period of time is required for fish to become habituated to a novel environment.

Place preference of the fish was assessed by splitting the tank into four zones within the tank, with zone 1 delineating the bottom of the tank and zone 4, the top. The position of the fish was automatically recorded from frame to frame across the full 10 minute video using a neural network (developed by Yushi Yang, PhD student, University of Bristol). Place preference did vary between the genotypes with the *lmx1ba*$^{-/+}$, *lmx1bb*$^{-/+}$ and *dHet* mutants spending less time in zone 1 and more time in zones 2-4 compared to *wt*, therefore, exhibiting more exploratory behaviour which is suggestive of reduced anxiety in a new environment (Figure 5.2.15D). Conversely, the *lmx1ba* homozygous mutants showed no changes to place preference, with results very comparable to *wt* (Figure 5.2.15D, *orange data points*). This is interesting as the *lmx1ba*$^{-/-}$ mutants showed the greatest level of cell death in the head region by acridine orange staining compared to the *lmx1bb*$^{-/-}$ mutants, and an overall reduction in dopaminergic cell number at 1dpf. This result could have been influenced by the age of the *lmx1ba*$^{-/-}$ mutants used, as they were only 3mpf when filmed, whilst *wt* and other mutants were all 5-6mpf. Therefore, changes to behaviour may only manifest beyond a certain age, as the fish move out of juvenile stages (1mpf-3mpf) and become adults (<3mpf).

The *lmx1bb*$^{-/+}$ and *dHet* mutants spent the least time of all genotypes in zone 1 (89% for *lmx1bb*$^{-/+}$ and 88% for *dHet* mutants, compared to 99% for *wt*), although overall, the *dHet* mutants spent more time in the higher zones (3 and 4) compared to the *lmx1bb*$^{-/+}$ mutants. Overall, these data suggest that compared to *wt*, loss of *lmx1b* affects the risk aversive behaviour of adult fish and that these mutants are less anxious, with the cumulative loss of *lmx1b* enhancing this effect.

Taken altogether, these data show that loss of *lmx1b* affects neuronal cell survival and DA cell number in the developing brain, which is in line with the phenotype seen in *Lmx1b* knock-out mice. Going further, these changes alter the behaviour of mutant fish as adults, demonstrating that early developmental changes caused by loss of *lmx1b* have a functional effect that manifests as the fish age. In the final section, the truncated body phenotype of the *dKO* mutants will be explored.

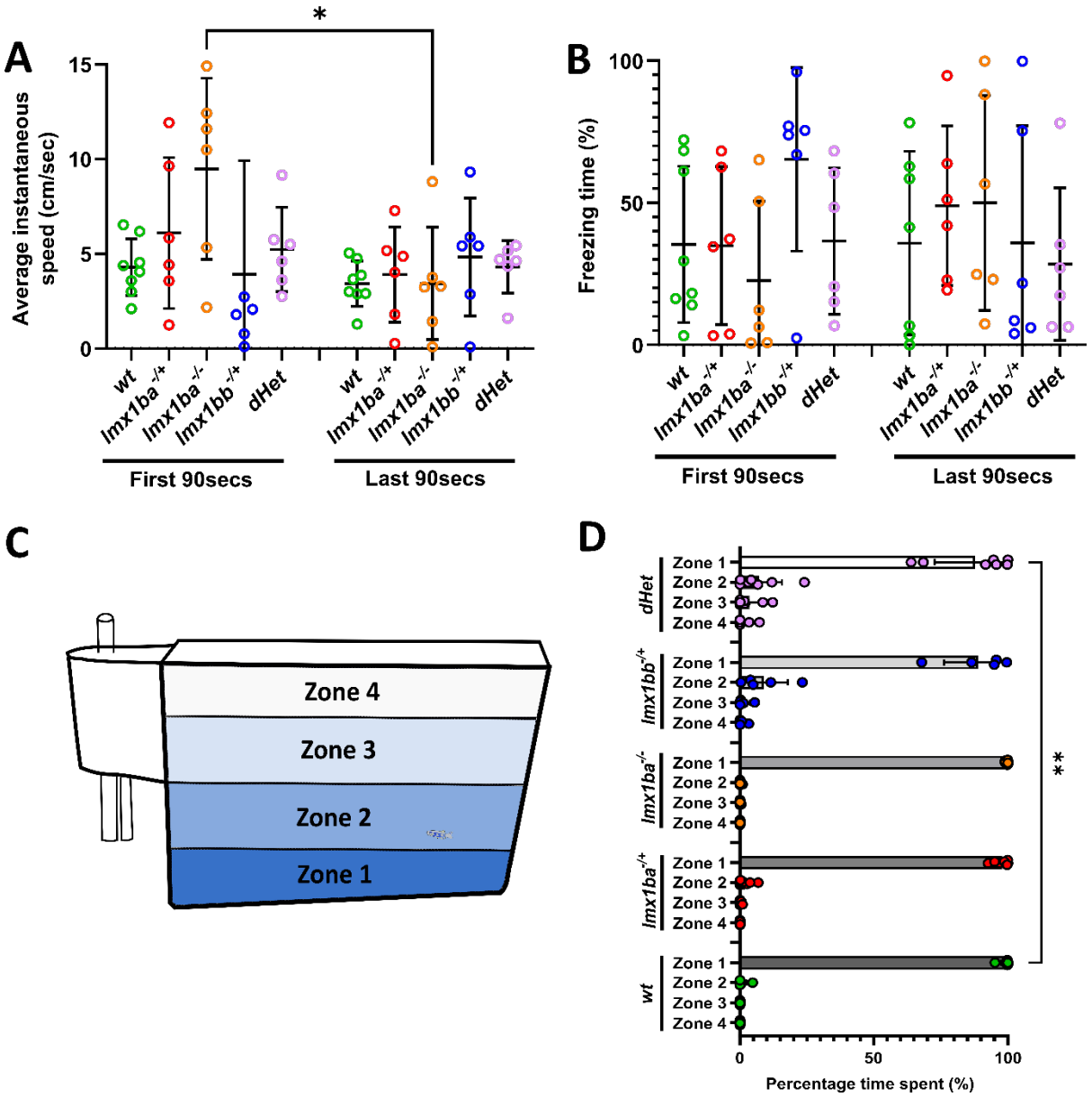

Figure 5.2.15 – Cumulative loss of *lmx1b* results in reduced anxiety in adult fish but no changes to swim speed, Graphs showing the **(A)** average instantaneous speed and **(B)** percentage of time spent frozen of *wt* and *lmx1ba*$^{-/+}$, *lmx1ba*$^{-/-}$, *lmx1bb*$^{-/+}$ and *dHet* mutant fish at 3mpf for *lmx1ba*$^{-/-}$, 5mpf for *wt* and *lmx1bb*$^{-/+}$ and 6mpf for *lmx1ba*$^{-/+}$ and *dHet*. Measurements taken during the first and last 90 seconds of a 10 minute video. Freezing time calculated as the total amount of time spent where a fish's speed was <0.8 cm/sec. N = 8 for *wt* and 6 for all *lmx1b* mutants. **(C)** Schematic showing the splitting of the tank into zones. **(D)** Graph showing the percentage of time each fish spent in each zone over 10 minutes. N = 8 for *wt*, and *lmx1ba*$^{-/+}$ and *lmx1ba*$^{-/-}$ mutants, 5 for *lmx1bb*$^{-/+}$ mutants and 7 for *dHet* mutants. Two-way ANOVA performed for all where, * *P*=.044 and ** *P*=.0053.

Characterising the muscular phenotype of *dKO* mutants

5.2.16 Loss of lmx1b affects trunk muscle formation

Given the truncated body phenotype of the *dKO* mutants, an examination of the effect of *lmx1b* mutations on trunk muscle formation was performed. Larvae were immunostained against heavy chain skeletal myosin at 5dpf, and their trunk somites imaged by confocal microscopy (Figure 5.2.16A-F). The *lmx1ba* and *lmx1bb* mutants showed comparable trunk muscle formation compared to *wt,* with no obvious abnormalities in muscle fibre (myofibril) organisation (Figure 5.2.16A-C). The only minor observed differences seen were an increase in the gap between myofibrils, which appears slightly wider in both single mutants, and greater 'waviness' of some fibres, seen in the *lmx1ba* mutants. However, examples of both can also be seen in *wt* trunk muscle and therefore, they do not represent a large change to the normal, healthy phenotype. In comparison, the *dKO* mutants show a range of affected muscle phenotypes compared to *wt* (Figure 5.2.16D-F). The *dKO* mutants showed a high incidence of gaps between myofibrils (large gaps indicated in Figure 5.2.16D and E, *pink asterisks*), and branching of myofibrils perpendicular to the organisation of the somite fibres (Figure 5.2.16E, *white arrowheads*). In one case, complete loss of myofibril organisation was seen, with fibres forming no discernible pattern or structure within somites (Figure 5.2.16F).

To analyse these effects to trunk muscle formation, changes to somite size, fibre length and fibre organisation were quantified (Figure 5.2.16G-I). As expected, the *lmx1ba* and *lmx1bb* mutants showed minimal changes to somite size or fibre alignment (quantified as the percentage of green fluorescence coverage per somite, where decreased coverage indicates greater distance (i.e., gaps) between fibres) compared to *wt.* Compared to these three genotypes, the *dKO* mutants, however, have significantly smaller somites and decreased muscle coverage, indicating reduced fibre alignment and greater gaps between fibres (Figure 5.2.16G and I).

All three mutant genotypes did show a significant decrease in myofibril length compared to *wt,* with the *dKO* mutants showing the greatest difference in length (Figure 5.2.16H). For the *dKO* mutants this result, along with the decreased somite area, correlates with their vastly decreased body length at 5dpf. As somite number in the *dKO* mutants is comparable to *wt,*

these data suggest that the reduction in body length may be due to reduced myofibril elongation in the trunk. The decreased myofibril length in the *lmx1ba* and *lmx1bb* mutants is more intriguing as the *lmx1bb* mutants show only a slight decrease in whole body length at 5dpf, whilst the *lmx1ba* mutants are a comparable size to *wt*.

5.2.17 Abnormalities to dKO muscle formation are seen at early stages in larval development and their severity increases with age

Given the significant changes to *dKO* mutant trunk muscle at 5dpf, *wt* and *dKO* mutant larvae at 3dpf were analysed to determine whether these changes occur before or after 3dpf (Figure 5.2.17). At 3dpf, the *dKO* mutants showed a similar range of disturbed trunk muscle phenotypes as observed at 5dpf (Figure 5.2.17B-D). For some mutants, the disturbance to muscle formation seemed less severe (Figure 5.2.17C), although there was still an incidence of absent muscle patterning (Figure 5.2.17D), suggesting that this is an initial state rather than a progressive phenotype. A decrease in somite area, myofibril length, and percentage myosin coverage compared to *wt* was still seen at 3dpf in the *dKO* mutants, indicating that these abnormalities in muscle formation occur before 3dpf (Figure 5.2.17E-G). However, compared to 5dpf, differences in all three of these measurements between *wt* and the *dKO* mutants were less, demonstrating that muscle abnormalities increase in severity as the *dKO* fish age.

To explore this further, abnormalities such as large gaps between myofibrils and branching of myofibrils was quantified (Figure 5.2.17H, *pink asterisks*, and I, *white arrowheads*). At both 3dpf and 5dpf, there were no incidences of myofibril branching or large gaps between fibres, expect in one *wt* larvae. In contrast, all *dKO* mutants had a number of gaps between myofibrils, with this number increasing from an average of 11 gaps at 3dpf, to 26 gaps at 5dpf (Figure 5.2.17H, *pink datapoints*). Meanwhile, the majority of *dKO* mutants also showed branching of fibres, as demonstrated by the white arrowheads in Figure 5.2.17I. The number of branching events also increased from 3dpf to 5dpf. Therefore, these changes to muscle formation in the *dKO* mutants occur before 3dpf and progressively deteriorate as the fish age.

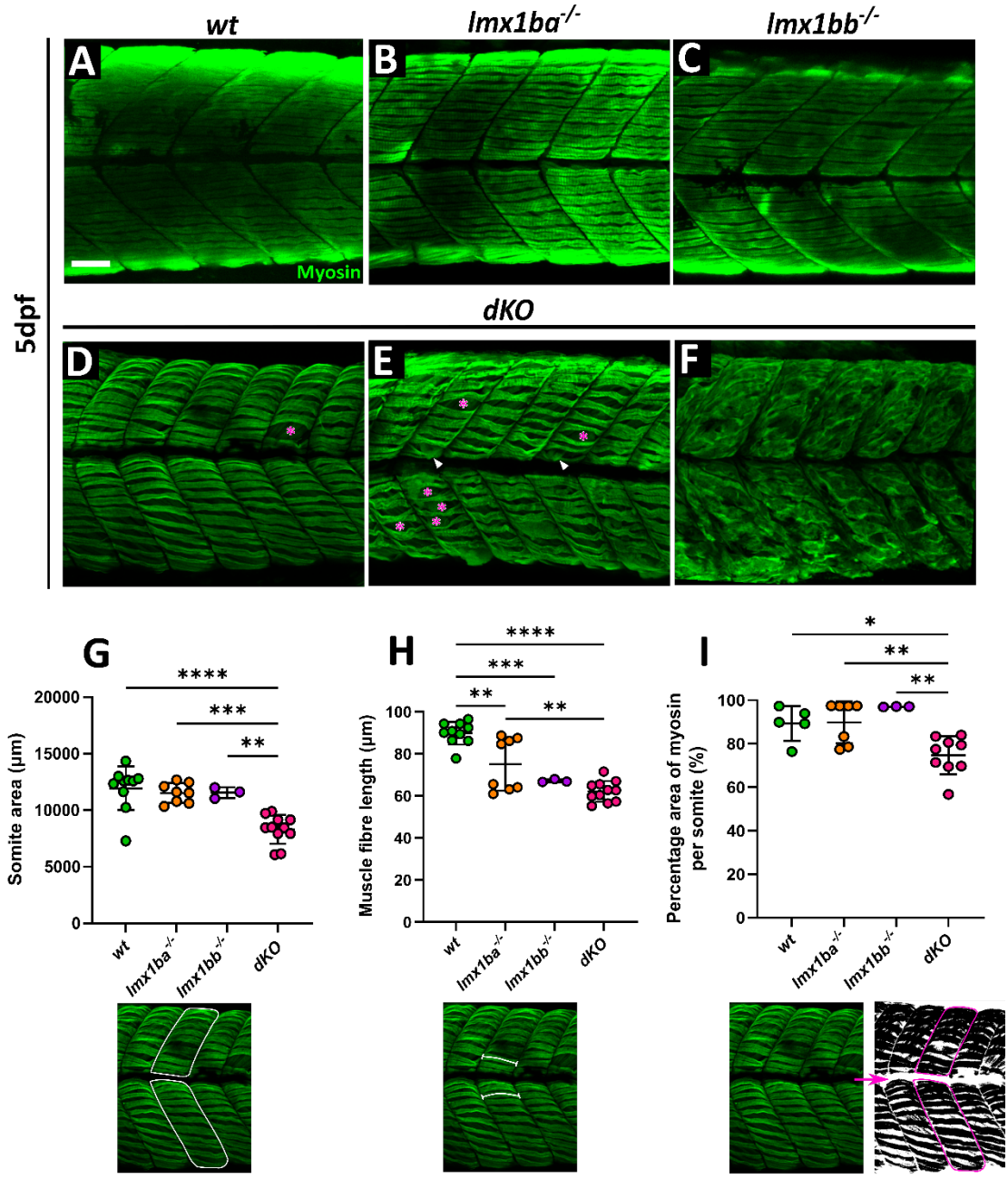

Figure 5.2.16 – The *dKO* mutants show a range of trunk muscle defects not seen in *wt*, or either *lmx1ba* and *lmx1bb* mutant, Representative confocal images of **(A)** *wt,* and **(B)** *lmx1ba,* **(C)** *lmx1bb* and **(D-F)** *dKO* mutant larval trunk somites at 5dpf, immunostained for muscle (green). Scale bar = 50µm. Pink asterisks in **(D)** and **(E)** indicate large gaps between myofibrils; white arrowheads in **(E)** indicate abnormal fibre branching. Quantification of **(G)** somite area**, (H)** myofibril length**,** and **(I)** the percentage coverage of muscle (myosin) staining per somite across all genotypes. Each data point is an average of measurements taken from three separate somites per fish. Schematics below graphs show how measurements were made. N = 11 for *wt* and *dKO* mutants, 8 for *lmx1ba* mutants, and 3 for *lmx1bb* mutants. In some instances, the quality of immunostaining meant that not all analyses could be performed on every image which will account for any differences in data point number between graphs. One-way ANOVAs performed for all graphs where, **** *P*<.0001, *** *P*<.001, ** *P*<.01 and * *P*<.05.

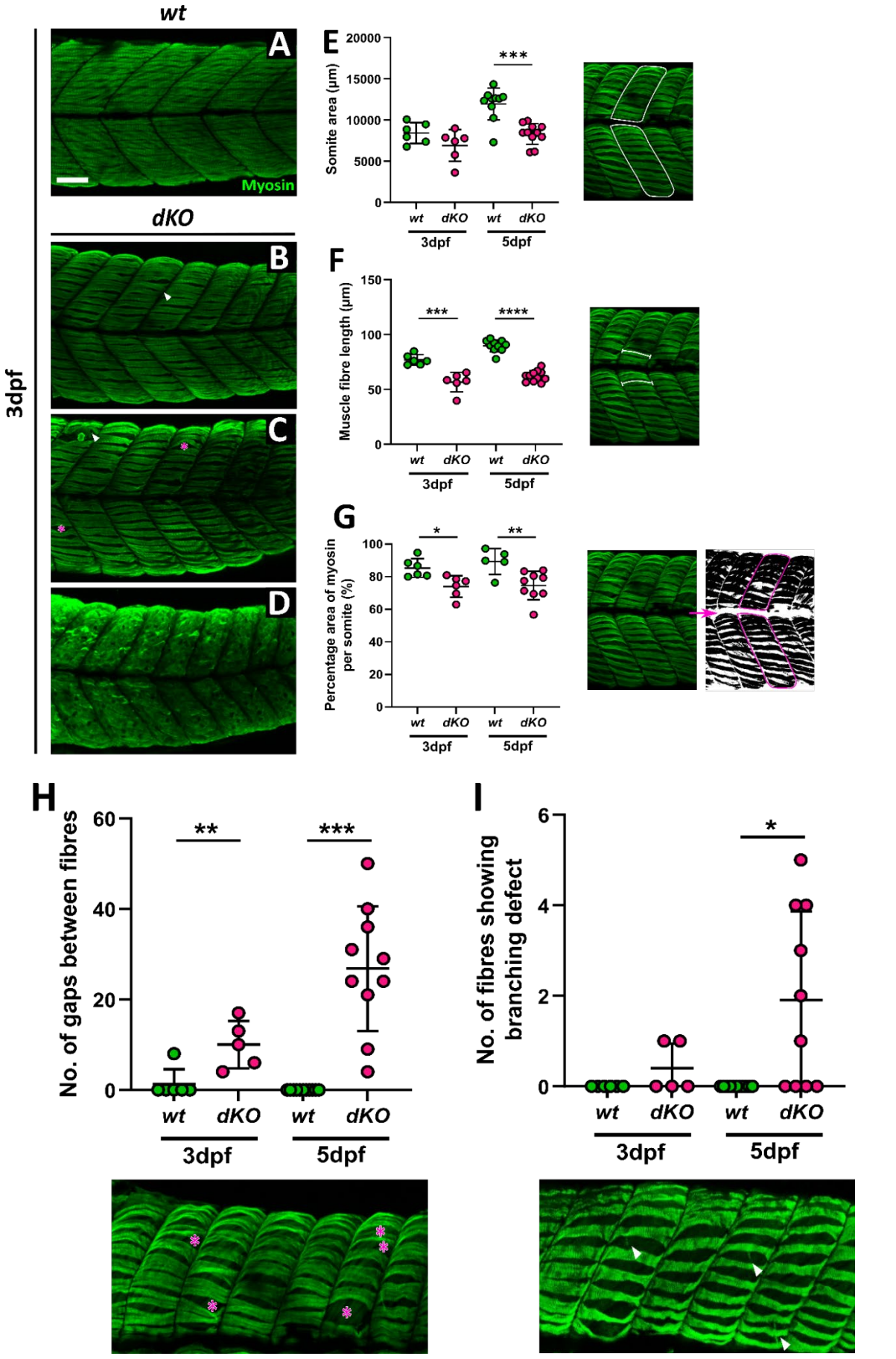
wt
dKO
3dpf
A
B
C
D
Myosin
E
Somite area (µm)
20000
15000
10000
5000
0
***
wt
dKO
wt
dKO
3dpf
5dpf
F
Muscle fibre length (µm)
150
100
50
0
***
****
G
Percentage area of myosin per somite (%)
100
80
60
40
20
0
*
**
H
No. of gaps between fibres
60
40
20
0
**
***
I
No. of fibres showing branching defect
6
4
2
0
*

Figure 5.2.17 – Changes to myofibril formation in *dKO* mutants seen from 3dpf, Representative confocal images of **(A)** *wt,* and **(B-D)** *dKO* mutants at 3dpf, immunostained for muscle (green). Scale bar = 50μm. Pink asterisks in **(B)** and **(C)** indicate large gaps between fibres; white arrowheads abnormal fibre branching. Quantification of **(E)** somite area**, (F)** myofibril length, **(G)** and the percentage coverage of muscle (myosin) staining per somite across both genotypes. Schematics to right hand side of graphs show how measurements were made. Each data point is an average of measurements taken from three separate somites per fish. N = 11 for *wt* and *dKO* mutants. Student's unpaired t-test or Welch's unpaired t-test performed at each age for all graphs where, **** *P*<.0001, *** *P*<.001, ** *P*<.01 and * *P*<.05. Graphs show **(H)** number of large fibre gaps and **(I)** fibre branching events in *wt* and *dKO* mutants at 3dpf and 5dpf. Schematics below graphs show how measurements were made where pink asterisks indicate large gaps between fibres and the white arrowheads, abnormal fibre branching events. N = 6 for *wt* and *dKO* mutants at 3dpf, and 11 for *wt* and *dKO* mutants at 5dpf. Welch's unpaired t-test performed at each age on both graphs where, *** *P*=.0002, ** *P*=.0084 and * *P*=.0138. In some instances, the quality of immunostaining meant that not all analyses could be performed on every image which will account for any differences in data point number between graphs.

5.2.18 No major changes to craniofacial musculature in dKO mutants during development

Given the significant changes to trunk musculature in the *dKO* mutants, formation of the craniofacial muscle was explored to see this is also affected by loss of *lmx1b*. As before, *wt* and *dKO* mutant larvae were immunostained against heavy chain skeletal myosin and co-stained with DAPI to highlight the lower jaw cartilage at 3-5dpf. Lateral images of the head of each fish at 5dpf showed no obvious changes to craniofacial musculature (Figure 5.2.18A). To analyse this further, the musculature of the lower jaws was imaged, and the width of muscle fibre bundles and length of selected muscle fibres measured (Figure 5.2.18B-G). At 3dpf and 5dpf, muscle fibre length of the intermandibularis posterior (imp) and interhyal (ih) muscles was consistent between the *wt* and *dKO* mutants (Figure 5.2.18C,D,F). The width of these muscles was significantly greater in the *dKO* mutants at 3dpf compared to *wt*, although this difference was diminished by 5dpf (Figure 5.2.18E and G). Given the similarity in pattern with lower jaw growth, it is likely that these initial changes to muscle width are related to development of the lower jaw, which is significantly accelerated in the *dKO* mutants up to 3dpf. How these processes are impacting each other, and in which order requires further investigation, although this initial result, even if null later, is intriguing. Overall, these results indicate that loss of *lmx1b* does not affect the development and formation of craniofacial muscle in the *dKO* mutants.

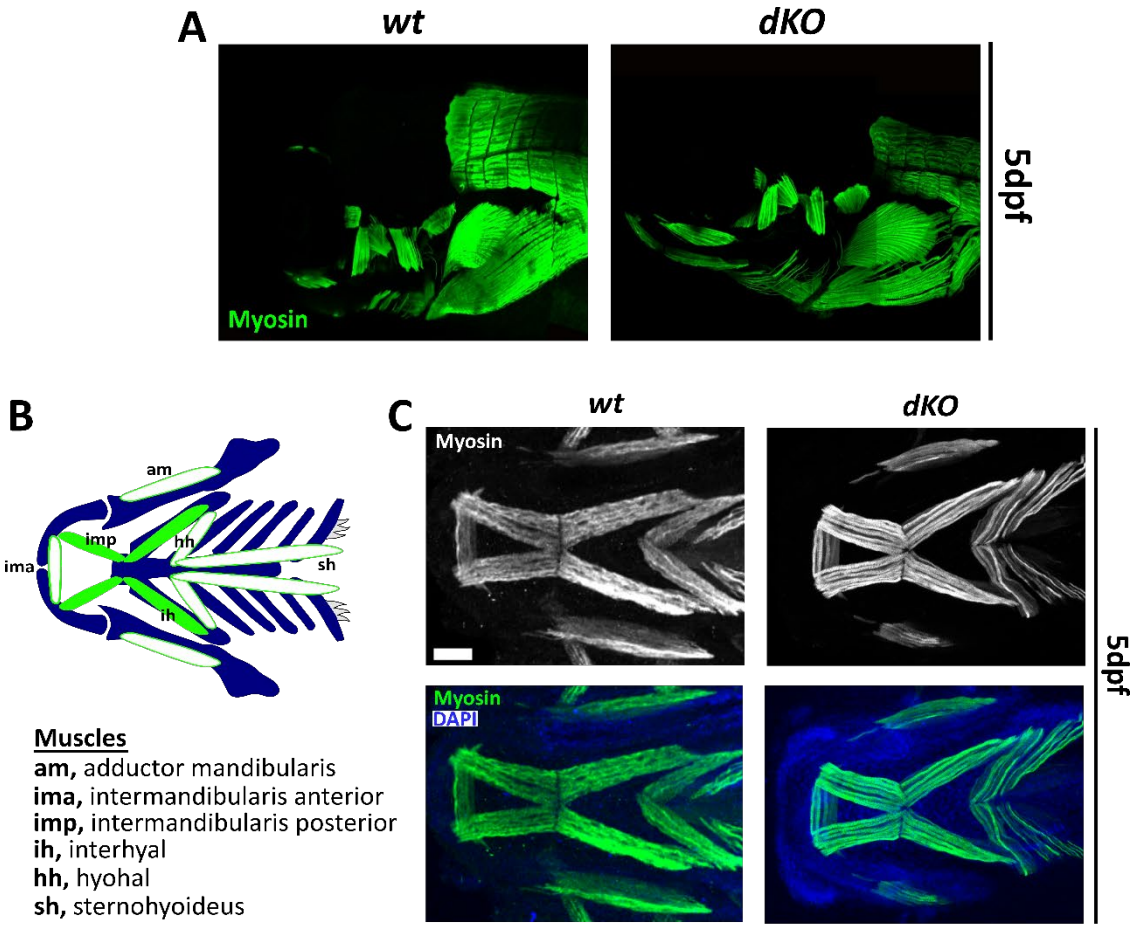
A
wt
dKO
Myosin
5dpf
B
am
ima
imp
hh
sh
ih
C
wt
dKO
Myosin
Myosin
DAPI
5dpf
Muscles
am, adductor mandibularis
ima, intermandibularis anterior
imp, intermandibularis posterior
ih, interhyal
hh, hyohal
sh, sternohyoideus
3dpf
5dpf
D
F
Fibre Length (µm)
wt
dKO
imp
ih
E
G
Fibre Width (µm)
***

Figure 5.2.18 – Craniofacial muscle formation is not affected in the *dKO* mutants, (A) Lateral confocal images of *wt* and *dKO* mutants at 5dpf, immunostained for muscle (green), showing craniofacial musculature in the head. **(B)** Confocal maximum projections of *wt* and *dKO* mutant larvae at 5dpf immunostained for muscle (white/green) and co-stained with DAPI (blue). Scale bar = 100μM. **(C)** Schematic showing location and names of key muscles in the lower jaw of zebrafish. Muscles measured here are filled in in green. Graphs showing quantification of **(D,F)** muscle fibre length and **(E,G)** width in the intermandibularis posterior (*imp*) and interhyal (*ih*) muscles at 3dpf and 5dpf. N = 3 for *wt* and *dKO* mutants at 3dpf; 5 for *wt* and 7 for *dKO* mutants at 5dpf. Two datapoints plotted per fish, per age as measurements taken from right and left side of the lower jaw. Student's unpaired t-test performed at each age for all graphs where, *** *P*=.001.

5.2.19 Truncation of dKO mutant body is likely due to lack of vacuolated cell inflation within the notochord

Although there are clear abnormalities in the muscle structure and formation in the *dKO* mutants, these do not fully explain why their growth is so severely limited. The 'looser' appearance of the muscle fibres and the incidence of large gaps between fibres suggests that the issue may be due to lack of body extension which may be limiting trunk muscle growth and elongation. Therefore, to determine the cause behind the lack of body length growth beyond 2dpf in the *dKO* mutants, the notochord was investigated next.

In embryonic zebrafish, the notochord is formed of two cell types: the outer sheath cells, which secrete an ECM to surround the notochord, and an inner vacuolated cell layer, formed of individual, fluid-filled vacuoles (371). During early development, these vacuoles inflate rapidly and expand to fill the notochord sheath (372). It has been shown in zebrafish that the morphogenic force of the inflated vacuoles is required for body axis elongation, and that loss or damage to these cells can cause body shortening and later kinking in the spine (372). To see if this was occurring in the *dKO* mutants, first, an average notochord width was taken for individual *wt* and *dKO* mutants at 3dpf and 5dpf (Figure 5.2.19A-D). These measurements were made proportional to whole body width to account for any differences in body size between *wt* and *dKO* mutants. At both 3dpf and 5dpf the *dKO* mutants showed a significant decrease in average notochord width, suggesting that the vacuolated cells within the notochord are not inflating as normal.

Preliminary observations of vacuolated cells in *wt* and *dKO* mutant notochords were made to assess whether this hypothesis was true (Figure 5.2.19E). In the *wt,* the membrane edges

of vacuolated cells could be clearly seen in the notochord, in either a stacked formation (Figure 5.2.19E, *white arrowheads*), or packed tightly together (Figure 5.2.19E, *pink arrowheads*), with no space between or around the cells. In the *dKO* mutants, however, the vacuolated cells were less well organised and appeared to be smaller (Figure 5.2.19E, *white asterisks*). The cell membranes were also harder to see which indicates that the vacuolated cells are not packed together as closely, pointing to a reduction in vacuole size and inflation.

These initial data suggest that loss of *lmx1b* has an effect on vacuole inflation which is impeding notochord extension and overall body growth. This in turn may be affecting muscle formation and elongation, although the complete loss of muscle fibre patterning in some *dKO* mutants suggests a separate role for *lmx1b* in muscle formation which will need to be investigated further.

Figure 5.2.19 – *dKO* mutants show decreased notochord width during development compared to *wt*, Representative confocal images of the notochord in Collagen Type II immunostained larvae at **(A)** 3dpf and **(B)** 5dpf, in *wt* and *dKO*. Scale bar = 50μm. **(C)** Schematic showing position of notochord (pink, dotted line) and three measurements made (light blue lines) to calculate average width of notochord per fish. Calculated as percentage of body width (dark blue line). **(D)** Graph showing width of notochord as a percentage of body width at 3dpf and 5dpf. N = 7 for *wt* at 3dpf and 5 at 5dpf; 8 for *dKO* at 3dpf and 7 at 5dpf. Student's unpaired t-test performed at each age, where *** *P*=.0009 and *** *P*=.0004, respectively. **(E)** Confocal images of *wt* and *dKO* mutant notochords with insets showing shape and size of vacuolated cells. Clear cell boundaries in *wt* highlighted by white arrowheads, or tightly packed cells by pink arrowheads. White asterisks in *dKO* mutant show location of smaller cells in centre of notochord. *Figure overleaf.*

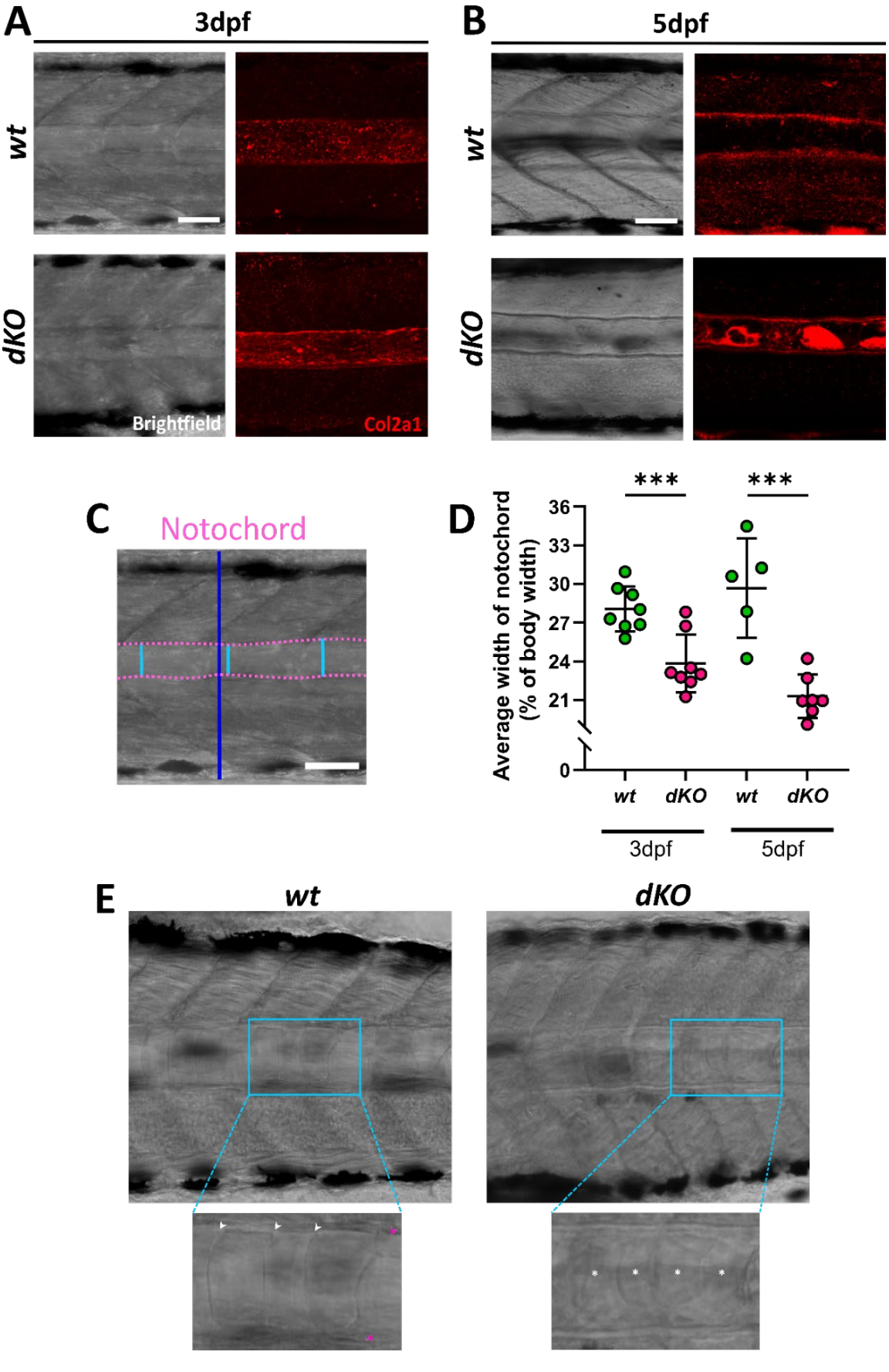
A
3dpf
B
5dpf
wt
dKO
Brightfield
Col2a1
C
Notochord
D
***
***
Average width of notochord (% of body width)
36
33
30
27
24
21
0
wt
dKO
wt
dKO
3dpf
5dpf
E
wt
dKO

5.3. Discussion

Using the *lmx1ba*, *lmx1bb* and *dKO* zebrafish models, the effect of partial or full loss of *lmx1b* on the skeletal, renal, and neuronal system was explored. Phenotypic analysis of the two single mutant lines showed that loss of each paralogue resulted in very specific and divergent phenotypes. The *lmx1ba* mutants showed abnormalities to skeletal and neurological development, whilst the *lmx1bb* mutants showed abnormalities in renal development. Whilst collectively, these developmental abnormalities are similar to those seen in human NPS patients, it is intriguing that these phenotypes show only minimal overlap between the paralogues, indicative of a functional divergence between the paralogues. Loss of both paralogues in the *dKO* mutants was lethal and lead to an intriguing body and muscle phenotype not seen in either single mutant. Here, the phenotypic characterisation of these lines will be discussed and their relevance as a model for NPS evaluated.

Initially, characterisation of the mutant lines as larvae was performed, focussing on larval growth, eye development, and body phenotype. Up to 5dpf, both the *lmx1ba* and *lmx1bb* mutants showed normal body growth, with only the *lmx1bb* mutant showing a delay in growth from 6dpf. This result, along with only a small proportion of *lmx1bb* larvae inflating their swim bladder, indicates a delay in development and a failure to thrive, which given their larval lethality by 13dpf, is not surprising. The *dKO* mutants also showed no swim bladder inflation by 5dpf as well as complete abrogation of body growth from 2dpf, which will be discussed further below. A recent study has implicated autophagy in swim bladder inflation as it is required for lamellar body maturation (41). Under loss of autophagy, the delivery of surfactant lipids to lamellar bodies is reduced which inhibits swim bladder inflation as the surface tension at the air-liquid interface cannot be overcome (41). Therefore, given the role of *LMX1B* in autophagy regulation, this defect could also be due to disrupted autophagy activity in these mutants; however, analysis of autophagy flux in these mutants,

through immunoblotting with p62 or analysis of GFP-Lc3 and LysoTracker puncta numbers in the presence and absence of BafA1 would be required to determine this.

For both single mutants, minimal differences in eye size were seen in early development compared to their respective siblings, with only the *lmx1bb* homozygous mutants showing a reduced eye diameter from 6-7dpf. This is likely due to oedema in the eye which appears at around this stage. The *dKO* mutants, however, did show a significant decrease in eye diameter from as early as 2dpf. The *dKO* mutants also show eye oedema but this appears later indicating that this decrease is more likely due to a developmental defect. This is in line with studies from *Lmx1b* knock-out mice and morpholino *lmx1b* zebrafish which both show a smaller eye size (188, 217). Due to time constraints, further investigations into the eye development of the *dKO* mutants were not performed although previous studies indicate that optic cup deformities are likely (188).

Analysis of gross body phenotypes showed that by 5dpf, the majority of *lmx1bb* and *dKO* mutants develop some form of oedema, in contrast to only 14% of *lmx1ba* mutants. For the *lmx1ba* mutants, this indicates a difference in mutation penetrance as no oedema is observed in the remaining siblings. Although there can be several causes of oedema in zebrafish such as defects to the lymphatic (373), cardiac (374) or renal system (345), the strong association of *Lmx1b* with kidney development and maintenance suggest that defective kidney function is the most likely cause here. The prevalence of oedema in the *lmx1bb* mutants but not in the *lmx1ba* mutants correlates with morpholino studies where the single knock-down of *lmx1bb* resulted in severe oedema, whilst the single knock-down of *lmx1ba* gave a less penetrant phenotype (214). The high incidence of oedema in the *dKO* mutants supports this finding, as loss of both paralogues resulted in a more severe phenotype.

In the *lmx1bb* mutants, the incidence of oedema was striking as it was found to occur in all larvae by 7dpf, including larvae showing no observable developmental defects at 5dpf. This indicates that loss of *lmx1bb* has a severe effect on kidney formation and that this phenotype is completely penetrant. This was confirmed by ultrastructural analysis which showed a disorganised and disrupted glomerulus morphology in the *lmx1bb* mutants by 6dpf. GBM formation was largely disrupted or when present, showing irregular thickening, and the number of podocyte foot processes appeared reduced, with some areas showing a 'moth-

eaten' appearance similar to that seen in *Lmx1b* knock-out mouse models and NPS patients (336, 358). In the *lmx1bb* mutants, the mitochondria also appeared round and swollen, which is a sign of mitochondrial dysfunction and in human disease, is a recognised sign of kidney pathology (357). This loss of structure would have a severe effect on kidney function and the proper regulation of water within the body. Therefore, this demonstrates an essential role for *lmx1bb* in kidney development, which is required for survival in zebrafish.

Looking ahead, analysis of kidney development from earlier ages by electron microscopy would help establish when these defects occur and whether loss of *lmx1bb* is affecting the initial formation of the GBM and differentiation of podocytes, or their survival beyond these stages. As glomerular filtration is established by 40hpf, the larvae should be analysed at 2-3dpf to help answer this question (375). Glomerular filtration assays could also be performed to assess the functionality of the GBM. Here, fluorescently labelled, inert molecules of low and high molecular weights, such as dextran or inulin, are injected into the vasculature and their location and fluorescence intensity tracked within the larvae by live imaging (376-378). In healthy larvae, the lower molecular weight molecules (~10kDa) would be quickly cleared from circulation and accumulate in the kidney tubules and around the cloaca for excretion, whilst the molecules at ~500kDa would remain in the vasculature only. However, larvae with disruption to kidney function would show loss of both molecules from circulation and fluorescence in the kidney tubules and cloaca, indicating loss of GBM integrity (377). Similarly, transgenic lines for vitamin D binding protein (VDBP), a zebrafish equivalent of albumin, fused to GFP are available (~80kDa), which operate in the same way where loss of GFP fluorescence from major veins, the retinal vascular bed or over the heart, or its presence in the tubules, would indicate defective GBM filtration (379). In comparison, these lines are easier and quicker to use as larval injections into the vasculature can be labour and time intensive, and they minimise the risk of varying molecule concentrations between individual fish (380).

These studies would help clarify the role of *lmx1bb* in zebrafish kidney development and maintenance. Given the increased severity of oedema seen in the *dKO* mutants, it is likely that *lmx1ba* plays some role in this process which could also be identified through these experiments. Together, these would help better characterise the role of each paralogue in

zebrafish kidney development and better establish these lines as a model for kidney disease and NPS studies.

When looking at skeletal development, initial analysis identified *lmx1ba* and not *lmx1bb* as having a role in skeletal development and formation. In the lower jaw, the *lmx1ba* mutant showed a significant reduction to the longitudinal growth at 3dpf and 5dpf, which was not replicated in the *lmx1bb* mutant or, intriguingly, the *dKO* mutants. Instead, jaw growth was accelerated in the *dKO* mutants at 3dpf, although by 5dpf, only the width of the Meckel's cartilage was significantly greater than *wt.* This result was unexpected, especially as the proliferation of chondrocytes in the jaw was decreased compared to *wt* and unchanged at the joint site where most proliferation occurs and is responsible for cartilage extension. However, this may be because the proliferation assay was timed at 5dpf when jaw growth had largely normalised to *wt* levels.

Alongside changes to jaw growth, the *lmx1ba* mutants showed reduced chondrocyte proliferation and changes to chondrocyte density and organisation by ultrastructural analysis. The increased number of vesicles and reduced proportion of properly intercalated chondrocytes is suggestive of a delay in chondrocyte maturation, which would explain the impediment in cartilage growth, as hypertrophication of chondrocytes is one of the main drivers required for skeletal growth (381). Analysis of Sox9a expression, which can be used to assess the level of chondrocyte maturation, showed no significant changes compared to *wt.* Although a relative increase in Sox9a expression in the *lmx1ba* mutants over *wt* might be expected, a decreased chondrocyte cell number within the jaw caused by the reduced jaw size and chondrocyte proliferation rate could reduce the volume of cells which are Sox9a-positive. Taken altogether, these results indicate that loss of *lmx1ba* delays chondrocyte maturation rate and cartilage growth. These data contrast with the chondrocyte phenotype observed in the *atg13* mutants, suggesting that dysregulation of autophagy is not the cause of the changes to chondrocyte maturation seen here. A possible *lmx1ba*-mediated mechanism for these changes to cartilage development will be discussed further in Section 6.2.4 of Chapter 6. Beyond cartilage development, delays to bone mineralisation rate were also observed in the *lmx1ba* mutant. Between 5-7dpf, the *lmx1ba* mutants show very little

mineralisation of vertebrae compared to *wt.* This rate increases by 10dpf, indicating that vertebral mineralisation is not defective but instead delayed.

By 3mpf, changes to body curvature were observed in the *lmx1ba* mutants compared to *wt*, with mutants showing a decrease in how far they can bend their spines to the left and right. This could be due to degenerative changes to the spine, such as vertebral fusions and dislocations affecting overall movement, however, 3mpf is very young for these changes to have occurred. Analysis of the skeletons of older fish by micro-computed tomography revealed that by 9mpf, *lmx1ba* mutants showed signs of premature OA and vertebral degeneration, which increased in severity as the fish aged. Vertebral fusions and calcifications of the cartilage between vertebrae, known as the intervertebral disc (IVD), were the most common symptoms. These correlate with the skeletal phenotype seen in some NPS patients, who show calcifications on their vertebrae which are often attributed to scoliosis (382). Therefore, loss of *lmx1ba* can cause clear acceleration of bone degeneration in the *lmx1ba* mutants. How this is occurring is unclear, however, these data reveal two possible alternatives. Firstly, changes to vertebral structure and morphology, such as the vertebral fusions and spinal bends, could be contributing to the reduced movement of the *lmx1ba* mutants seen at 3mpf, although this cannot be confirmed here given the difference in ages between the fish used in these experiments. Alternatively, potential changes to spinal formation from development could be triggering the accelerated deterioration of the spine seen by 9mpf, as skeletal malformations between joints, such as the vertebrae, can affect joint function, leading to impaired joint loading and premature joint deterioration.

To explore these hypotheses, skeletal formation of *lmx1ba* mutants from juvenile to young adult stages (45-90dpf) could be investigated using Alizarin red staining. This would show whether changes to spine morphology occur from development or as the fish ages. The swim behaviour of the *lmx1ba* mutants could also be tracked from earlier than 3mpf to see if normal spinal curvature can be exhibited in the *lmx1ba* mutants, or if this is a permanent phenotype, and at older ages to observe whether these changes progress in severity with ageing.

Aside from skeletal abnormalities, muscular changes caused by the *lmx1ba* mutation could also be affecting body curvature and swim behaviour. Observationally, the *lmx1ba*

homozygous mutants appear slimmer as adults compared to age-matched *wt* or *lmx1bb* heterozygous fish. This could be similar to the phenotype seen in some patients with NPS, who show reduced muscle mass in the upper arms and legs, reminiscent of dystrophic muscular disease and can struggle to build muscle mass (209). A reduction in trunk muscle mass can impair swimming ability as seen in zebrafish models for muscular dystrophies (383, 384). Therefore, an evaluation of adult skeletal muscle would help elucidate any changes to muscle mass or function seen in the *lmx1ba* mutants. Transverse sections of adult skeletal muscle labelled with antibodies against A4.1025 or mf20 to highlight all muscle, or against f59 and s58 for fast and slow muscle fibres, respectively, and laminin for labelling the basal lamina of adult skeletal muscle would be helpful for identifying changes to gross muscle formation and maintenance. Meanwhile, quantification of myofibril number would highlight any changes to muscle mass.

Altogether, these results demonstrate a role for *lmx1ba,* but not *lmx1bb,* in skeletal development and the regulation of chondrocyte maturation. These disruptions to skeletal development in the *lmx1ba* mutants lead to abnormalities in the spines of adult *lmx1ba* mutant fish which indicate premature OA onset. Whether these effects are due to a developmental role for *lmx1ba* in skeletal development or whether *lmx1ba* is required for skeletal maintenance as well will require further investigation.

In situ expression studies in zebrafish have shown that expression of *lmx1ba* and *lmx1bb* are seen in *wt* embryos from as early as 5hpf (185). Both transcripts are expressed initially in the presumptive mesencephalic and metencephalic regions of the brain, which sit either side of the mid-hindbrain boundary (MHB) (185). In either single mutant, no significant changes to the MHB or ventricle formation were observed, indicating a level of functional redundancy between the two paralogues. This correlates with zebrafish *in situ* data which demonstrated that *lmx1ba* and *lmx1bb* show only minor divergence in brain expression, with both having strong expression around the MHB (185). This is also supported by the phenotype of the *dKO* mutants which showed that loss of both paralogues, and therefore any compensatory effects, was sufficient to significantly alter early brain formation. Moving forward, it would be interesting to follow the brain development of the *dKO* mutants from beyond 1dpf to observe whether brain formation remains defective or is just delayed. Initially, this was

attempted using two antibodies; acetylated tubulin, which labels axonal tracts, and HuC/D, a pan-neuronal nuclear marker, as both label key structures in the brain. However, issues with staining and differences between staining protocols meant that these antibodies did not work or could not be used alongside other neuronal antibodies. Therefore, further work will need to be done to optimise these protocols or to identify alternative antibodies or markers.

Even without changes to gross brain morphology, the *lmx1ba* mutants did show an increase in apoptotic cell number at 1dpf, around the brain and eye region. Again, being able to co-stain with a neuronal marker would be very useful for determining whether the *lmx1ba* mutation is affecting the survival of DA and 5-HT neuronal populations, as predicted from *Lmx1b* mouse models. This would be especially interesting in the *dKO* mutants which also showed an increase in cell death, although unfortunately, due to time constraints, these results could not be further analysed using TUNEL. Being able to follow where cell death is occurring in the brain, would help elucidate whether loss of MHB formation is due to loss of neuronal progenitor cell populations or defects in neuronal cell differentiation and proliferation.

Through staining with a TH antibody, which can be used as a marker for DA neurons, it was found both the *lmx1ba* and *dKO* mutants show a decrease in TH-positive cell number in the forebrain and midbrain at 3dpf compared to *wt.* This corresponds with data from *Lmx1b* knock-out mice which also show TH-positive neurons in the developing brains; however, during embryonic maturation this subset of TH-positive neurons is lost (218). This is believed to be due to loss of *Lmx1b* inhibiting *Ptx3* (Pentraxin-related protein 3) expression which is required for the repair and protection of DA neurons (218). From the initial acridine orange and TUNEL assay results, it could be concluded that loss of *lmx1ba* and *lmx1b* is affecting DA neuron survival, leading to a decreased number of TH-positive neurons by 3dpf. By continuing this staining beyond 3dpf, it would be interesting to see whether there is a further loss in TH-neuron number as shown in the *Lmx1b* knock-out mouse model.

Following these changes to early brain development, the effect of the *lmx1ba* and *dKO* mutations on adult behaviour was investigated. In a previous study it was shown that loss of TH expression during zebrafish development, through morpholino injection, was sufficient to affect behaviour of these zebrafish as adults (239). Although TH levels in these

injected fish returned to normal levels by adulthood, these fish exhibited reductions in risk aversive behaviour and appeared less anxious in novel environments, demonstrating that early, and even transient, alterations to DA neuron formation are sufficient to cause disturbances in adult brain function. Here it was found that the *lmx1bb* and *dHet* mutant fish showed a reduction in anxiety-related behaviours and an increase in exploratory behaviour compared to *wt* fish. Unexpectedly, this result was not replicated in the *lmx1ba* mutants, which suggests that changes to behaviour occur only as the fish get older, as these fish were only 3mpf when filmed. It would be intriguing to explore this hypothesis by repeating this experiment on the same fish as they age. Firstly, to discover if the *lmx1ba* mutants show the same behavioural patterns as the other mutants at 6mpf and secondly, to see if the mutants become progressively less risk aversive as they age.

Similar to these behaviour profiles, mice lacking in serotonergic neurons were shown to exhibit reduced anxiety and altered fear responses (385). Therefore, these changes to behaviour could also be being influenced by loss of serotonergic neurons as *lmx1b* is required for their development and survival (311). Exploring the expression and survival of these neurons during development would help show whether they are being affected by the *lmx1b* mutations and to what extent.

Taken altogether, these data show that loss of *lmx1b* affects the survival of neuronal cells during early development, resulting in fewer DA neurons in the midbrain and forebrain of fish. These results correlate with findings from *Lmx1b* knock-out mouse models and *lmx1b* morpholino studies in zebrafish, indicating that the *dKO* mutants are a representative model for studying the role for *lmx1b* in brain development (175, 239). As the *lmx1ba* mutants showed a similar neuronal phenotype to the *dKO* mutants, this indicates that *lmx1ba* plays a greater role in neuronal development compared to *lmx1bb*, demonstrating a divergence in function. Into adulthood, the changes to neuronal development were shown to alter swim behaviour, with mutants with the fewest functioning copies of *lmx1b* displaying the biggest reduction in risk aversive behaviours and danger perception, supporting the importance of *lmx1b* for the maintenance of neuronal cells beyond development.

The most significant phenotype observed in the *dKO* mutants was the lack of body axis extension beyond 2dpf and the resulting truncation in body length. Somite number in the

dKO mutants was comparable to *wt*, indicating that abnormalities to somite development were not the cause. Analysis of trunk muscle revealed changes to the structure and formation of slow muscle fibres, which was not replicated in the craniofacial musculature. This is not unexpected, as craniofacial muscle and trunk muscle develop from different cell progenitor sites in the developing embryo; craniofacial muscle being derived from neural crest cells, and trunk muscle from the paraxial mesoderm which differentiates to form the somites (386, 387).

At both 3dpf and 5dpf, myofibrils in the *dKO* mutants were shorter, as expected, but also displayed large gaps between fibres and branching of myofibrils perpendicular to the normal direction of growth, with the phenotype worsening with age. Strikingly, neither single *lmx1ba* or *lmx1bb* mutant gave any indication of trunk muscle abnormalities. This indicates either a high degree of compensation between the paralogues, or that this muscle phenotype is secondary symptom to another growth abnormality which is triggered only by the loss of both *lmx1b* paralogues. The inflation and expansion of vacuolated cells within the notochord is known to be essential for body elongation during development (372). The decreased notochord width in the *dKO* mutants and observed differences in vacuolated cell size and organisation compared to *wt*, indicate that this process is not occurring which would account for the lack of body growth beyond 2dpf. Additionally, the presence of smaller and rounder vacuoles in *dKO* mutant notochords is reminiscent of the phenotype seen in zebrafish with mutations in genes responsible for vacuolated cell function, such as H+-ATPase (mutant line name, *atp6v1e1b*^{hi577aTg}) and the sodium-dependent neutral amino acid transporter, Slc38a8b, which regulates vacuolated cell volume (388). Therefore, together these indicate that a vacuolated cell defect is present in the *dKO* mutants, however, the mechanism behind this defect still needs to be identified.

To expand on these initial results, staining with a vital dye such as BODIPY-TR ceramide, a lipophilic stain which can selectively mark endomembranous organelles, would be useful as this has been previously used in vacuolated cell studies to efficiently highlight vacuole membranes (388). Alternatively, a lipid marker such as Nile red could be used as this can also highlight cell membranes. In the case of the vacuoles, this would give a much clearer indication of cell boundaries and how well inflated and packed these cells are within the

notochord. From this staining, quantification of vacuole size and number between *wt* and *dKO* mutants could be more accurately performed to better analyse the defect in vacuolated cell inflation in the *dKO* mutants. This would also highlight whether fragmentation of vacuolated cells is occurring, as this has been shown to result in shortened larvae due to a reduction in vacuole size and increased packing density (388).

The vacuoles within vacuolated cells have been identified as lysosome-related organelles (LRO) which means they are specialized structures that share several characteristics with lysosomes (371). For example, similar to lysosomes, all LRO's are formed and maintained by late endosomal trafficking which is regulated by Rab32a and H+-ATPase–dependent acidification (372). These vacuoles also have Lamp-1 (lysosomal-associated membrane protein 1) present on their membrane, a transmembrane protein which plays an important role in lysosome biogenesis and autophagy (372). Interestingly, lamellar bodies, which are required for swim bladder inflation, are also LRO's and, as mentioned above, require autophagy for their maturation and function in swim bladder inflation (41). Therefore, autophagy dysregulation, through loss of *lmx1b,* could be affecting vacuolated cell inflation in the *dKO* mutants. By exploring autophagy flux in the *dKO* mutants, this would help show whether autophagy is being dysregulated in these mutants. For example, the GFP-Lc3 transgenic line along with a lysosomal dye such as LysoTracker, could be used to image autophagosomes in vacuolated cells and monitor autophagy activity. It would also be interesting to see whether treatment of *wt* fish with an autophagy inhibitor such as 3-Methyladenine (3-MA), which does not affect lysosomal or LRO function such as BafA1, causes a similar phenotype to the *dKO* mutants. These experiments would help establish the role of autophagy in this process and identify the cause behind the reduction in vacuolated cell inflation.

It has been shown that changes to whole body growth can affect skeletal muscle development in zebrafish (389). One possible hypothesis for this is that the growth and extension of muscle fibres is aided by the tension put on muscle fibres, which in the developing trunk normally occurs via body elongation. Therefore, lack of body growth in the *dKO* mutants could be disrupting normal muscle fibre growth in the trunk resulting in the disturbed muscle phenotype. Alternatively, increased motility of larvae beyond 3dpf

could also contribute to the progression of this phenotype, as the 'looser' muscle fibres become detached and are less able to stay in alignment, however, this would need to be investigated further to be confirmed.

There are several experiments that could be performed to determine if loss of *lmx1b* is affecting trunk muscle development and formation. For example, ultrastructural analysis of trunk muscle would identify any changes to myofibril orientation and organisation. Birefringence, where alterations to the passage of light through ordered matter, such as muscle sarcomeres, can be used to analyse changes to myofibril organisation and degeneration. For example, fish with disorganised muscle fibres would show an overall reduction in light brightness, or birefringence (390). Cell proliferation assays using EdU would be helpful for determining whether sarcomere proliferation is affected in the *dKO* mutants and whether this is having any effect on muscle growth. Similarly, immunostaining for Pax7, a transcription factor that regulates muscle precursor cell proliferation, would also help identify any changes to muscle growth in the *dKO* mutant.

In summary, these data indicate that loss of *lmx1b* affects vacuolated cell inflation, which impedes notochord extension and disrupts trunk muscle formation and structure. This could be due to dysregulation of autophagy caused by the loss *lmx1b,* which affects the inflation of vacuoles within notochord vacuolated cells in a similar mechanism to the swim bladder. However, the complete loss of muscle fibre organisation seen in some *dKO* mutants suggests that *lmx1b* may also have a role in muscle organisation and patterning, which is reflective of its role in skeletal patterning during development. As neither single mutant shows a clear muscle or growth phenotype, it could be that each paralogue functions in either process, but that loss of both is required to have a significant effect. Therefore, further characterisation of the muscle and notochord phenotypes of the *lmx1ba* and *lmx1bb* mutants could help dissect these roles and determine if compensation between the paralogues is occurring.

Throughout the characterisation of these lines, attempts were made to assess the levels of *lmx1b* in each line. Immunoblotting for *lmx1b* and qRT-PCR analysis were both performed although, unfortunately, neither experiment worked. However, as the observed phenotypes of both mutant lines appear similar to other *Lmx1b* knock-out mouse and zebrafish morpholino models, and to the symptoms characteristic of NPS patients, it strongly suggests

that these effects are due to the *lmx1b* mutations and not due to other potential gene mutations. Alongside this, genotyping of each mutant line reveals sequence changes and the presence of premature stop codons which would be expected to abrogate *lmx1ba* and *lmx1bb* expression.

Although growing, the availability of antibodies either against zebrafish proteins, or that work in zebrafish are limited compared to other mammalian systems. This alongside the reduced number of antibodies available against Lmx1b, even for human or mice systems, means that the detection of Lmx1b can be difficult. Three different antibodies for immunoblotting of *lmx1b* were tried, but they either did not work or give consistent results. The high conservation between human and zebrafish *lmx1b* sequences (82-87%), especially in the core domains indicates that this is not likely to be the issue, although this is dependent upon where in the sequence the antibody epitope binds.

Analysis of RNA transcript level by qRT-PCR was also attempted, although due to time constraints, the primers for *lmx1ba* and *lmx1bb* could not be optimised for use. Looking ahead, quantification of transcript levels would be useful in the single mutants to see if either paralogue is upregulated when expression of the other is lost. This would help determine the level of compensation occurring between the paralogues, which could explain phenotypic differences seen between the single and *dKO* mutants. Together, these analyses would help define the effect of the *lmx1ba* and *lmx1bb* mutations on *lmx1b* expression and determine categorically whether these mutations abolish *lmx1b* expression.

Similar studies could also be used to explore the effect of the *lmx1b* mutations on the expression of related genes. For example, *LMX1A*, the sister gene to *LMX1B*, shares a similar role in brain development, specifically in the specification and differentiation of midbrain-DA neurons, formation of the spinal cord roof plate, and in MHB development (310, 346). Along with some overlapping functions, during midbrain-DA neuron differentiation, these genes have been shown to cross-regulate each other (391). Therefore, changes to *lmx1a* expression in the *dKO* mutants could be influencing the neuronal phenotype. Using qRT-PCR analysis or *in situ* hybridisation for *lmx1a,* any changes to *lmx1a* expression in the *lmx1b* mutants could be investigated and the contribution of this gene to the *lmx1b* mutant phenotypes explored.

Taking all of these observations together, these results demonstrate that the *lmx1ba* and *lmx1bb* mutant zebrafish lines closely follow the expected phenotype of an *LMX1B* knock-out model. With the survival of all mutant lines into late larval stages, and the fact that zebrafish develop externally, these lines enable the effect of loss of *lmx1b* on body formation to be observed all the way through development and into the formation of a functional animal. As demonstrated here, the functional effects of these *lmx1b* mutations on key systems and organs can also be examined, unlike other rodent models. Therefore, the *lmx1ba, lmx1bb* and *dKO* mutant lines generated and characterised in this chapter provide an alternative and representative model for the study of NPS and the role of *lmx1b* in developmental processes.

Chapter 6. General Discussion

At a glance…

In this final chapter, the results presented in this thesis will be summarised and the areas where these results have contributed to the current literature will be highlighted. Firstly, the mechanisms by which loss of autophagy, through the atg13 mutation, affects chondrocyte maturation and joint function, and how this could contribute to OA onset will be explored. Then the relevance of the lmx1b mutant lines as a model for NPS will be discussed. Finally, suggestions of future work that could performed using these models will be examined.

CHAPTER

6

General Discussion

6.1. Introduction

The outset of this thesis was to explore the role of autophagy in skeletal development and joint function through the use of zebrafish lines carrying mutations in two separate autophagy-related genes. In Chapter 3, the characterisation of a novel autophagy-null *atg13* mutant line showed that loss of autophagy is lethal at larval stages. The mutant larvae showed that chondrocyte maturation was accelerated, leading to a reduction in ECM secretion and restricted joint mobility in the lower jaw. These results point towards a mechanism by which dysregulation of autophagy in development could increase OA risk in later life, emphasising the importance of autophagy in skeletal formation and maintenance.

Chapter 4 described the process of generating an *LMX1B* knock-out cell and zebrafish lines, which showed that complete loss of *LMX1B* in human HEK293T cells, and *lmx1bb* and *lmx1b* in zebrafish is lethal, although *lmx1ba* mutant zebrafish were able to survive to adulthood. Finally, in Chapter 5, the phenotypes of three *lmx1b* mutant zebrafish lines, *lmx1ba*$^{-/-}$, *lmx1bb*$^{-/-}$ and *lmx1b dKO*, were characterised, and their relevance as a model for NPS was assessed. It was found that *lmx1ba* and *lmx1bb* have divergent roles in zebrafish development, affecting skeletal and neuronal development, and kidney development, respectively. Whilst loss of both paralogues resulted in muscular abnormalities and loss of body growth, concomitant with defects in vacuolated cell inflation in the notochord. The impact of these developmental

changes on adult fish was initially explored and showed that greater loss of *lmx1b* results in behavioural changes indicative of decreased anxiety and danger perception. Loss of *lmx1ba* was also shown to cause changes to the skeleton reminiscent of premature ageing, in addition to alterations to body movement when swimming. Altogether, these results indicate that these lines provide a relevant model for the study of NPS and for investigating the role of *lmx1b* in neuronal, renal, and musculoskeletal development.

6.2. Discussion

6.2.1 Understanding the role of autophagy in the regulation of chondrogenesis

A role for autophagy in skeletal development and for the functioning of skeletal-specific cells has been well established, with autophagy-null animal models showing defects in skeletal formation and mineralisation, growth retardation, increased incidences of bone fractures, and premature OA onset. Specifically in chondrocytes, loss of autophagy through *Atg* mutations has been shown to affect chondrocyte proliferation and survival, triggering ER stress and the retention of ECM components, which leads to a disorganised ECM and signs of premature OA in some models (82, 271). Whilst these studies highlight a clear role for autophagy in bone and cartilage development and maintenance, how autophagy impacts chondrocyte differentiation and by what mechanism(s) has been less well investigated.

Here, a novel zebrafish line with a 5 nucleotide deletion in the *atg13* gene, causing a premature stop codon and ablation of Atg13 protein expression, is reported to have defective autophagy flux and alterations to jaw joint function which are caused by an acceleration to chondrocyte maturation. Reductions to jaw movement were not caused by changes to jaw musculature which appeared normal, and instead were due to altered cartilage formation. A reduction in Sox9a expression and an increase in Col10a1 expression by 7dpf indicated premature hypertrophication of chondrocytes in the lower jaw, which resulted in abnormal chondrocyte organisation and intercalation. As one of the major

transcription factors involved in regulating chondrogenesis, Sox9 is highly expressed during cartilage differentiation (278, 293). Loss of Sox9 expression is embryonically lethal, whilst heterozygous mutations in humans causes campomelic dysplasia, a syndrome characterised by malformations to the skeletal and reproductive system, which is usually lethal at neonatal stages (392). Inactivation of Sox9 in juvenile and adult mice has been shown to reduce growth plate size in long bones and the proteoglycan content of articular cartilage, which can be an early sign of OA onset (393, 394). More recently, in mice, Sox9 has been reported to play a protective role for chondrocytes in load-bearing regions of the articular cartilage (395). This correlates with data which show that the expression of SOX9 is reduced in the chondrocytes of late-stage OA patients (396). Together, these studies highlight that normal Sox9 expression and activity is essential for proper cartilage development and for the maintenance of articular cartilage beyond developmental stages.

As mentioned in Section 3.3 of Chapter 3, Sox9 has been shown to be regulated by mTORC1, a master controller of autophagy (295). Through RNA translational control, mTORC1 accelerates the translation of Sox9 through phosphorylation of eukaryotic translation initiation factor 4E (eIF4E)-binding proteins (4E-BPs) (295). Previous studies have highlighted a role for mTORC1 in skeletogenesis, as inactivation of mTORC1 signalling, via loss of *mTOR* or *Raptor* (two components of mTORC1), decreases embryonic skeletal growth (381). Therefore, it is thought that mTORC1 influences skeletal development in part via the Sox9 pathway (295). As a negative regulator of autophagy activity, mTORC1 is inhibited when autophagy activity is required by the cell, usually under high stress or low nutrient conditions (296). Therefore, here it is proposed that reduced levels of autophagy, as seen in the *atg13* mutant fish, could cause a compensatory further reduction of mTORC1 activity, predicted to alter Sox9 expression and activity. This could explain why Sox9a expression is decreased in the *atg13* mutants, leading to changes in chondrocyte maturation and joint function (Figure 6.2.1). Further investigations would be needed to confirm changes to mTORC1 activity in the *atg13* mutants. As mTORC1 is also responsible for controlling the expression of other chondrocyte-regulating genes, such as *RUNX2*, parathyroid hormone-related peptide (*PTHrP*) and Indian Hedgehog (*IHH*) (397-400), there are other routes

through which changes to mTORC1 activity could affect skeletal growth, which could also be altered in the *atg13* mutants.

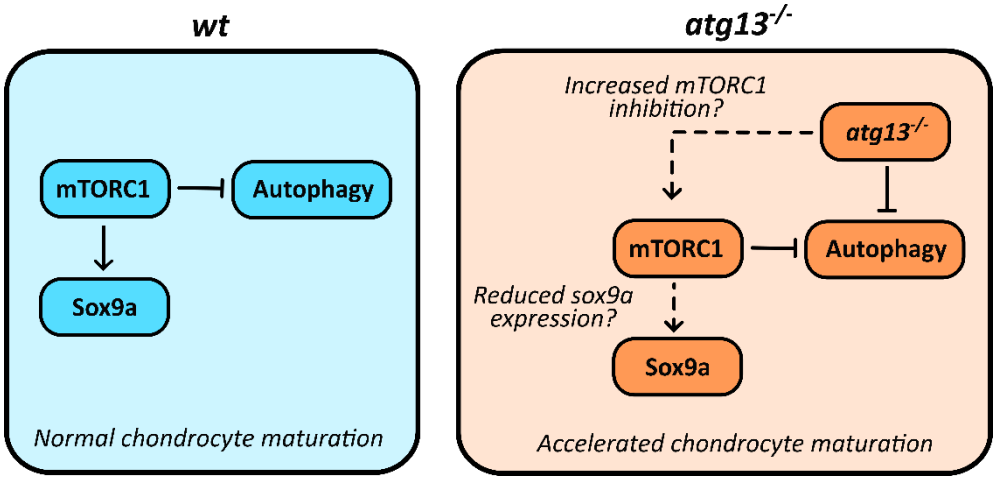

Figure 6.2.1 – Overview of proposed effect of *atg13* mutation on mTORC1 activity and Sox9a expression, In *wt* fish (*blue box*), under basal conditions, mTORC1 activity inhibits autophagy and induces Sox9a expression. In *atg13* mutants (*orange box*), loss of autophagy activity through the *atg13* mutation may cause mTORC1 activity to be further inhibited, reducing Sox9a expression (*dotted arrows*). This loss of Sox9a expression disrupts chondrocyte maturation and cartilage formation leading to reduced jaw mobility in the *atg13* mutants.

Overall, these results demonstrate the importance of autophagy activity for retaining normal Sox9 expression, which, as highlighted above, is critical not just for cartilage formation but also for its maintenance into adulthood. They also present a potential mechanism through which autophagy dysregulation alters chondrocyte maturation and cartilage formation in development via changes to mTORC1 activity and Sox9a expression.

6.2.2 Characterisation of the *lmx1b* mutant zebrafish lines as a model for *lmx1b* and NPS studies

Previous studies have established a key role for *Lmx1b* during development across multiple organ systems. These roles have been well studied in murine models, primarily through the use of *Lmx1b* knock-out lines. In contrast to humans, where heterozygous loss of LMX1B causes NPS, mice with heterozygous knock-out of *Lmx1b* show largely normal development, indicating that haploinsufficiency of *Lmx1b* does not cause a mutant phenotype in mice (308). Mice with a homozygous mutation for *Lmx1b* show a phenotype much closer to human NPS patients, although as this mutation is perinatally lethal, this model has a more

limited use (194). The generation of conditional, cell-specific *Lmx1b* knock-out mouse lines have helped overcome this early lethality and are useful for the study of *Lmx1b* in specific cell types within an organ (175, 214, 351). However, the conditionality of these models means that the effect of loss of *Lmx1b* on the whole organ, and the interplay of *Lmx1b* activity within the different cell types present cannot be explored.

Studies into *lmx1b* using zebrafish have been carried out, primarily through morpholino experiments, and two *lmx1b* knock-out lines have been generated but not fully characterised (183, 315, 316). In one study, the *lmx1bb*^{jj410} mutant, generated by Schibler *et al.*, was used to identify a role for *lmx1bb* in inner ear formation in zebrafish (315, 316). Meanwhile, Hilinski *et al.*, generated a *lmx1ba*^{mw80} mutant line and used this alongside the *lmx1bb*^{jj410} mutant line to explore their roles in the regulation of interneuron neurotransmitters in the spinal cord (183). Therefore, in comparison to *Lmx1b* mouse models, work using these lines has been more limited and a characterisation of the effect of these mutations on the whole body has not been done. In this thesis, two new *lmx1ba* and *lmx1bb* knock-out zebrafish lines were generated and the role of each paralogue in development was investigated and characterised. The phenotypes of each single mutant, although divergent, align with the phenotype of *Lmx1b* mutant mouse models and NPS patient symptoms, indicating that these lines are relevant for the study of *lmx1b.* Although previous zebrafish studies have indicated differences between *lmx1ba* and *lmx1bb* expression during development (183, 188, 401, 402), here functional divergence between the paralogues is demonstrated and characterised across the whole body for the first time. Despite these differences, an overlap in function between the paralogues remains, as shown by the more severe *dKO* mutant phenotype, demonstrating that both paralogues still maintain the same roles as mammalian *Lmx1b*. As the loss of either paralogue, which is similar to a heterozygous genotype, resulted in NPS-like symptoms, this also indicates that zebrafish could be a more representative model for NPS compared to murine models, as heterozygous loss of *lmx1b* has a similar effect on zebrafish development as observed in humans.

The adult data shown in Chapter 5 also highlight an advantage of zebrafish as a model for *lmx1b* and NPS studies. The presence of the two *lmx1b* paralogues in zebrafish, although more complex, allows for the generation of more *lmx1b* mutant models to model the effects

of haploinsufficiency. For example, the *lmx1ba*$^{-/-}$;*lmx1bb*$^{-/+}$ (*KO;Het*) line is the genetically closest model to a full *lmx1b* knock-out but can still survive to adulthood. This enables the effect of loss of *lmx1b* to be explored beyond developmental stages and during ageing. This could be useful when studying the effect of loss of *lmx1b* on brain disorders and their associated behaviours, such as Parkinson's disease, which cannot be done in *Lmx1b* rodent models. Or for elucidating the role of *lmx1b* in other neurological conditions which have been linked to *lmx1b* but not fully characterised, such as ADHD, autism, and schizophrenia (176, 177, 219, 403). Similarly, the musculoskeletal phenotype of this line could be characterised to explore whether the further loss of *lmx1bb* accelerates the skeletal degeneration seen in the *lmx1ba* mutants. Observationally, these fish appear smaller and thinner compared to *lmx1ba*$^{-/-}$, *lmx1bb*$^{-/+}$ and *dHet* mutant adults which could indicate abnormalities in trunk muscle development and growth, akin to the phenotype seen in the *dKO* mutants. Therefore, these lines could widen the field for the study of *lmx1b* on the establishment and maintenance of key body systems, and potentially identify new roles for this gene, as shown in this thesis.

6.2.3 Understanding the differential activity of the *lmx1b* paralogues in zebrafish

As highlighted in the introduction to *LMX1B* in Chapter 1, the tissue diversity in which LMX1B functions as a regulator is achieved via its ability to form transcriptional regulation complexes with a variety of transcription factors and transcriptional co-factors (173). The binding of these co-factors influences the transcriptional activity of LMX1B, and they act in a tissue-specific manner (170). These binding events occur via the two LIM domains present in LMX1B; LIM-A and LIM-B, which act as an interface for protein-protein interactions (171).

Some differences in the amino acid sequences of the LIM-A and LIM-B domains can be observed between the lmx1ba and lmx1bb proteins, equating to a 79% and 86% sequence similarity between the paralogues for each domain, respectively. These differences could influence the binding affinity of these domains for different transcription factors and co-factors, altering the type of transcriptional regulation complexes each paralogue forms. As the homeodomain is 100% conserved from humans to zebrafish, the binding of *lmx1b* to its

various gene regulatory targets is very unlikely to be altered between the paralogues. Therefore, this could explain the deviation seen in *lmx1ba* and *lmx1bb* function and phenotype in zebrafish.

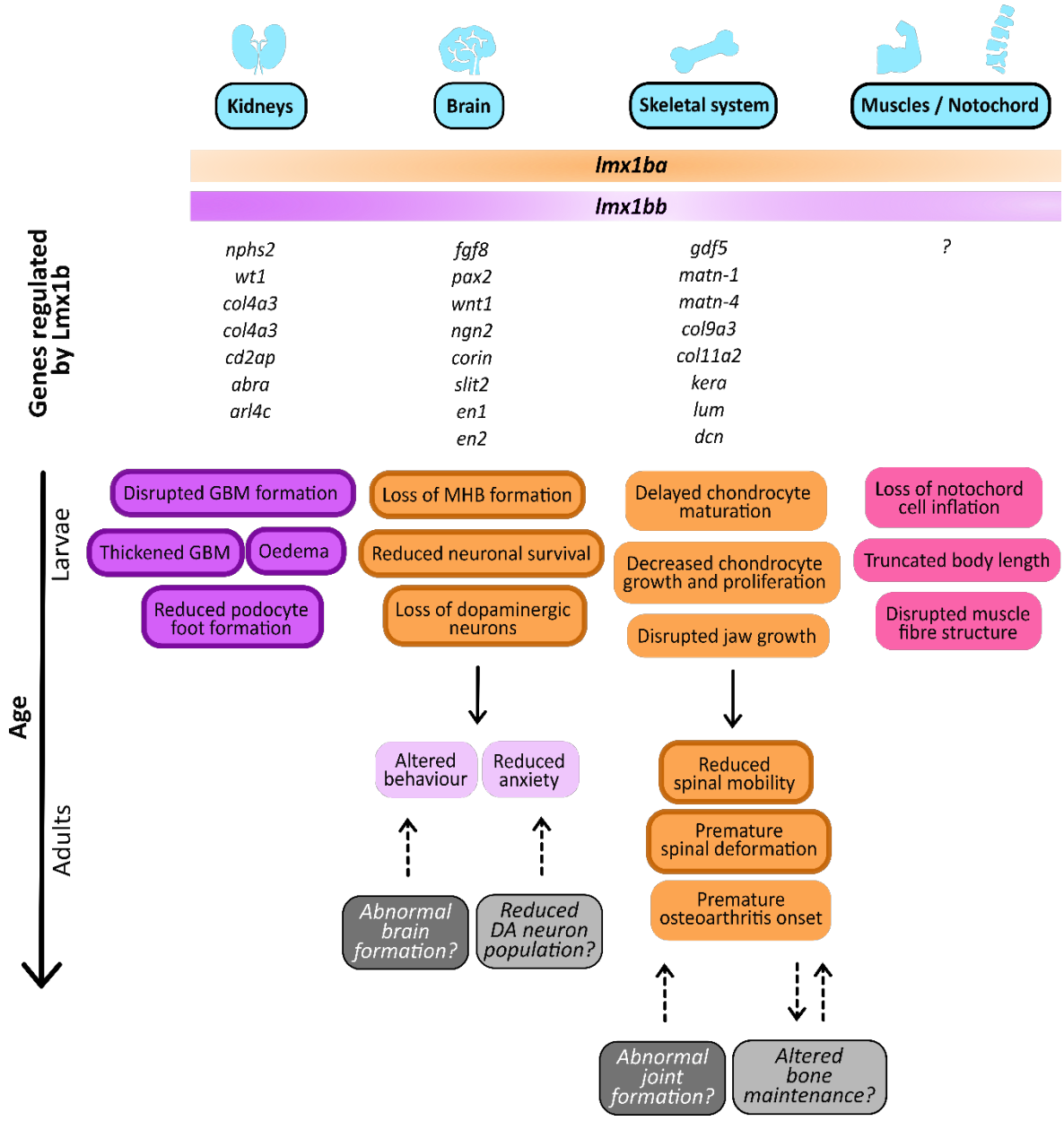

Figure 6.2.3 – Overview of proposed roles of *lmx1ba* and *lmx1bb* in organ development in zebrafish and the genes they regulate in these processes, Gradients show proposed influence of each *lmx1b* paralogue in the development of the kidneys, brain, skeletal system and musculature or notochord development, where a darker gradient indicates a greater involvement. Effect of loss of *lmx1b* paralogues on these organs is shown in coloured boxes where colour relates to a specific mutant: purple for *lmx1bb* mutants; orange for *lmx1ba* mutants; pale purple for *dHet* mutants and pink for *dKO* mutants. Phenotypes previously described in the literature from murine or zebrafish models or human NPS patients are indicated by darker box outline. Hypothesised effects of developmental (*dark grey*) or systemic (*light grey*) dysfunctions on adult phenotypes shown. Official gene names used.

6.2.4 Understanding the role of *lmx1ba* in cartilage development and regulation

As mentioned in Section 1.5.2 of the Chapter 1, *LMX1B* has been identified as a regulator of several genes involved in cartilage formation. Alongside regulating other transcription factors, proteoglycans, and matrix proteins, Feenstra *et al.,* showed that *Lmx1b* also regulates Type IX collagen α3 (Col9a3) and Type XI collagen α2 (Col11a2) (199). The authors found that in *Lmx1b* knock-out mice, the expression of these genes was decreased indicating that a similar effect might be present in the *lmx1ba* mutants here (Figure 6.2.3).

Type IX collagen, a heterotrimer formed of type XI α1, α2, and α3 chains, covalently crosslinks with type II collagen fibrils, helping to regulate their growth and organisation (404). Correspondingly, type XI collagen molecules are regulators of type II collagen fibrillogenesis, and interact with type II collagen fibrils to regulate their nucleation, formation and spacing (405). The correct spacing of type II collagen, via these minor collagens, is vital to its function in forming cartilage that is strong yet flexible and able to withstand a range of mechanical loads. In support of this, computational modelling has shown that dysregulation of collagen fibril spacing significantly affects its mechanical performance (406). Mutations in *COL9A3* have been shown to cause multiple epiphyseal dysplasia (MED), a degenerative cartilage disorder (407), whilst *COL11A2* is the causative gene behind the musculoskeletal disorder, Type III Stickler syndrome (408), with both disorders resulting in premature OA. Therefore, the expression of both of these genes is essential for the proper organisation and stabilisation of the type II collagen fibril network. As type II collagen forms over 90% of the total collagen in humans, this network is critical for the formation of a dense ECM which is required for proper cartilage function and health, especially during ageing (409). Thus, the reduced expression of these genes in *lmx1ba* mutants could be affecting cartilage formation or its stability, leading to the observed skeletal phenotype (Figure 6.2.3).

Similarly, the ECM-related *Matrilin* genes, *Matrilin-1* and *4*, are also regulated by *Lmx1b* and showed diminished expression in *Lmx1b* mutant mice (Figure 6.2.3) (199). These genes aid in skeletogenesis by binding to collagens and proteoglycans during cartilage matrix assembly (410), and are expressed in all cartilage regions, with expression of Matrilin-4 also observed

at the developing joint surface (411). In zebrafish, morpholino knock-down of Matrilin-1 leads to defects in body growth and in the formation of craniofacial cartilage, and a reduction in Col2a1 deposition, a key component of the ECM (412). Therefore, a reduction in the expression of these genes, via the *lmx1ba* mutation, could be affecting cartilage formation and growth during development. Meanwhile, changes to the stability of the ECM as the fish ages could be implicated in the premature vertebral degeneration seen in the adult *lmx1ba* mutants. This could be investigated by further ultrastructural analysis of *lmx1ba* mutant ECM or by exploring the material properties of the *lmx1ba* mutant cartilage. This can be done by atomic force microscopy and nano-indentation where the stiffness of the cartilage is measured to determine how well it deals with mechanical strain compared to *wt*, which can be used as an indication of ECM stability (413).

Altogether, these results correlate with data from previous studies which show that *Lmx1b* plays an active role in cartilage formation via the regulation of genes involved in its development (Figure 6.2.3). Here, *lmx1ba* is identified as the key paralogue in zebrafish behind cartilage development and regulation, and a mechanism through which loss of *lmx1ba* expression could mediate changes to cartilage formation is proposed. Given the later alterations to spinal morphology and movement, it is possible that these early developmental changes are the cause behind the premature onset of OA seen in the *lmx1ba* mutants. This will be discussed further in the following section.

6.3. Future perspectives

6.3.1 Exploring the relationship between skeletal changes in development and premature OA onset

One of the biggest questions that remains in the study of OA is how much of an impact developmental disturbances in joint formation have on the onset of this disease in adulthood. As established, OA is caused by the degeneration of articular cartilage between joint-forming bones. Changes to the structure and stability of articular cartilage can affect its

ability to absorb the impact of loading events, leading to disintegration of articular cartilage and damage to the underlying subchondral bone (414). Such changes can lead to the formation of secondary OA features, such as bone osteophytes, bone malalignment and sclerosis (415). Similarly, changes in joint shape have been suggested to increase the risk of OA at hip joints (416, 417), and in the absence of other symptoms, can be an early indicator for disease onset in later life for both knees and hips (266, 418). Therefore, it follows that genes which are involved in the development of articular cartilage or joint shape will likely carry the greatest genetic risk of premature joint damage and OA occurring if mutated. Several studies have demonstrated a heritable risk for OA at all joint sites, with family and twin studies indicating that this heritable component could be between 50-65% (419-422). Included in the list of genes linked to OA are several that are known to be involved in cartilage and joint development, such as *Gdf5, Col2a1,* and members of the Wingless (*Wnt*) and the bone morphogenetic protein (*Bmp*) family (206, 423-425). However, whether this increased susceptibility to OA is due to their direct effect on cartilage formation or joint shape is yet to be fully investigated.

In this thesis, two genes which have been implicated in skeletal development and OA were investigated for their effects on cartilage development and skeletal function. In the case of *atg13,* due to the early lethality of *atg13* homozygous mutants, the effect of the reduced joint mobility on OA onset could not be explored. Therefore, using the *atg13* heterozygous fish, it would be interesting to study whether partial loss of autophagy activity influences OA onset within an aged model. This could be explored using Alizarin red staining or μCT segmentation of the skeleton, looking specifically at the lower jaw joint where changes are seen in the *atg13*$^{-/-}$ mutants. Transverse sections through the vertebrae could also be done to investigate any changes to the stability and structure of the intervertebral discs, as degeneration of these cartilaginous structures can be a sign of OA (426).

For *lmx1ba,* the effect of delayed chondrocyte maturation and bone mineralisation on larval joint function was not explored; however, premature OA onset in the vertebral column and reductions in spine mobility were observed in adult *lmx1ba* mutants. Therefore, firstly, it would be helpful to establish whether these changes to chondrocyte development have an

effect on joint function at larval stages. Secondly, it would be interesting to see if developmental changes to spine formation precede the premature degeneration seen in the adults. For this, staining of the notochord using alizarin red or with antibodies against Col9a2 or Entpd5a would help show whether notochord segmentation is occurring normally as this forms the template for spinal patterning (427). Similar to above, staining of transverse vertebral sections in young and aged *lmx1ba* mutant fish would also help show the progression of the spinal abnormalities. Together these studies could help highlight the effect or role of developmental joint and cartilage changes on OA susceptibility in adulthood.

6.3.2 Use of the *lmx1b* mutant lines to model other skeletal diseases

LMX1B is also implicated in the development and patterning of the calvaria: the upper part of skull (337, 428). In *Lmx1b* mutant mice, calvaria bones are absent or hypoplasic, with the sutures between developing skull bones showing severe abnormalities (337). Through these studies, *Lmx1b* was identified as an anti-osteogenic factor which is expressed in the early migrating mesenchyme within the head, and helps prevent the premature ossification of foetal skull bones (428). Loss of *Lmx1b* was shown to result in heterotopic ossification of the early migrating mesenchyme and the development of craniosynostosis caused by premature suture closure (428). However, the anti-osteogenic activity of Lmx1b appears limited to the head as limb ossification remained unaffected in mutant mice. Craniosynostosis is not observed in NPS patients, which is thought to be due to be due to their heterozygous *LMX1B* genotype (428).

In humans, craniosynostosis is a rare congenital disorder which causes abnormalities in skull shape, and if left untreated, it can severely affect brain development and function (429). Currently, the main treatment option available for this condition is surgery, which in some cases has to be repeated multiple times due to resynostosis (430). Therefore, there is a need for better treatments for craniosynostosis and for the prevention of resynostosis. Using these zebrafish lines, investigation of their skulls by μCT combined with live imaging of osteoblast dynamics could be done to identify whether similar alterations to skull plate and suture formation can be seen. This characterisation would help identify the relevance of these lines

as a model for craniosynostosis and help further determine the role of *lmx1ba* and *lmx1bb* in skull formation.

In summary, this condition, along with the degenerative spinal phenotype seen in the *lmx1ba* mutants, highlights the different roles that *lmx1b* plays in skeletal development and maintenance. These future studies could help uncover the genes and pathways lmx1b regulates in these processes and help broaden our understanding of the molecular mechanisms behind these diseases.

6.4. Conclusion

Altogether, this thesis has demonstrated how zebrafish can be used as a valuable and relevant model for the study of molecular and genetic pathways in the development of a variety of body systems. Through the characterisation of the *atg13* mutant line, a new mechanism by which early changes to cartilage development, through autophagy dysregulation, can alter joint formation and function has been highlighted, and the possible interplay of various pathways in this process discussed. This thesis has also established a new model for the study of NPS and highlighted novel roles for *lmx1b* in notochord cell expansion and muscle formation, as well as a mechanism by which *lmx1ba* dysfunction can lead to premature OA onset. Overall, this work has expanded our understanding of the roles played by autophagy and *lmx1b* in the co-ordination of cartilage and joint development, among other systems, broadening our understanding of OA pathogenesis.

Chapter 7. Appendices

CHAPTER 7

Appendices

7.1. Appendix A

7.1.1 Vector Map of PX458 pSpCas9-2A-EGFP Plasmid

7.2. Appendix B

7.2.1 Modular Image Analysis for Adult Swim Behaviour Analysis

Cross SJ. MIA: Version 0.18.7. Zenodo: GitHub; 2021.

URL: https://githubcom/mianalysis/mia/releases/tag/v0187

7.2.2 Modular Image Analysis for Lower Jaw Cell Analysis

Cross SJ. MIA: Version 0.11.26. In: SJCross, editor. GitHub: Zenodo; 2020.

URL: https://githubcom/mianalysis/mia/releases/tag/v01126

For all MIA Links and Information

URL: https://github.com/sjcross

7.3. Appendix C

Both links will take you to a shared Google drive folder containing the videos related to Figure 3.2.6, Chapter 3. A separate link to the Google drive folder will have also been sent to you in the email containing a copy of this thesis.

7.3.1 Video 1 - Jaw movement is unaffected in wt larvae at 5dpf

Link: https://bit.ly/3Cwmy37

Video clip of larval jaw movements from 5dpf *wt* larvae. Video clip taken from longer videos filmed at 1 frame per second for 1000 frames.

7.3.2 Video 2 - The atg13 mutants show reduced jaw mobility and function at 5dpf

Link: https://bit.ly/3sWHLjK

Video clip of larval jaw movements from 5dpf *atg13 mutant* larvae. Video clip taken from longer videos filmed at 1 frame per second for 1000 frames.

Bibliography

1. Moss JJ, Hammond CL, Lane JD. Zebrafish as a model to study autophagy and its role in skeletal development and disease. Histochemistry and Cell Biology. 2020:1-16.
2. Dikic I, Elazar Z. Mechanism and medical implications of mammalian autophagy. Nat Rev Mol Cell Biol. 2018;19(6):349-64.
3. Kroemer G, Mariño G, Levine B. Autophagy and the integrated stress response. Molecular cell. 2010;40(2):280-93.
4. Mizushima N, Komatsu M. Autophagy: renovation of cells and tissues. Cell. 2011;147(4):728-41.
5. Orenstein SJ, Cuervo AM, editors. Chaperone-mediated autophagy: molecular mechanisms and physiological relevance. Seminars in cell & developmental biology; 2010: Elsevier.
6. Wang B, Abraham N, Gao G, Yang Q. Dysregulation of autophagy and mitochondrial function in Parkinson's disease. Translational neurodegeneration. 2016;5(1):19.
7. Mizushima N. Autophagy: process and function. Genes Dev. 2007;21(22):2861-73.
8. Klionsky DJ. Look people,"Atg" is an abbreviation for "autophagy-related." That's it. Autophagy. 2012;8(9):1281.
9. Tsukada M, Ohsumi Y. Isolation and characterization of autophagy-defective mutants of Saccharomyces cerevisiae. FEBS letters. 1993;333(1-2):169-74.
10. Mizushima N. A brief history of autophagy from cell biology to physiology and disease. Nat Cell Biol. 2018;20(5):521-7.
11. Wei Y, Liu M, Li X, Liu J, Li H. Origin of the Autophagosome membrane in mammals. BioMed research international. 2018;2018.
12. Kuma A, Komatsu M, Mizushima N. Autophagy-monitoring and autophagy-deficient mice. Autophagy. 2017;13(10):1619-28.
13. Ohsumi Y. Protein turnover. IUBMB life. 2006;58(5-6):363-9.
14. Ohsumi Y. Historical landmarks of autophagy research. Cell research. 2014;24(1):9-23.
15. Lamb CA, Yoshimori T, Tooze SA. The autophagosome: origins unknown, biogenesis complex. Nature reviews Molecular cell biology. 2013;14(12):759-74.
16. Qi S, Stjepanovic G, Hurley JH. Structure of the human Atg13-Atg101 HORMA heterodimer: an interaction hub within the ULK1 complex. Structure. 2015;23(10):1848-57.

17. Alers S, Wesselborg S, Stork B. ATG13: just a companion, or an executor of the autophagic program? Autophagy. 2014;10(6):944-56.

18. Musiwaro P, Smith M, Manifava M, Walker SA, Ktistakis NT. Characteristics and requirements of basal autophagy in HEK 293 cells. Autophagy. 2013;9(9):1407-17.

19. Haspel J, Shaik RS, Ifedigbo E, Nakahira K, Dolinay T, Englert JA, et al. Characterization of macroautophagic flux in vivo using a leupeptin-based assay. Autophagy. 2011;7(6):629-42.

20. Mizushima N, Levine B. Autophagy in mammalian development and differentiation. Nature cell biology. 2010;12(9):823-30.

21. Qu X, Yu J, Bhagat G, Furuya N, Hibshoosh H, Troxel A, et al. Promotion of tumorigenesis by heterozygous disruption of the beclin 1 autophagy gene. The Journal of clinical investigation. 2003;112(12):1809-20.

22. Yue Z, Jin S, Yang C, Levine AJ, Heintz N. Beclin 1, an autophagy gene essential for early embryonic development, is a haploinsufficient tumor suppressor. Proceedings of the National Academy of Sciences. 2003;100(25):15077-82.

23. Gan B, Peng X, Nagy T, Alcaraz A, Gu H, Guan J-L. Role of FIP200 in cardiac and liver development and its regulation of TNFα and TSC–mTOR signaling pathways. The Journal of cell biology. 2006;175(1):121-33.

24. Komatsu M, Wang QJ, Holstein GR, Friedrich VL, Iwata J-i, Kominami E, et al. Essential role for autophagy protein Atg7 in the maintenance of axonal homeostasis and the prevention of axonal degeneration. Proceedings of the National Academy of Sciences. 2007;104(36):14489-94.

25. Yorimitsu T, Klionsky DJ. Autophagy: molecular machinery for self-eating. Cell Death & Differentiation. 2005;12(2):1542-52.

26. He C, Klionsky DJ. Regulation mechanisms and signaling pathways of autophagy. Annual review of genetics. 2009;43:67-93.

27. Wirawan E, Berghe TV, Lippens S, Agostinis P, Vandenabeele P. Autophagy: for better or for worse. Cell research. 2012;22(1):43-61.

28. Choi AM, Ryter SW, Levine B. Autophagy in human health and disease. N Engl J Med. 2013;368(7):651-62.

29. Blommaart EF, Luiken JJ, Blommaart PJ, van Woerkom GM, Meijer AJ. Phosphorylation of ribosomal protein S6 is inhibitory for autophagy in isolated rat hepatocytes. Journal of Biological Chemistry. 1995;270(5):2320-6.

30. Codogno P, Meijer A. Autophagy and signaling: their role in cell survival and cell death. Cell Death & Differentiation. 2005;12(2):1509-18.

31. Hosokawa N, Hara T, Kaizuka T, Kishi C, Takamura A, Miura Y, et al. Nutrient-dependent mTORC1 association with the ULK1–Atg13–FIP200 complex required for autophagy. Molecular biology of the cell. 2009;20(7):1981-91.

32. Kim J, Kundu M, Viollet B, Guan K-L. AMPK and mTOR regulate autophagy through direct phosphorylation of Ulk1. Nature cell biology. 2011;13(2):132-41.

33. Hara K, Yonezawa K, Weng Q-P, Kozlowski MT, Belham C, Avruch J. Amino acid sufficiency and mTOR regulate p70 S6 kinase and eIF-4E BP1 through a common effector mechanism. Journal of Biological Chemistry. 1998;273(23):14484-94.

34. Puente C, Hendrickson RC, Jiang X. Nutrient-regulated phosphorylation of ATG13 inhibits starvation-induced autophagy. Journal of Biological Chemistry. 2016;291(11):6026-35.

35. Li J, Kim SG, Blenis J. Rapamycin: one drug, many effects. Cell metabolism. 2014;19(3):373-9.

36. Vakifahmetoglu-Norberg H, Xia H-g, Yuan J. Pharmacologic agents targeting autophagy. The Journal of clinical investigation. 2015;125(1):5-13.

37. Yamamoto A, Tagawa Y, Yoshimori T, Moriyama Y, Masaki R, Tashiro Y. Bafilomycin A1 prevents maturation of autophagic vacuoles by inhibiting fusion between autophagosomes and lysosomes in rat hepatoma cell line, H-4-II-E cells. Cell structure and function. 1998;23(1):33-42.

38. Füllgrabe J, Ghislat G, Cho D-H, Rubinsztein DC. Transcriptional regulation of mammalian autophagy at a glance. Journal of cell science. 2016;129(16):3059-66.

39. Deter RL, De Duve C. Influence of glucagon, an inducer of cellular autophagy, on some physical properties of rat liver lysosomes. The Journal of cell biology. 1967;33(2):437-49.

40. Zhou X, Takatoh J, Wang F. The mammalian class 3 PI3K (PIK3C3) is required for early embryogenesis and cell proliferation. PloS one. 2011;6(1):e16358.

41. Morishita H, Kanda Y, Kaizuka T, Chino H, Nakao K, Miki Y, et al. Autophagy Is Required for Maturation of Surfactant-Containing Lamellar Bodies in the Lung and Swim Bladder. Cell reports. 2020;33(10):108477.

42. Tsuboyama K, Koyama-Honda I, Sakamaki Y, Koike M, Morishita H, Mizushima N. The ATG conjugation systems are important for degradation of the inner autophagosomal membrane. Science. 2016;354(6315):1036-41.

43. Nguyen TN, Padman BS, Usher J, Oorschot V, Ramm G, Lazarou M. Atg8 family LC3/GABARAP proteins are crucial for autophagosome–lysosome fusion but not autophagosome formation during PINK1/Parkin mitophagy and starvation. Journal of Cell Biology. 2016;215(6):857-74.

44. Mizushima N. The role of the Atg1/ULK1 complex in autophagy regulation. Current opinion in cell biology. 2010;22(2):132-9.

45. Cheong H, Nair U, Geng J, Klionsky DJ. The Atg1 kinase complex is involved in the regulation of protein recruitment to initiate sequestering vesicle formation for nonspecific autophagy in Saccharomyces cerevisiae. Molecular biology of the cell. 2008;19(2):668-81.

46. Cadwell K, Debnath J. Beyond self-eating: The control of nonautophagic functions and signaling pathways by autophagy-related proteins. Journal of Cell Biology. 2018;217(3):813-22.

47. Levine B, Kroemer G. Biological functions of autophagy genes: a disease perspective. Cell. 2019;176(1-2):11-42.

48. Badadani M. Autophagy Mechanism, Regulation, Functions, and Disorders. ISRN Cell Biology. 2012;2012:1-11.

49. Carames B, Taniguchi N, Otsuki S, Blanco FJ, Lotz M. Autophagy is a protective mechanism in normal cartilage, and its aging-related loss is linked with cell death and osteoarthritis. Arthritis Rheum. 2010;62(3):791-801.

50. Lee W-S, Yoo W-H, Chae H-J. ER stress and autophagy. Current molecular medicine. 2015;15(8):735-45.

51. Husain A, Jeffries MA. Epigenetics and bone remodeling. Current osteoporosis reports. 2017;15(5):450-8.

52. Horigome Y, Ida-Yonemochi H, Waguri S, Shibata S, Endo N, Komatsu M. Loss of autophagy in chondrocytes causes severe growth retardation. Autophagy. 2020;16(3):501-11.

53. Chang J, Wang W, Zhang H, Hu Y, Wang M, Yin Z. The dual role of autophagy in chondrocyte responses in the pathogenesis of articular cartilage degeneration in osteoarthritis. Int J Mol Med. 2013;32(6):1311-8.

54. Ochotny N, Voronov I, Owen C, Aubin JE, Manolson MF. The R740 S mutation in the V-ATP ase a3 subunit results in osteoclast apoptosis and defective early-stage autophagy. Journal of cellular biochemistry. 2013;114(12):2823-33.

55. Yin X, Zhou C, Li J, Liu R, Shi B, Yuan Q, et al. Autophagy in bone homeostasis and the onset of osteoporosis. Bone Res. 2019;7:28.

56. Stenbeck G, Coxon FP. Role of vesicular trafficking in skeletal dynamics. Current opinion in pharmacology. 2014;16:7-14.

57. Silva IA, Conceição N, Gagnon É, Caiado H, Brown JP, Gianfrancesco F, et al. Effect of genetic variants of OPTN in the pathophysiology of Paget's disease of bone. Biochimica et Biophysica Acta (BBA)-Molecular Basis of Disease. 2018;1864(1):143-51.

58. Bouderlique T, Vuppalapati KK, Newton PT, Li L, Barenius B, Chagin AS. Targeted deletion of Atg5 in chondrocytes promotes age-related osteoarthritis. Annals of the rheumatic diseases. 2016;75(3):627-31.

59. Cheng NT, Meng H, Ma LF, Zhang L, Yu HM, Wang ZZ, et al. Role of autophagy in the progression of osteoarthritis: The autophagy inhibitor, 3-methyladenine, aggravates the severity of experimental osteoarthritis. Int J Mol Med. 2017;39(5):1224-32.

60. Aghajanian P, Mohan S. The art of building bone: emerging role of chondrocyte-to-osteoblast transdifferentiation in endochondral ossification. Bone Res. 2018;6:19.

61. Oliver L, Hue E, Priault M, Vallette FM. Basal autophagy decreased during the differentiation of human adult mesenchymal stem cells. Stem cells and development. 2012;21(15):2779-88.

62. Ma Y, Qi M, An Y, Zhang L, Yang R, Doro DH, et al. Autophagy controls mesenchymal stem cell properties and senescence during bone aging. Aging Cell. 2018;17(1):e12709.

63. Nollet M, Santucci-Darmanin S, Breuil V, Al-Sahlanee R, Cros C, Topi M, et al. Autophagy in osteoblasts is involved in mineralization and bone homeostasis. Autophagy. 2014;10(11):1965-77.

64. Nuschke A, Rodrigues M, Stolz DB, Chu CT, Griffith L, Wells A. Human mesenchymal stem cells/multipotent stromal cells consume accumulated autophagosomes early in differentiation. Stem cell research & therapy. 2014;5(6):140.

65. Liu F, Fang F, Yuan H, Yang D, Chen Y, Williams L, et al. Suppression of autophagy by FIP200 deletion leads to osteopenia in mice through the inhibition of osteoblast terminal differentiation. Journal of Bone and Mineral Research. 2013;28(11):2414-30.

66. Bird NC, Mabee PM. Developmental morphology of the axial skeleton of the zebrafish, Danio rerio (Ostariophysi: Cyprinidae). Developmental dynamics: an official publication of the American Association of Anatomists. 2003;228(3):337-57.

67. Mundlos S, Olsen B. Heritable diseases of the skeleton. Part I: Molecular insights into skeletal development-transcription factors and signaling pathways. The FASEB journal. 1997;11(2):125-32.

68. Ofer L, Dean MN, Zaslansky P, Kult S, Shwartz Y, Zaretsky J, et al. A novel nonosteocytic regulatory mechanism of bone modeling. PLoS biology. 2019;17(2):e3000140.

69. Vuppalapati KK, Bouderlique T, Newton PT, Kaminskyy VO, Wehtje H, Ohlsson C, et al. Targeted deletion of autophagy genes Atg5 or Atg7 in the chondrocytes promotes caspase-dependent cell death and leads to mild growth retardation. Journal of Bone and Mineral Research. 2015;30(12):2249-61.

70. Zhang M, Zhang J, Lu L, Qiu Z-Y, Zhang X, Yu S-B, et al. Enhancement of chondrocyte autophagy is an early response in the degenerative cartilage of the temporomandibular joint to biomechanical dental stimulation. Apoptosis. 2013;18(4):423-34.

71. Ralston SH. Paget's disease of bone. New England Journal of Medicine. 2013;368(7):644-50.

72. Azzam E, Helfrich M, Hocking L. Paget's disease-causing mutations in Sequestosome-1 impair autophagic protein degradation. J Bone Miner Res. 2011;26:1081.

73. Shen G, Ren H, Shang Q, Qiu T, Yu X, Zhang Z, et al. Autophagy as a target for glucocorticoid-induced osteoporosis therapy. Cellular and Molecular Life Sciences. 2018;75(15):2683-93.

74. Bo T, Yan F, Guo J, Lin X, Zhang H, Guan Q, et al. Characterization of a relatively malignant form of osteopetrosis caused by a novel mutation in the PLEKHM1 gene. Journal of Bone and Mineral Research. 2016;31(11):1979-87.

75. Gioia R, Panaroni C, Besio R, Palladini G, Merlini G, Giansanti V, et al. Impaired osteoblastogenesis in a murine model of dominant osteogenesis imperfecta: a new target for osteogenesis imperfecta pharmacological therapy. Stem Cells. 2012;30(7):1465-76.

76. Besio R, Iula G, Garibaldi N, Cipolla L, Sabbioneda S, Biggiogera M, et al. 4-PBA ameliorates cellular homeostasis in fibroblasts from osteogenesis imperfecta patients by enhancing autophagy and stimulating protein secretion. Biochimica et Biophysica Acta (BBA)-Molecular Basis of Disease. 2018;1864(5):1642-52.

77. Zhang L, Guo YF, Liu YZ, Liu YJ, Xiong DH, Liu XG, et al. Pathway-based genome-wide association analysis identified the importance of regulation-of-autophagy pathway for ultradistal radius BMD. Journal of Bone and Mineral Research. 2010;25(7):1572-80.

78. Xia X, Kar R, Gluhak-Heinrich J, Yao W, Lane NE, Bonewald LF, et al. Glucocorticoid-induced autophagy in osteocytes. Journal of bone and mineral research. 2010;25(11):2479-88.

79. Lieberman AP, Puertollano R, Raben N, Slaugenhaupt S, Walkley SU, Ballabio A. Autophagy in lysosomal storage disorders. Autophagy. 2012;8(5):719-30.

80. Berendsen AD, Olsen BR. Bone development. Bone. 2015;80:14-8.

81. Srinivas V, Bohensky J, Shapiro IM. Autophagy: a new phase in the maturation of growth plate chondrocytes is regulated by HIF, mTOR and AMP kinase. Cells Tissues Organs. 2009;189(1-4):88-92.

82. Cinque L, Forrester A, Bartolomeo R, Svelto M, Venditti R, Montefusco S, et al. FGF signalling regulates bone growth through autophagy. Nature. 2015;528(7581):272-5.

83. Li D, Yu J, Xiao L, Miao W, Ji K, Wang S, et al. Autophagy attenuates the oxidative stress-induced apoptosis of Mc3T3-E1 osteoblasts. Eur Rev Med Pharmacol Sci. 2017;21:5548-56.

84. Zahm AM, Bohensky J, Adams CS, Shapiro IM, Srinivas V. Bone cell autophagy is regulated by environmental factors. Cells Tissues Organs. 2011;194(2-4):274-8.

85. Piemontese M, Onal M, Xiong J, Han L, Thostenson JD, Almeida M, et al. Low bone mass and changes in the osteocyte network in mice lacking autophagy in the osteoblast lineage. Scientific reports. 2016;6(1):1-13.

86. Li H, Li D, Ma Z, Qian Z, Kang X, Jin X, et al. Defective autophagy in osteoblasts induces endoplasmic reticulum stress and causes remarkable bone loss. Autophagy. 2018;14(10):1726-41.

87. Riggs BL, Parfitt AM. Drugs used to treat osteoporosis: the critical need for a uniform nomenclature based on their action on bone remodeling. Journal of bone and mineral research. 2005;20(2):177-84.

88. Kawai M, Mödder UI, Khosla S, Rosen CJ. Emerging therapeutic opportunities for skeletal restoration. Nature reviews Drug discovery. 2011;10(2):141-56.

89. Zhao Q, Shao J, Chen W, Li Y-P. Osteoclast differentiation and gene regulation. Front Biosci. 2007;12(1):2519-29.

90. Mortensen M, Soilleux EJ, Djordjevic G, Tripp R, Lutteropp M, Sadighi-Akha E, et al. The autophagy protein Atg7 is essential for hematopoietic stem cell maintenance. Journal of Experimental Medicine. 2011;208(3):455-67.

91. Wang K, Niu J, Kim H, Kolattukudy PE. Osteoclast precursor differentiation by MCPIP via oxidative stress, endoplasmic reticulum stress, and autophagy. Journal of molecular cell biology. 2011;3(6):360-8.

92. Zhao Y, Chen G, Zhang W, Xu N, Zhu JY, Jia J, et al. Autophagy regulates hypoxia-induced osteoclastogenesis through the HIF-1α/BNIP3 signaling pathway. Journal of cellular physiology. 2012;227(2):639-48.

93. Shi J, Wang L, Zhang H, Jie Q, Li X, Shi Q, et al. Glucocorticoids: Dose-related effects on osteoclast formation and function via reactive oxygen species and autophagy. Bone. 2015;79:222-32.

94. DeSelm CJ, Miller BC, Zou W, Beatty WL, van Meel E, Takahata Y, et al. Autophagy proteins regulate the secretory component of osteoclastic bone resorption. Developmental cell. 2011;21(5):966-74.

95. Chung Y-H, Yoon S-Y, Choi B, Sohn DH, Yoon K-H, Kim W-J, et al. Microtubule-associated protein light chain 3 regulates Cdc42-dependent actin ring formation in osteoclast. The international journal of biochemistry & cell biology. 2012;44(6):989-97.

96. Dallas SL, Bonewald LF. Dynamics of the transition from osteoblast to osteocyte. Annals of the New York Academy of Sciences. 2010;1192:437.

97. Onal M, Piemontese M, Xiong J, Wang Y, Han L, Ye S, et al. Suppression of autophagy in osteocytes mimics skeletal aging. Journal of Biological Chemistry. 2013;288(24):17432-40.

98. Murray CJ, Lopez AD. Alternative projections of mortality and disability by cause 1990–2020: Global Burden of Disease Study. The lancet. 1997;349(9064):1498-504.

99. Woo T, Lau L, Cheung N, Chan P, Tan K, Gardner A. Efficacy of oral collagen in joint pain—osteoarthritis and rheumatoid arthritis. J Arthritis. 2017;6(233):2.

100. Neogi T. The epidemiology and impact of pain in osteoarthritis. Osteoarthritis and cartilage. 2013;21(9):1145-53.

101. Li YS, Zhang FJ, Zeng C, Luo W, Xiao WF, Gao SG, et al. Autophagy in osteoarthritis. Joint Bone Spine. 2016;83(2):143-8.

102. Litwic A, Edwards MH, Dennison EM, Cooper C. Epidemiology and burden of osteoarthritis. British medical bulletin. 2013;105(1):185-99.

103. Sophia Fox AJ, Bedi A, Rodeo SA. The basic science of articular cartilage: structure, composition, and function. Sports health. 2009;1(6):461-8.

104. Pennock AT, Robertson CM, Emmerson BC, Harwood FL, Amiel D. Role of apoptotic and matrix-degrading genes in articular cartilage and meniscus of mature and aged rabbits during development of osteoarthritis. Arthritis & Rheumatism. 2007;56(5):1529-36.

105. Pesesse L, Sanchez C, Delcour J-P, Bellahcene A, Baudouin C, Msika P, et al. Consequences of chondrocyte hypertrophy on osteoarthritic cartilage: potential effect on angiogenesis. Osteoarthritis and cartilage. 2013;21(12):1913-23.

106. Kamekura S, Kawasaki Y, Hoshi K, Shimoaka T, Chikuda H, Maruyama Z, et al. Contribution of runt-related transcription factor 2 to the pathogenesis of osteoarthritis in mice after induction of knee joint instability. Arthritis & Rheumatism: Official Journal of the American College of Rheumatology. 2006;54(8):2462-70.

107. Barranco C. Activate autophagy to prevent cartilage degeneration? Nature Reviews Rheumatology. 2015;11(3):127-8.

108. Caramés B, Taniguchi N, Otsuki S, Blanco FJ, Lotz M. Autophagy is a protective mechanism in normal cartilage, and its aging-related loss is linked with cell death and osteoarthritis. Arthritis & Rheumatism. 2010;62(3):791-801.

109. Liu J, Fu Q, Liu S. Transcriptional Regulation Based on Network of Autophagy Identifies Key Genes and Potential Mechanisms inHuman Osteoarthritis. Cartilage. 2020:1947603520951632.

110. Almonte-Becerril M, Navarro-Garcia F, Gonzalez-Robles A, Vega-Lopez M, Lavalle C, Kouri J. Cell death of chondrocytes is a combination between apoptosis and autophagy during the pathogenesis of Osteoarthritis within an experimental model. Apoptosis. 2010;15(5):631-8.

111. Zhang Y, Vasheghani F, Li Y-h, Blati M, Simeone K, Fahmi H, et al. Cartilage-specific deletion of mTOR upregulates autophagy and protects mice from osteoarthritis. Annals of the rheumatic diseases. 2015;74(7):1432-40.

112. Cibrián Uhalte E, Wilkinson JM, Southam L, Zeggini E. Pathways to understanding the genomic aetiology of osteoarthritis. Human molecular genetics. 2017;26(R2):R193-R201.

113. Beliaeva N, Kashirtseva V, Medvedeva N, IuIu K, Ipatova O, Archakov A. Zebrafish as a model organism for biomedical studies. Biomeditsinskaia khimiia. 2010;56(1):120-31.

114. Brittijn SA, Duivesteijn SJ, Belmamoune M, Bertens LF, Bitter W, Debruijn JD, et al. Zebrafish development and regeneration: new tools for biomedical research. International Journal of Developmental Biology. 2009;53(5-6):835-50.

115. Kabashi E, Brustein E, Champagne N, Drapeau P. Zebrafish models for the functional genomics of neurogenetic disorders. Biochimica et Biophysica Acta (BBA)-Molecular Basis of Disease. 2011;1812(3):335-45.

116. Streisinger G, Walker C, Dower N, Knauber D, Singer F. Production of clones of homozygous diploid zebra fish (Brachydanio rerio). Nature. 1981;291(5813):293-6.

117. Lieschke GJ, Currie PD. Animal models of human disease: zebrafish swim into view. Nature Reviews Genetics. 2007;8(5):353-67.

118. Bedell VM, Wang Y, Campbell JM, Poshusta TL, Starker CG, Krug II RG, et al. In vivo genome editing using a high-efficiency TALEN system. Nature. 2012;491(7422):114-8.

119. Talbot JC, Amacher SL. A streamlined CRISPR pipeline to reliably generate zebrafish frameshifting alleles. Zebrafish. 2014;11(6):583-5.

120. Liu K, Petree C, Requena T, Varshney P, Varshney GK. Expanding the CRISPR toolbox in zebrafish for studying development and disease. Frontiers in cell and developmental biology. 2019;7:13.

121. Briggs JP. The zebrafish: a new model organism for integrative physiology. American Journal of Physiology-Regulatory, Integrative and Comparative Physiology. 2002;282(1):R3-R9.

122. Klionsky DJ, Emr SD. Autophagy as a regulated pathway of cellular degradation. Science. 2000;290(5497):1717-21.

123. Reggiori F, Klionsky DJ. Autophagy in the eukaryotic cell. Eukaryotic cell. 2002;1(1):11-21.

124. Mathai BJ, Meijer AH, Simonsen A. Studying Autophagy in Zebrafish. Cells. 2017;6(3).

125. He C, Bartholomew CR, Zhou W, Klionsky DJ. Assaying autophagic activity in transgenic GFP-Lc3 and GFP-Gabarap zebrafish embryos. Autophagy. 2009;5(4):520-6.

126. Sasaki T, Lian S, Qi J, Bayliss PE, Carr CE, Johnson JL, et al. Aberrant autolysosomal regulation is linked to the induction of embryonic senescence: differential roles of Beclin 1 and p53 in vertebrate Spns1 deficiency. PLoS Genet. 2014;10(6):e1004409.

127. Sasaki T, Lian S, Khan A, Llop JR, Samuelson AV, Chen W, et al. Autolysosome biogenesis and developmental senescence are regulated by both Spns1 and v-ATPase. Autophagy. 2017;13(2):386-403.

128. Mawed SA, Zhang J, Ren F, Mei J. Autophagy-related genes atg7 and beclin1 are essential for energy metabolism and survival during the larval-to-juvenile transition stage of zebrafish. BioRxiv. 2019:666883.

129. Siddiqi FH, Menzies FM, Lopez A, Stamatakou E, Karabiyik C, Ureshino R, et al. Felodipine induces autophagy in mouse brains with pharmacokinetics amenable to repurposing. Nature communications. 2019;10(1):1-14.

130. Lu DL, Ma Q, Wang J, Li LY, Han SL, Limbu SM, et al. Fasting enhances cold resistance in fish through stimulating lipid catabolism and autophagy. The Journal of physiology. 2019;597(6):1585-603.

131. Dong G, Zhang Z, Duan K, Shi W, Huang R, Wang B, et al. Beclin 1 deficiency causes hepatic cell apoptosis via endoplasmic reticulum stress in zebrafish larvae. FEBS letters. 2020;594(7):1155-65.

132. Zhang R, Varela M, Forn-Cuni G, Torraca V, van der Vaart M, Meijer AH. Deficiency in the autophagy modulator Dram1 exacerbates pyroptotic cell death of Mycobacteria-infected macrophages. Cell Death & Disease. 2020;11(4):1-16.

133. Meneghetti G, Skobo T, Chrisam M, Facchinello N, Fontana CM, Bellesso S, et al. The epg5 knockout zebrafish line: a model to study Vici syndrome. Autophagy. 2019;15(8):1438-54.

134. Dvornikov AV, Wang M, Yang J, Zhu P, Le T, Lin X, et al. Phenotyping an adult zebrafish lamp2 cardiomyopathy model identifies mTOR inhibition as a candidate therapy. Journal of molecular and cellular cardiology. 2019;133:199-208.

135. Zhang R, Varela M, Vallentgoed W, Forn-Cuni G, van der Vaart M, Meijer AH. The selective autophagy receptors Optineurin and p62 are both required for zebrafish host resistance to mycobacterial infection. PLoS Pathog. 2019;15(2):e1007329.

136. Kabeya Y, Mizushima N, Ueno T, Yamamoto A, Kirisako T, Noda T, et al. LC3, a mammalian homologue of yeast Apg8p, is localized in autophagosome membranes after processing. The EMBO journal. 2000;19(21):5720-8.

137. Mizushima N, Yamamoto A, Matsui M, Yoshimori T, Ohsumi Y. In vivo analysis of autophagy in response to nutrient starvation using transgenic mice expressing a fluorescent autophagosome marker. Molecular biology of the cell. 2004;15(3):1101-11.

138. Mostowy S, Boucontet L, Moya MJM, Sirianni A, Boudinot P, Hollinshead M, et al. The zebrafish as a new model for the in vivo study of Shigella flexneri interaction with phagocytes and bacterial autophagy. PLoS Pathog. 2013;9(9):e1003588.

139. Varga M, Sass M, Papp D, Takács-Vellai K, Kobolak J, Dinnyés A, et al. Autophagy is required for zebrafish caudal fin regeneration. Cell Death & Differentiation. 2014;21(4):547-56.

140. Cui J, Sim TH-F, Gong Z, Shen H-M. Generation of transgenic zebrafish with liver-specific expression of EGFP-Lc3: a new in vivo model for investigation of liver autophagy. Biochemical and Biophysical Research Communications. 2012;422(2):268-73.

141. Klionsky DJ, Abdelmohsen K, Abe A, Abedin MJ, Abeliovich H, Acevedo Arozena A, et al. Guidelines for the use and interpretation of assays for monitoring autophagy. Autophagy. 2016;12(1):1-222.

142. Gomes P, Fernandes M. Rodent models in bone-related research: the relevance of calvarial defects in the assessment of bone regeneration strategies. Laboratory animals. 2011;45(1):14-24.

143. Sommer NG, Hahn D, Okutan B, Marek R, Weinberg A-M. Animal Models in Orthopedic Research: The Proper Animal Model to Answer Fundamental Questions on Bone Healing Depending on Pathology and Implant Material. Animal Models in Medicine and Biology: IntechOpen; 2019.

144. Schilling TF, Kimmel CB. Musculoskeletal patterning in the pharyngeal segments of the zebrafish embryo. Development. 1997;124(15):2945-60.

145. Brunt LH, Norton JL, Bright JA, Rayfield EJ, Hammond CL. Finite element modelling predicts changes in joint shape and cell behaviour due to loss of muscle strain in jaw development. Journal of biomechanics. 2015;48(12):3112-22.

146. Spoorendonk KM, Hammond CL, Huitema LF, Vanoevelen J, Schulte-Merker S. Zebrafish as a unique model system in bone research: the power of genetics and in vivo imaging. Journal of Applied Ichthyology. 2010;26(2):219-24.

147. Busse B, Galloway JL, Gray RS, Harris MP, Kwon RY. Zebrafish: an emerging model for orthopedic research. Journal of Orthopaedic Research®. 2020;38(5):925-36.

148. Hammond CL, Moro E. Using transgenic reporters to visualize bone and cartilage signaling during development in vivo. Frontiers in endocrinology. 2012;3:91.

149. Dietrich K, Fiedler IA, Kurzyukova A, López-Delgado AC, McGowan LM, Geurtzen K, et al. Skeletal biology and disease modeling in zebrafish. Journal of Bone and Mineral Research. 2021;36(3):436-58.

150. Weigele J, Franz-Odendaal TA. Functional bone histology of zebrafish reveals two types of endochondral ossification, different types of osteoblast clusters and a new bone type. Journal of anatomy. 2016;229(1):92-103.

151. Crotwell PL, Mabee PM. Gene expression patterns underlying proximal–distal skeletal segmentation in late-stage zebrafish, Danio rerio. Developmental dynamics: an official publication of the American Association of Anatomists. 2007;236(11):3111-28.

152. Flores MV, Tsang VWK, Hu W, Kalev-Zylinska M, Postlethwait J, Crosier P, et al. Duplicate zebrafish runx2 orthologues are expressed in developing skeletal elements. Gene expression patterns. 2004;4(5):573-81.

153. Li N, Felber K, Elks P, Croucher P, Roehl HH. Tracking gene expression during zebrafish osteoblast differentiation. Developmental dynamics. 2009;238(2):459-66.

154. Avaron F, Hoffman L, Guay D, Akimenko M. Characterization of two new zebrafish members of the hedgehog family: atypical expression of a zebrafish indian hedgehog gene in skeletal elements of both endochondral and dermal origins. Developmental dynamics: an official publication of the American Association of Anatomists. 2006;235(2):478-89.

155. Askary A, Smeeton J, Paul S, Schindler S, Braasch I, Ellis NA, et al. Ancient origin of lubricated joints in bony vertebrates. Elife. 2016;5:e16415.

156. Smeeton J, Askary A, Crump JG. Building and maintaining joints by exquisite local control of cell fate. Wiley Interdisciplinary Reviews: Developmental Biology. 2017;6(1):e245.

157. Mackay EW, Apschner A, Schulte-Merker S. A bone to pick with zebrafish. BoneKEy reports. 2013;2.

158. Lawrence EA, Kague E, Aggleton JA, Harniman RL, Roddy KA, Hammond CL. The mechanical impact of col11a2 loss on joints; col11a2 mutant zebrafish show changes to joint development and function, which leads to early-onset osteoarthritis. Philosophical Transactions of the Royal Society B: Biological Sciences. 2018;373(1759):20170335.

159. Carnovali M, Banfi G, Mariotti M. Zebrafish Models of Human Skeletal Disorders: Embryo and Adult Swimming Together. BioMed Research International. 2019;2019.

160. Hayes AJ, Reynolds S, Nowell MA, Meakin LB, Habicher J, Ledin J, et al. Spinal deformity in aged zebrafish is accompanied by degenerative changes to their vertebrae that resemble osteoarthritis. PLoS One. 2013;8(9):e75787.

161. Wang Y, Zhou Y, Graves DT. FOXO transcription factors: their clinical significance and regulation. BioMed research international. 2014;2014.

162. Zhou J, Liao W, Yang J, Ma K, Li X, Wang Y, et al. FOXO3 induces FOXO1-dependent autophagy by activating the AKT1 signaling pathway. Autophagy. 2012;8(12):1712-23.

163. Almeida M. Unraveling the role of FoxOs in bone—insights from mouse models. Bone. 2011;49(3):319-27.

164. Ambrogini E, Almeida M, Martin-Millan M, Paik J-H, DePinho RA, Han L, et al. FoxO-mediated defense against oxidative stress in osteoblasts is indispensable for skeletal homeostasis in mice. Cell metabolism. 2010;11(2):136-46.

165. Shapiro IM, Layfield R, Lotz M, Settembre C, Whitehouse C. Boning up on autophagy: the role of autophagy in skeletal biology. Autophagy. 2014;10(1):7-19.

166. Yang X, Matsuda K, Bialek P, Jacquot S, Masuoka HC, Schinke T, et al. ATF4 is a substrate of RSK2 and an essential regulator of osteoblast biology: implication for Coffin-Lowry syndrome. Cell. 2004;117(3):387-98.

167. Elefteriou F, Benson MD, Sowa H, Starbuck M, Liu X, Ron D, et al. ATF4 mediation of NF1 functions in osteoblast reveals a nutritional basis for congenital skeletal dysplasiae. Cell metabolism. 2006;4(6):441-51.

168. Curtiss J, Heilig JS. DeLIMiting development. Bioessays. 1998;20(1):58-69.

169. Hobert O, Westphal H. Functions of LIM-homeobox genes. Trends in genetics. 2000;16(2):75-83.

170. Rascle A, Neumann T, Raschta A-S, Neumann A, Heining E, Kastner J, et al. The LIM-homeodomain transcription factor LMX1B regulates expression of NF-kappa B target genes. Experimental cell research. 2009;315(1):76-96.

171. Bach I. The LIM domain: regulation by association. Mechanisms of development. 2000;91(1-2):5-17.

172. Johnson JD, Zhang W, Rudnick A, Rutter WJ, German MS. Transcriptional synergy between LIM-homeodomain proteins and basic helix-loop-helix proteins: the LIM2 domain determines specificity. Molecular and Cellular Biology. 1997;17(7):3488-96.

173. Suleiman H, Heudobler D, Raschta A-S, Zhao Y, Zhao Q, Hertting I, et al. The podocyte-specific inactivation of Lmx1b, Ldb1 and E2a yields new insight into a transcriptional network in podocytes. Developmental biology. 2007;304(2):701-12.

174. Marini M, Bocciardi R, Gimelli S, Di Duca M, Divizia MT, Baban A, et al. A spectrum of LMX1B mutations in Nail-Patella syndrome: new point mutations, deletion, and evidence of mosaicism in unaffected parents. Genetics in Medicine. 2010;12(7):431-9.

175. Laguna A, Schintu N, Nobre A, Alvarsson A, Volakakis N, Jacobsen JK, et al. Dopaminergic control of autophagic-lysosomal function implicates Lmx1b in Parkinson's disease. Nature Neuroscience. 2015;18(6):826-35.

176. Bergman O, Westberg L, Nilsson L-G, Adolfsson R, Eriksson E. Preliminary evidence that polymorphisms in dopamine-related transcription factors LMX1A, LMX1B and PITX3 are associated with schizophrenia. Progress in Neuro-Psychopharmacology and Biological Psychiatry. 2010;34(6):1094-7.

177. Thanseem I, Nakamura K, Anitha A, Suda S, Yamada K, Iwayama Y, et al. Association of transcription factor gene LMX1B with autism. PLoS One. 2011;6(8):e23738.

178. Park S, Jamshidi Y, Vaideanu D, Bitner-Glindzicz M, Fraser S, Sowden JC. Genetic risk for primary open-angle glaucoma determined by LMX1B haplotypes. Investigative ophthalmology & visual science. 2009;50(4):1522-30.

179. Vollrath D, Jaramillo-Babb VL, Clough MV, McIntosh I, Scott KM, Lichter PR, et al. Loss-of-function mutations in the LIM-homeodomain gene, LMX1B, in nail-patella syndrome. Human molecular genetics. 1998;7(7):1091-8.

180. Lane JD, Jimenez-Moreno N, Stathakos P, Anton Z, Shoemark D, Sessions R, et al. LIR-dependent LMX1A/LMX1B autophagy crosstalk shapes human midbrain dopaminergic neuronal resilience. bioRxiv. 2019:636712.

181. Dreyer SD, Morello R, German MS, Zabel B, Winterpacht A, Lunstrum GP, et al. LMX1B transactivation and expression in nail–patella syndrome. Human molecular genetics. 2000;9(7):1067-74.

182. Doucet-Beaupré H, Gilbert C, Profes MS, Chabrat A, Pacelli C, Giguère N, et al. Lmx1a and Lmx1b regulate mitochondrial functions and survival of adult midbrain dopaminergic neurons. Proceedings of the National Academy of Sciences. 2016;113(30):E4387-E96.

183. Hilinski WC, Bostrom JR, England SJ, Juárez-Morales JL, de Jager S, Armant O, et al. Lmx1b is required for the glutamatergic fates of a subset of spinal cord neurons. Neural development. 2016;11(1):16.

184. Chizhikov VV, Millen KJ. Control of roof plate development and signaling by Lmx1b in the caudal vertebrate CNS. Journal of Neuroscience. 2004;24(25):5694-703.

185. O'Hara FP, Beck E, Barr LK, Wong LL, Kessler DS, Riddle RD. Zebrafish Lmx1b.1 and Lmx1b.2 are required for maintenance of the isthmic organizer. Development. 2005;132(14):3163-73.

186. Guo C, Qiu H-Y, Huang Y, Chen H, Yang R-Q, Chen S-D, et al. Lmx1b is essential for Fgf8 and Wnt1 expression in the isthmic organizer during tectum and cerebellum development in mice. Development. 2007;134(2):317-25.

187. Swinburne IA, Mosaliganti KR, Upadhyayula S, Liu T-L, Hildebrand DGC, Tsai T, et al. Lamellar junctions in the endolymphatic sac act as a relief valve to regulate inner ear pressure. BioRxiv. 2017:143826.

188. McMahon C, Gestri G, Wilson SW, Link BA. Lmx1b is essential for survival of periocular mesenchymal cells and influences Fgf-mediated retinal patterning in zebrafish. Developmental biology. 2009;332(2):287-98.

189. Haro E, Watson BA, Feenstra JM, Tegeler L, Pira CU, Mohan S, et al. Lmx1b-targeted cis-regulatory modules involved in limb dorsalization. Development. 2017;144(11):2009-20.

190. Filippi A, Dürr K, Ryu S, Willaredt M, Holzschuh J, Driever W. Expression and function of nr4a2, lmx1b, and pitx3 in zebrafish dopaminergic and noradrenergic neuronal development. BMC developmental biology. 2007;7(1):1-21.

191. Morello R, Zhou G, Dreyer SD, Harvey SJ, Ninomiya Y, Thorner PS, et al. Regulation of glomerular basement membrane collagen expression by LMX1B contributes to renal disease in nail patella syndrome. Nature genetics. 2001;27(2):205-8.

192. Liu P, Johnson RL. Lmx1b is required for murine trabecular meshwork formation and for maintenance of corneal transparency. Developmental Dynamics. 2010;239(8):2161-71.

193. Vogel A, Rodriguez C, Warnken W, Belmonte JCI. Dorsal cell fate specified by chick Lmxl during vertebrate limb development. Nature. 1995;378(6558):716-20.

194. Chen H, Lun Y, Ovchinnikov D, Kokubo H, Oberg KC, Pepicelli CV, et al. Limb and kidney defects in Lmx1b mutant mice suggest an involvement of LMX1B in human nail patella syndrome. Nature genetics. 1998;19(1):51-5.

195. Riddle RD, Ensini M, Nelson C, Tsuchida T, Jessell TM, Tabin C. Induction of the LIM homeobox gene Lmx1 by WNT6a establishes dorsoventral pattern in the vertebrate limb. Cell. 1995;83(4):631-40.

196. Cygan JA, Johnson RL, McMahon AP. Novel regulatory interactions revealed by studies of murine limb pattern in Wnt-7a and En-1 mutants. Development. 1997;124(24):5021-32.

197. Loomis CA, Kimmel RA, Tong C-X, Michaud J, Joyner AL. Analysis of the genetic pathway leading to formation of ectopic apical ectodermal ridges in mouse Engrailed-1 mutant limbs. Development. 1998;125(6):1137-48.

198. Dreyer SD, Naruse T, Morello R, Zabel B, Winterpacht A, Johnson RL, et al. Lmx1b expression during joint and tendon formation: localization and evaluation of potential downstream targets. Gene expression patterns. 2004;4(4):397-405.

199. Feenstra JM, Kanaya K, Pira CU, Hoffman SE, Eppey RJ, Oberg KC. Detection of genes regulated by Lmx1b during limb dorsalization. Development, growth & differentiation. 2012;54(4):451-62.

200. Gu WX, Kania A. Identification of genes controlled by LMX1B in E13. 5 mouse limbs. Developmental Dynamics. 2010;239(8):2246-55.

201. Krawchuk D, Kania A. Identification of genes controlled by LMX1B in the developing mouse limb bud. Developmental Dynamics. 2008;237(4):1183-92.

202. Francis-West P, Abdelfattah A, Chen P, Allen C, Parish J, Ladher R, et al. Mechanisms of GDF-5 action during skeletal development. Development. 1999;126(6):1305-15.

203. Nicolae C, Ko Y-P, Miosge N, Niehoff A, Studer D, Enggist L, et al. Abnormal collagen fibrils in cartilage of matrilin-1/matrilin-3-deficient mice. Journal of biological chemistry. 2007;282(30):22163-75.

204. Saklatvala J. Does decorin stabilize the extracellular matrix of articular cartilage and slow the progression of osteoarthritis? Osteoarthritis and Cartilage. 2021.

205. Li P, Fleischhauer L, Nicolae C, Prein C, Farkas Z, Saller MM, et al. Mice lacking the matrilin family of extracellular matrix proteins develop mild skeletal abnormalities and are susceptible to age-associated osteoarthritis. International journal of molecular sciences. 2020;21(2):666.

206. Miyamoto Y, Mabuchi A, Shi D, Kubo T, Takatori Y, Saito S, et al. A functional polymorphism in the 5′ UTR of GDF5 is associated with susceptibility to osteoarthritis. Nature genetics. 2007;39(4):529-33.

207. Barreto G, Senturk B, Colombo L, Brück O, Neidenbach P, Salzmann G, et al. Lumican is upregulated in osteoarthritis and contributes to TLR4-induced pro-inflammatory activation of cartilage degradation and macrophage polarization. Osteoarthritis and Cartilage. 2020;28(1):92-101.

208. Melrose J, Fuller ES, Roughley PJ, Smith MM, Kerr B, Hughes CE, et al. Fragmentation of decorin, biglycan, lumican and keratocan is elevated in degenerate human meniscus, knee and hip articular cartilages compared with age-matched macroscopically normal and control tissues. Arthritis research & therapy. 2008;10(4):1-10.

209. Sweeney E, Fryer A, Mountford R, Green A, McIntosh I. Nail patella syndrome: a review of the phenotype aided by developmental biology. Journal of medical genetics. 2003;40(3):153-62.

210. Marini M, Giacopelli F, Seri M, Ravazzolo R. Interaction of the LMX1B and PAX2 gene products suggests possible molecular basis of differential phenotypes in nail–patella syndrome. European journal of human genetics. 2005;13(6):789-92.

211. Bongers EM, Gubler M-C, Knoers NV. Nail-patella syndrome. Overview on clinical and molecular findings. Pediatric nephrology. 2002;17(9):703-12.

212. Bongers EM, Huysmans FT, Levtchenko E, de Rooy JW, Blickman JG, Admiraal RJ, et al. Genotype–phenotype studies in nail-patella syndrome show that LMX1B mutation location is involved in the risk of developing nephropathy. European journal of human genetics. 2005;13(8):935-46.

213. Lovelace PD, May LA. Nail patella syndrome. StatPearls [Internet]. 2021.

214. Burghardt T, Kastner J, Suleiman H, Rivera-Milla E, Stepanova N, Lottaz C, et al. LMX1B is essential for the maintenance of differentiated podocytes in adult kidneys. J Am Soc Nephrol. 2013;24(11):1830-48.

215. Bennett WM, Musgrave JE, Campbell RA, Elliot D, Cox R, Brooks RE, et al. The nephropathy of the nail-patella syndrome: clinicopathologic analysis of 11 kindred. The American journal of medicine. 1973;54(3):304-19.

216. Looij B, Te Slaa R, Hogewind B, Van de Kamp J. Genetic counselling in hereditary osteo-onychodysplasia (HOOD, nail-patella syndrome) with nephropathy. Journal of medical genetics. 1988;25(10):682-6.

217. Pressman CL, Chen H, Johnson RL. LMX1B, a LIM homeodomain class transcription factor, is necessary for normal development of multiple tissues in the anterior segment of the murine eye. genesis. 2000;26(1):15-25.

218. Smidt MP, Asbreuk CH, Cox JJ, Chen H, Johnson RL, Burbach JPH. A second independent pathway for development of mesencephalic dopaminergic neurons requires Lmx1b. Nature neuroscience. 2000;3(4):337-41.

219. López-Arvizu C, Sparrow EP, Strube MJ, Slavin C, DeOleo C, James J, et al. Increased symptoms of attention deficit hyperactivity disorder and major depressive disorder symptoms in nail-patella syndrome: potential association with LMX1B loss-of-function. American Journal of Medical Genetics Part B: Neuropsychiatric Genetics. 2011;156(1):59-66.

220. Morris JA, Kemp JP, Youlten SE, Laurent L, Logan JG, Chai RC, et al. An atlas of genetic influences on osteoporosis in humans and mice. Nature genetics. 2019;51(2):258-66.

221. Tachmazidou I, Hatzikotoulas K, Southam L, Esparza-Gordillo J, Haberland V, Zheng J, et al. 2018.

222. Ryu S, Mahler J, Acampora D, Holzschuh J, Erhardt S, Omodei D, et al. Orthopedia homeodomain protein is essential for diencephalic dopaminergic neuron development. Current Biology. 2007;17(10):873-80.

223. Livak K, Schmittgen T. Analysis of relative gene expression data using real-time quantitative PCR and the 2 (-Delta Delta C (T)) Method. Methods [Internet]. 2001 Dec; 25 (4): 402–8.

224. Schindelin J, Arganda-Carreras I, Frise E, Kaynig V, Longair M, Pietzsch T, et al. Fiji: an open-source platform for biological-image analysis. Nature methods. 2012;9(7):676-82.

225. Ran FA, Hsu PD, Wright J, Agarwala V, Scott DA, Zhang F. Genome engineering using the CRISPR-Cas9 system. Nature protocols. 2013;8(11):2281.

226. Montague TG, Cruz JM, Gagnon JA, Church GM, Valen E. CHOPCHOP: a CRISPR/Cas9 and TALEN web tool for genome editing. Nucleic acids research. 2014;42(W1):W401-W7.

227. Westerfield M. The zebrafish book: a guide for the laboratory use of zebrafish. http://zfin org/zf_info/zfbook/zfbk html. 2000.

228. Mitchell RE, Huitema L, Skinner R, Brunt L, Severn C, Schulte-Merker S, et al. New tools for studying osteoarthritis genetics in zebrafish. Osteoarthritis and Cartilage. 2013;21(2):269-78.

229. Moss JJ, Wirth M, Tooze SA, Lane JD, Hammond CL. Autophagy coordinates chondrocyte development and early joint formation in zebrafish. The FASEB Journal. 2021;35(11):e22002.

230. Moreno-Mateos MA, Vejnar CE, Beaudoin J-D, Fernandez JP, Mis EK, Khokha MK, et al. CRISPRscan: designing highly efficient sgRNAs for CRISPR-Cas9 targeting in vivo. Nature methods. 2015;12(10):982-8.

231. Rozen S, Skaletsky H. Primer3 on the WWW for general users and for biologist programmers. Bioinformatics methods and protocols: Springer; 2000. p. 365-86.

232. Kastenhuber E, Kratochwil CF, Ryu S, Schweitzer J, Driever W. Genetic dissection of dopaminergic and noradrenergic contributions to catecholaminergic tracts in early larval zebrafish. Journal of Comparative Neurology. 2010;518(4):439-58.

233. Prewitt JM, Mendelsohn ML. The analysis of cell images. Annals of the New York Academy of Sciences. 1966;128(3):1035-53.

234. Munkres J. Algorithms for the assignment and transportation problems. Journal of the society for industrial and applied mathematics. 1957;5(1):32-8.

235. Cleveland WS. Robust locally weighted regression and smoothing scatterplots. Journal of the American statistical association. 1979;74(368):829-36.

236. Stewart A, Gaikwad S, Kyzar E, Green J, Roth A, Kalueff AV. Modeling anxiety using adult zebrafish: a conceptual review. Neuropharmacology. 2012;62(1):135-43.

237. Bencan Z, Sledge D, Levin ED. Buspirone, chlordiazepoxide and diazepam effects in a zebrafish model of anxiety. Pharmacology Biochemistry and Behavior. 2009;94(1):75-80.

238. López-Patiño MA, Yu L, Cabral H, Zhdanova IV. Anxiogenic effects of cocaine withdrawal in zebrafish. Physiology & behavior. 2008;93(1-2):160-71.

239. Formella I, Scott EK, Burne TH, Harms LR, Liu P-Y, Turner KM, et al. Transient knockdown of tyrosine hydroxylase during development has persistent effects on behaviour in adult zebrafish (Danio rerio). 2012.

240. Cross SJ. MIA: Version 0.18.7. https://githubcom/mianalysis/mia/releases/tag/v0187. Zenodo: GitHub; 2021.

241. Cross SJ. MIA: Version 0.11.26. In: SJCross, editor. https://githubcom/mianalysis/mia/releases/tag/v01126. GitHub: Zenodo; 2020.

242. Otsu N. A threshold selection method from gray-level histograms. IEEE transactions on systems, man, and cybernetics. 1979;9(1):62-6.

243. Edelsbrunner H, Kirkpatrick D, Seidel R. On the shape of a set of points in the plane. IEEE Transactions on information theory. 1983;29(4):551-9.

244. Brunt LH, Begg K, Kague E, Cross S, Hammond CL. Wnt signalling controls the response to mechanical loading during zebrafish joint development. Development. 2017;144(15):2798-809.

245. Ganley IG, Lam DH, Wang J, Ding X, Chen S, Jiang X. ULK1· ATG13· FIP200 complex mediates mTOR signaling and is essential for autophagy. Journal of Biological Chemistry. 2009;284(18):12297-305.

246. Hieke N, Loffler AS, Kaizuka T, Berleth N, Bohler P, Driessen S, et al. Expression of a ULK1/2 binding-deficient ATG13 variant can partially restore autophagic activity in ATG13-deficient cells. Autophagy. 2015;11(9):1471-83.

247. Hegedűs K, Nagy P, Gáspári Z, Juhász G. The putative HORMA domain protein Atg101 dimerizes and is required for starvation-induced and selective autophagy in Drosophila. BioMed research international. 2014;2014.

248. Jao CC, Ragusa MJ, Stanley RE, Hurley JH. A HORMA domain in Atg13 mediates PI 3-kinase recruitment in autophagy. Proceedings of the National Academy of Sciences. 2013;110(14):5486-91.

249. Park J-M, Jung CH, Seo M, Otto NM, Grunwald D, Kim KH, et al. The ULK1 complex mediates MTORC1 signaling to the autophagy initiation machinery via binding and phosphorylating ATG14. Autophagy. 2016;12(3):547-64.

250. Suzuki H, Kaizuka T, Mizushima N, Noda NN. Structure of the Atg101–Atg13 complex reveals essential roles of Atg101 in autophagy initiation. Nature structural & molecular biology. 2015;22(7):572.

251. Fujioka Y, Suzuki SW, Yamamoto H, Kondo-Kakuta C, Kimura Y, Hirano H, et al. Structural basis of starvation-induced assembly of the autophagy initiation complex. Nature structural & molecular biology. 2014;21(6):513.

252. Chang Y-Y, Neufeld TP. An Atg1/Atg13 complex with multiple roles in TOR-mediated autophagy regulation. Molecular biology of the cell. 2009;20(7):2004-14.

253. Tian E, Wang F, Han J, Zhang H. epg-1 functions in autophagy-regulated processes and may encode a highly divergent Atg13 homolog in C. elegans. Autophagy. 2009;5(5):608-15.

254. Kraft C, Kijanska M, Kalie E, Siergiejuk E, Lee SS, Semplicio G, et al. Binding of the Atg1/ULK1 kinase to the ubiquitin-like protein Atg8 regulates autophagy. The EMBO journal. 2012;31(18):3691-703.

255. Karanasios E, Stapleton E, Manifava M, Kaizuka T, Mizushima N, Walker SA, et al. Dynamic association of the ULK1 complex with omegasomes during autophagy induction. Journal of cell science. 2013;126(22):5224-38.

256. Alers S, Löffler AS, Paasch F, Dieterle AM, Keppeler H, Lauber K, et al. Atg13 and FIP200 act independently of Ulk1 and Ulk2 in autophagy induction. Autophagy. 2011;7(12):1424-33.

257. Kaizuka T, Mizushima N. Atg13 is essential for autophagy and cardiac development in mice. Molecular and cellular biology. 2016;36(4):585-95.

258. Komatsu M, Waguri S, Ueno T, Iwata J, Murata S, Tanida I, et al. Impairment of starvation-induced and constitutive autophagy in Atg7-deficient mice. Journal of Cell Biology. 2005;169(3):425-34.

259. Neufeld TP. Autophagy and cell growth–the yin and yang of nutrient responses. Journal of cell science. 2012;125(10):2359-68.

260. Deegan S, Saveljeva S, Gorman AM, Samali A. Stress-induced self-cannibalism: on the regulation of autophagy by endoplasmic reticulum stress. Cellular and Molecular Life Sciences. 2013;70(14):2425-41.

261. Jeon H, Im GI. Autophagy in osteoarthritis. Connect Tissue Res. 2017;58(6):497-508.

262. Duan R, Xie H, Liu Z-Z. The Role of Autophagy in Osteoarthritis. Frontiers in Cell and Developmental Biology. 2020;8:1437.

263. Faber BG, Baird D, Gregson CL, Gregory JS, Barr RJ, Aspden RM, et al. DXA-derived hip shape is related to osteoarthritis: findings from in the MrOS cohort. Osteoarthritis and cartilage. 2017;25(12):2031-8.

264. Waarsing J, Rozendaal R, Verhaar J, Bierma-Zeinstra S, Weinans H. A statistical model of shape and density of the proximal femur in relation to radiological and clinical OA of the hip. Osteoarthritis and cartilage. 2010;18(6):787-94.

265. Beck M, Kalhor M, Leunig M, Ganz R. Hip morphology influences the pattern of damage to the acetabular cartilage: femoroacetabular impingement as a cause of early osteoarthritis of the hip. The Journal of bone and joint surgery British volume. 2005;87(7):1012-8.

266. Baker-LePain JC, Lane NE. Relationship between joint shape and the development of osteoarthritis. Current opinion in rheumatology. 2010;22(5):538.

267. Provot S, Schipani E. Molecular mechanisms of endochondral bone development. Biochemical and biophysical research communications. 2005;328(3):658-65.

268. Dodds G. Row formation and other types of arrangement of cartilage cells in endochondral ossification. The Anatomical Record. 1930;46(4):385-99.

269. Davidson LA, Joshi SD, Kim HY, Von Dassow M, Zhang L, Zhou J. Emergent morphogenesis: elastic mechanics of a self-deforming tissue. Journal of biomechanics. 2010;43(1):63-70.

270. Akkiraju H, Nohe A. Role of chondrocytes in cartilage formation, progression of osteoarthritis and cartilage regeneration. Journal of developmental biology. 2015;3(4):177-92.

271. Kang X, Yang W, Feng D, Jin X, Ma Z, Qian Z, et al. Cartilage-specific autophagy deficiency promotes ER stress and impairs chondrogenesis in PERK-ATF4-CHOP–dependent manner. Journal of Bone and Mineral Research. 2017;32(10):2128-41.

272. Mawed SA, Zhang J, Ren F, He Y, Mei J. atg7 and beclin1 are essential for energy metabolism and survival during the larval-to-juvenile transition stage of zebrafish. Aquaculture and Fisheries. 2021.

273. Khuansuwan S, Barnhill LM, Cheng S, Bronstein JM. A novel transgenic zebrafish line allows for in vivo quantification of autophagic activity in neurons. Autophagy. 2019;15(8):1322-32.

274. Tian Y, Li Z, Hu W, Ren H, Tian E, Zhao Y, et al. C. elegans screen identifies autophagy genes specific to multicellular organisms. Cell. 2010;141(6):1042-55.

275. Liang Q, Yang P, Tian E, Han J, Zhang H. The C. elegans ATG101 homolog EPG-9 directly interacts with EPG-1/Atg13 and is essential for autophagy. Autophagy. 2012;8(10):1426-33.

276. Hernández LP, Barresi MJ, Devoto SH. Functional morphology and developmental biology of zebrafish: reciprocal illumination from an unlikely couple. Integrative and comparative biology. 2002;42(2):222-31.

277. Kronenberg HM. Developmental regulation of the growth plate. Nature. 2003;423(6937):332-6.

278. Bi W, Deng JM, Zhang Z, Behringer RR, De Crombrugghe B. Sox9 is required for cartilage formation. Nature genetics. 1999;22(1):85-9.

279. Chiang EF-L, Pai C-I, Wyatt M, Yan Y-L, Postlethwait J, Chung B-c. Two sox9 genes on duplicated zebrafish chromosomes: expression of similar transcription activators in distinct sites. Developmental biology. 2001;231(1):149-63.

280. Harlick RM, Shanmugam K. ITS'Hak Dinstein.". Textural feature for image classification" IEEE Transaction on systems Man and Cybernetics Vol-SMS. 1973(6).

281. Materka A. Texture analysis methodologies for magnetic resonance imaging. Dialogues in clinical neuroscience. 2004;6(2):243.

282. Kumar RM, Sreekumar K. A survey on image feature descriptors. Int J Comput Sci Inf Technol. 2014;5:7668-73.

283. Loganathan R, Potetz BR, Rongish BJ, Little CD. Spatial anisotropies and temporal fluctuations in extracellular matrix network texture during early embryogenesis. PloS one. 2012;7(5):e38266.

284. Joseph GB, Baum T, Carballido-Gamio J, Nardo L, Virayavanich W, Alizai H, et al. Texture analysis of cartilage T 2 maps: individuals with risk factors for OA have higher and more heterogeneous knee cartilage MR T 2 compared to normal controls-data from the osteoarthritis initiative. Arthritis research & therapy. 2011;13(5):1-12.

285. Lane JD, Korolchuk VI, Murray JT, Zachari M, Ganley IG. The mammalian ULK1 complex and autophagy initiation. Essays in biochemistry. 2017;61(6):585-96.

286. Itakura E, Mizushima N. Characterization of autophagosome formation site by a hierarchical analysis of mammalian Atg proteins. Autophagy. 2010;6(6):764-76.

287. Pankiv S, Clausen TH, Lamark T, Brech A, Bruun J-A, Outzen H, et al. p62/SQSTM1 binds directly to Atg8/LC3 to facilitate degradation of ubiquitinated protein aggregates by autophagy. Journal of biological chemistry. 2007;282(33):24131-45.

288. Henault J, Martinez J, Riggs JM, Tian J, Mehta P, Clarke L, et al. Noncanonical autophagy is required for type I interferon secretion in response to DNA-immune complexes. Immunity. 2012;37(6):986-97.

289. Kim J-Y, Zhao H, Martinez J, Doggett TA, Kolesnikov AV, Tang PH, et al. Noncanonical autophagy promotes the visual cycle. Cell. 2013;154(2):365-76.

290. Lee E, Koo Y, Ng A, Wei Y, Luby-Phelps K, Juraszek A, et al. Autophagy is essential for cardiac morphogenesis during vertebrate development. Autophagy. 2014;10(4):572-87.

291. Santos-Ledo A, Garcia-Macia M, Campbell PD, Gronska M, Marlow FL. Kinesin-1 promotes chondrocyte maintenance during skeletal morphogenesis. PLoS Genetics. 2017;13(7):e1006918.

292. Streeter A, Menzies FM, Rubinsztein DC. LC3-II tagging and western blotting for monitoring autophagic activity in mammalian cells. Systems biology of Alzheimer's disease: Springer; 2016. p. 161-70.

293. Akiyama H, Chaboissier M-C, Martin JF, Schedl A, de Crombrugghe B. The transcription factor Sox9 has essential roles in successive steps of the chondrocyte differentiation pathway and is required for expression of Sox5 and Sox6. Genes & development. 2002;16(21):2813-28.

294. Yan Y-L, Willoughby J, Liu D, Crump JG, Wilson C, Miller CT, et al. A pair of Sox: distinct and overlapping functions of zebrafish sox9 co-orthologs in craniofacial and pectoral fin development. Development. 2005;132(5):1069-83.

295. Iezaki T, Horie T, Fukasawa K, Kitabatake M, Nakamura Y, Park G, et al. Translational control of Sox9 RNA by mTORC1 contributes to skeletogenesis. Stem cell reports. 2018;11(1):228-41.

296. Rabanal-Ruiz Y, Otten EG, Korolchuk VI. mTORC1 as the main gateway to autophagy. Essays in biochemistry. 2017;61(6):565-84.

297. Samsa WE, Zhou X, Zhou G, editors. Signaling pathways regulating cartilage growth plate formation and activity. Seminars in cell & developmental biology; 2017: Elsevier.

298. Dreier R. Hypertrophic differentiation of chondrocytes in osteoarthritis: the developmental aspect of degenerative joint disorders. Arthritis research & therapy. 2010;12(5):1-11.

299. Lefebvre V, Behringer R, De Crombrugghe B. L-Sox5, Sox6 and Sox9 control essential steps of the chondrocyte differentiation pathway. Osteoarthritis and cartilage. 2001;9:S69-S75.

300. Ng L-J, Wheatley S, Muscat GE, Conway-Campbell J, Bowles J, Wright E, et al. SOX9 binds DNA, activates transcription, and coexpresses with type II collagen during chondrogenesis in the mouse. Developmental biology. 1997;183(1):108-21.

301. Hatta K, Tsujii H, Omura T. Cell tracking using a photoconvertible fluorescent protein. Nature protocols. 2006;1(2):960-7.

302. Pan YA, Freundlich T, Weissman TA, Schoppik D, Wang XC, Zimmerman S, et al. Zebrabow: multispectral cell labeling for cell tracing and lineage analysis in zebrafish. Development. 2013;140(13):2835-46.

303. Cong L, Ran FA, Cox D, Lin S, Barretto R, Habib N, et al. Multiplex genome engineering using CRISPR/Cas systems. Science. 2013;339(6121):819-23.

304. Makarova KS, Wolf YI, Alkhnbashi OS, Costa F, Shah SA, Saunders SJ, et al. An updated evolutionary classification of CRISPR–Cas systems. Nature Reviews Microbiology. 2015;13(11):722-36.

305. Shmakov S, Abudayyeh OO, Makarova KS, Wolf YI, Gootenberg JS, Semenova E, et al. Discovery and functional characterization of diverse class 2 CRISPR-Cas systems. Molecular cell. 2015;60(3):385-97.

306. Makarova K, Grishin N, Shabalina S, Wolf Y, Koonin E. A putative RNA-interference-based immune system in prokaryotes: Computational analysis of the. 2006.

307. Hwang WY, Fu Y, Reyon D, Maeder ML, Tsai SQ, Sander JD, et al. Efficient genome editing in zebrafish using a CRISPR-Cas system. Nature biotechnology. 2013;31(3):227-9.

308. Cross SH, Macalinao DG, McKie L, Rose L, Kearney AL, Rainger J, et al. A dominant-negative mutation of mouse Lmx1b causes glaucoma and is semi-lethal via LBD1-mediated dimerisation. PLoS genetics. 2014;10(5):e1004359.

309. Dunston JA, Reimschisel T, Ding Y-Q, Sweeney E, Johnson RL, Chen Z-F, et al. A neurological phenotype in nail patella syndrome (NPS) patients illuminated by studies of murine Lmx1b expression. European journal of human genetics. 2005;13(3):330-5.

310. Mishima Y, Lindgren AG, Chizhikov VV, Johnson RL, Millen KJ. Overlapping function of Lmx1a and Lmx1b in anterior hindbrain roof plate formation and cerebellar growth. Journal of Neuroscience. 2009;29(36):11377-84.

311. Ding Y-Q, Marklund U, Yuan W, Yin J, Wegman L, Ericson J, et al. Lmx1b is essential for the development of serotonergic neurons. Nature neuroscience. 2003;6(9):933-8.

312. Rohr C, Prestel J, Heidet L, Hosser H, Kriz W, Johnson RL, et al. The LIM-homeodomain transcription factor Lmx1b plays a crucial role in podocytes. The Journal of clinical investigation. 2002;109(8):1073-82.

313. Amores A, Force A, Yan Y-L, Joly L, Amemiya C, Fritz A, et al. Zebrafish hox clusters and vertebrate genome evolution. Science. 1998;282(5394):1711-4.

314. Gates MA, Kim L, Egan ES, Cardozo T, Sirotkin HI, Dougan ST, et al. A genetic linkage map for zebrafish: comparative analysis and localization of genes and expressed sequences. Genome research. 1999;9(4):334-47.

315. Schibler A, Malicki J. A screen for genetic defects of the zebrafish ear. Mechanisms of development. 2007;124(7-8):592-604.

316. Obholzer N, Swinburne IA, Schwab E, Nechiporuk AV, Nicolson T, Megason SG. Rapid positional cloning of zebrafish mutations by linkage and homozygosity mapping using whole-genome sequencing. Development. 2012;139(22):4280-90.

317. Labun K, Montague TG, Krause M, Torres Cleuren YN, Tjeldnes H, Valen E. CHOPCHOP v3: expanding the CRISPR web toolbox beyond genome editing. Nucleic acids research. 2019;47(W1):W171-W4.

318. Dunston JA, Hamlington JD, Zaveri J, Sweeney E, Sibbring J, Tran C, et al. The human LMX1B gene: transcription unit, promoter, and pathogenic mutations. Genomics. 2004;84(3):565-76.

319. Hamlington JD, Jones C, McIntosh I. Twenty-two novel LMX1B mutations identified in nail patella syndrome (NPS) patients. Human mutation. 2001;18(5):458-.

320. Seri M, Melchionda S, Dreyer S, Marini M, Carella M, Cusano R, et al. Identification of LMX1B gene point mutations in italian patients affected with Nail-Patella syndrome. International journal of molecular medicine. 1999;4(3):285-375.

321. Knoers NV, Bongers EM, Van Beersum SE, Lommen EJ, VAN BOKHOVEN H, Hol FA. Nail-patella syndrome: identification of mutations in the LMX1B gene in Dutch families. Journal of the American Society of Nephrology. 2000;11(9):1762-6.

322. Bongers EM, De Wijs IJ, Marcelis C, Hoefsloot LH, Knoers NV. Identification of entire LMX1B gene deletions in nail patella syndrome: evidence for haploinsufficiency as the main pathogenic mechanism underlying dominant inheritance in man. European journal of human genetics. 2008;16(10):1240-4.

323. Jao L-E, Wente SR, Chen W. Efficient multiplex biallelic zebrafish genome editing using a CRISPR nuclease system. Proceedings of the National Academy of Sciences. 2013;110(34):13904-9.

324. Kotani H, Taimatsu K, Ohga R, Ota S, Kawahara A. Efficient multiple genome modifications induced by the crRNAs, tracrRNA and Cas9 protein complex in zebrafish. PloS one. 2015;10(5):e0128319.

325. Lee J-S, Kwak S-J, Kim J, Kim A-K, Noh HM, Kim J-S, et al. RNA-guided genome editing in Drosophila with the purified Cas9 protein. G3: Genes, Genomes, Genetics. 2014;4(7):1291-5.

326. Stepanenko A, Dmitrenko V. HEK293 in cell biology and cancer research: phenotype, karyotype, tumorigenicity, and stress-induced genome-phenotype evolution. Gene. 2015;569(2):182-90.

327. Bylund L, Kytölä S, Lui W-O, Larsson C, Weber G. Analysis of the cytogenetic stability of the human embryonal kidney cell line 293 by cytogenetic and STR profiling approaches. Cytogenetic and genome research. 2004;106(1):28-32.

328. Lin Y-C, Boone M, Meuris L, Lemmens I, Van Roy N, Soete A, et al. Genome dynamics of the human embryonic kidney 293 lineage in response to cell biology manipulations. Nature communications. 2014;5(1):1-12.

329. Qi LS, Larson MH, Gilbert LA, Doudna JA, Weissman JS, Arkin AP, et al. Repurposing CRISPR as an RNA-guided platform for sequence-specific control of gene expression. Cell. 2013;152(5):1173-83.

330. Voordeckers K, Verstrepen KJ. Experimental evolution of the model eukaryote Saccharomyces cerevisiae yields insight into the molecular mechanisms underlying adaptation. Current opinion in microbiology. 2015;28:1-9.

331. Force A, Lynch M, Pickett FB, Amores A, Yan Y-l, Postlethwait J. Preservation of duplicate genes by complementary, degenerative mutations. Genetics. 1999;151(4):1531-45.

332. Ota S, Hisano Y, Ikawa Y, Kawahara A. Multiple genome modifications by the CRISPR/Cas9 system in zebrafish. Genes to Cells. 2014;19(7):555-64.

333. Kim S, Kim D, Cho SW, Kim J, Kim J-S. Highly efficient RNA-guided genome editing in human cells via delivery of purified Cas9 ribonucleoproteins. Genome research. 2014;24(6):1012-9.

334. Lino CA, Harper JC, Carney JP, Timlin JA. Delivering CRISPR: a review of the challenges and approaches. Drug delivery. 2018;25(1):1234-57.

335. Ramakrishna S, Dad A-BK, Beloor J, Gopalappa R, Lee S-K, Kim H. Gene disruption by cell-penetrating peptide-mediated delivery of Cas9 protein and guide RNA. Genome research. 2014;24(6):1020-7.

336. Dreyer SD, Zhou G, Baldini A, Winterpacht A, Zabel B, Cole W, et al. Mutations in LMX1B cause abnormal skeletal patterning and renal dysplasia in nail patella syndrome. Nature genetics. 1998;19(1):47-50.

337. Chen H, Ovchinnikov D, Pressman CL, Aulehla A, Lun Y, Johnson RL. Multiple calvarial defects in lmx1b mutant mice. Developmental genetics. 1998;22(4):314-20.

338. Malhotra R, Warne JP, Salas E, Xu AW, Debnath J. Loss of Atg12, but not Atg5, in pro-opiomelanocortin neurons exacerbates diet-induced obesity. Autophagy. 2015;11(1):145-54.

339. Saitoh T, Fujita N, Jang MH, Uematsu S, Yang B-G, Satoh T, et al. Loss of the autophagy protein Atg16L1 enhances endotoxin-induced IL-1β production. Nature. 2008;456(7219):264-8.

340. Deegens JK, Dijkman HB, Borm GF, Steenbergen EJ, Van Den Berg JG, Weening JJ, et al. Podocyte foot process effacement as a diagnostic tool in focal segmental glomerulosclerosis. Kidney international. 2008;74(12):1568-76.

341. Miner JH, Morello R, Andrews KL, Li C, Antignac C, Shaw AS, et al. Transcriptional induction of slit diaphragm genes by Lmx1b is required in podocyte differentiation. The Journal of clinical investigation. 2002;109(8):1065-72.

342. Drummond IA, Davidson AJ. Zebrafish kidney development. Methods in cell biology. 100: Elsevier; 2010. p. 233-60.

343. Wingert R, Davidson A. The zebrafish pronephros: a model to study nephron segmentation. Kidney international. 2008;73(10):1120-7.

344. Ding Y-J, Wang B-C, Wen C-C, Sun C-Y, Lee H-H, Lee F-P, et al. Evaluation of the teratogenic effects of three traditional Chinese medicines, Si Jun Zi Tang, Liu Jun Zi Tang and Shenling Baizhu San, during zebrafish pronephros development. Journal of Toxicologic Pathology. 2015;28(3):141-9.

345. Outtandy P, Russell C, Kleta R, Bockenhauer D. Zebrafish as a model for kidney function and disease. Pediatric Nephrology. 2019;34(5):751-62.

346. Yan CH, Levesque M, Claxton S, Johnson RL, Ang S-L. Lmx1a and lmx1b function cooperatively to regulate proliferation, specification, and differentiation of midbrain dopaminergic progenitors. Journal of Neuroscience. 2011;31(35):12413-25.

347. Wever I, Largo-Barrientos P, Hoekstra EJ, Smidt MP. Lmx1b influences correct post-mitotic coding of mesodiencephalic dopaminergic neurons. Frontiers in molecular neuroscience. 2019;12:62.

348. Nakamura H, Katahira T, Matsunaga E, Sato T. Isthmus organizer for midbrain and hindbrain development. Brain research reviews. 2005;49(2):120-6.

349. Adams KA, Maida JM, Golden JA, Riddle RD. The transcription factor Lmx1b maintains Wnt1 expression within the isthmic organizer. Development. 2000;127(9):1857-67.

350. Chabrat A, Brisson G, Doucet-Beaupré H, Salesse C, Schaan Profes M, Dovonou A, et al. Transcriptional repression of Plxnc1 by Lmx1a and Lmx1b directs topographic dopaminergic circuit formation. Nature communications. 2017;8(1):1-15.

351. Zhao Z-Q, Scott M, Chiechio S, Wang J-S, Renner KJ, Gereau RW, et al. Lmx1b is required for maintenance of central serotonergic neurons and mice lacking central serotonergic system exhibit normal locomotor activity. Journal of Neuroscience. 2006;26(49):12781-8.

352. Tachmazidou I, Hatzikotoulas K, Southam L, Esparza-Gordillo J, Haberland V, Zheng J, et al. Identification of new therapeutic targets for osteoarthritis through genome-wide analyses of UK Biobank data. Nature genetics. 2019;51(2):230-6.

353. Cavallin JE, Ankley GT, Blackwell BR, Blanksma CA, Fay KA, Jensen KM, et al. Impaired swim bladder inflation in early life stage fathead minnows exposed to a deiodinase inhibitor, iopanoic acid. Environmental toxicology and chemistry. 2017;36(11):2942-52.

354. Winata CL, Korzh S, Kondrychyn I, Zheng W, Korzh V, Gong Z. Development of zebrafish swimbladder: The requirement of Hedgehog signaling in specification and organization of the three tissue layers. Developmental biology. 2009;331(2):222-36.

355. Hill AJ, Bello SM, Prasch AL, Peterson RE, Heideman W. Water permeability and TCDD-induced edema in zebrafish early-life stages. Toxicological Sciences. 2004;78(1):78-87.

356. Kramer-Zucker AG, Wiessner S, Jensen AM, Drummond IA. Organization of the pronephric filtration apparatus in zebrafish requires Nephrin, Podocin and the FERM domain protein Mosaic eyes. Developmental biology. 2005;285(2):316-29.

357. Qi W, Keenan HA, Li Q, Ishikado A, Kannt A, Sadowski T, et al. Pyruvate kinase M2 activation may protect against the progression of diabetic glomerular pathology and mitochondrial dysfunction. Nature medicine. 2017;23(6):753-62.

358. Kolhe N, Stoves J, Will EJ, Hartley B. Nail-patella syndrome—renal and musculo-skeletal features. Nephrology Dialysis Transplantation. 2002;17(1):169-70.

359. Vogel A, Rodriguez C, Izpisúa-Belmonte J-C. Involvement of FGF-8 in initiation, outgrowth and patterning of the vertebrate limb. Development. 1996;122(6):1737-50.

360. BEALS RK, ECKHARDT AL. Hereditary onycho-osteodysplasia (nail-patella syndrome): a report of nine kindreds. JBJS. 1969;51(3):505-16.

361. Guo X, Piao H, Xue Y, Liu Y, Zhao H. LMX1B-associated gankyrin expression predicts poor prognosis in glioma patients. Journal of International Medical Research. 2020;48(9):0300060520954764.

362. Zang C, Zhao F, Pu Y. LMX1B involved in the radioresistance, proliferation and migration of esophageal cancer cells. Biomedicine & Pharmacotherapy. 2019;118:109358.

363. Lowery LA, Sive H. Initial formation of zebrafish brain ventricles occurs independently of circulation and requires the nagie oko and snakehead/atp1a1a. 1 gene products. 2005.

364. Milhorat TH. Structure and function of the choroid plexus and other sites of cerebrospinal fluid formation. International review of cytology. 1976;47:225-88.

365. Cushing H, Goetsch E. Concerning the secretion of the infundibular lobe of the pituitary body and its presence in the cerebrospinal fluid. American Journal of Physiology-Legacy Content. 1910;27(1):60-86.

366. Louvi A, Alexandre P, Métin C, Wurst W, Wassef M. The isthmic neuroepithelium is essential for cerebellar midline fusion. 2003.

367. Gutzman JH, Graeden EG, Lowery LA, Holley HS, Sive H. Formation of the zebrafish midbrain–hindbrain boundary constriction requires laminin-dependent basal constriction. Mechanisms of development. 2008;125(11-12):974-83.

368. Molinoff PB, Axelrod J. Biochemistry of catecholamines. Annual review of biochemistry. 1971;40(1):465-500.

369. Weihe E, Depboylu C, Schütz B, Schäfer MK-H, Eiden LE. Three types of tyrosine hydroxylase-positive CNS neurons distinguished by dopa decarboxylase and VMAT2 co-expression. Cellular and molecular neurobiology. 2006;26(4):657-76.

370. Antunes GF, Gouveia FV, Rezende FS, de Jesus Seno MD, de Carvalho MC, de Oliveira CC, et al. Dopamine modulates individual differences in avoidance behavior: A pharmacological, immunohistochemical, neurochemical and volumetric investigation. Neurobiology of stress. 2020;12:100219.

371. Ellis K, Hoffman BD, Bagnat M. The vacuole within: how cellular organization dictates notochord function. Bioarchitecture. 2013;3(3):64-8.

372. Ellis K, Bagwell J, Bagnat M. Notochord vacuoles are lysosome-related organelles that function in axis and spine morphogenesis. Journal of Cell Biology. 2013;200(5):667-79.

373. Karpanen T, Schulte-Merker S. Zebrafish provides a novel model for lymphatic vascular research. Methods in cell biology. 105: Elsevier; 2011. p. 223-38.

374. Miura GI, Yelon D. A guide to analysis of cardiac phenotypes in the zebrafish embryo. Methods in cell biology. 2011;101:161-80.

375. Drummond IA, Majumdar A, Hentschel H, Elger M, Solnica-Krezel L, Schier AF, et al. Early development of the zebrafish pronephros and analysis of mutations affecting pronephric function. Development. 1998;125(23):4655-67.

376. Christou-Savina S, Beales PL, Osborn DP. Evaluation of zebrafish kidney function using a fluorescent clearance assay. JoVE (Journal of Visualized Experiments). 2015(96):e52540.

377. Kotb AM, Müller T, Xie J, Anand-Apte B, Endlich K, Endlich N. Simultaneous assessment of glomerular filtration and barrier function in live zebrafish. American Journal of Physiology-Renal Physiology. 2014;307(12):F1427-F34.

378. Hentschel DM, Park KM, Cilenti L, Zervos AS, Drummond I, Bonventre JV. Acute renal failure in zebrafish: a novel system to study a complex disease. American Journal of Physiology-Renal Physiology. 2005;288(5):F923-F9.

379. Zhou W, Hildebrandt F. Inducible podocyte injury and proteinuria in transgenic zebrafish. Journal of the American Society of Nephrology. 2012;23(6):1039-47.

380. Elmonem MA, Berlingerio SP, Van den Heuvel LP, De Witte PA, Lowe M, Levtchenko EN. Genetic renal diseases: the emerging role of zebrafish models. Cells. 2018;7(9):130.

381. Chen J, Long F. mTORC1 signaling controls mammalian skeletal growth through stimulation of protein synthesis. Development. 2014;141(14):2848-54.

382. Towers AL, Clay CA, Sereika SM, McIntosh I, Greenspan SL. Skeletal integrity in patients with nail patella syndrome. The Journal of Clinical Endocrinology & Metabolism. 2005;90(4):1961-5.

383. Zhang R, Yang J, Zhu J, Xu X. Depletion of zebrafish Tcap leads to muscular dystrophy via disrupting sarcomere–membrane interaction, not sarcomere assembly. Human molecular genetics. 2009;18(21):4130-40.

384. Novarino G, Fenstermaker AG, Zaki MS, Hofree M, Silhavy JL, Heiberg AD, et al. Exome sequencing links corticospinal motor neuron disease to common neurodegenerative disorders. science. 2014;343(6170):506-11.

385. Dai J-X, Han H-L, Tian M, Cao J, Xiu J-B, Song N-N, et al. Enhanced contextual fear memory in central serotonin-deficient mice. Proceedings of the National Academy of Sciences. 2008;105(33):11981-6.

386. Kaucka M, Ivashkin E, Gyllborg D, Zikmund T, Tesarova M, Kaiser J, et al. Analysis of neural crest–derived clones reveals novel aspects of facial development. Science advances. 2016;2(8):e1600060.

387. Liu G, Ito T, Kijima Y, Yoshitake K, Asakawa S, Watabe S, et al. Zebrafish Danio rerio trunk muscle structure and growth from a spatial transcriptomics perspective. bioRxiv. 2021.

388. Ellis KL. Molecular Mechanisms of Notochord Vacuole Formation and Their Role in Zebrafish Development 2014.

389. Faria M, Garcia-Reyero N, Padrós F, Babin PJ, Sebastián D, Cachot J, et al. Zebrafish models for human acute organophosphorus poisoning. Scientific reports. 2015;5(1):1-16.

390. Keenan SR, Currie PD. The developmental phases of zebrafish myogenesis. Journal of Developmental Biology. 2019;7(2):12.

391. Chung S, Leung A, Han B-S, Chang M-Y, Moon J-I, Kim C-H, et al. Wnt1-lmx1a forms a novel autoregulatory loop and controls midbrain dopaminergic differentiation synergistically with the SHH-FoxA2 pathway. Cell stem cell. 2009;5(6):646-58.

392. Foster JW, Dominguez-Steglich MA, Guioli S, Kwok C, Weller PA, Stevanović M, et al. Campomelic dysplasia and autosomal sex reversal caused by mutations in an SRY-related gene. Nature. 1994;372(6506):525-30.

393. Henry SP, Liang S, Akdemir KC, De Crombrugghe B. The postnatal role of Sox9 in cartilage. Journal of Bone and Mineral Research. 2012;27(12):2511-25.

394. Wu P-J, Masouleh MI, Dini D, Paterson C, Török P, Overby DR, et al. Detection of proteoglycan loss from articular cartilage using Brillouin microscopy, with applications to osteoarthritis. Biomedical optics express. 2019;10(5):2457-66.

395. Haseeb A, Kc R, Angelozzi M, de Charleroy C, Rux D, Tower RJ, et al. SOX9 keeps growth plates and articular cartilage healthy by inhibiting chondrocyte dedifferentiation/osteoblastic redifferentiation. Proceedings of the National Academy of Sciences. 2021;118(8).

396. Song H, Park K-H, editors. Regulation and function of SOX9 during cartilage development and regeneration. Seminars in cancer biology; 2020: Elsevier.

397. Dai Q, Xu Z, Ma X, Niu N, Zhou S, Xie F, et al. mTOR/Raptor signaling is critical for skeletogenesis in mice through the regulation of Runx2 expression. Cell Death & Differentiation. 2017;24(11):1886-99.

398. Yan B, Zhang Z, Jin D, Cai C, Jia C, Liu W, et al. mTORC1 regulates PTHrP to coordinate chondrocyte growth, proliferation and differentiation. Nature communications. 2016;7(1):1-15.

399. Gao B, Guo J, She C, Shu A, Yang M, Tan Z, et al. Mutations in IHH, encoding Indian hedgehog, cause brachydactyly type A-1. Nature genetics. 2001;28(4):386-8.

400. Phornphutkul C, Wu KY, Auyeung V, Chen Q, Gruppuso PA. mTOR signaling contributes to chondrocyte differentiation. Developmental dynamics: an official publication of the American Association of Anatomists. 2008;237(3):702-12.

401. He B, Ebarasi L, Zhao Z, Guo J, Ojala JR, Hultenby K, et al. Lmx1b and FoxC combinatorially regulate podocin expression in podocytes. J Am Soc Nephrol. 2014;25(12):2764-77.

402. Burzynski GM, Reed X, Maragh S, Matsui T, McCallion AS. Integration of genomic and functional approaches reveals enhancers at LMX1A and LMX1B. Molecular genetics and genomics. 2013;288(11):579-89.

403. Reinstein E. Schizophrenia and Nail Patella Syndrome: The Dopamine Connection. The Israel Medical Association Journal: IMAJ. 2018;20(8):496-8.

404. Eyre D, Wu J. Collagen structure and cartilage matrix integrity. The Journal of rheumatology Supplement. 1995;43:82-5.

405. Fernandes RJ, Weis M, Scott MA, Seegmiller RE, Eyre DR. Collagen XI chain misassembly in cartilage of the chondrodysplasia (cho) mouse. Matrix Biology. 2007;26(8):597-603.

406. Chen Y-c, Chen M, Gaffney EA, Brown CP. Effect of crosslinking in cartilage-like collagen microstructures. Journal of the mechanical behavior of biomedical materials. 2017;66:138-43.

407. Bönnemann CG, Cox GF, Shapiro F, Wu J-J, Feener CA, Thompson TG, et al. A mutation in the alpha 3 chain of type IX collagen causes autosomal dominant multiple epiphyseal dysplasia with mild myopathy. Proceedings of the National Academy of Sciences. 2000;97(3):1212-7.

408. Vikkula M, Madman EC, Lui VC, Zhidkova NI, Tiller GE, Goldring MB, et al. Autosomal dominant and recessive osteochondrodysplasias associated with the COL11A2 locus. Cell. 1995;80(3):431-7.

409. Gelse K, Pöschl E, Aigner T. Collagens—structure, function, and biosynthesis. Advanced drug delivery reviews. 2003;55(12):1531-46.

410. Hauser N, Paulsson M, Heinegård D, Mörgelin M. Interaction of cartilage matrix protein with aggrecan: increased covalent cross-linking with tissue maturation. Journal of Biological Chemistry. 1996;271(50):32247-52.

411. Klatt AR, Paulsson M, Wagener R. Expression of matrilins during maturation of mouse skeletal tissues. Matrix biology. 2002;21(3):289-96.

412. Neacsu CD, Ko Y-P, Tagariello A, Karlsen KR, Neiss WF, Paulsson M, et al. Matrilin-1 is essential for zebrafish development by facilitating collagen II secretion. Journal of Biological Chemistry. 2014;289(3):1505-18.

413. Zhang Y, Cui F, Wang X, Feng Q, Zhu X. Mechanical properties of skeletal bone in gene-mutated stöpseldtl28d and wild-type zebrafish (Danio rerio) measured by atomic force microscopy-based nanoindentation. Bone. 2002;30(4):541-6.

414. Man G, Mologhianu G. Osteoarthritis pathogenesis–a complex process that involves the entire joint. Journal of medicine and life. 2014;7(1):37.

415. Li G, Yin J, Gao J, Cheng TS, Pavlos NJ, Zhang C, et al. Subchondral bone in osteoarthritis: insight into risk factors and microstructural changes. Arthritis research & therapy. 2013;15(6):1-12.

416. Lane NE, Lin P, Christiansen L, Gore LR, Williams EN, Hochberg MC, et al. Association of mild acetabular dysplasia with an increased risk of incident hip osteoarthritis in elderly white women: the study of osteoporotic fractures. Arthritis & Rheumatism: Official Journal of the American College of Rheumatology. 2000;43(2):400-4.

417. Shepstone L, Rogers J, Kirwan J, Silverman B. Shape of the intercondylar notch of the human femur: a comparison of osteoarthritic and non-osteoarthritic bones from a skeletal sample. Annals of the rheumatic diseases. 2001;60(10):968-73.

418. Cicuttini F, Wluka A, Hankin J, Wang Y. Longitudinal study of the relationship between knee angle and tibiofemoral cartilage volume in subjects with knee osteoarthritis. Rheumatology. 2004;43(3):321-4.

419. Spector TD, Cicuttini F, Baker J, Loughlin J, Hart D. Genetic influences on osteoarthritis in women: a twin study. Bmj. 1996;312(7036):940-3.

420. Spector TD, MacGregor AJ. Risk factors for osteoarthritis: genetics. Osteoarthritis and cartilage. 2004;12:39-44.

421. Valdes AM, Spector TD. Genetic epidemiology of hip and knee osteoarthritis. Nature Reviews Rheumatology. 2011;7(1):23-32.

422. Page WF, Hoaglund FT, Steinbach LS, Heath AC. Primary osteoarthritis of the hip in monozygotic and dizygotic male twins. Twin Research and Human Genetics. 2003;6(2):147-51.

423. Capellini TD, Chen H, Cao J, Doxey AC, Kiapour AM, Schoor M, et al. Ancient selection for derived alleles at a GDF5 enhancer influencing human growth and osteoarthritis risk. Nat Genet. 2017;49(8):1202-10.

424. Valdes AM, Spector TD. The clinical relevance of genetic susceptibility to osteoarthritis. Best practice & research Clinical rheumatology. 2010;24(1):3-14.

425. Bian Q, Wang Y-J, Liu SF, Li Y-P. Osteoarthritis: genetic factors, animal models, mechanisms, and therapies. Front Biosci (Elite Ed). 2012;4(1):74-100.

426. Urban JP, Roberts S. Degeneration of the intervertebral disc. Arthritis Res Ther. 2003;5(3):1-11.

427. Wopat S, Bagwell J, Sumigray KD, Dickson AL, Huitema LF, Poss KD, et al. Spine patterning is guided by segmentation of the notochord sheath. Cell reports. 2018;22(8):2026-38.

428. Cesario JM, Malt AL, Chung JU, Khairallah MP, Dasgupta K, Asam K, et al. Anti-osteogenic function of a LIM-homeodomain transcription factor LMX1B is essential to early patterning of the calvaria. Developmental biology. 2018;443(2):103-16.

429. Johnson D, Wilkie AO. Craniosynostosis. European Journal of Human Genetics. 2011;19(4):369-76.

430. Yu M, Ma L, Yuan Y, Ye X, Montagne A, He J, et al. Cranial suture regeneration mitigates skull and neurocognitive defects in craniosynostosis. Cell. 2021;184(1):243-56. e18.